

**Global Ionospheric Total Electron Content Mapping
Using the Global Positioning System**

by

Attila Komjathy

Dipl. Ing. University of Miskolc, Hungary, 1989

A Thesis Submitted in Partial Fulfillment of
the Requirements for the Degree of

Doctor of Philosophy

in the Graduate Academic Unit of the
Department of Geodesy and Geomatics Engineering

Supervisor: **Richard B. Langley, Ph.D., Department of Geodesy
and Geomatics Engineering**

Examining Board: **Abdelhaq Hamza, Ph.D., Physics Department**
**Alfred Kleusberg, Ph.D., Department of Geodesy
and Geomatics Engineering**
**James Tranquilla, Ph.D., Department of Electrical
Engineering**

External Examiner: **John A. Klobuchar, M.S., Total Electronics
Concepts**

THE UNIVERSITY OF NEW BRUNSWICK

August, 1997

© Attila Komjathy, 1997



National Library
of Canada

Acquisitions and
Bibliographic Services

395 Wellington Street
Ottawa ON K1A 0N4
Canada

Bibliothèque nationale
du Canada

Acquisitions et
services bibliographiques

395, rue Wellington
Ottawa ON K1A 0N4
Canada

Your file Votre référence

Our file Notre référence

The author has granted a non-exclusive licence allowing the National Library of Canada to reproduce, loan, distribute or sell copies of this thesis in microform, paper or electronic formats.

The author retains ownership of the copyright in this thesis. Neither the thesis nor substantial extracts from it may be printed or otherwise reproduced without the author's permission.

L'auteur a accordé une licence non exclusive permettant à la Bibliothèque nationale du Canada de reproduire, prêter, distribuer ou vendre des copies de cette thèse sous la forme de microfiche/film, de reproduction sur papier ou sur format électronique.

L'auteur conserve la propriété du droit d'auteur qui protège cette thèse. Ni la thèse ni des extraits substantiels de celle-ci ne doivent être imprimés ou autrement reproduits sans son autorisation.

0-612-29468-4

ABSTRACT

Space-based radio navigation systems such as the Navstar Global Positioning System (GPS) can provide us with a unique opportunity to study the effect of the ionosphere as the signals propagate from the satellites to the GPS receivers.

Based on a modified version of UNB's DIPOP software package, I developed an algorithm to produce regional or global total electron content (TEC) maps on an hourly basis using dual frequency GPS observations from stations of the International GPS Service for Geodynamics (IGS). The algorithm uses a spatial linear approximation of the vertical TEC above each IGS station using stochastic parameters in a Kalman filter estimation to describe the local time and geomagnetic latitude dependence of the TEC. I used a new concept to take into account the temporally and spatially varying ionospheric shell height as opposed to a commonly adopted fixed shell height. I demonstrated that the UNB algorithm was capable of modelling the diurnal variation of TEC even during a geomagnetic storm period. I also have modified the International Reference Ionosphere 1995 (IRI-95) model to update its coefficient sets using the UNB GPS-derived regional ionospheric maps, based on a 5 week long GPS campaign, in order to provide more precise IRI-95-derived ionospheric delay predictions for e.g., single frequency GPS receivers.

I enhanced the UNB algorithm to estimate ionospheric model parameters from a global set of GPS stations to independently produce hourly snapshots of the global ionosphere. The previously modified IRI-95 model as a sophisticated interpolator was used between two GPS-derived TEC updates to provide improved IRI-95 ionospheric delay predictions. During the update procedure, I enhanced the IRI-95 model with an empirical plasmaspheric electron content model.

Based on 3 days' worth of global GPS data during a medium solar activity period in 1993 (33 IGS stations for each day) there was better than a 9 TECU level (1 sigma) agreement in the TEC on a global scale with TOPEX/Poseidon-derived (T/P) TEC data. For a low solar activity 1995 data set (74 IGS stations for each day), the UNB results showed an agreement with the T/P data at better than the 5 TECU level (1 sigma).

The UNB global ionospheric TEC modelling technique in conjunction with the IRI-95 update procedure has been demonstrated to be a viable alternative to provide independently-derived ground-based ionospheric delay corrections for single frequency applications such as single frequency radar altimeter missions.

TABLE OF CONTENTS

ABSTRACT	i
TABLE OF CONTENTS.....	iii
LIST OF TABLES.....	vi
LIST OF FIGURES	vii
ACKNOWLEDGEMENTS	x
CHAPTER 1: INTRODUCTION	1
1.1 Motivation of the Research.....	1
1.2 Literature Overview	4
1.2.1 Previous Ionospheric Work at UNB.....	5
1.2.2 Previous Work Elsewhere.....	7
1.3 Contribution of the Research.....	10
1.4 Outline of the Dissertation.....	12
CHAPTER 2: GPS AND ITS PLACE AMONG THE IONOSPHERIC PROBING TECHNIQUES.....	14
2.1 The Ionosphere	14
2.1.1 The Earth's Magnetic Field.....	15
2.1.2 Vertical Profile of the Ionosphere	15
2.1.2.1 The D Layer	18
2.1.2.2 The E Layer.....	19
2.1.2.3 The F1 Layer	20
2.1.2.4 The F2 Layer	20
2.1.3 Major Geographic Regions of the Ionosphere	21
2.1.3.1 Equatorial Region.....	22
2.1.3.2 Mid-Latitude Region.....	22
2.1.3.3 High-Latitude Region	23
2.1.4 Ionospheric Disturbances.....	24
2.1.4.1 Ionospheric Storms.....	25
2.1.4.2 Geomagnetic Storms.....	26
2.1.4.3 Ionospheric Scintillation.....	26
2.1.5 Solar-Terrestrial Indices	27
2.1.5.1 Kp and Ap Indices	27
2.1.5.2 Zurich Sunspot Number.....	29
2.1.5.3 Ottawa 10.7 cm (2800 MHz) Solar Radio Flux	30
2.1.5.4 IG Index	32
2.2 The Effects of the Ionosphere on the Propagation of Electromagnetic Waves	33

2.3 Global Ionospheric Modelling Techniques	41
2.3.1 Ionospheric Modelling Using the International Reference Ionosphere.....	42
2.3.2 Ionospheric Modelling Using the Parameterized Ionospheric Model.....	43
2.4 Ground-Based Techniques for Probing the Ionosphere	44
2.4.1 Ionosonde	46
2.4.2 Oblique Backscatter Radar	48
2.4.3 Incoherent Backscatter Radar	49
2.5 Satellite and Other Techniques	50
2.5.1 Global Positioning System	50
2.5.2 GLONASS.....	54
2.5.3 Transit.....	55
2.5.4 TOPEX/Poseidon	57
2.5.5 Faraday Rotation Technique	58
2.5.6 Topside Sounders.....	59
2.5.7 PRARE	59
2.5.8 DORIS	61
CHAPTER 3: MODELLING THE IONOSPHERE USING EMPIRICAL	
MODELS	63
3.1 Behaviour of the GPS Single Frequency Broadcast Model.....	64
3.2 Behaviour of the International Reference Ionosphere Model.....	70
3.3 Comparison of Predicted and Measured Ionospheric Range Error Corrections.....	73
3.4 Conclusions of the Long-Term Stability Between the Broadcast and IRI-90	
Models.....	75
CHAPTER 4: THE UNB APPROACH TO IONOSPHERIC MODELLING USING	
GPS.....	78
4.1 Commonly Used Modelling Techniques.....	78
4.1.1 Regional and Global Ionospheric Modelling.....	79
4.1.2 Ionospheric Tomography	81
4.1.3 GPS/Met	82
4.1.4 Real-Time Ionospheric Modelling: the WAAS Concept	84
4.1.5 Combination of Different Techniques.....	86
4.1.6 Ionospheric Modelling Using a Single Frequency GPS Receiver.....	87
4.2 The UNB Ionospheric Modelling Technique.....	89
4.2.1 Ionospheric Observable	90
4.2.2 Estimation Strategy	97
4.2.3 Ionospheric Shell Height Determination.....	100
4.2.4 Ionospheric Mapping Functions.....	101
4.2.5 Interpolation Scheme Used to Create, Display and Use the UNB TEC	
Maps	106
4.2.6 Plasmaspheric Electron Content Model.....	111
4.2.7 International Reference Ionosphere 1995 Modifications.....	113
CHAPTER 5: REGIONAL IONOSPHERIC MODELLING: A SENSITIVITY	
ANALYSIS	119

5.1 The UNB Regional Ionospheric Modelling Based on an IGS Campaign: A Sensitivity Analysis	119
5.1.1 The Effect of Different Elevation Cutoff Angles.....	121
5.1.2 The Effect of Ionospheric Shell Height	124
5.1.3 The Effect of a Geomagnetic Disturbance.....	128
5.1.4 Conclusion of the Sensitivity Analysis.....	134
5.2 The Varying Ionospheric Shell Height: A New Concept	135
5.2.1 Conclusions of the Investigation on the Varying Ionospheric Shell Height....	147
5.3 Improvement of the International Reference Ionosphere 1995 Model.....	148
5.3.1 Conclusions of the IRI-95 Modifications.....	158
5.4 Comparison of UNB's Regional TEC Maps with Those of Other Research Centers	159
5.5 Investigation of Different Ionospheric Mapping Functions	161
5.5.1 Conclusions of the Ionospheric Mapping Function Investigation	167
CHAPTER 6: GLOBAL IONOSPHERIC MODELLING: DATA PROCESSING AND ANALYSIS OF RESULTS.....	169
6.1 A Potential Application: Single Frequency Radar Altimetry	170
6.2 The UNB Ionospheric Modelling Technique for Correcting Single Frequency Altimeter Data	173
6.3 Data Processing and Analysis of Results.....	175
CHAPTER 7: CONCLUSIONS AND RECOMMENDATIONS FOR FUTURE RESEARCH	203
7.1 Conclusions of the Research.....	203
7.2 Recommendations for Future Work.....	206
REFERENCES.....	212
APPENDIX 1: KALMAN FILTER ESTIMATION.....	227
APPENDIX 2: THE UNB HOURLY GLOBAL IONOSPHERIC TOTAL ELECTRON CONTENT MAPS.....	230
APPENDIX 3: COMPARISON OF UPDATED IRI-95 MODEL WITH OTHER INDEPENDENT TECHNIQUES	238

LIST OF TABLES

Table 5.1: List of IGS stations used for regional ionospheric modelling	120
Table 5.2: Summary of comparison of differential delay differences between UNB and DLR, and r.m.s. of UNB ionospheric residuals	123
Table 5.3: Comparison of GPS-derived TEC estimates with IRI-90 predictions	133
Table 5.4: Summary of the weekly statistics to support the IRI-95 update procedure ...	154
Table 5.5: Summary of CPU times concerning the IRI-95 update procedure	155
Table 5.6: Investigation of different ionospheric mapping functions	165
Table 6.1: List of IGS stations used for the global ionospheric modelling	176
Table 6.2: Summary of statistics comparing the different TEC techniques with the 11 representative T/P passes	188
Table 6.3: Summary of results from the comparison between UNB global TEC maps and T/P-derived TEC data	196

LIST OF FIGURES

Figure 2.1:	Typical vertical profile of the ionosphere.....	16
Figure 2.2:	Major geographic regions of the ionosphere.....	21
Figure 2.3:	Illustration of geomagnetic field variation.....	29
Figure 2.4:	Solar sunspot activity during the last four solar cycles.....	31
Figure 2.5:	Observed daily solar flux variation.....	31
Figure 2.6:	System of orthogonal axes x, y, z.....	34
Figure 2.7:	Sample ionosonde data.....	48
Figure 3.1:	Vertical ionospheric delay predictions using 53 sets of Broadcast model coefficients.....	67
Figure 3.2:	Vertical ionospheric range error corrections on L1 predicted by GPS single frequency Broadcast model.....	68
Figure 3.3:	Broadcast model coefficients dependency on smoothed daily solar flux numbers.....	69
Figure 3.4:	Vertical ionospheric range error corrections using the IRI-90 model.....	72
Figure 3.5:	Vertical ionospheric range error corrections on L1 predicted by the IRI-90 model.....	72
Figure 3.6:	Predicted versus measured vertical ionospheric range error corrections on L1.....	74
Figure 3.7:	R.m.s. of day-time differences between vertical ionospheric range error corrections computed from Faraday rotation data and two empirical models.....	75
Figure 3.8:	R.m.s. of night-time differences between vertical ionospheric range error corrections computed from Faraday rotation data and two empirical models.....	75
Figure 4.1:	Interpolation method used to compute TEC between grid TEC values.....	109
Figure 5.1:	Locations of IGS stations used for regional ionospheric modelling.....	120
Figure 5.2:	Comparison of TEC estimates using different elevation cutoff angles.....	122
Figure 5.3:	Comparison of TEC estimates using different ionospheric shell heights.....	125
Figure 5.4:	An example of the diurnal variation of TEC for magnetically quiet and disturbed days for station Madrid.....	128
Figure 5.5:	An example of the diurnal variation of TEC for magnetically quiet and disturbed days for station Onsala.....	129

Figure 5.6: Ionospheric residuals for geomagnetically active day 292	131
Figure 5.7: Diurnal variation of TEC for 7 consecutive days using a network of 6 IGS stations.....	132
Figure 5.8: Illustration of ionospheric shell height determination	136
Figure 5.9: IRI-90 profile.....	137
Figure 5.10: The diurnal variation of the ionospheric shell height	138
Figure 5.11: Ionospheric shell height predictions using the IRI-90 model	139
Figure 5.12: Comparison of satellite-receiver differential delay estimates using IRI-90-derived and 400 km ionospheric shell heights.....	142
Figure 5.13: Comparison of TEC estimates using IRI-90-derived and 400 km ionospheric shell heights	142
Figure 5.14: Comparison of differential delay differences between IGS processing centers.....	144
Figure 5.15: Illustration for different ionospheric modelling techniques currently used at UNB.....	150
Figure 5.16: Hourly r.m.s. statistics to support the IRI-95 update procedure.....	153
Figure 5.17: Daily r.m.s. statistics to support the IRI-95 update procedure	154
Figure 5.18: Number of IRI-95 runs required to arrive at the proper scaling factor.....	156
Figure 5.19: Measured between-receiver differential delays during the zero-baseline experiment.....	163
Figure 5.20: Zero-baseline experiment at the University of New Brunswick, Fredericton, Canada.....	164
Figure 6.1: IGS stations used for the 1993 global ionospheric data processing	176
Figure 6.2: IGS stations used for the 1995 global ionospheric data processing	176
Figure 6.3: An example of hourly snapshot of the global ionosphere	180
Figure 6.4: Indication of geomagnetic field disturbance.....	182
Figure 6.5: Geomagnetic activity for the 1995 data	184
Figure 6.6: An example of the comparison of different techniques with T/P data	186
Figure 6.7: An example of the differences of TEC between different techniques with respect to a T/P pass	186
Figure 6.8: An example displaying the corresponding T/P pass.....	187
Figure 6.9: Comparison of updated IRI-95 and original IRI-95 with T/P for 13 March 1993	193
Figure 6.10: Comparison of updated IRI-95 and original IRI-95 with T/P for 14 March 1993	193

Figure 6.11: Comparison of the UNB global TEC maps with T/P-derived TEC data for 15 March 1993.....	194
Figure 6.12: Comparison of the UNB global TEC maps with T/P-derived TEC data for 6 April 1995.....	194
Figure 6.13: Comparison of the UNB global TEC maps with T/P-derived TEC data for 7 April 1995.....	195
Figure 6.14: Comparison of the UNB global TEC maps with T/P-derived TEC data for 8 April 1995.....	195
Figure 6.15: Comparison of different techniques with Faraday rotation data for 26 March 1993 at Palehua, HI.....	200
Figure 6.16: Comparison of different techniques with Faraday rotation data for 26 March 1993 at Taoyuan, Taiwan.....	200
Figure 6.17: Comparison of different techniques with Faraday rotation data for 26 March 1993 at Cape Canaveral, FL.....	201
Figure 6.18: Comparison of different techniques with Faraday rotation data for 26 March 1993 at Osan, Korea.....	201
Figure 6.19: Comparison of different techniques with Faraday rotation data for 26 March 1993 at Boulder, CO.....	201
Figure 6.20: Comparison of different techniques with Faraday rotation data for 26 March 1993 at Anchorage, AK.....	202

ACKNOWLEDGEMENTS

I would like to express my sincere gratitude to my supervisor Professor Richard Langley who supported me, encouraged me and kept my spirits up all through my graduate studies at the University of New Brunswick. His vast knowledge and experience in science will always remain with me as an example to follow. Professor Langley has helped my graduate studies to be a rewarding and enjoyable experience.

Funding for this research was provided by the University of New Brunswick and the Natural Sciences and Engineering Research Council of Canada. From September 1991, a 10-month scholarship was awarded by the Hungarian Széchenyi István Scholarship Foundation to support my doctoral studies in Canada. Their help is gratefully acknowledged.

A special thanks goes to Nav Canada (formerly part of Transport Canada Aviation) who gave me the opportunity to get involved in several exciting GPS-related projects during the six years of my graduate studies. These projects have helped me understand GPS, data processing and data analysis. Rob Butler, George Dewar and Bill Boucher are those I am the most grateful to.

Many thanks goes to Dr. Dieter Bilitza for his support and suggestions with regards to my ionospheric research. I am also grateful for the travel grants provided by the University of Colorado and the Committee on Space Research (COSPAR).

A heartfelt thanks goes to my former and present fellow graduate students for exchanging ideas and experiences. Among them are: Simon Newby, Virgílio Mendes, Marcelo Santos, Anthony van der Wal, Xin Chen, Paul Collins and Sunil Bisnath to mention only a few of them.

Finally, I would like to dedicate this dissertation to my wife, Katalin without whom I would not have been able to accomplish this. Her dedication to and appreciation of my work has had an enormous contribution to this research. Also, very special thanks goes to my extended family in Hungary: my parents, Erzsébet and Zoltán Komjáthy for their unconditional support and understanding that always encouraged me to follow the path I have chosen; Katalin's parents, Anna and Árpád Tóth; and Kriszta, Zsolt, Fanni, Adrienn and Csaba.

CHAPTER 1

INTRODUCTION

The ionosphere is an important error source for the signals of the Navstar Global Positioning System (GPS) satellites which is often treated in the analysis of the GPS measurements as a nuisance. On the other hand we can also determine the error induced by the ionosphere in order to study the temporal and spatial variation of the ionosphere which is the subject of this dissertation. In this chapter I will describe the motivation of my work. This will be followed by a literature review that inspired me. The chapter will be concluded by the contribution of the dissertation and a brief outline of each subsequent chapter.

1.1 Motivation of the Research

The signals of the GPS satellites must travel through the earth's ionosphere on their way to GPS receivers on or near the earth's surface. To achieve the highest possible positioning accuracies from GPS, one must correct for the carrier phase advance and pseudorange group delay imposed on the signals by the ionosphere. If we have dual frequency GPS receivers, then the ionospheric effect can be almost totally accounted for by taking advantage of the ionosphere's dispersive nature. If we have single frequency GPS receivers, then we can ignore the effect and live with the consequences or we can try to minimize the effect using processing techniques such as the double difference solution

of the L1 carrier phase or pseudorange observations. We can also model the effect by using a global empirical model such as the International Reference Ionosphere 1995 (IRI-95) [Bilitza, 1990] or the Bent model [Bent and Liewellyn, 1973] or a physics-based ionospheric model such as the Parameterized Ionospheric Model (PIM) [Daniell et al., 1995]. Whereas this ionospheric effect may be considered a nuisance by most GPS users, they will provide the ionospheric community with an opportunity to use GPS as a tool to better understand the plasma surrounding the earth.

The ionosphere is a dispersive medium for radio waves implying that the refractive index is a function of the radio waves' frequency, the electron density, and to a minor degree, the intensity of the earth's magnetic field. After integrating the phase and group refractive indices along the path of the GPS signal we will obtain a range between the satellite and the receiver which is different from the true geometric range by the amount that we call ionospheric error. The error is negative for the carrier phases (phase is advanced; that is, the measured range is shorter than the geometric range), and positive for the pseudoranges (a group delay; that is, the measured range is longer than the geometric range). The phase advance and group delay are of equal size but opposite sign. To an excellent first order approximation, ionospheric error is proportional to the integrated electron density along the signal path (total electron content, TEC) and inversely proportional to the square of the carrier phase frequency [Langley, 1996].

The currently used global ionospheric models can only model the monthly mean total electron content to about ± 10 percent. These models cannot tell us about the day-to-day variability of the TEC which can be 20 to 25 percent (1 sigma) of the monthly mean value. So, even if the monthly mean TEC is modelled perfectly using one of the global ionospheric models, TEC predictions can be off by 20 to 25 percent. If the bias between the monthly mean TEC and the predictions provided by these models is 10 percent of the monthly mean values, then the performances of these models are considered to be excellent. The combined effect of the error in the monthly mean predictions and the day-to-day variability of the TEC will result in an overall performance of these models to be at about 22-27 percent (r.m.s.) of the ionospheric delay. The performance can only be worse if we take into account the potential effect of a solar or geomagnetic storm during medium or high solar activity times [Klobuchar, 1996].

To achieve better modelling accuracy, we need to have some additional information on the day-to-day variability of the TEC. There are several data sources which one could use to improve the performance of such a model. These external data sources can be ionosonde data, incoherent backscatter radar data, topside sounder data, Faraday rotation data, Navy Navigation Satellite System (Transit)-derived TEC data, TOPEX/Poseidon-derived TEC, and GPS-derived TEC data.

In my research, I have focused on GPS-derived TEC data which can be used to improve the performance of the global ionospheric models such as the IRI-95. An

improved ionospheric model can be used to help single frequency GPS users to account for the ionospheric effect. GPS-derived TEC data can also be used to provide Wide Area Augmentation System (WAAS) [El-Arini et al., 1994] ionospheric delay corrections for single frequency GPS users. Another interesting application of the GPS-derived TEC data is to provide ionospheric delay corrections for single frequency radar altimeter missions which will be addressed in this dissertation as well.

On the other hand, modelling TEC gives scientists the opportunity to study the temporal and spatial variation of the global ionosphere to learn more about various ionospheric structures influencing electromagnetic waves propagating from satellites to receivers. GPS can provide a unique tool to study the ionosphere as well as help provide ionospheric corrections for single frequency navigation, surveillance and communication systems.

1.2 Literature Overview

In this section, I will briefly summarize the history of the ionospheric work that has been done at the Geodetic Research Laboratory thus far. This will be followed by the summary of the ionospheric work done elsewhere in the context of the research outlined in this dissertation.

1.2.1 Previous Ionospheric Work at UNB

The Geodetic Research Laboratory of the University of New Brunswick has been involved in ionosphere-related research since the middle of the 1980s. The early GPS-related ionospheric work concentrated on modelling the ionospheric delay for static relative baseline positioning. Kleusberg [1986] showed that the differential carrier phase advance on single frequency carrier phase observations can be at the decimeter level for baselines lengths of 40 km. Subsequently, Georgiadou and Kleusberg [1988] derived an expression for differential ionospheric delay as a function of vertical electron content of the ionospheric shell (infinitesimally thin spherical shell [spherical layer] with an electron content equal to the integrated vertical electron density), ionospheric shell height (height of the centroid of the density profile above the earth's surface) and elevation angle of the satellite. The authors concluded that unaccounted differential ionospheric delay can lead to a baseline shortening of 0.25 part per million (ppm) per 1 m vertical ionospheric delay. The baseline shortening is proportional to the differential ionospheric range error affected by the differences in the ionospheric profile at the two stations. Santerre [1989] looked at the impact of the GPS satellite sky distribution on the propagation of errors in precise relative positioning. The study found that the absolute ionospheric refraction depending on the geographic latitude region can cause -0.71 to -0.76 ppm horizontal scale bias for every 10 total electron content units (TECUs) (1 TECU corresponds to 10^{16} electrons in a vertical column with a cross section area of 1 m^2) using a 10 degrees elevation cutoff angle. To correct data from a single frequency GPS receiver for the ionospheric effect, it is possible to use empirical models. Newby [1992], Newby and Langley [1992], and

Newby et al. [1990] looked at four different global ionospheric models (Bent, ICED, IRI-86 and the GPS single frequency Broadcast model) under low, medium and high solar activity conditions to investigate the performances of different ionospheric models. The study compared ionospheric delays derived using the first three models with the ones derived from Faraday rotation data. The performances of all four models were also compared with computed ionospheric delays from dual frequency GPS measurements. Based on the Faraday rotation data, it was concluded that the Bent and IRI-86 models performed the best. Comparison with Faraday rotation data showed that the Broadcast and the IRI-86 models proved to be the best. The Broadcast model was able to account for 70 to 90 percent of the daytime ionospheric delay and 60 to 70 percent of the night-time delay. Langley et al. [1991] investigated different types of surveying precision receivers under highly dynamic ionospheric conditions for high solar activity times. Webster [1993] investigated the effect of ionospheric delay on airborne single frequency GPS receivers. The single frequency GPS observations collected onboard a fixed wing aircraft were corrected for the ionospheric delay using three nearby dual frequency GPS receivers. It was concluded that after applying a regional ionospheric model derived using the three dual frequency GPS receivers, aircraft positions with respect to monitor stations were at the 1 ppm level. Before applying ionospheric corrections, the differences were found to be at the 2 to 3 ppm level with periods of up to 50 ppm. Walford [1995] investigated a network of GPS baselines in which both dual frequency and single frequency receivers were used under humid climate conditions of the equatorial region. Uncorrected ionospheric effect on the single frequency receivers was eliminated by

estimating scale changes for the baselines affected within the network. Global ionospheric TEC modelling technique using spherical harmonics was demonstrated by Brunini and Kleusberg [1996]. Recently, Stewart [1997] estimated differential ionospheric delay corrections using a Kalman filter approach to aid GPS carrier phase ambiguity resolution.

1.2.2 Previous Work Elsewhere

The literature of relevance to this research is large. In this section, I will concentrate on the studies that are closely related to my work. Further references on other TEC determination techniques will be provided in Chapter 2. In Chapter 6, additional techniques will be explained and references provided that use GPS measurements to estimate TEC. Early ionospheric studies using GPS utilized single station observations to estimate the line-of-sight pseudo-TEC which is the sum of the satellite-receiver differential delays and the actual line-of-sight TEC (e.g., Lanyi and Roth [1988], Coco et al. [1991]). The Self-Calibration Of pseudorange Error (SCORE) technique developed by Bishop et al. [1995] infers TEC and satellite-receiver differential delays by requiring maximum agreement between ionospheric measurements when the observed paths of two satellites cross. Coster et al. [1992] used a single station to estimate local TEC model coefficients with azimuth and elevation dependence above the observing station using a Kalman filter approach.

The necessity to produce global ionospheric maps to provide ionospheric corrections for single frequency GPS receivers or correcting single frequency altimeter measurements has encouraged the ionospheric community to develop regional and global ionospheric mapping techniques. There are several research groups producing regional or global scale TEC maps along with satellite-receiver differential delays depending on the type of ionospheric observable used. Undifferenced dual frequency pseudorange, undifferenced dual frequency carrier phase observations or these two combined can be used for the ionospheric observable. The most advanced techniques use the combined (phase-levelled) technique, estimating the ionospheric parameters as stochastic parameters whereby the temporal variation of the ionospheric parameters is taken into account. The phase-levelling technique implies that the L1 minus L2 (L1-L2) carrier phase measurements are adjusted by a constant value determined for each phase-connected arc of data using precise pseudorange measurements. By doing so, we are taking advantage of the fact that the L1-L2 ionospheric observable, using e.g., Turbo Rogue receiver, has a noise level 1-2 orders of magnitude below the pseudorange ionospheric observable. The technique has been demonstrated by Wilson and Mannucci [1993], Runge et al. [1995] and others. It is widely used to estimate various ionospheric model parameters as well as satellite-receiver differential delays (see e.g., Gao et al. [1994] and Sardon et al. [1994; 1995]). There exists another approach that uses the double-differenced L1-L2 carrier phase observations to estimate global or regional ionospheric models [Schaer et al., 1995; 1996]. In the case of the double-differenced ionospheric observable, we do not have to estimate the satellite-receiver differential delays as they cancel out when forming the ionospheric observable.

The International GPS Service for Geodynamics (IGS) routinely produces GPS orbits, earth orientation parameters and satellite clock information. Recently, IGS has decided [Beutler, 1995] to include ionospheric information among the IGS products. At the 1996 IGS Workshop in Silver Spring, Maryland, for the first time, there was a separate session dedicated to ionospheric research [Feltens, 1996]. There are several groups which are capable of producing regional and/or global ionospheric maps: Schaer et al. [1995; 1996] produces regional and global TEC maps as part of the daily routine processing at the IGS Processing Center at the Astronomical Institute of the University of Bern. At the Orbit Attitude Division of the European Space Operations Centre, regional and global ionospheric maps are produced using the stations from the IGS network [Feltens et al., 1996]. At the Deutsches Fernerkundungsstation of Deutsche Forschungsanstalt für Luft und Raumfahrt (DLR), regional ionospheric maps are routinely produced and made available on the Internet [Sardon et al., 1995; Jakowski et al., 1996]. At the GPS Network and Operations Group of the Jet Propulsion Laboratory, global (IGS-station-based) ionospheric maps (GIMs) are also routinely produced [Mannucci et al., 1993] to provide real-time updates for the Parameterized Real-time Ionospheric Specification Model (PRISM) [Daniell and Anderson, 1996]. The routinely produced GIMs can also be used to provide corrections to mitigate the ionospheric effect on single frequency radar altimetry measurements [Yuan et al., 1996]. Recently Ho et al. [1996] showed that a global network of dual frequency GPS receivers can be used to monitor the global TEC changes

during a magnetic storm. A travelling ionospheric disturbance (TID) was identified moving from the auroral region to the low latitude region.

1.3 Contribution of the Research

I have developed the capabilities to independently produce regional and global total electron content (TEC) maps on an hourly basis. The UNB TEC maps can be input directly into a modified version of the International Reference Ionosphere (IRI-95) model to update its CCIR/URSI coefficient sets on an hourly basis. These updated IRI-95 coefficient sets serve as a basis for improved IRI-95 predictions by using the modified IRI-95 model as a sophisticated interpolator between two GPS-derived TEC updates.

The contributions of my dissertation is as follows: the UNB global TEC mapping technique provides an alternative way of modelling the temporal and spatial variation of the global ionosphere. Beyond the conventional way of treating the ionospheric model parameters as stochastic and estimating them using a Kalman filter approach, the new algorithm uses a varying ionospheric shell height concept taking into account both its temporal and spatial variability. The same varying ionospheric shell height is used as a parameter when mapping the line-of-sight TEC into the vertical using a commonly adopted geometric mapping function.

I have merged the GPS-derived TEC data with a global empirical ionospheric model: the IRI-95. I have made extensive modifications to the IRI-95 model to ingest GPS-derived TEC data. The approach is to update the IRI-95 coefficient sets which involves the computation of an inferred solar effective sunspot number (IG index) which is assumed to be a function of geographic latitude, longitude and Universal Time. This is achieved by the implementation of an efficient search technique to find the IG index that results in the best match between the IRI-95 predicted TEC and the UNB global TEC maps.

In order to find the correct IG index, I also used an empirical plasmaspheric electron content model which takes into account the fact that the IRI-95 model computes TEC predictions only up to an altitude of 1000 km whereas the UNB global TEC maps provide estimates up to the altitude of the GPS satellites. I also made modifications to the IRI-95 model and to the code to increase the efficiency of the code's execution.

The GPS-derived global TEC maps can also serve as a basis to provide ionospheric corrections for single frequency GPS users. The combination of the GPS-derived TEC and the modified IRI-95 model allows, in particular, the provision of ionospheric corrections for single frequency altimeter missions the benefit of which will be demonstrated in this dissertation.

1.4 Outline of the Dissertation

Chapter 1: Introduction -- I set the outline and the direction of the dissertation. This is followed by a review of the ionospheric research work at UNB and work elsewhere in the context of this dissertation. I also discuss the contributions of this dissertation.

Chapter 2: GPS and Its Place Among the Ionospheric Probing Techniques. -- In this chapter, I describe the ionosphere and its structure. Electromagnetic waves are affected in propagating through the ionosphere. This impact of the ionosphere on electromagnetic waves is described in this chapter, establishing the theoretical background for the research described in this dissertation. After that I introduce the different modelling and measuring techniques that are currently available to the ionospheric community to study the ionosphere.

Chapter 3: Modelling the Ionosphere Using Empirical Models. -- In this chapter, I introduce my early ionospheric work dealing with global empirical ionospheric models such as the Broadcast model and the International Reference Ionosphere model. The performances of these models were compared against Faraday rotation data. Based on this investigation, a decision was made to use the IRI model for further research and development.

Chapter 4: The UNB Approach to Ionospheric Modelling Using GPS. -- In this chapter, I introduce the different methods developed to investigate the ionosphere using signals from

the Global Positioning System satellites. I introduce in detail the UNB method developed to model the ionospheric effect, the modifications I made to the IRI-95 model including a plasmaspheric electron content extension.

Chapter 5: Regional Ionospheric Modelling: A Sensitivity Analysis. -- In this chapter, I discuss a sensitivity analysis of the TEC and bias estimates as a function of ionospheric shell height, elevation cutoff angle and adopted ionospheric mapping function. I demonstrate the UNB method for regional ionospheric modelling based on a particular IGS campaign. An investigation on using different ionospheric mapping functions will also be discussed.

Chapter 6: Global Ionospheric Modelling: Data Processing and Analysis of Results. -- I further enhanced the UNB software to enable me the production of global ionospheric maps. These global ionospheric maps in a combination with the modified IRI-95 model makes it possible to use this technique to provide ionospheric corrections for single frequency altimeter missions. I demonstrate this capability by presenting results based on an ionospheric experiment using TEC data from the TOPEX/Poseidon spacecraft.

Chapter 7: Conclusions and Recommendations for Future Research. -- This chapter highlights the contributions of the dissertation and points out possible areas in which further contributions can be made.

CHAPTER 2

GPS AND ITS PLACE AMONG THE IONOSPHERIC PROBING TECHNIQUES

In this chapter, I will introduce the ionosphere, its structure, and behaviour and how it affects the electromagnetic waves propagating through it. I will describe the modelling techniques currently used by the ionospheric research community to mitigate the effect of the ionosphere. After that, I will turn the readers' attention to the ionospheric probing, or measuring techniques used to study the ionosphere. One of these techniques is the Global Positioning System which turns out to be one of the most powerful state-of-the-art tools available to the ionospheric science community for studying the temporal and spatial variations of the global ionosphere.

2.1 The Ionosphere

The term ionosphere was first used by Sir Robert Watson-Watt in a letter to the secretary of the British Radio Research Board in 1926. The expression came into wide use during the period 1932-34 when Watson-Watt, Appleton, Ratcliff and others used it in papers and books. Before the term ionosphere gained worldwide acceptance, it was called the Kennelly-Heaviside layer, the upper conducting layer, ionized upper atmosphere [Hunsucker, 1991].

2.1.1 The Earth's Magnetic Field

The earth's magnetic field plays an important role in the formation of the ionosphere. This highlights the importance of using geomagnetic field coordinates to describe or model the ionosphere. The first approximation to the earth's magnetic field is that of a sphere uniformly magnetized in the direction of the centered dipole axis. This axis cuts the surface of the earth at points known as the austral (south) and boreal (north) dipole poles. The intersection between the plane through the earth center perpendicular to the dipole axis and the earth surface is called the geomagnetic equator. Scientists use dip latitude to describe the earth's actual magnetic field. In this case, the poles are referred to as dip poles, locations where the geomagnetic field is vertical to the earth's surface, and dip equator where the geomagnetic field is horizontal. Detailed descriptions of the earth's magnetic field, and relationships among geographic, geomagnetic, and dip latitudes have been given by e.g., Tascione [1988], McNamara [1994], and Davies [1990].

2.1.2 Vertical Profile of the Ionosphere

There are numerous monographs describing the physical and chemical processes within the ionosphere. Detailed explanations of the processes can be found in e.g., McNamara [1994] and Davies [1990]. Here, I will provide a short summary of these processes. The height at which the ionosphere starts to become sensible is about 50 km and it reaches as high as about 1000 km (see Figure 2.1). In fact the upper boundary of the ionosphere is

not well defined since it can be interpreted as the electron densities thinning into the plasmasphere (or protonosphere) and subsequently the interplanetary plasma [Langley, 1996]. The plasmasphere may be thought of as the region above an altitude of about 1000 km where the neutral atmospheric densities are so small and the positive ions are predominantly protons hence the term is synonymous to protonosphere. At the altitude of about 30,000 km the plasmasphere decays out to the plasmopause (a boundary between the plasmasphere and the interplanetary plasma) and the typical electron densities of the plasmasphere (about 10^{10} electron/m³) drops by 1 to 2 orders of magnitude [Davies, 1990].

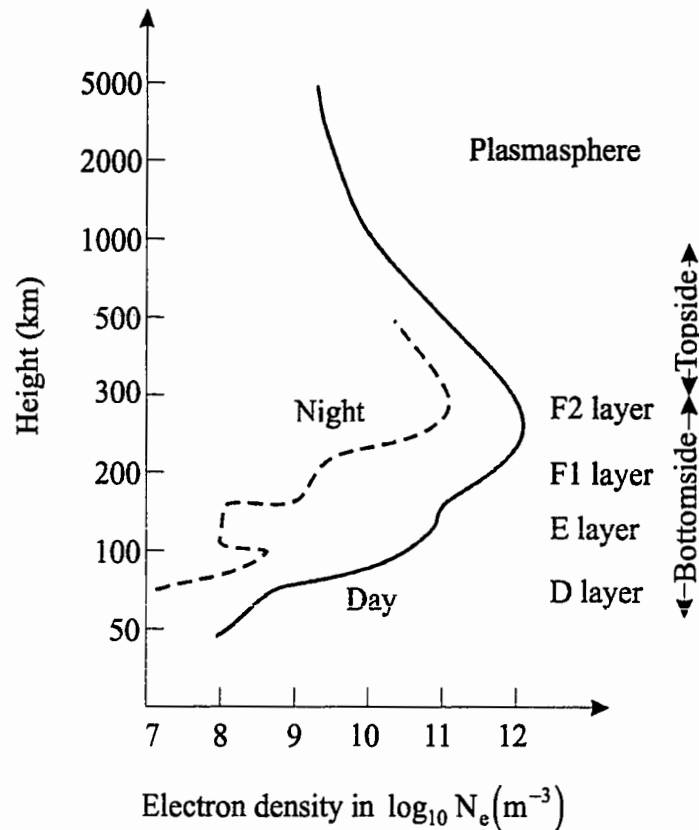


Figure 2.1: Typical vertical profile of the ionosphere (after Davies [1990]).

The sun's extreme ultraviolet (EUV) light and X-ray emissions encountering gaseous atoms and molecules in the atmosphere can impart enough energy for photoionization to occur producing positively charged ions and negatively charged free electrons. A secondary ionizing force of lesser importance is cosmic radiation. A counteracting process in the ionosphere is recombination, in which the ions and electrons join again producing neutral atoms and molecules. In the lower regions of the ionosphere, free electrons can combine with neutral atoms to produce negatively charged ions a process which is called attachment. The absorption of EUV light increases as altitude decreases and the net result of this and the increasing density of neutral molecules is the formation of a layer of maximum electron density. However, due to different molecules and atoms in the atmosphere and their differing rates of absorption, a series of distinct regions or layers of electron density exist. These are denoted by letters D, E, F1 and F2 and usually are collectively referred to as the bottomside of the ionosphere. The part of the ionosphere between the F2 layer and the upper boundary of the ionosphere is termed the topside of the ionosphere (for illustration see Figure 2.1). It is the F2 layer where usually the maximum electron density occurs as a consequence of the combination of the absorption of the EUV light and increase of neutral atmospheric density as the altitude decreases.

The minimum frequency of an electromagnetic wave for it to penetrate an ionospheric layer is called the critical, plasma or penetration frequency of the particular layer and it is denoted by f_oD , f_oE , f_oF1 , and f_oF2 according to the designation of the ionospheric layer (see Section 2.2 for more details). The square of a critical frequency is linearly

proportional to the maximum electron density of the individual layer and these are denoted by N_mD , N_mE , N_mF1 and N_mF2 respectively. The changes in f_oD , f_oE and f_oF1 are in phase with solar variation and f_oF2 is in antiphase. The existence of the D, E, and F1 layers seems to be primarily controlled by the solar zenith angle showing a strong diurnal, seasonal and latitudinal variation. The diurnal variation of the D, E, and F1 layers also implies that they tend to vanish or greatly reduce in size at night. The F1 layer disappears in winter time when the solar zenith angle is higher than in summer time at which time the F1 layer is consistently present. The critical frequencies of all layers follow the 11 year solar cycle variation caused by the change in intensity of solar radiation. Now, I will give short descriptions of the individual ionospheric layers. The interested reader is referred to ionospheric physics monographs such as Davies [1990], McNamara [1991, 1994], Tascione [1988], Ratcliffe [1970], and Risbeth and Garriott [1969] for further details.

2.1.2.1 The D Layer

The D layer ranges in height from about 50 to 90 km. In this layer, the primary source of ionization is cosmic radiation which is the same by day and by night manifesting itself in a strong solar cycle variation in the D layer electron density. Despite this, by night, the electrons may become attached to atoms and molecules forming negative ions that cause the D layer to disappear. By day, as a consequence of sun's radiation, the electrons tend to detach themselves from the ions causing the D layer electrons to re-appear. As a consequence of that, at the altitude of about 60 to 70 km, the D layer electrons are present

by day but not by night causing a distinct diurnal variation in the electron density. Electric charges transfer between different species, and positive and negative ions form complex clusters with water molecules. The typical values for the noon time electron densities of the D layer at the mid-latitude region range between $6.1 \cdot 10^8$ to $13.1 \cdot 10^8$ electron/m³ according to the solar activity. In Davies [1990], the lower part of D layer is referred to as the C layer where the cosmic radiation is the only source of ionization compared to the middle and upper part of the D layer where both the cosmic radiation and X-ray emissions are present.

2.1.2.2 The E Layer

The behaviour of the E layer almost entirely depends on the level of solar activity and the zenith angle of the sun. The E layer is free of disturbances unlike the D and F layers and is only present by day. The primary source of ionization is the sun's X-ray emissions resulting in electron densities showing distinct solar-cycle, seasonal and daily variations. The E layer does not completely vanish at night, however, for practical purposes it is often assumed that its electron density drops to zero at night. The atmosphere is rare and only 2-body collisions occur, so atomic ions cannot recombine easily with electrons; however molecular ions do recombine easily. The overall effect is that the positive ions are mostly molecular. Some charges are attached to trace metal atoms to form very long-lived ions which are probably the main ionic component of mid-latitude sporadic E layer. Typical

values for mid-latitude noon time electron densities are between $1.3 \cdot 10^{11}$ and $1.7 \cdot 10^{11}$ electrons/m³.

2.1.2.3 The F1 Layer

The main source of ionization in the F1 layer is the EUV light. The F1 layer is only observed during the day since the electron densities are primarily controlled by the zenith angle of the sun. When it is present, it changes rapidly in a matter of minutes. It is more pronounced during the summer than during the winter months for low solar sunspot numbers and for periods with ionospheric storms. Typical noon time mid-latitude electron densities range between $2.3 \cdot 10^{11}$ and $3.3 \cdot 10^{11}$ electrons/m³ according to the solar activity.

2.1.2.4 The F2 Layer

The F2 layer is the most important ionospheric layer from the point of view of HF propagation. The F2 layer does not follow the solar zenith angle dependence. In fact, the January noon F2 layer critical frequency (foF2) is more than twice the summer value. Interestingly, this winter anomaly occurs in the daytime only which is thought to be due to the large summer electron loss caused by the increased molecular to atomic composition of the neutral atmosphere. In summer, foF2 shows little diurnal variation. The global spatial distribution of foF2 reveals a strong geomagnetic dependence. The most distinctive

features are the two regions of high foF2 lying about ± 20 degrees dip latitude which is called the equatorial anomaly (see Section 2.1.3.1). F2 layer critical frequencies also show a linear dependence with solar sunspot numbers. Typical mid-latitude noon time electron densities range between $2.8 \cdot 10^{11}$ and $5.2 \cdot 10^{11}$ electrons/m³ according to the solar activity.

2.1.3 Major Geographic Regions of the Ionosphere

There are three major regions of the global ionosphere. These are the high-latitude, mid-latitude and equatorial regions. In this section, I will briefly describe the main characteristics of the individual regions (see Figure 2.2).

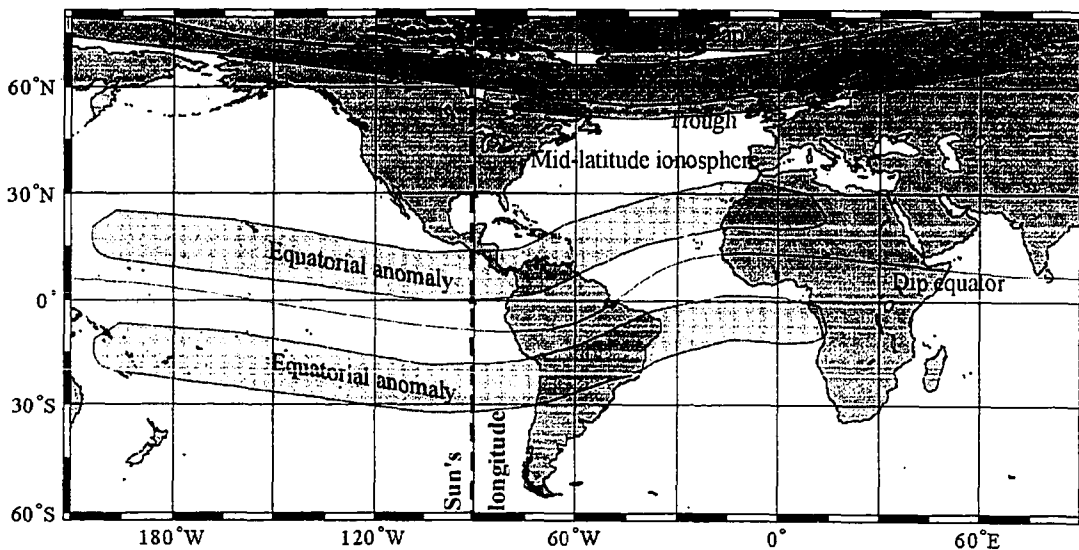


Figure 2.2: Major geographic regions of the ionosphere (after Bishop et al. [1991]).

2.1.3.1 Equatorial Region

The equatorial region can be characterized with the highest values of the peak-electron density with the most pronounced amplitude and phase scintillation effects. For the explanation of amplitude and phase scintillation see Section 2.1.4.3. The combined effect of the high radiation level from the sun, and the electric and the magnetic fields of the earth results in the electrons rising and moving along the horizontal lines of the magnetic field: this phenomenon is called the fountain effect. The electrons move as far as the geomagnetic latitudes of 10 to 20 degrees causing the high concentration of electrons there which are often termed equatorial anomalies.

2.1.3.2 Mid-Latitude Region

The mid-latitude ionosphere is the least variable and undisturbed among the different ionospheric regions. It is usually free of the effect imposed by the horizontal magnetic field geometry peculiar to the equatorial region. Also, this is the region from where we have most of the ionospheric observations available due to the fact that most of the ionosphere-sensing instruments are located in countries situated in the mid-latitude region.

2.1.3.3 High-Latitude Region

In addition to photonization, collisional ionization is another source of ionization in the high-latitude region. The main reason for this is the fact that the geomagnetic field lines are nearly vertical in this region leading to the charged particles descending to E layer altitudes (about 100 km). These particles can collide with the neutral atmospheric gases causing local enhancements in the electron concentration, a phenomenon which is associated with auroral activity. Auroral activity can also be regarded as an interaction between magnetosphere, ionosphere, and atmosphere. The auroral zones are relatively narrow rings situated between the northern and southern geomagnetic latitudes of about 64 and 70 degrees. In general, the intensity and the positions of the auroral ovals are related to geomagnetic disturbances. The ovals expand towards the equator with increasing levels of geomagnetic disturbance [McNamara, 1991].

On the equatorial side of the auroral ovals lies the mid-latitude trough which is a narrow region of the ionosphere with a width of a few degrees. It can be characterized by a sudden drop in the critical frequencies and electron densities by a factor of two or more. This occurs essentially at night time primarily due to the increased recombination as a consequence of the shorter high latitude day time ionization periods [Tascione, 1988].

The direct interaction between the magnetosphere and the interplanetary magnetic field results in the dayside cusp or cleft. It is typically 2 to 4 degrees wide and located at

the geomagnetic latitude of 78 to 80 degrees near local noon. The phenomenon can be characterized with enhancements in electron densities at all altitudes.

The geographical regions enclosed by the auroral rings are called the polar caps. Our understanding of the polar cap region is rather limited due to the lack of available information. The polar caps are largely affected by solar flares and mass ejections from coronal holes (relatively cool “open” structures of the solar corona) causing D region electron density enhancements.

2.1.4 Ionospheric Disturbances

Ionospheric disturbances can result from solar disturbances or geomagnetic field disturbances. The ionospheric disturbances are associated directly or indirectly with the events on the sun. The geomagnetic disturbances are also caused by events initiated from the sun, however, these events rather affect the outermost geomagnetic field line (also called the magnetopause) and compress the geomagnetic field causing the geomagnetic disturbances.

2.1.4.1 Ionospheric Storms

Ionospheric storms can be caused by intense solar eruptions hurling out energetic particles also known as solar flares that can endanger astronauts and destroy satellite electronics. X-rays which are emitted as part of the explosion can penetrate as far as the D-region causing the phenomenon known as shortwave fadeout. The energetic flares can also eject protons that can hit the earth causing a polar cap absorption event. If the solar flare is sufficiently large, a cloud of plasma can also hit the earth causing an ionospheric storm. This can manifest itself by sudden, unpredictable changes in F2 layer critical frequency, foF2. Whether the critical frequency is increased or decreased at a particular location depends on such things as the time of the day when the plasma cloud hits the earth, local time, season and latitude, and how long the storm has been going on. Ionospheric disturbances can also be initiated by a high speed solar wind stream (HSSWS) which is caused by mass ejections from coronal holes. The sun's magnetic field lines stretch out into interplanetary space making it possible for the ionized material to travel along the field lines and eventually reach the earth. The effect of HSSWS on the ionosphere is usually not as devastating as those of a large solar flare. This is partly because HSSWS does not overtake the earth as fast as the cloud from a solar flare hits it. Its effect also tends to last longer since it takes a couple of days to sweep over the earth. Another potential trigger for an ionospheric storm can be sudden disappearing filaments which can be distinguished from HSSWS: they are large relatively cool structures on the sun's surface potentially blowing out material into the interplanetary space affecting the earth's geomagnetic field [McNamara, 1991; Davies, 1990].

2.1.4.2 Geomagnetic Storms

Geomagnetic storms usually occur in conjunction with ionospheric storms and can be caused by solar flares, high speed solar wind stream (coronal holes) and sudden disappearing filaments. The storms are usually associated with increased electron densities in the lower ionosphere and a simultaneous increase in absorption of radio waves. A geomagnetic storm usually starts with an increase in the earth's geomagnetic field intensity called the initial phase followed by a large decrease termed the main phase. A solar-flare-originated geomagnetic storm usually starts with a sudden commencement as an initial phase. On the other hand, a high speed solar wind stream induced geomagnetic storm is expected to start with a gradual commencement with storms tending to reoccur every 27 days or so following the sun's rotation [McNamara, 1991; Tascione, 1988].

2.1.4.3 Ionospheric Scintillation

Small-scale structures in the electron content of the ionosphere can range from a few meters to a few kilometers in extent which can cause both refraction and diffraction effects on the electromagnetic waves propagating through the ionosphere. Without going into details, refraction is associated with the bending of the electromagnetic waves which takes place when the wave front moves obliquely across two media with different propagation velocities. However, bending can also take place when the electromagnetic waves pass by an obstacle such as a localized ionospheric disturbance [Serway, 1986]. As a consequence

of refraction and diffraction, the wavefront becomes crinkled giving rise to amplitude and phase fluctuations of the signal. These fluctuations caused by small-scale ionospheric structures are called ionospheric scintillations [Wanninger, 1993]. The amplitude scintillation during high solar activity times at the equatorial region can reach 20 dB at 1.5 GHz [Bishop et al., 1996]. The phase scintillations are rapid changes in signal phase that can be attributed to rapid but very small changes in the ionospheric electron content. A change of 1 radian in phase is required at 1.5 GHz (corresponding to $0.19 \cdot 10^{16}$ TEC or only 0.2% of a typical 10^{18} TEC) to cause problems for the GPS receiver's tracking loop [Langley, 1996].

2.1.5 Solar-Terrestrial Indices

Most empirical and physics-based models of the ionosphere need solar and/or geomagnetic indices to specify the solar and geomagnetic disturbance level. These indices can be derived by continuously monitoring with ground-based equipment or they can be derived from continuously monitored parameters.

2.1.5.1 Kp and Ap Indices

The K index, for each 3 hour period of every UT day, is a measure for the irregular variations of the Cartesian components of the earth's magnetic field (X, Y, Z). These

irregular variations are associated with geomagnetic field disturbances measured in gammas (nanoTeslas). The range R between the largest and the smallest of the three geomagnetic field components measured in gammas is used to define a particular K . 13 observatories which lie between 46 and 63 degrees north and south geomagnetic latitude determine their own integer K ranging from 0 to 9 for each 3 hour period of the day based on the measured ranges in the geomagnetic field components. A particular K scale is adopted for each observatory but the scale differs from observatory to observatory. The highest values for R is about 500 gammas at a typical mid-latitude station and about 2000 gammas for a station at the auroral zone. The planetary 3 hour index K_p is designed to give a global measure of geomagnetic activity and computed as an arithmetic mean of the K values calculated at the 13 observatories. The K_p index has 28 steps from zero (quiet) to 9 (greatly disturbed) with fractional parts expressed in third of units.

There is a logarithmic relationship between the K index and R . Sometimes it is more useful to use a linear scale. To do that, the “equivalent planetary amplitude” of the geomagnetic field variation “ a_p ” is derived from K_p . The daily A_p index is the average of the eight a_p values. An example of a time series of the A_p index is shown in Figure 2.3 displaying the A_p index variation for a period of 15 months. The data was provided by the National Oceanic and Atmospheric Administration (NOAA) National Geophysical Data Center (NGDC) Solar Terrestrial Physics Division [NGDC, 1997a]. We can clearly see a seasonal variation of the geomagnetic field peaking in February-March and September-October.

Ap or Planetary Equivalent Daily Amplitude (1994-95)

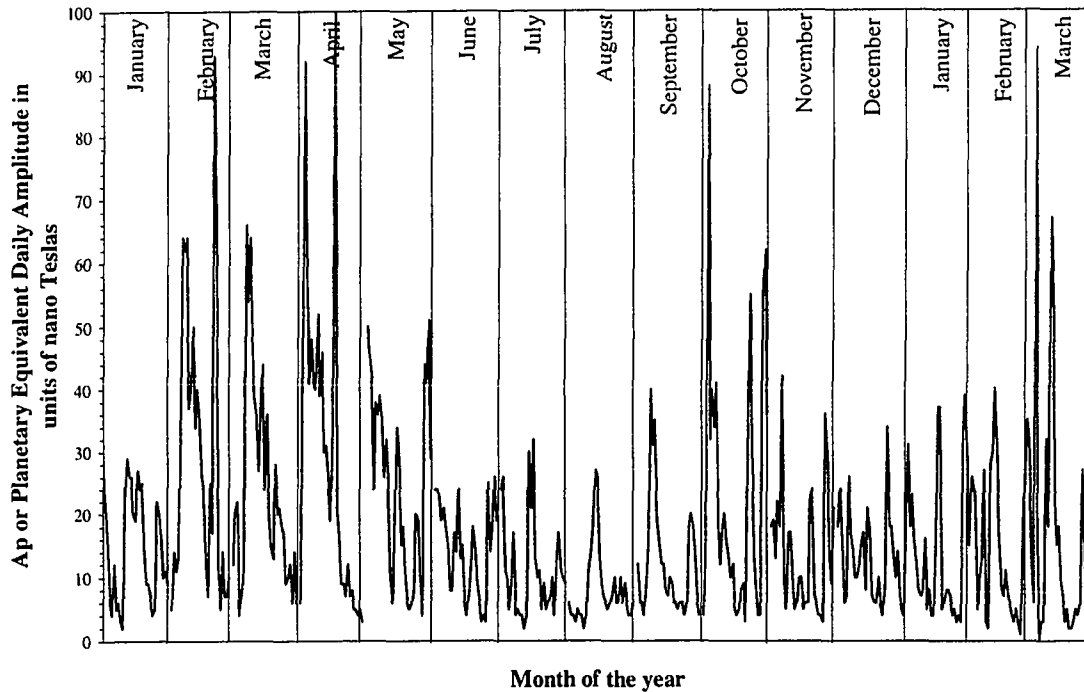


Figure 2.3: Illustration of geomagnetic field variation.

2.1.5.2 Zurich Sunspot Number

The visible surface of the sun is known as the photosphere. A sunspot is an area seen as a dark spot on the photosphere of the sun. They are concentrations of magnetic flux, typically occurring in bipolar clusters or groups. They appear dark because they are cooler than the surrounding photosphere. As the number of spots increases and magnetic complexity grows, they become likely sources of large eruptive energy releases known as solar flares. The daily index of sunspot activity (R) is defined as $R = k \cdot (10 \cdot g + s)$ where s is the number of individual spots, g is the number of sunspot groups, and k is an

observatory factor. Since for many years, solar sunspot numbers were derived at the Zurich Observatory, this index is known as the Zurich Sunspot Number. Figure 2.4 shows the twelve-month smoothed solar sunspot numbers for the last four solar cycles (cycles 19 through 22). The data was obtained from the National Oceanic and Atmospheric Administration National Geophysical Data Center Solar Terrestrial Physics Division [NGDC, 1997b]. The approximately 11 year solar cycle can be clearly identified from Figure 2.4. It is also interesting to see that there are significant differences in the peaks of the solar cycles. Also, the climb-up period usually takes 3 to 4 years whereas the going-down period usually takes 7 to 8 years.

2.1.5.3 Ottawa 10.7 cm (2800 MHz) Solar Radio Flux

The sun emits radio energy with normally slowly varying intensity. This radio flux changes from day to day seemingly in response to the number of spot groups on the disk. Solar flux from the entire disk has been routinely recorded at a frequency of 2800 MHz by radio telescopes close to Ottawa (February 1947 - 1961), Algonquin Radio Observatory (1961-1991) and at the Dominion Radio Astrophysical Observatory, Penticton, British Columbia (1991 - present). The observed values are adjusted for the changing sun-earth distance and for uncertainties in antenna gain. The daily values between January 1994 and March 1995 can be seen in Figure 2.5. The data was provided by the National Research Council of Canada's Dominion Radio Astrophysical Observatory [NRC, 1997]. The figure displays a

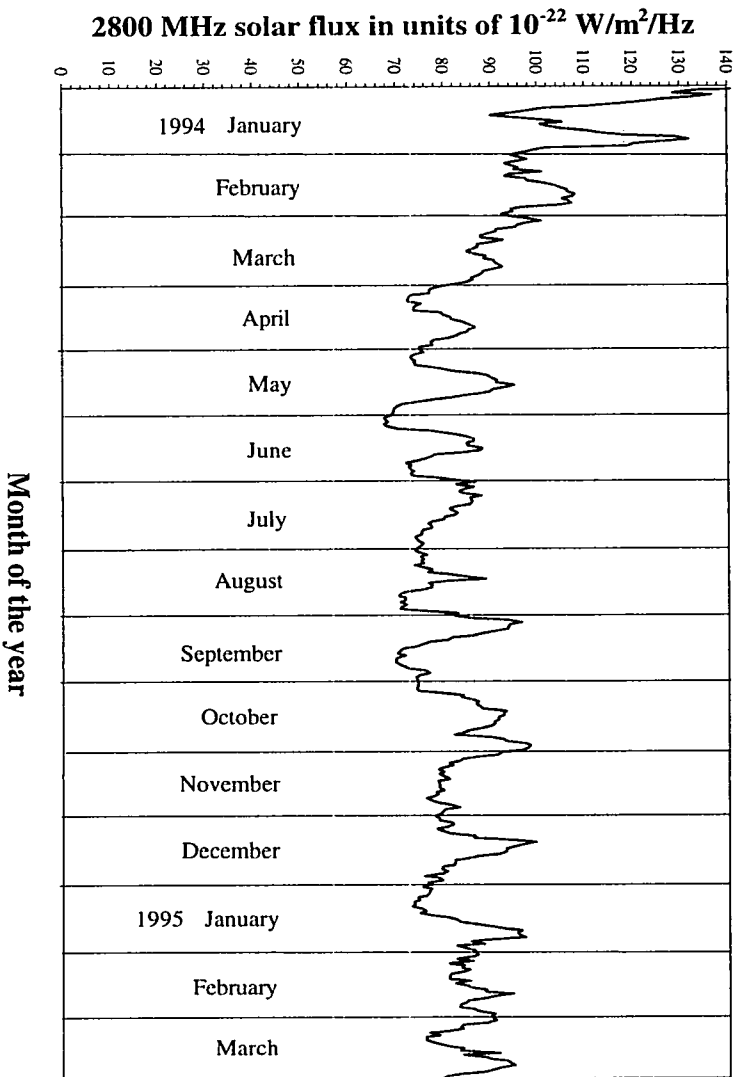


Figure 2.5: Observed daily solar flux variation.

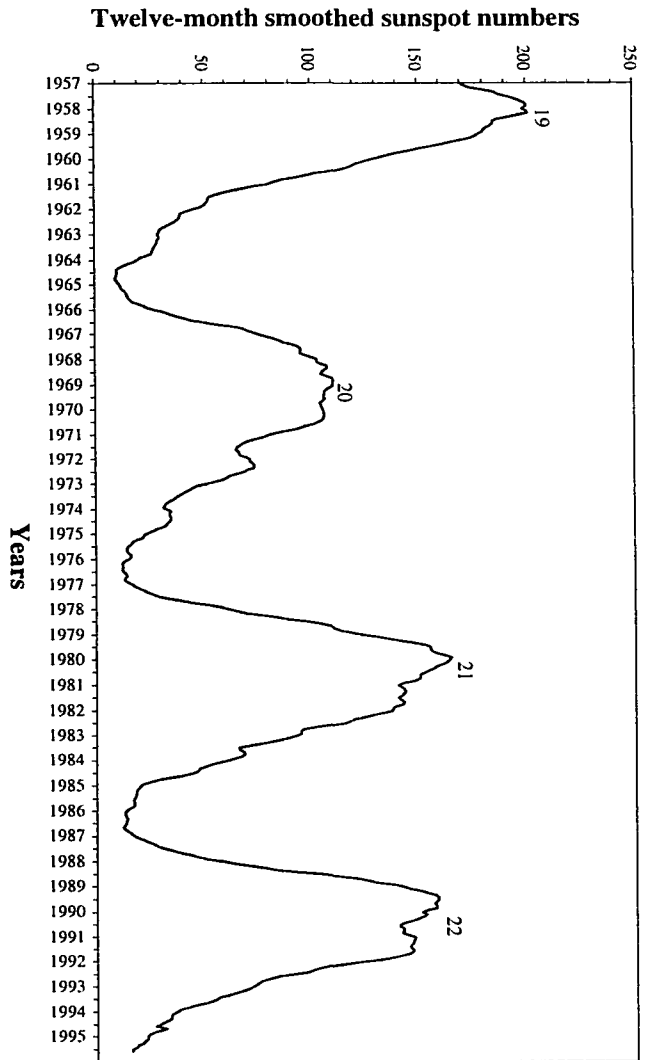


Figure 2.4: Solar sunspot activity during the last four solar cycles.

time period of 15 months during a period of low-solar activity. The 27 day solar rotation periods can be readily identified in the figure.

2.1.5.4 IG Index

The IG (International Global) index is independent of the observed sunspot numbers and it is referred to as a global effective sunspot number. It can be interpreted as a derived solar sunspot number as opposed to a sunspot number which is based on visual observations (see Section 2.1.5.2). The IG index is determined from the noontime monthly median values of F2 layer critical frequencies, foF2, that are observed at 13 middle-latitude stations throughout the world in order to determine what value of the IG index is needed to produce the observed foF2 values using the global foF2 numerical maps available in forms of coefficient sets from the Comité Consultatif International des Radiocommunications (CCIR) [Davies, 1990]. These coefficient sets are used by the IRI-95 [Bilitza, 1990] and Bent models [Bent and Liewellyn, 1973] to reconstruct the numerical maps in order to predict foF2 given a geographic location, Universal Time and the IG index. The numerical maps have been derived using some 180 ionosonde stations worldwide and are defined by two sets of coefficients representing low and high solar activity times for each month. The parameterization of the numerical maps is discussed in detail in Section 4.2.7.

2.2 The Effects of the Ionosphere on the Propagation of Electromagnetic Waves

The effect of the ionosphere on electromagnetic waves cannot be described by simple dispersion. To adequately describe the complete behaviour of radio waves in the ionosphere, we have to realize that the “ionosphere is a partially ionized, spherically stratified plasma with a wide spectrum of nonuniformly spaced irregularities, upon which is imposed a nonuniform magnetic field - which is itself distorted by perturbations in the solar wind” [Hunsucker, 1991].

The complex refractive index of the ionosphere as a magnetoionic medium was derived by the number of people but the name most commonly associated with the theory is Sir Edward Appleton who was first to point out that a plane polarized wave would be split into two opposite rotating circularly polarized waves by the magnetized plasma [Hunsucker, 1991]. In 1931, Hartree suggested the inclusion of the Lorentz polarization term after which event the complex refractive index was often referred to as the Appleton-Hartree formula.

The detailed derivation of the formula can be found in Davies [1966, 1990]. First, we have to apply Maxwell’s equations to the wave, and secondly we have to impose the properties of the medium, the so-called “constitutive relations”.

The Appleton-Hartree magnetoionic theory applies to a medium that is electrically neutral with no resultant space charge and an equal number of electrons and positive ions

upon which a constant magnetic field is impressed and the effect of positive ions on the wave is negligible. Let us consider a plane electromagnetic wave travelling in the x direction of the orthogonal coordinate system displayed in Figure 2.6. Let us also consider

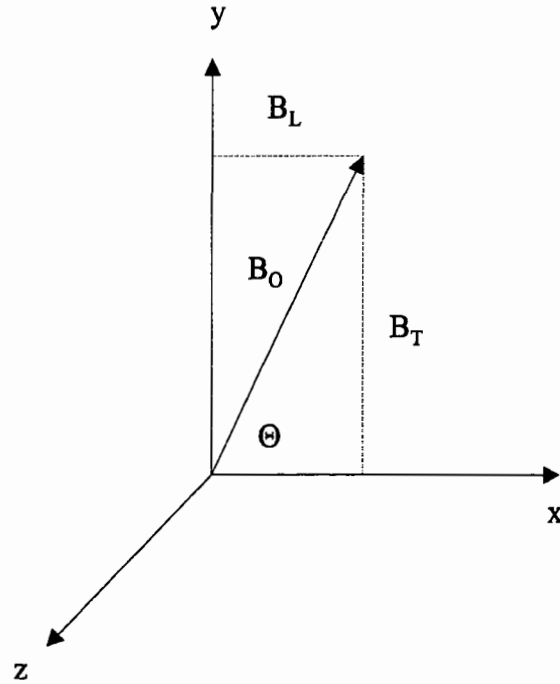


Figure 2.6: System of orthogonal axes x, y, z (after Davies [1990]).

a uniform external magnetic field that lies in the x-y plane and makes an angle θ with the direction of propagation. The complex refractive index n is given by the Appleton-Hartree magnetoionic dispersion equation (see e.g., Langley [1996]; Davies [1966; 1990]; Hunsucker [1991]; Hall and Barclay [1989]):

$$n^2 = 1 - \frac{X}{(1 - jZ) - \left[\frac{Y_T^2}{2(1 - X - jZ)} \right] \pm \left[\frac{Y_T^4}{4(1 - X - jZ)^2} + Y_L^2 \right]^{1/2}}, \quad (2.1)$$

where

n is the complex refractive index $(\mu - j\chi)$ with μ being the real part and χ being the imaginary part. Furthermore:

$$X = \frac{\omega_N^2}{\omega^2} = \frac{f_N^2}{f^2}, \quad (2.2)$$

$$Y = \frac{\omega_H}{\omega} = \frac{f_H}{f}, \quad (2.3)$$

$$Y_L = \frac{\omega_L}{\omega}, \quad Y_T = \frac{\omega_T}{\omega}, \quad (2.4)$$

$$Z = \frac{\omega_c}{\omega}, \quad (2.5)$$

where

ω (radian/s) is the angular frequency of the “exploring wave” f (Hz), and ω_c (radian/s) is the angular collision frequency between electrons and heavier particles;

ω_N is the angular plasma frequency with $\omega_N^2 = \frac{Ne^2}{\epsilon_0 m}$ with electron density N ($1/m^3$), electron charge e ($1.6 \cdot 10^{-19}$ coulomb), permittivity of free space ϵ_0 ($8.8542 \cdot 10^{-12}$ farad/m), and electron mass m ($9.1095 \cdot 10^{-31}$ kg);

ω_H is the angular gyrofrequency and $\omega_H = \frac{B_0 |e|}{m}$ (radian/s) with the electromagnetic field strength B_0 (Wb/m²);

ω_L is the longitudinal angular gyrofrequency and $\omega_L = \frac{B_0 |e|}{m} \cos \Theta$ (radian/s);

ω_T is the transverse angular gyrofrequency and $\omega_T = \frac{B_0 |e|}{m} \sin \Theta$ (radian/s).

When collisions are negligible (i.e., $Z \approx 0$):

$$n^2 \equiv \mu^2 = 1 - \frac{2X(1-X)}{2(1-X) - Y_T^2 \pm [Y_T^4 + 4(1-X)^2 Y_L^2]^{1/2}}, \quad (2.6)$$

According to the magnetoionic theory, a plane polarized electromagnetic wave will be split into two characteristic waves: an ordinary wave which approximates the behaviour of a wave propagating without an imposed magnetic field displayed with a sign “+” in eqn. (2.6) and the wave with the sign “-” is called extraordinary wave.

The expansion of eqn. (2.6) into series up to the 4th inverse power of frequency ($1/f^4$) following Bassiri and Hajj [1993] and Brunner and Gu [1991] yields:

$$n \equiv 1 - \frac{1}{2}X \pm \frac{1}{2}XY|\cos\Theta| - \frac{1}{8}X^2 - \frac{1}{4}XY^2(1 + \cos^2\Theta), \quad (2.7)$$

where it can be seen that the 2nd and 4th terms are functions of the maximum electron density and frequency whereas the 3rd and 5th terms are functions of the maximum electron density, the earth magnetic field strength and the frequency. Often we truncate the series (eqn. (2.7)) after the 2nd term neglecting the subsequent terms. Can we safely do that? What is the error we introduce into the refractive index when truncating the expression after the 2nd term? In other words, what are the contributions of the 2nd, 3rd, 4th and 5th terms to the error budget of determination of the refractive index?

To compute that let us evaluate X using typical values for the F2 layer maximum electron density $N = 10^{12}$ ($1/m^3$) and Y using typical value for the earth’s magnetic field strength $B_0 = 0.5 \cdot 10^{-4}$ (Wb/m^2). After evaluating the X and Y terms according to eqns.

(2.2) and (2.3) using the L1 GPS frequency (1575.42 MHz), the values turn out to be about $3.2 \cdot 10^{-5}$ and $1 \cdot 10^{-3}$ (unitless) respectively. After substituting these values for X and Y into eqn. (2.7) and assuming $\Theta = 0$, we arrive at the following equation providing us with the order of magnitude error that the individual terms can contribute to the accuracy of the refractive index n:

$$n \cong 1 - 1.6 \cdot 10^{-5} \pm 1.6 \cdot 10^{-8} - 1.3 \cdot 10^{-10} - 1.6 \cdot 10^{-11}. \quad (2.8)$$

This gives us an indication that the magnitude of the 3rd, 4th, and 5th terms are 3, 5, 6 orders of magnitudes less than the 2nd term.

When both collisions and the magnetic field are negligible then we will only use the 1st and 2nd terms in eqn. (2.7). For the phase refractive index of the ionosphere, appropriate for the carrier phase observations, we get:

$$n_{\varphi} \cong 1 - \frac{40.3 \cdot N}{f^2}, \quad (2.9)$$

and for the group refractive index appropriate for the pseudorange observations following Langley [1996]:

$$n_g \cong 1 + \frac{40.3 \cdot N}{f^2}. \quad (2.10)$$

After integrating eqns. (2.9) or (2.10) along the line of sight of the radio signal we get for the ionospheric delay d_{ion} (m):

$$d_{\text{ion}} \cong 40.3 \cdot \frac{\text{TEC}}{f^2}, \quad (2.11)$$

where TEC is the total electron content in TEC units ($1 \text{ TECU} = 10^{16} \text{ 1/m}^2$). If the vertical ionospheric delay on L1 GPS frequency (1575.42 MHz) is e.g., 16 meters computed from

the 1st and 2nd terms (corresponding to about 100 TECU at the zenith), then the 3rd term gives us 1.6 cm ionospheric delay (3 orders of magnitude less than the 2nd term). Following the same reasoning, the 4th term gives us submillimeter accuracy for the ionospheric delay (2 orders of magnitude less than the 3rd term). We can safely neglect the 5th term which is 1 order of magnitude smaller than the 4th term. Bassiri and Hajj [1993] showed that by neglecting the higher than 2nd terms, we could introduce as much as 4 cm ionospheric delay error at low elevation angles using the “ionospheric free” combination of the GPS observations. Using the ionospheric free combination, we can eliminate ionospheric effect up to the 2nd terms only. The 4 cm ionospheric delay error with satellites at low elevation angles is primarily due to the neglected 3rd term. This can also be supported by the computed 1.6 cm ionospheric delay error at the zenith projected into the line sight using an obliquity factor of 3 ($1.6 \text{ cm} \cdot 3 = 4.8 \text{ cm}$). Also, when using the 1st and 2nd terms only in eqn. (2.7), at GPS frequencies we do not concern ourselves with the extraordinary wave “-” which only appears in the 3rd term. The 3rd term either representing ordinary “+” or extraordinary waves have been shown to have an effect on the ionospheric delay error at the few cm level.

The Appleton-Hartree formula assumes that the electron collision frequency ν is not dependent on the electron velocity. In the lower D and E regions where the collision frequency ν is comparable with the wave frequency ω , this assumption no longer holds. To take this effect into account it is necessary to generalize the magnetoionic theory. Also, without using the generalized magnetoionic theory, the interaction of electrons and heavy

particles (absorption) is neglected in the equation above. What is the error incurred by assuming that the collision frequency ν is zero, i.e., $Z \cong 0$? Now, let us go back to eqn. (2.1) and for the sake of simplicity we set the magnetic field strength components $Y_T = Y_L = 0$, so that

$$n^2 \cong 1 - \frac{X}{1 - iZ} = 1 - \frac{X}{1 + Z^2} - \frac{iXZ}{1 + Z^2}. \quad (2.12)$$

In eqn. (2.12), after considering the real part of the refractive index only, using the binomial expansion for refractive index n , and then integrating it along the line of sight of the radio signal, we get for the ionospheric delay:

$$d_{\text{ion}} \cong 40.3 \cdot \frac{\text{TEC}}{f^2 + \nu^2}, \quad (2.13)$$

where ν is the collision frequency (Hz). Equation (2.13) is very similar to eqn. (2.11) with the difference of the inclusion of the term ν^2 . The collision frequency ν becomes comparable with the GPS frequency in the D layer where it can be as high as 10^9 (Hz) [Davies, 1990]. Above the D layer, ν has a value about 10^4 (Hz). Using the largest D layer electron density at the high solar activity time ($1.3 \cdot 10^9 \text{ (m}^{-3}\text{)}$) [Bilitza, 1990] and assuming that the D layer ranges from 50 km up to about 90 km, it turns out that by neglecting the collision frequency, in a worst case, we are introducing an error into the ionospheric delay using the GPS L1 frequency at the 0.06 mm level. It is interesting to point out that the inclusion of the collision frequency ν actually reduces the refracting properties of the medium. By neglecting the collision frequency, the magnitude of the error is at the submillimeter level, similar to the magnitude and sign of the error that

occurs when neglecting the 4th term in the Appleton-Hartree formula expansion (see eqn. (2.7)).

From the eqn. (2.9), it follows that the phase velocity v_p (m/s) is:

$$v_p = \frac{c}{n_\phi} \cong \frac{c}{1 - \frac{40.3 \cdot N}{f^2}} \cong c \cdot \left(1 + \frac{40.3 \cdot N}{f^2} \right), \quad (2.14)$$

where c is the speed of light in free space ($2.99792458 \cdot 10^8$ (m/s)).

Similarly from eqn. (2.10) the group velocity v_g (m/s) is:

$$v_g = \frac{c}{n_g} \cong \frac{c}{1 + \frac{40.3 \cdot N}{f^2}} \cong c \cdot \left(1 - \frac{40.3 \cdot N}{f^2} \right). \quad (2.15)$$

From eqn. (2.9), we can now define the vertical incidence reflection which takes place when $n = 0$ that is:

$$1 - \left(\frac{f_N^2}{f^2} \right) = 0, \quad (2.16)$$

where

f_N (Hz) is the plasma frequency at which a slab of neutral plasma with density N naturally oscillates after the electrons have been displaced from the ions and are allowed to move freely. f_N can also be expressed as

$$f_N^2 = \frac{Ne^2}{4\pi^2 \epsilon_0 m}, \quad (2.17)$$

where the individual parameters are described earlier in this section. For earth's ionosphere with e.g., $N = 10^{12}$ (m^{-3}), a typical value for f_N is about 8.9 MHz [Bassiri and

Hajj, 1993]. The condition for a wave to be reflected at vertical incidence is $f = f_N$ which is the physical principle that will make it possible to use the techniques introduced in Sections 2.4.1 and 2.4.2 for ionospheric studies [Hunsucker, 1991].

2.3 Global Ionospheric Modelling Techniques

Ionospheric models can be subdivided into two major groups: empirical climatological and theoretical climatological models. Empirical climatological models are based on a parameterization of a large amount of ionospheric data collected over a long period of time. Given the long time series of data, it is possible to perform the parameterization in terms of solar activity, seasonal variation, geographic latitude, longitude, and local time variation. The theoretical climatology yields a “representative ionosphere”, i.e., an ionospheric profile is constructed by using a specific set of geophysical conditions. The theoretical climatology is based on ionospheric physics and chemistry included in the theoretical climatological models. The modelled ionospheric features will have locations, dimensions, similar to those that might be observed on any given day under the specified geophysical conditions [Daniell et al., 1995].

The global empirical climatological ionospheric model by Chiu describes the large scale variation of the ionospheric electron density with local time, latitude, and solar sunspot number [Chiu, 1975]. The Bent global empirical climatological ionospheric model [Bent and Liewellyn, 1973] describes the ionospheric electron density as a function of

latitude, longitude, time, season and solar radio flux. The model is based on some 50,000 Alouette topside ionograms, 6,000 Ariel 3 in situ measurements, and some 400,000 bottomside ionograms from 1962 to 1969.

The Semi-empirical Low-latitude Ionospheric Model (SLIM) [Anderson et al., 1987] is based on a theoretical simulation of the low-latitude ionosphere. Electron density profiles are determined for different latitudes and local times by solving the continuity equation for oxygen (O^+) ions. The Fully Analytical Ionospheric Model (FAIM) [Anderson et al., 1989] combines the Chiu model with coefficients fitted to the SLIM model profiles.

Now, I will briefly describe two recent, most often used, state-of-the-art ionospheric models: the empirical climatological International Reference Ionosphere 1995 [Bilitza, 1990] and the theoretical climatological Parameterized Ionospheric Model [Daniell, 1995]. These are the models that most research groups, using GPS as a tool for studying the ionosphere, are working with and carrying out modifications on.

2.3.1 Ionospheric Modelling Using the International Reference Ionosphere

In this section, I only provide a general overview of the model since it will be described and dealt with more fully later in this dissertation (see Section 4.2.7). The International Reference Ionosphere (IRI) is an international project sponsored by the COmmittee on

SPace Research (COSPAR) and the International Union of Radio Science (URSI). These organizations formed a working group in the late 1960s to produce an empirical standard model of the ionosphere, based on all available data sources. The first version of IRI was released in 1978 which was followed by several steadily improved editions in 1986, 1990 and 1995. For a given location, time and date, IRI describes the electron density, electron temperature, ion temperature, and ion composition in the altitude range from about 50 km to about 1000 km; and also the electron content. It provides monthly averages in the non-auroral ionosphere for magnetically quiet conditions. The major data sources are the worldwide network of ionosondes, the powerful incoherent scatter radars, the ISIS and Alouette topside sounders (see Section 2.5.6), and in situ instruments on several other satellites and rockets [Bilitza, 1996a, 1996b]. A historical overview of the IRI model can be found in [Bilitza, 1990]. Each year the IRI working group members reconvene to discuss the latest developments and possible enhancements of the IRI model. The latest workshop was held at the Institute for Atmospheric Physics in Kühlungsborn, Germany where UNB was also represented with a presentation of material described in detail in Chapter 6 of this dissertation [Komjathy et al., 1997].

2.3.2 Ionospheric Modelling Using the Parameterized Ionospheric Model

The Parameterized Ionospheric Model (PIM) is made up of four different physical models: a low-latitude F layer model, a mid-latitude F layer model, a combined low and middle latitude E layer model, and a high-latitude E and F layer model. These four models are

based on a tilted dipole representation of the geomagnetic field and the corresponding geomagnetic coordinate system. Unlike the IRI model which is based on empirical climatology, the PIM model is based on theoretical climatology producing electron density, ion composition profiles, and profile parameters (foF2, hmF2, TEC) based on the physics-based numerical model for a variety of geophysical conditions. The Parameterized Real-Time Ionospheric Specification Model version 1.6 (PRISM) uses PIM with ground-based or space-based data to update the climatological model in near real-time [Daniell et al., 1995]. A new version of PRISM, version 2.0, is currently under development. It will feature a plasmaspheric electron content model which was not included in the model before. Moreover, the new version will be based on a single global ionospheric model so there will not be discontinuities or ramps between ionospheric regions. Thermospheric wind and equatorial vertical drift modelling techniques will also be included in the new model. This will allow the user to capture the variability of the equatorial anomaly [Daniell and Anderson, 1996; Daniell et al., 1996].

2.4 Ground-Based Techniques for Probing the Ionosphere

In Section 2.2, I introduced the concepts of the refractive index for the magnetoionic medium, plasma frequency, and the electromagnetic wave refracting at vertical incidence (see eqn. (2.16)).

The determination of the height of the ionospheric layer by emitting an unmodulated radio-frequency pulse vertically upward is one of the most useful ionospheric characteristics. This height (true height) cannot, however, be determined directly by measuring the time t it takes this pulse to propagate to the ionospheric layer, at which it is reflected, and return to earth. This is because the radio-frequency pulse always travels more slowly in the layer than in free space. The true height h_r can, however, be determined from the virtual height h_v which is a function of frequency, electron density, and magnetic field strength. The virtual height of a layer is always greater than the true height since the group refractive index n_g is greater than unity. Following Davies [1990], the virtual height is given by the integral equation:

$$h_v = \int_0^{h_r} n_g dh = h_0 + \int_{\varphi_0}^{\varphi_r} \frac{dh}{d\varphi} n_g(\varphi) d\varphi, \quad (2.18)$$

where h_r is the real height of the reflection, "0" is the surface of the earth, n_g is the group refractive index. The parameter φ is a function of the electron density, φ_0 and φ_r are the values of φ at the bottom of the ionosphere, h_0 , and at the real height of the reflection respectively. If we choose to neglect the effect of the earth's magnetic field and the collision frequency then solving the integral in eqn. (2.18) is relatively straight forward and it can provide us with the true height of the reflection. In general, the inclusion of the magnetic field and the collision frequency terms require numerical techniques that are otherwise readily available [Titheridge, 1988]. As we have seen the virtual (h_v) and true

(h_r) heights of reflection are related to the frequency of the radio wave emitted vertically upward (vertical incidence frequency).

The radio waves can also be emitted upward at an oblique angle. The secant law establishes the relationship between the vertical incidence frequency and oblique incidence frequency giving us the theoretical basis for the use of the oblique backscatter radar. Further relationships between vertical or oblique incidence frequencies, virtual and true heights can be found in e.g., Hunsucker [1991] and Davies [1990]. The ionosonde, a technique utilizing the measurement of the virtual height will be introduced in Section 2.4.1. The oblique backscatter radar will be described in Section 2.4.2.

2.4.1 Ionosonde

Ionosondes function by emitting high frequency radio waves, sweeping from lower frequency to the higher, to measure the time required for the signal to travel and return from the refracting ionospheric layer. As explained in the previous section, radio-frequency pulse travels more slowly (group velocity) in the ionosphere than in free space, therefore the virtual height is recorded instead of the true height. For frequencies approaching the maximum plasma frequency in a particular layer, the virtual height tends to become infinity because the wave has to travel a finite distance at effectively zero speed.

Ionograms can provide the relationship between the radio wave frequency and virtual height of the reflecting ionospheric layer. From the ionograms, the characteristic values of virtual heights h_vE , h_vF1 and h_vF2 and critical (penetration) frequencies (for definition see Section 2.1.2) f_oE , f_oF1 and f_oF2 can be scaled manually or digitally. Modern ionosondes (digisondes) routinely scale ionograms. I present a sample ionogram in Figure 2.7 provided by Haystack Observatory [1996a]. The data was observed with the Millstone Hill Digisonde 256 at 19:34 local time on April 1st, 1996. The radio wave frequency is plotted against the virtual height of the reflecting layer. We can clearly see that the virtual height steadily increases with the frequency up to the critical (penetration) frequency. In Figure 2.7, the critical frequencies f_oE , f_oF1 , and f_oF2 can be obtained by taking a frequency reading when the virtual height has a local minimum (f_oE , f_oF1) or when it tends to approach infinity (f_oF2). In the figure, we can identify two curves representing the ordinary and extraordinary waves. The curves with the higher critical frequencies f_xF1 , and f_xF2 are the extraordinary waves. The ordinary and extraordinary waves can be derived by using eqn. (2.6) and then using $n = 0$ as a criterion for reflection at an ionospheric layer. After solving the equation, we will get separate solutions for the ordinary and the extraordinary waves. We can also identify a curve at the bottom of the plot which can be attributed to background interference [Davies, 1990]. The so-called 2-hop reflection is due to the twice reflected waves from the ionospheric layers with an intermediate ground reflection.

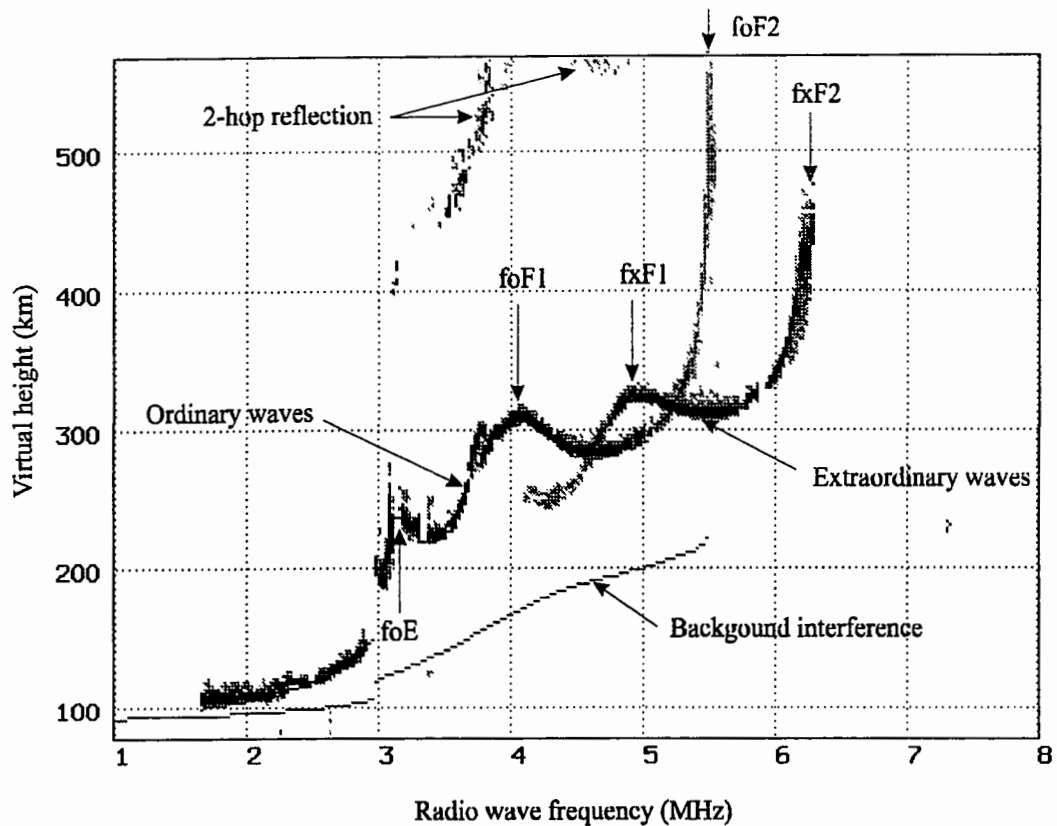


Figure 2.7: Sample ionosonde data.

2.4.2 Oblique Backscatter Radar

If the sounder directs radio waves at an oblique angle to the ionosphere, then we are dealing with oblique backscatter sounders. In this case, a train of short pulses of radio frequency energy is refracted by the ionosphere and scattered nonuniformly at the surface of earth. Some of the incident radio frequency energy is backscattered along the same path, amplified and detected at the receiver. We can distinguish groundscatter and direct backscatter modes. In the case of groundscatter, the RF energy is reflected by the ground and the ionosphere and some energy returns to the receiver. In the case of direct

backscatter, the RF energy is backscattered by the ionosphere and reflected back to the receiver. The direct backscatter echoes can be used to detect ionospheric irregularities in the auroral region [Hunsucker, 1991]. Maximum electron densities derived from oblique backscatter measurements are routinely reported as a validity check for electron density profiles derived using ionosondes [Levy and Bamford, 1997].

2.4.3 Incoherent Backscatter Radar

The incoherent scatter radar is the most powerful ground-based technique for the study of the earth's ionosphere and the interactions with the upper atmosphere, magnetosphere, and the interplanetary medium.

The technique is based on the radar principle which is the technique for detecting and studying remote targets by transmitting a radio wave in the direction of a target and observing the reflection of the wave. The target of any incoherent scatter radar is the electrons comprising the ionosphere. Since the amount of energy scattered by each electron is well known, the strength of the echo received from the ionosphere measures the number of electrons in the scattering volume, and thus the electron density. The width of the spectrum is a measure of temperature of the ionosphere which can be different for ions and electrons. The shape of the spectrum is a sensitive function of the ratio of the electron and ion temperatures. Since the mixture of ions and electrons (also known as plasma) is constantly in motion in addition to the thermal motion, an overall shift of the

spectrum can be detected from which the speed of the ions and electrons can be inferred. The currently operating incoherent scatter radar facilities include Arecibo, Puerto Rico; EISCAT, Norway/Sweden/Finland; Sondrestrom, Greenland; Irkutsk, Russia; Jicamarca, Peru; Kharkov, Ukraine; Millstone Hill, U.S.A.; and MU, Japan. For more detailed explanations of the incoherent backscatter radar theory, the interested reader is referred to Hunsucker [1991] and Haystack Observatory [1996b].

2.5 Satellite and Other Techniques

There are also satellite-based techniques available to measure TEC up to the altitude of the satellite which can be anywhere within or above the ionosphere.

2.5.1 Global Positioning System

Since the main topic of this dissertation is TEC modelling using GPS, in this section I will only discuss the characteristics of the GPS signals and the most common positioning strategies for which GPS is primarily used.

The literature of GPS is extensive. The principles of GPS are described in e.g., Wells et al. [1987], Kleusberg and Teunissen [1996], Parkinson et al. [1996], Leick [1995], and Hoffmann-Wellenhoff et al. [1994]. Theoretical and everyday practical information about

GPS can be accessed via Langley [1997a], Langley [1997b] and Freymueller [1997] maintain e-mail discussion lists dealing with GPS-related scientific and practical questions. Specific GPS-related scientific and technical issues are covered in the Innovation column of the monthly GPS World magazine.

GPS satellites transmit positioning signals on two L-band frequencies. A signal component includes positioning and health status information of the satellites. Ranging to the GPS satellites is carried out by measuring the time required for a signal to propagate from a GPS satellite to the receiver. GPS consists of three major segments: space, control and user. The Space Segment consists of 24 operational satellites in six orbital planes (four satellites in each plane). The satellites operate in nominally circular orbits at a height of about 20,200 km and an inclination angle of 55 degrees. The corresponding orbit period is about 12 sidereal hours. The Control Segment consists of five Monitor Stations (Hawaii, Kwajalein, Ascension Island, Diego Garcia, Colorado Springs) passively tracking all satellites in view, accumulating data. The information is processed at the Master Control Station to estimate satellite orbits, satellite clock error, and other navigation data parameters such as *satellite health* for each satellite. This information is transmitted to each satellite via Ground Antennas (Ascension Island, Diego Garcia, Kwajalein, Cape Canaveral, and Colorado Springs). The User Segment consists of antennas and receivers providing positioning, velocity and precise timing.

The two L-band frequencies on which the GPS satellites transmit are: $L1 = 1575.42$ MHz and $L2 = 1227.6$ MHz. Two pseudorandom noise codes (PRN) are modulated onto the carrier signals, the C/A-code and the P-code. The coarse/acquisition (C/A) code is modulated on the L1 carrier only. The P-code (precision code) is modulated onto both L1 and L2 carriers. A low bit rate (50 b.p.s.) navigation message is modulated onto both L1 and L2 carriers.

Users of single frequency receivers have access to lower accuracy C/A code which is provided in the GPS Standard Positioning Service (SPS), the level of service authorized for civilian users. The Precise Positioning Service (PPS) provides access to both C/A code and encrypted P-code and is designed for military users. The SPS incorporates denial of full accuracy (Selective Availability or SA) which can be accomplished by intentionally degrading the broadcast orbit ephemeris (the “epsilon-process”) and dithering the satellite clock (the “delta-process”). Operationally, the current SA approach uses the delta-process. The U.S. Department of Defense can also encrypt the P-code, as a procedure known as Anti-spoofing (AS), by combining it with a secret W-code. AS was activated on 31 January 1994 and now is in continuous operation on Block II satellites [Langley, 1996].

The pseudorange and the carrier phase are the two basic observables. The GPS receiver generates a replica of the two L-band frequencies transmitted by the satellites and then the receiver differences it with the incoming Doppler shifted signal to produce a beat

frequency. The receiver keeps a running cycle count on the carriers and it provides us with the raw carrier phases that can be measured with high precision, in the case of modern receivers it is typically at the 0.9 mm level with A/S turned off and 1.4 mm level with A/S turned on. With an appropriate smoothing, the raw carrier phase precision can be improved typically by a factor of 6. Furthermore, modern receivers synthesized P(Y)-code raw measurement precision is about 25 cm (L1 and L2) with A/S turned on and between elevation angles 30 to 50 degrees. With A/S turned off, the P-code raw measurement precision is about 15 cm on L1, and 21 cm on L2. With an appropriate smoothing, these precisions can be improved typically by a factor of 16 [Ashtech, 1997]. After testing a high-performance GPS receiver with narrow correlator technology, it was found that the C/A-code measurement noise (ignoring the contribution of the antenna preamplifier) was at the 4 cm level [Wells et al., 1995].

The simplest positioning technique also known as point positioning uses one GPS receiver with access to one or both of the codes from at least four simultaneously observed satellites. Three satellites are needed to compute the receiver's position and the fourth is required to remove the receiver clock offset from GPS time. The horizontal accuracy of point positioning is about 22 m (2 d.r.m.s.) if P-code is used and 100 m (2 d. r.m.s.) if C/A code is tracked. The vertical accuracy is about 28 m (2 sigma) if P-code and about 156 m (2 sigma) if C/A code is used [Parkinson et al., 1996]. The different error sources contributing to the point positioning error budget is discussed by Langley [1997c].

With the use of relative or differential techniques, error sources such as satellite position errors, satellite clock errors, tropospheric and ionospheric delays that are common to simultaneously observing receivers, one with a well determined position, can be eliminated or greatly reduced. Depending on the sophistication of the algorithm, code differential techniques can routinely achieve accuracies at the level between 1 to 10 metres (2 sigma) [Komjathy and Langley, 1995]. For high precision geodetic applications, carrier phase observations are used. Depending on the level of sophistication of the post-processing software, a few parts in 10^9 (1 sigma) precision can be achieved over baseline lengths of thousands of kilometers.

2.5.2 GLONASS

The Global Navigation Satellite System (GLONASS) is the Russian equivalent of GPS. It will consist of 24 satellites including three spares. The GLONASS satellites are arranged in three orbital planes. Each orbital plane contains 8 equally spaced satellites. GLONASS, like GPS, is a one-way ranging system. Two carrier signals in the L-band are broadcast and the signals are modulated by binary codes and a navigation message. The GLONASS satellites transmit code and carrier phase data on different frequencies for each GLONASS satellite in view separately on L1 and L2. The GLONASS constellation contains 21 operational satellites at the moment (July 1997). The last GLONASS satellite was launched in December 1995. (Detailed descriptions of the GLONASS system can be found

in e.g., Langley [1997d], Parkinson et al. [1996], Kleusberg [1990], Seeber [1993], Kaplan [1996], and Hoffmann-Wellenhoff et al. [1994].

Zarraoa et al. [1995] investigated the use of GLONASS P-code and carrier phase measurements to estimate the diurnal variation of TEC. The results were compared with those of GPS TEC estimates and an agreement of about 1.6 TECU (r.m.s.) was found between GPS and GLONASS estimates. Based on 1 day's worth of GLONASS and GPS data, the differences between the GLONASS and GPS-derived TEC data were between -4 and 3 TECU. GLONASS dual frequency observations can potentially be used either in combination with GPS or as a stand-alone system to provide ionospheric data. The GLONASS P-code data is comparable with GPS dual frequency measurements with the advantage of the fact that there is no Anti-spoofing imposed on the GLONASS system. Danaher et al. [1993] also demonstrated the potential of dual frequency GLONASS receivers using P-code and carrier phase measurements for TEC monitoring.

2.5.3 Transit

The immediate predecessor of today's modern satellite-based positioning systems is the Navy Navigational Satellite System (NNSS), also called Transit which was based on the concept of differential Doppler and was used for various geodetic purposes (Seeber [1993], Vanicek and Krakiwsky [1986] and Wells et al. [1987]). Transit has been one of the major sensors of the ionosphere over the last 36 years. The line-of-sight total electron

content between an NNSS satellite and the receiver can be inferred from integrated Doppler measurements. These measurements are based on phase differences between two radio signals transmitted coherently on two carrier frequencies (150 MHz and 400 MHz). TEC data cannot directly be measured without resolving the initial phase value. This can be achieved by e.g., means of comparison with TEC from Faraday rotation data (for explanation see Section 2.5.5), from simultaneous evaluation of integrated Doppler measurement from two suitably located stations ("two-station method") or by making assumptions about the spatial variation of the local ionospheric electron density profile. The satellites are orbiting in a nearly circular orbit at an altitude of approximately 1100 km. Since the orbits are of polar type, the measurements from a chain of ground-based receivers can provide line-of-sight and vertical TEC data making the NNSS satellites an ideal tool to investigate the latitudinal variation of the ionosphere. Furthermore, Leitinger et al. [1984] reported that a network of NNSS receivers can be used to detect large TEC variations induced by a major geomagnetic storm. TEC data derived from NNSS satellites was compared against Faraday rotation measurement for a geomagnetic storm period. Large latitudinal and longitudinal gradients were detected apparently caused by the geomagnetic storm. Another experiment involved a tomographic reconstruction (see Section 4.1.2) of electron density profiles along five North American stations corresponding to the ground tracks of NNSS satellites. During the experiment, the stations - one of them at the University of New Brunswick - were occupied with Doppler receivers [Pakula et al., 1995]. Transit is based on the technology in the year 1960. Some of the early satellites were used for up to 20 years. Currently there are 6 operational

NNSS satellites available for ionospheric monitoring [Raymund, personal communication, 1997].

2.5.4 TOPEX/Poseidon

The Ocean Topography Experiment (TOPEX/Poseidon or T/P) is a joint effort between NASA and the French Space Agency (CNES) to study Earth's ocean (map basin-wide variations in current, and monitor the effects of currents, such as the Gulf Stream, on global climate change). The T/P satellite travels at an altitude of about 1366 km. The satellite's position is known to within 10 cm and that is achieved with data from a dual frequency GPS receiver as part of the payload. The satellite has dual and single frequency altimeters on board, laser reflector array, TOPEX microwave radiometer, dual frequency GPS receiver, and DORIS dual frequency Doppler receiver. Data from the dual frequency altimeter can be used to provide accurate TEC measurements over the oceans by taking advantage of the dispersive nature of the ionosphere. Anderson and Johnson [1996] showed global ionospheric TEC maps derived from T/P data. The data compares favourably with existing global ionospheric models such as IRI-95 and PRISM. The TOPEX mission is described in detail in TOPEX/Poseidon [1997]. In this research, T/P-derived TEC data was used as a "ground-truth" against which GPS-derived TEC estimates were compared. The investigation will be discussed in Chapter 6.

2.5.5 Faraday Rotation Technique

The principle of Faraday rotation is based on the characteristics of ordinary and extraordinary waves. When linearly polarized radio waves emitted from a satellite are exposed to the earth's magnetic field, the two characteristic waves' (ordinary and extraordinary) plane of polarization rotates (Faraday rotation) gradually since the two characteristic waves have different phase velocities propagating through the magnetoionic medium. The Faraday rotation is proportional to the total electron content, the magnetic field strength and the inverse squared frequency of the wave. Since the magnetic field strength decays approximately as an inverse cube of the radial distance, electron contribution higher than about 2000 km is negligible; therefore Faraday rotation measurements cannot be used to detect electron content above an altitude greater than about 2000 km [Davies, 1990]. A comprehensive study of the determination of the total electron content of the ionosphere can be found in Titheridge [1972]. In comparison with another phase techniques, GPS or GLONASS can measure TEC up to the altitude of the satellites (about 20,000 km). The currently operating Geosynchronous Operational Environmental Satellites (GOES-1, GOES-2) are providing the opportunity to gather Faraday rotation measurements using polarimeters [SPACEWARN, 1997].

2.5.6 Topside Sounders

Topside sounders are small ionosondes that are carried by earth-orbiting satellites. With advanced technology, it became possible to explore the ionosphere above the level of maximum ionization on a global scale. Learning about the topside ionosphere is of utmost importance since up to about 2/3 of the total electron content can be attributed to the topside electron content. Only two techniques have been used to investigate the topside ionosphere: these are the topside sounders and the incoherent backscatter radar. In a Canadian-U.S. undertaking, a Canadian designed and built sweep-frequency ionosonde was placed on the Alouette 1 satellite flying at the altitude of about 1000 km [Hunsucker, 1991]. The Alouette 1 mission was active between 1962 and 1972, whereas the Alouette 2 follow-on mission, carrying a similar ionosonde, was operational between 1965 and 1975 [Satellite Encyclopedia Online, 1997]. Topside ionospheric measurements on board the Alouette missions made it possible to improve the topside profile of the International Reference Ionosphere [Bilitza, 1996b].

2.5.7 PRARE

PRARE, which stands for Precise Range and Range Rate Experiment, is a satellite-based tracking system for precise orbit determination and for relative and absolute positioning of ground stations. The system has been developed by the Institut für Navigation, University of Stuttgart, the Deutsches Geodätisches Forschungsinstitut, München, and the

Geoforschungszentrum, Potsdam. The PRARE mission objectives include long-arc satellite orbit determination; global gravity field monitoring; PRARE station positioning; and TEC determination in support of oceanography, glaciology, geophysics and geodesy [Seeber, 1993].

Two pseudorandom noise (PRN) coded microwave signals in the X (8.5 GHz) and S (2.2 GHz) bands are transmitted simultaneously from the space segment (European Remote Sensing satellites ERS-1, ERS-2) to the ground station. At dedicated ground station transponders, the time delays in the reception of both signals are measured and transmitted to the space segment for the calculation of ionospheric correction. At the same time, meteorological parameters (temperature, humidity and atmospheric pressure) are collected at the ground station transponder to compute tropospheric corrections to be transmitted back to the space segment. Using PRARE, there are two ways of estimating vertical and line-of-sight TEC. One can either measure the one-way code travel time difference between the simultaneously transmitted X and S-band signals or compute it using two-way ranging measurements based on the different propagation velocities (group delay vs. phase advance)(for more information see Geoforschungszentrum [1997] and Lechner et al. [1989]).

The first preliminary results of a worldwide determination of TEC using PRARE were presented by Flechtner [1997]. TEC derived from the network of PRARE tracking stations compared favorably with T/P, DORIS and IRI-95-derived TEC values.

2.5.8 DORIS

DORIS (Doppler Orbitography and Radio Positioning Integrated by Satellite) is a French system with similar objectives as PRARE. The basic principle is based on the accurate measurement on board the spacecraft of the Doppler shift of radiofrequency signals emitted by ground beacons. The system now includes a network of about 50 transmitting beacons spread all over the world. Measurements are made on two frequencies: about 2 GHz for accurate Doppler measurements together with 401.25 MHz for ionospheric correction. The latter frequency is also used for measurement time-tagging and auxiliary data transmission. Assuming that the Doppler measurement at both frequencies are equal except for the ionospheric effect, one can deduce from these measurements the ionospheric correction to be applied to the 2 GHz measurement. This correction is related to the slant ionospheric electron content which can also be related to vertical TEC. DORIS on-board equipment is currently flying on remote sensing satellites SPOT-2, SPOT-3 and the TOPEX/Poseidon oceanography satellite. Global ionospheric maps using DORIS data by Picot and Escudier [1996] compared with TOPEX/Poseidon-derived TEC data at the 4 TECU level. Recent comparisons on the global scale have revealed a 2.5 TECU level agreement between DORIS-derived TEC data and the IRI-95 model [Picot, 1997].

In this chapter I have described the different techniques that can be used to infer TEC. In the next chapter I will concentrate on two ionospheric models; one being the Broadcast

model and the other the IRI-90 model. Results will be presented on the comparison of these models with Faraday rotation data.

CHAPTER 3

MODELLING THE IONOSPHERE USING EMPIRICAL MODELS

One of the major error sources in GPS positioning is ionospheric refraction which causes signal propagation delays and advances. To correct data from a single frequency GPS receiver for the ionospheric effect, it is possible to use empirical models. In this chapter, I will investigate the GPS single frequency Broadcast [Klobuchar, 1986] and the International Reference Ionosphere (IRI-90) [Bilitza, 1990] models. The GPS single frequency Broadcast model is available to GPS users as part of the navigation message. The IRI-90 model is a standard ionospheric model developed by the International Union of Radio Science (URSI) and the Committee on Space Research (COSPAR). Several IRI model versions have been investigated at the Geodetic Research Laboratory of the University of New Brunswick as an ongoing study to evaluate different global empirical ionospheric models. As far as the IRI model versions are concerned, the research started with IRI-86 by Newby et al. [1990], and then for my research I used the subsequent version known as IRI-90 after it was released in 1990. In this chapter, I will report on my earlier investigation using IRI-90. As I was making progress with my ionospheric research, I also started using the most recent version of the IRI model also known as IRI-95. In the subsequent chapters, discussions of further investigations using IRI-90 and IRI-95 will follow.

The results of the earlier IRI-related UNB studies have been reported by Newby et al. [1990], Newby and Langley [1992], and Newby [1992]. Newby found that based on a week's worth of dual frequency GPS receiver-derived TEC data, the Broadcast model was, at times, able to account for 80 percent r.m.s. of the ionospheric delay. The performance of the IRI-86 model (predecessor to IRI-90 and IRI-95) was slightly worse than the Broadcast model.

After Newby [1992] investigated the IRI-86 model's performance, I decided to include the new IRI-90 model in my ionospheric research. I have used Faraday rotation data as ground-truth with which I compared the vertical ionospheric range error corrections predicted by the Broadcast and IRI-90 models. The results shown here have been presented by Komjathy et al. [1995; 1996b].

3.1 Behaviour of the GPS Single Frequency Broadcast Model

The GPS single frequency Broadcast model is described by e.g., Klobuchar [1986], Newby [1992], and Hakegard [1995]. The Broadcast model uses a half cosine representation of the diurnal ionospheric delay on L1, T_{iono} (in seconds) [Klobuchar, 1975; 1986; 1991; 1996; ARINC Research Corporation, 1992]:

$$T_{iono} = F \cdot \left(DC + A \cdot \cos \left[\frac{2\pi(t - \phi)}{P} \right] \right), \quad (3.1)$$

where

DC (seconds) is the night-time constant offset term (set to 5 ns corresponding to 1.5 metres ionospheric delay on L1),

A is the amplitude term (seconds),

ϕ is the phase of the maximum vertical ionospheric delay which is assumed to be at 14:00 hours local mean solar time (50400 seconds),

P is the period (seconds),

t is local mean solar time (seconds), and

F is the obliquity factor projecting vertical ionospheric delay into the line-of-sight.

The ϕ and P terms each have four time and solar-activity dependent coefficients to represent the behaviour of the global ionosphere. To analytically represent the amplitude and period terms, a cubic polynomial in geomagnetic latitude is used to represent ionospheric delays computed by the Bent model [Bent and Liewellyn, 1973] which was the best available to model worldwide TEC at the time of the model's development [Klobuchar, 1975].

The short-term stability of the Broadcast model performance has been studied by several researchers based on limited sets of Broadcast model coefficients, among them Coco et al. [1990] and Newby [1992]. Klobuchar and Doherty [1990] showed that the Broadcast model's performance is significantly better than 50 percent r.m.s. for day-time data based on a long-term comparison with Faraday rotation data. I decided to examine the long-term stability of the Broadcast model performance in describing the diurnal and

seasonal variations of the mid-latitude ionosphere at a level of low solar activity and have compared it with another global empirical ionospheric model.

I examined 53 sets of Broadcast model coefficients archived by the Department of Radio Engineering of the Czech Technical University in Prague which started archiving the coefficients in April 1994. The data set I used covers a period of 11 months, from April 1994 to March 1995.

I computed hourly vertical ionospheric range error corrections from the Broadcast model for those days when a new set of model coefficients were transmitted and received. The reason why only the days with a new set of model coefficients were used relies on the fact that the archiving procedure was not continuous at the time when the coefficients were monitored and recorded. In order to avoid occasions that could occur when new model coefficients may have been undetected I did not use days for the analysis between two subsequent updates. This resulted in a discontinuous time series during the 11-month period. The Broadcast model was evaluated for the Boulder, CO region from where I also have the Faraday rotation data for comparison purposes.

In Figure 3.1, I plotted the Broadcast-model-predicted diurnal variation of the vertical ionospheric range error corrections on L1. We can clearly see the amplitude and period changing over the course of one year. We can also clearly see, as given by the algorithm, the night-time vertical ionospheric term (DC) is set to a constant 5 ns level which

corresponds to about 1.5 metres at the L1 frequency. Moreover, the algorithm sets the peak of the cosine curve to 14:00 hours local time.

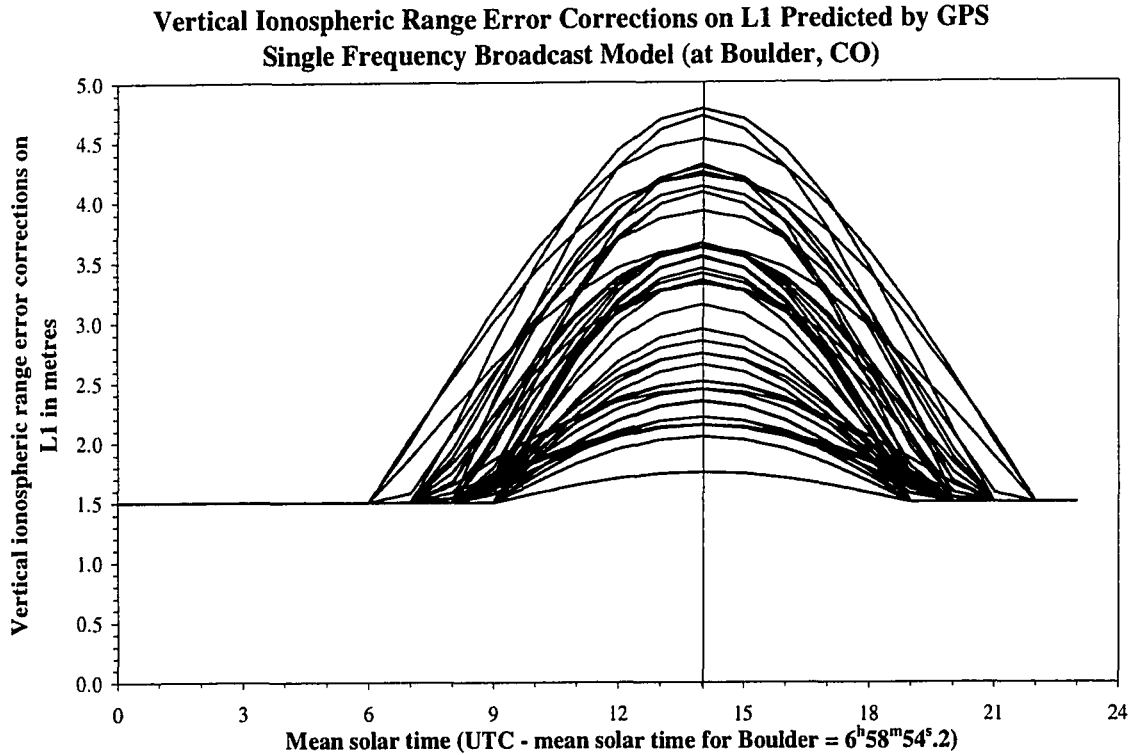


Figure 3.1: Vertical ionospheric delay predictions using 53 sets of Broadcast model coefficients.

In Figure 3.2, the predicted diurnal variation of the vertical ionospheric range error corrections are plotted one after the other. Each successive curve represents a new set of Broadcast model coefficients describing the diurnal variation of the vertical ionospheric range error corrections showing a distinct seasonal variation with peaks in February-March and September-October. The selection of a particular set of Broadcast model coefficients to be sent in the navigation message is based on the day of year and the running average of the observed solar flux numbers for the past five days. One year is

divided into 37 ten-day-periods. Each period is represented by ten different solar activity levels. The following solar flux numbers separate the different solar activity levels: 75, 100, 120, 140, 155, 170, 185, 200, 215 and 230 flux units. Solar activity less than 75 flux units is set to level 1 and greater than 230 flux units is set by default to level 10. Based on my sample data set, the average update rate of the coefficients turned out to be 6.4 days with a range of 1 to 10 days. The diurnal curves with larger amplitudes correspond to solar activity levels when the five-day running average of the observed solar flux numbers exceeded a predetermined flux level: for the period covered by my time series, the first or 75 solar flux unit level.

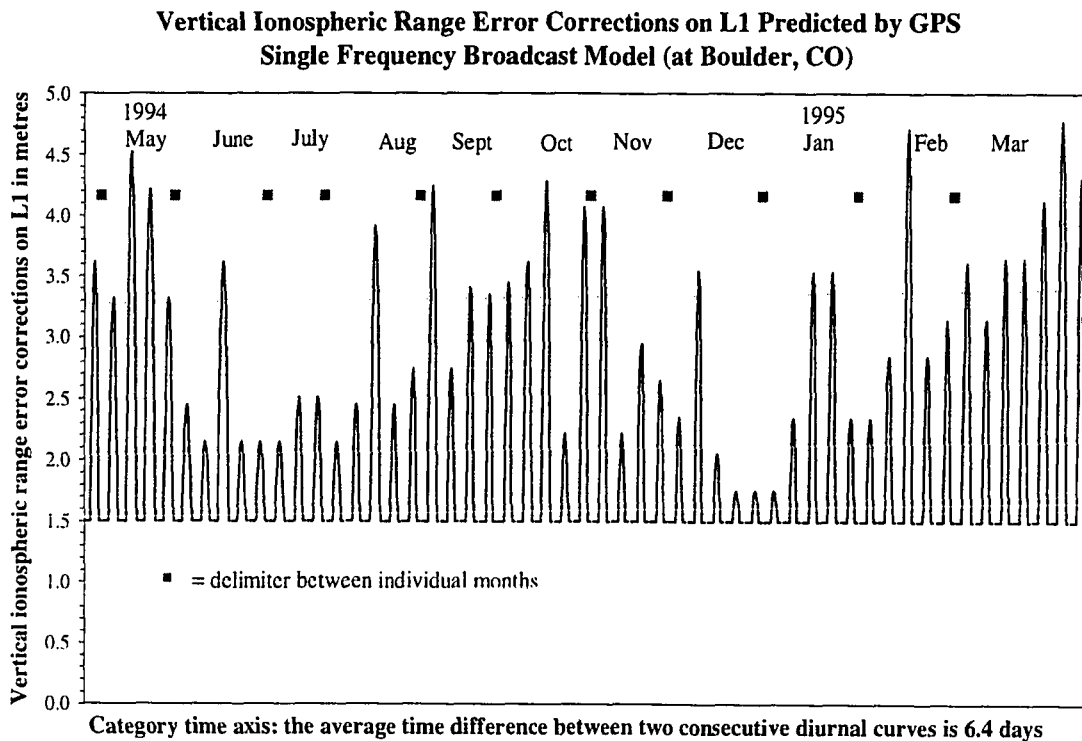


Figure 3.2: Vertical ionospheric range error corrections on L1 predicted by GPS single frequency Broadcast model.

In Figure 3.3, the five-day running average of observed solar flux numbers provided by the National Oceanic and Atmospheric Administration (NOAA) National Geophysical Data Center (NGDC) Solar Terrestrial Physics Division is displayed. The 75 solar flux unit crossovers indicate the need for choosing a new set of coefficients corresponding to a different solar activity level, in this case separated by the 75 flux solar activity level (the separation value between activity levels 1 and 2).

Five Day Running Average of Observed Daily Solar Flux (1994-95)

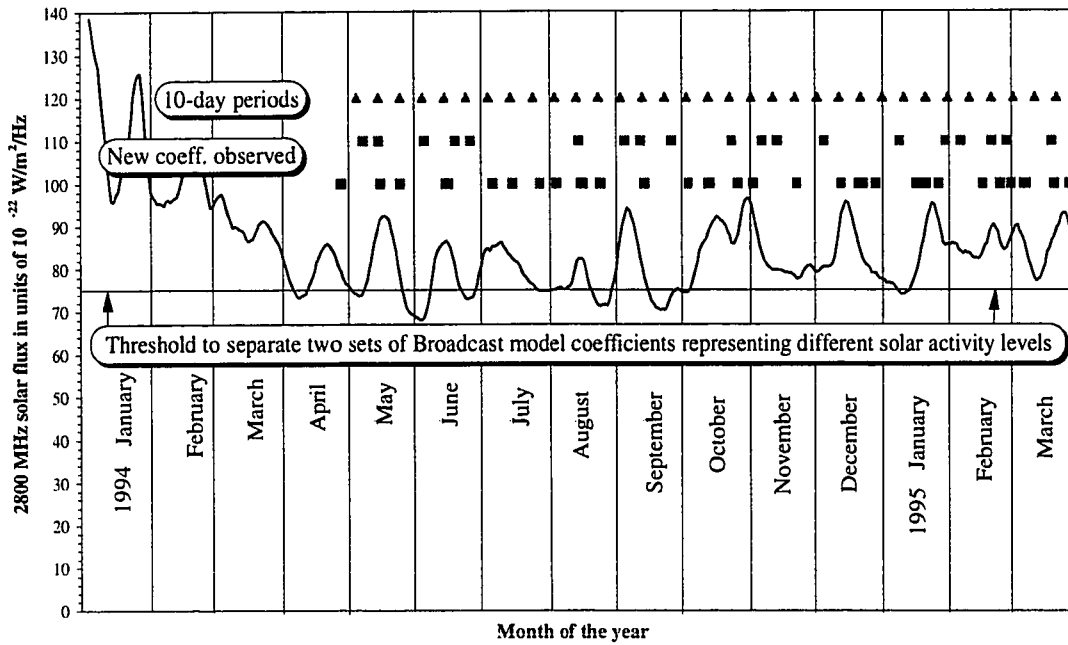


Figure 3.3: Broadcast model coefficients dependency on smoothed daily solar flux numbers.

In Figure 3.3, I indicated the need for changing the Broadcast model coefficient sets based on the ten-day-periods demarcated with triangles. The second criterion that can dictate a change in the Broadcast model coefficient set is the fact that the 5-day running

average of the observed solar flux numbers crosses the 75 flux solar activity level. The actual observed time of occurrence of a change in the Broadcast model coefficients are designated with rectangles. The upper row of rectangles shows the changes in the model coefficients observed on Mondays due to the fact that the monitoring computer at the Department of Electrical Engineering of the Czech Technical University in Prague was typically shut down for the period between Friday afternoon and Monday morning. The lower row of rectangles represents the observed changes in the Broadcast model coefficients during weekdays. A careful study of the Figure 3.3 reveals that the changes occurring in the different Broadcast model coefficient sets correspond either to the transitions in ten-day-periods or the fact that the 5-day running average of the daily solar flux numbers cross the 75 flux solar activity level. However, this finding cannot be supported for all cases of new coefficient sets due to the fact that changes either in solar activity level or the ten-day-periods could have occurred during weekends which were only detected on subsequent Mondays. In the figure, this was illustrated by the distinction between new Broadcast model coefficients observed on Mondays (upper row of rectangles) and regular weekdays (lower row rectangles).

3.2 Behaviour of the International Reference Ionosphere Model

The second model that I focused on is the IRI-90. I have modified the original version of the model to suit my needs for computing total electron content (TEC) profiles for multiple epochs. Using the model, I computed the diurnal variation of the vertical

ionospheric range error correction for those days for which I computed the corrections using the Broadcast model. In Figure 3.4, similarly as I showed before for the Broadcast model in Figure 3.1, I plotted the diurnal variation of vertical ionospheric range error corrections computed using the IRI-90 model for all 53 days.

In Figure 3.5, the predicted corrections are sequentially plotted. A distinct seasonal dependence with a peak around October-November is evident. The shape of the diurnal curves is quite different from season to season. From October to November the day-time peak of the delay was about twice as high as the delay for the period between June to July. It is interesting to note that the shape of the diurnal curves exhibits a double-peak from May to August. Studying Figure 3.4 and Figure 3.5 together, reveals that not only do the day-time curves show a strong seasonal variation but the night-time values are different from season to season as well. This is also different from the Broadcast model in which the night-time delay is set to 1.5 metres regardless of epoch during the solar cycle or season. The IRI-90 model uses F2 layer critical frequencies (f_oF2) as well as F2 layer critical heights (h_mF2) to compute vertical TEC profiles. These coefficients are stored as monthly median sets; this explains the monthly variations seen in Figure 3.5. The input parameters of the IRI-90 model are the day of the year and the 12-month smoothed sunspot numbers. In the case of the IRI-90 model predictions, there are never any large day to day variations in diurnal amplitudes indicating that short-term changes in the solar activity level are not represented.

Vertical Ionospheric Range Error Corrections on L1 Predicted by the IRI-90 Model (at Boulder, CO)

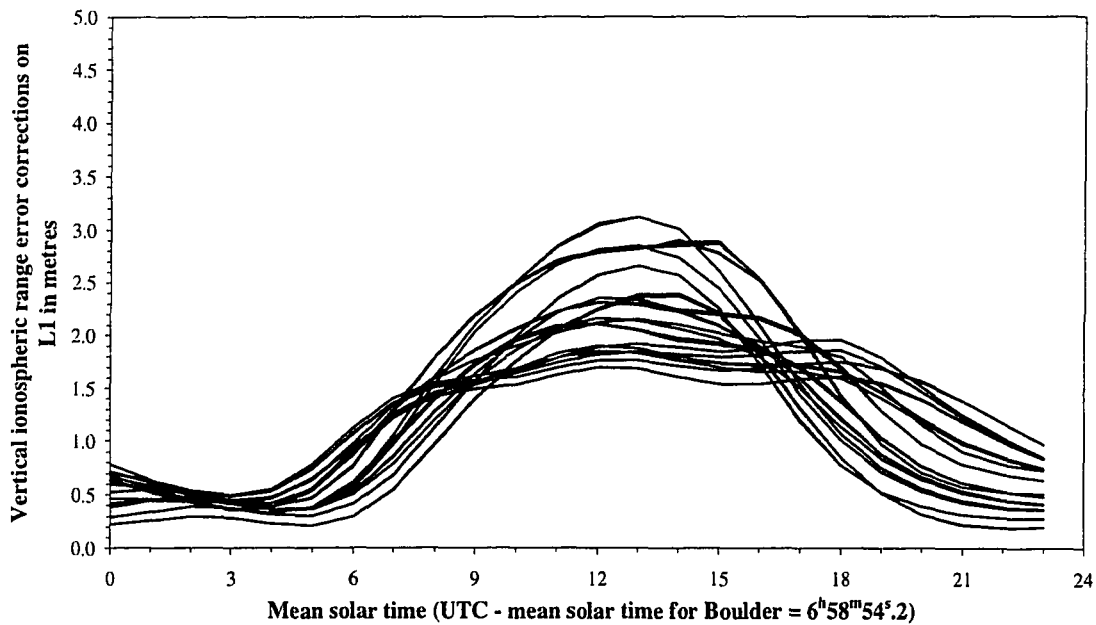


Figure 3.4: Vertical ionospheric range error corrections using the IRI-90 model.

Vertical Ionospheric Range Error Corrections on L1 Predicted by the IRI-90 Model (at Boulder, CO)

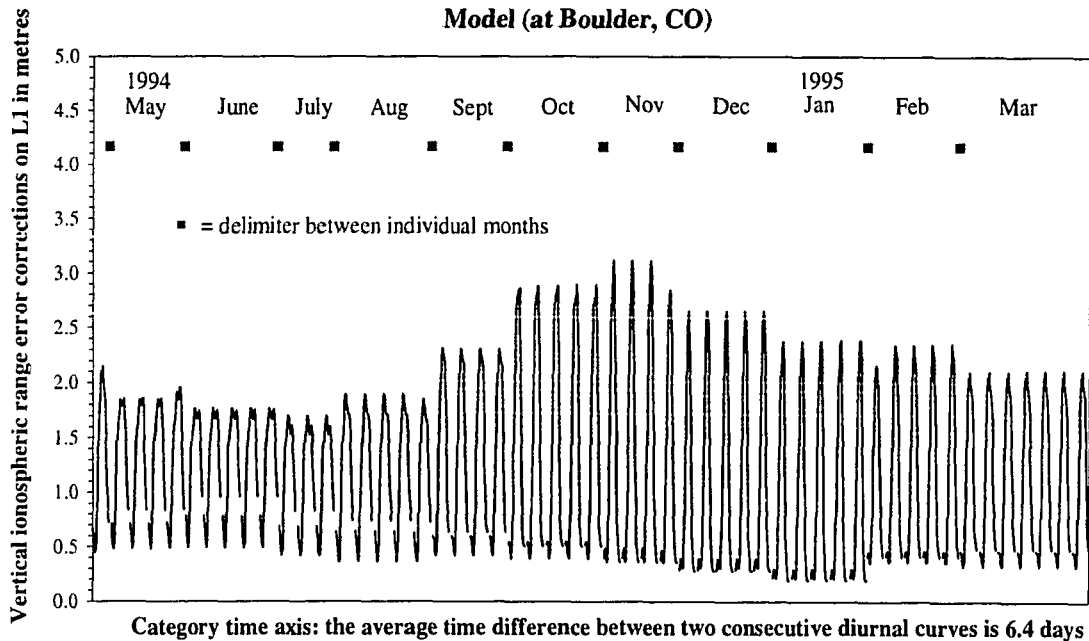


Figure 3.5: Vertical ionospheric range error corrections on L1 predicted by the IRI-90 model.

Clearly, this is a consequence of using 12-month smoothed sunspot numbers that average out the short-term variations in solar activity. The smoothed numbers for cycle 22 are shown in Figure 2.4 along with those from the previous 3 solar cycles. As we can see in the figure, we are currently at the very bottom of the beginning 23rd solar cycle.

3.3 Comparison of Predicted and Measured Ionospheric Range Error Corrections

I decided to compare the predictions of the Broadcast and IRI-90 models with Faraday rotation data in an effort to see which model is more accurate. The Faraday rotation data was provided by the Solar Terrestrial Physics Division of the U.S. National Oceanic and Atmospheric Administration's National Geophysical Data Center. Due to malfunction of Faraday rotation equipment, I was able to use only 27 day's worth of Faraday rotation data to assess the accuracy of the two models.

In Figure 3.6, a sample of predicted and measured vertical ionospheric range error corrections can be seen for 5 days in April/May 1994.

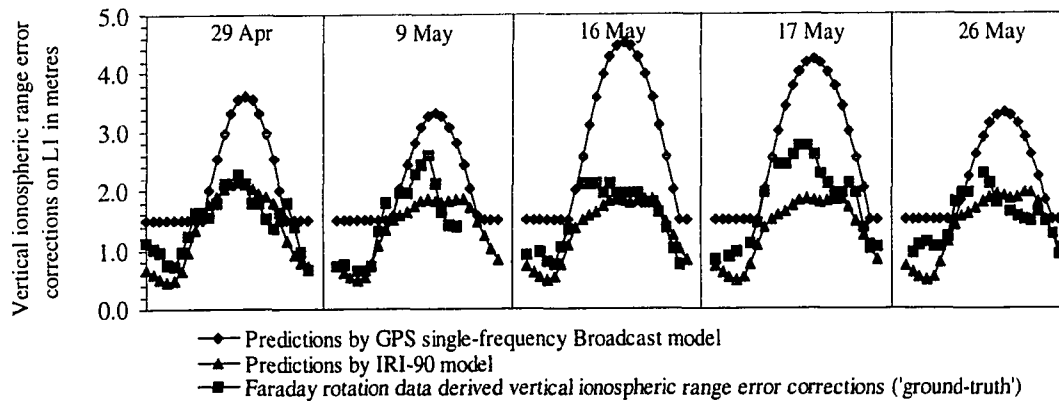


Figure 3.6: Predicted versus measured vertical ionospheric range error corrections on L1.

As delineated by the Broadcast model, I calculated separately the r.m.s. of the day-time and night-time differences of the vertical ionospheric range error corrections computed from the Faraday rotation data and IRI-90/Broadcast models. From Faraday rotation data, the vertical ionospheric range error corrections were computed by realizing the fact that 1 TEC unit corresponds to 0.163 meter ionospheric delay on the L1 frequency. Figure 3.7 shows that the day-time IRI-90 model predictions are more accurate than those of the Broadcast model in 20 cases out of 27. Figure 3.8 reveals that the night-time IRI-90 model predictions are more accurate than those of the Broadcast model in 21 cases out of 27.

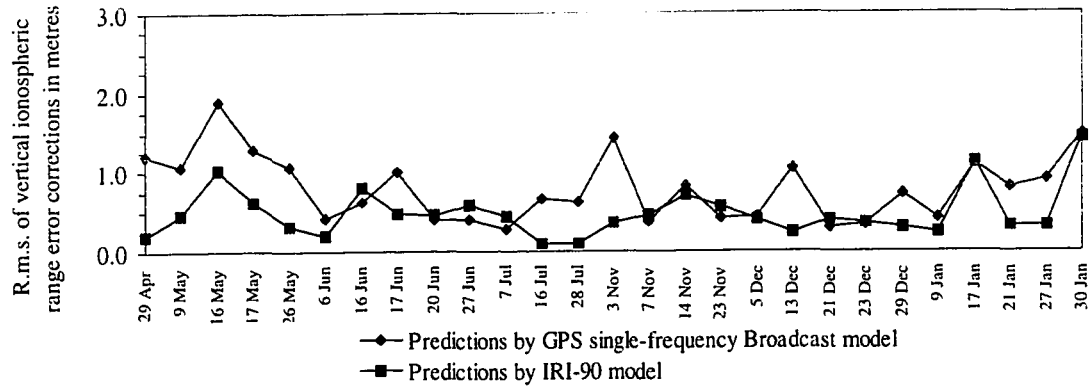


Figure 3.7: R.m.s. of day-time differences between vertical ionospheric range error corrections computed from Faraday rotation data and two empirical models.

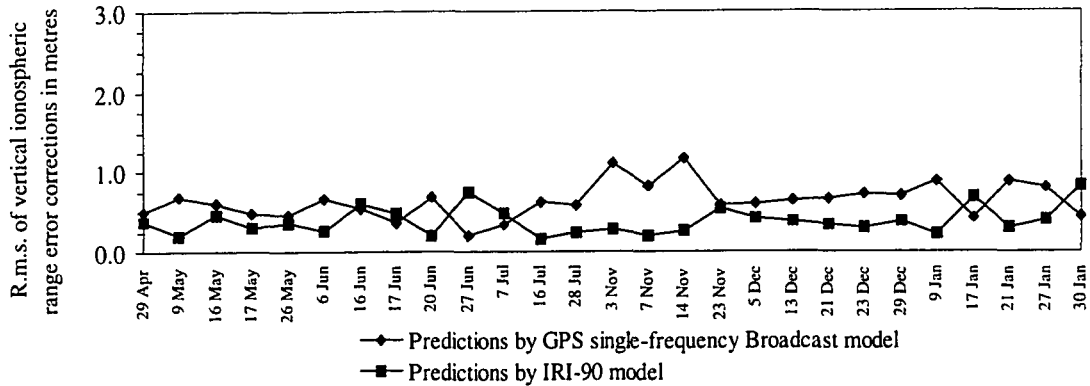


Figure 3.8: R.m.s. of night-time differences between vertical ionospheric range error corrections computed from Faraday rotation data and two empirical models.

3.4 Conclusions of the Long-Term Stability Between the Broadcast and IRI-90 Models

Based on the comparison between the Broadcast and IRI-90 models, I can conclude that both for day-time and night-time periods, the IRI-90 model appears to be more accurate than the Broadcast model. However, I have to point out that this conclusion assumes that

the Faraday rotation data represents the “ground truth” against which I compared the other two models’ performances. The error associated with the Faraday rotation measurements is up to 5% of the TEC [Titheridge, 1972] which corresponds to about 1 TECU (assuming a maximum TEC of about 20 TECU) for station Boulder in a low solar activity period. Furthermore, the Faraday rotation data can only provide us with TEC measurements up to an altitude of about 2000 km (see Section 2.5.5), as opposed to the GPS satellites’ orbital altitude which is about 20,200 km. Therefore, the Faraday rotation data underestimates the TEC with respect to the GPS-derived TEC and overestimates it with respect to IRI which predicts TEC up to 1000 km. I estimated this difference by using the Gallagher et al. [1988] plasmaspheric electron content model between the altitudes of 2000 km and 20,200 km (see Section 4.2.6). For station Boulder the model predicts about 0.5 TECU (8 cm ionospheric delay on L1) as a maximum daily plasmaspheric electron content between 2000 km and 20,200 km; and about 0.3 TECU (5 cm ionospheric delay on L1) between 1000 to 2000 km. These values are within the error bar of the Faraday rotation measurements which is about 16 cm delay on L1. Since neither the IRI-90 nor the Bent model (the latter was used to derive the Broadcast model coefficients) take into account the plasmaspheric electron content, comparing Faraday rotation data with the other two models only introduces into the results an absolute bias of about 5 cm on L1. In a relative sense this would not compromise the results discussed in this chapter. However, using IRI-90 or Broadcast models to correct GPS observations for ionospheric delay would require a rigorous approach, taking into account the plasmaspheric electron content, such as the one that will be introduced in Section 4.2.6.

These conclusions here are specific to the low solar activity, and mid-latitude conditions associated with the test data sets. Further investigation is needed for medium and high solar activity periods and for low and high latitude regions of the earth. Based on these results I concluded that the use of the IRI-90 model might be a suitable candidate to compute ionospheric range error corrections for single frequency GPS receivers. This investigation has helped me learn about the capabilities of the IRI-90 model. Based on this experience, I have made software modifications to the model which will be described in subsequent chapters.

In this chapter I have used Faraday rotation data as a ground-truth against which I compared the Broadcast and IRI-90-model-derived ionospheric range error corrections. Since Faraday rotation data is no longer readily available and it only provides TEC data for specific geographic locations, I realized that GPS might be a potential candidate for providing TEC data on a regional or global scale. In the next chapter, I will concentrate on the software development I made to derive GPS-inferred regional ionospheric TEC maps.

CHAPTER 4

THE UNB APPROACH TO IONOSPHERIC MODELLING USING GPS

The focus of Chapter 4 will be on the GPS signals that we can use to study the temporal and spatial variation of the ionosphere as a plasma surrounding the earth. Learning more about the structure and behaviour of the ionosphere will enable us to contribute not only to the knowledge base of ionospheric science but it could have a profound impact on single frequency radio navigation systems that are affected by the presence of the ionosphere. In the first part of this chapter, I will discuss techniques that use GPS to study the temporal and spatial characteristics of the ionosphere. In the context of other ionospheric researchers' work, in the second half of this chapter I will lay the foundation and introduce the UNB approach I developed to model regional and global ionospheric total electron content.

4.1 Commonly Used Modelling Techniques

The literature referring to my research areas has been discussed in Section 1.2.2. In this section I will briefly address the most commonly used modelling techniques in the scope of my studies. I will also describe other ionospheric modelling techniques all of which use GPS observations but for different purposes, e.g., 3-dimensional ionospheric modelling, generating vertical electron density profiles, providing ionospheric range error corrections

for single frequency GPS users, and the use of ionospheric divergence to model the ionospheric effect.

4.1.1 Regional and Global Ionospheric Modelling

Dual frequency GPS receivers are not only able to eliminate almost all of the effect of the ionosphere using the linear combination of the pseudorange and/or the carrier phase observations but also we can use these observables to “solve for” the ionospheric effect. The fundamental problem here is that there are inherent electrical path differences between the L1 and L2 signals due to the physical differences in the electronic circuitry inside the receiver and the GPS satellites. Therefore, when forming the pseudorange differences (the ionospheric observable), they will be biased due to the path delay differences in the satellite and the receiver (the so-called satellite and receiver differential delays). As a consequence of that, we cannot directly measure the ionospheric effect, but rather we have to setup a mathematical model which takes into account the fact that the line-of-sight total electron content is a function of the elevation angle of the satellite whereas the satellite and receiver differential delays are independent of the elevation angle. Another possibility is to calibrate the GPS receiver used for ionospheric studies: in this case the path difference due to the differences in the electronic circuitry in the receiver can be calibrated in order for the electronic path difference to become zero. For example, the Allen Osborne Associates Rogue receiver can be calibrated, and receiver differential delay values usually lie in the range of ± 10 nanoseconds (ns) with an uncertainty of 0.2 ns [Wilson and

Mannucci, 1993]. Moreover, the satellite hardware delays are determined prior to the launch although these hardware delays are not accurate enough for use in high precision total electron content mapping [Cohen et al., 1992]. In conclusion, for high precision total electron content modelling, even if we have calibrated dual frequency GPS receivers, we will have to estimate the satellite differential delays along with the ionospheric model parameters.

The number of regional and global ionospheric modelling methods essentially corresponds to the number of ionospheric processing and analysis centers. They can produce TEC maps either on a regional or a global scale depending on the processing and analysis center's requirements, tasks and needs. For instance, if we require ionospheric maps for the European region, we will only need GPS stations from that region. However, if we need ionospheric corrections for e.g., single frequency orbiting radar altimeters, we will need a network of GPS stations with global coverage to be able to derive global ionospheric maps. Global maps usually use a spherical harmonics expansion, polynomial approximation or Gauss exponential function approximation to spatially interpolate the irregular grid of subionospheric points. Such a point is the intersection of the ray path of a signal broadcast from a satellite to a receiver with a thin spherical shell representing the ionosphere. For the estimated model parameters defining e.g., geomagnetic latitude, longitude, and time variation of TEC, one can use batch or sequential least squares estimation or a Kalman filter type estimation [Feltens et al., 1996]. These techniques can be used both for producing regional and global TEC maps. However, there are advantages

and disadvantages associated with these mathematical models and estimation techniques. For real-time applications, processing centers prefer to use a polynomial approximation with a Kalman filter type estimation. In the case of a spherical harmonics expansion, the batch least squares estimation technique is typically used.

4.1.2 Ionospheric Tomography

Two or three dimensional ionospheric tomography using GPS is a relatively new and exciting area of ionospheric research. Scientists have used the U.S. Navy Navigation Satellite System (Transit) for over 30 years to study the ionosphere by measuring the Doppler shift on the two Transit frequencies. Two dimensional contour maps using an algebraic reconstruction technique and the maximum entropy method were presented by Pakula et al. [1995] in which signals both from Transit and GPS satellites were used to compare tomographic results against incoherent scatter radar measurements. The algebraic reconstruction and maximum entropy methods are described by Raymund [1993]. The principles behind ionospheric imaging using computerized tomography and its limitations are described by Austen et al. [1988] and Yeh and Raymund [1991] respectively.

The Transit satellites are polar orbiting satellites, therefore it is only possible to measure the spatial distribution of TEC along a specific longitude region, hence ionospheric information by altitude, latitude and longitude but not in continuous fashion can be obtained. However, GPS can provide continuous coverage of TEC up to the orbital

altitude of 20,200 km with a global spatial resolution on the order of 1000 km, assuming that the currently about 100 continuously operating dual frequency GPS receivers worldwide are evenly distributed over the land masses. We can call this 3 dimensional tomography since the spatial and temporal variations include latitude, longitude, and time. The combination of the two techniques mentioned allows for the reconstruction of the ionosphere in 4 dimensions: altitude, latitude, longitude and time. By using the combined technique, it is possible to achieve an altitude resolution of 5 km, latitude resolution of 25-100 km, 1000 km in longitude (or 40 minutes in solar time), and continuous time coverage. The method is particularly useful for providing ionospheric corrections for single frequency altimeters where altitude and latitude are important considerations. The technique has been successfully implemented and tested by the ionospheric research group at the Applied Research Laboratory of the University of Texas. They routinely produce 2-D (latitude, altitude) ionospheric tomographic profiles using the Transit satellites within the contiguous U.S. (CONUS) region. As described above, they use GPS-derived 3-D (latitude, longitude, and time) tomographic images to “fill-up” the 2-D vertical TEC profiles. Agreement in TEC with TOPEX-derived TEC was found to be at the 1 TECU level [Coker et al., 1996].

4.1.3 GPS/Met

GPS for Meteorology (GPS/Met) is an experiment designed to test radio occultation limb sounding of the earth with a GPS receiver placed on the Microlab-1 low earth orbiting

(LEO) satellite. It is possible to use spaceborne GPS receivers to recover ionospheric electron density profiles corresponding to occultations when GPS satellites rise or set relative to the spacecraft carrying the GPS receiver. The phase and amplitude of the occulting L1 and L2 GPS signals are affected in ways that are characteristic of the index of refraction of the ionosphere. This can be quantified by using GPS receivers to determine the bending of the signals when the line of sight cuts through the ionosphere. The bending of the signals are computed by the excess Doppler shift which is the difference between the observed Doppler shift and the “unocculted” Doppler shift which would have been observed had the ionosphere not been present. Subsequently, we can use the Abel integral transform to derive the index of refraction from the bending. As a next step, the Appleton-Hartree formula helps us derive the electron densities using the index of refraction [Melbourne et al., 1994].

The largest error sources in the recovered electron density profiles are due to horizontal inhomogeneities in the ionosphere. The current algorithms use of the assumption spherical symmetry which is itself an approximation. A good agreement was found after matching a handful of occultations with electron density profiles derived from incoherent scatter radar data [Schreiner and Exner, 1996]. Due to the linear relationship between critical frequency and maximum electron density, F2 layer critical frequencies, foF2, can be computed from the F2 layer maximum electron densities inferred from GPS/Met data for example. These foF2 estimates can also be compared with ionosonde

data [Schreiner and Exner, 1996]. 1 km level vertical resolution of the ionospheric profiles can be achieved using GPS/Met measurements [Hajj and Romans, 1996].

4.1.4 Real-Time Ionospheric Modelling: the WAAS Concept

The Federal Aviation Administration is currently developing a GPS-based navigation system called the Wide Area Augmentation System (WAAS) that is intended to become the primary navigation aid for commercial aviation during all phases of flight [El-Arini et al., 1994; Loh et al., 1995]. For that purpose, the augmentation of GPS is essential because GPS by itself does not provide the required accuracy, availability, and integrity to serve as a primary navigation system. WAAS is anticipated to become a worldwide seamless global navigation satellite system (GNSS) by accommodating different components of WAAS from other countries [Loh, 1995]. Eventually, the end state WAAS will consist of 20 to 30 GPS wide-area reference stations (WRS) distributed in latitude and longitude at about 5 to 10 degrees spacing over the CONUS (plus Alaska and Hawaii) and the Canadian region. These reference stations will collect pseudorange and atmospheric measurements and send them to one or perhaps more wide-area master station (WMS). The WMS will process the data to provide differential corrections for the real-time WAAS user including GPS ephemerides, satellite clock and ionospheric delay corrections. The corrections will be sent to the single frequency GPS user by means of geosynchronous earth orbit (GEO) satellite. The augmented system will add an additional

GPS-like signal to improve availability and reliability; differential corrections that will improve accuracy and integrity; and monitoring capability that will improve safety.

The ionospheric delay corrections being part of the WAAS message seem to be one of the most difficult to model among the error sources affecting the real-time WAAS single frequency GPS users. Special attention must be paid to the spatial and temporal variability of the ionosphere, especially when ionospheric disturbances induced by solar or geomagnetic disturbances occur. A brief description of the proposed model for generating ionospheric delay correction for the WAAS user is as follows. All ionospheric measurements are processed using JPL's GIPSY/TRIN (GPS Inferred Positioning SYstem/TRiangular INterpretation) ionospheric correction algorithm. The algorithm includes an ionospheric thin shell model which assumes that the electrons are concentrated at a fixed 350 km altitude. The model interpolates the irregular grid of subionospheric points as a grid of vertices of uniformly distributed triangles. Since the ionosphere is strongly controlled by both the geomagnetic field and solar radiation, this triangular tiling scheme is tied to a solar-geomagnetic coordinate system. TEC values for the vertices are estimated as random walk stochastic parameters using a Kalman filter approach. The Kalman filter states are updated every 5 minutes. In the next step, updated values of grid vertices are transmitted via a GEO satellite to the user who will use them in a line-of-sight correction at the user's location. A simple interpolation technique is used among the nearest regularly spaced grid vertices to find the ionospheric correction for the user's location [Mannucci et al., 1995]. In addition to ionospheric corrections, the WAAS

message will contain values of grid ionospheric vertical error (GIVE) that will give the user an indication of the quality of the ionospheric delay correction.

4.1.5 Combination of Different Techniques

We can also combine the ionospheric data from LEO satellites with terrestrial GPS-derived TEC data which makes it possible to set up a 4-dimensional tomographic model. In simulation studies by Howe [1996], the spatial variation of the ionosphere is modelled in terms of empirical orthogonal functions (in altitude) and spherical harmonics (in the horizontal). The time dependence is modelled as a first-order Gauss-Markov process.

The combination of the regional and/or global electron content maps with GPS/Met-derived electron density profiles can lead to GPS-only 3-dimensional ionospheric modelling. The resulting 3-D maps could be of great benefit also to the ionospheric research community at large: the GPS-inferred 3-D electron density profiles could contribute to further improvements in the state-of-the-art, global empirical ionospheric models such as the IRI and physics-based models such as PIM. GPS-inferred electron density profiles can be used to determine a more accurate shape of the topside profile for IRI-95, for example. This is very important since the topside electron content could contribute, at times, up to about 60-70 percent of the vertical total electron content [Bilitza, 1990].

Other ionospheric probing techniques such as the ionosonde, satellite-based topside measurement, and in-situ rocket and satellite ionospheric data can also be used to compute electron density profiles. These electron densities could also be combined with GPS-inferred ionospheric data from spaceborne and terrestrial receivers.

4.1.6 Ionospheric Modelling Using a Single Frequency GPS Receiver

Efforts have been made to estimate the ionospheric delay using single frequency GPS pseudorange and carrier phase observations. In terms of the observation equations, subtracting the L1 carrier phase observations from the P1 pseudorange observations yields the ionospheric divergence, which is twice the ionospheric term plus additional terms such as the ambiguity term associated with the carrier phase observations, combined multipath and noise associated with both the pseudorange and carrier phase observations, and the differences between the satellite and receiver differential delays in the code and carrier phase generating circuitry. We can assume that the satellite and receiver differential delays are slowly varying so we can lump them together with the ambiguity term. We get a doubling of ionospheric delay term since the pseudorange delay and carrier phase advance are of equal magnitude and of opposite sign.

Cohen et al. [1992] and Xia [1992] used the pseudorange and carrier phase measurements to estimate absolute TEC. One limitation of the technique is the accuracy with which we can estimate the ambiguity term. The ambiguity term similar to the

satellite-receiver differential delay is independent of the elevation angle of the satellite, so in theory it is possible to separate the ambiguity term from the ionospheric delay using its elevation angle independence. Another limitation of the technique is that during the estimation process we have to cope with the multipath and noise on the pseudorange observations. The major limitation of the technique, however, is that one also has to set up an ionospheric model for the vertical ionospheric delay which, with a help of a mapping function is projected onto the line-of-sight between the satellite and the receiver. This implies that for actual ionospheric observations during a satellite pass that differ from the model, for which time the ionospheric observations are most needed, the GPS single frequency ionospheric correction will perform poorly [Klobuchar, 1996]. As an example, for the Ashtech Z-12 C/A-code it was found that a typical value for the peak-to-peak variation of the multipath and noise was at the 1 meter level over a time period of 2 minutes and with no carrier phase smoothing applied [Langley, 1996]. Since the multipath and noise on L1 carrier phase is negligible compared to that of C/A-code, the 1 meter level changes in e.g., 2 minutes (corresponding to about 6 TECU on L1) is higher than what we could expect from the rate of change of the ionosphere (2 TECUs in 1 minute). Consequently, the short-term variation of the ionosphere is buried in the noise generated by the multipath and receiver noise. This implies that the ultimate accuracy of the single frequency ionospheric correction technique will depend on the model we use to estimate the ionospheric delay. Since these models or other global empirical ionospheric models are not able to take into account the short-term variation of the ionospheric delay, typically the single frequency technique's performance is determined by that of the ionospheric

model which provides an overall error of approximately 22-27% (1 sigma) of the ionospheric delay [Klobuchar, 1996]. However, it might be worthwhile further exploring this technique as the technology improves. One also has to bear in mind that multipath error is site-specific, that is it can be reduced with a careful site selection. Carrier phase observations can also be used to smooth the pseudoranges in order to mitigate the multipath effect. As the multipath rejection techniques and receiver noise level further improve, we may be able to separate ionosphere-related changes from that of multipath and noise allowing us to use the ionospheric divergence to reduce the effect of the ionospheric delay on single frequency GPS observations.

4.2 The UNB Ionospheric Modelling Technique

In this section, I will address the UNB regional and global ionospheric modelling technique. In the first part, I will introduce the ionospheric observable what is known as the geometry-free linear combination of the pseudorange and carrier phase observations. This is followed by the explanation of the estimation strategy that was used to estimate ionospheric parameters. As part of the mathematical model I will put more emphasis on two issues one being the UNB ionospheric shell height determination method, and the second being the investigation of different ionospheric mapping functions. I will also describe the interpolation method that was used to find TEC values pertaining to a geographic location within the regularly spaced grid TEC values provided by the UNB technique. As a validation of the UNB method, I used TOPEX/Poseidon-derived TEC

data as an independent technique to provide this study with ground-truth. To be able to compare the TOPEX/Poseidon-derived TEC data with the UNB-derived TEC data, I also had to use a plasmaspheric electron content model. As part of the UNB technique, several modifications have been made to the International Reference Ionosphere 1995 which was augmented with a plasmaspheric electron content model.

4.2.1 Ionospheric Observable

The GPS pseudorange observation equations are well known from the various references such as Langley [1992; 1996], Wells et al. [1987], Chao et al. [1996], etc.:

$$P_1 = \rho + c \cdot (dT - dt) + d_{ion,L1} + d_{trop} + b^{si,L1} + b_{rj,L1} + mp_{P1} + \varepsilon_{P1}, \quad (4.1)$$

$$P_2 = \rho + c \cdot (dT - dt) + \gamma \cdot d_{ion,L1} + d_{trop} + b^{si,L2} + b_{rj,L2} + mp_{P2} + \varepsilon_{P2}, \quad (4.2)$$

where

P_1, P_2 are the pseudorange measurements on L1 and L2 respectively (in distance units),

ρ is the geometric range between the satellite and the receiver,

c is the vacuum speed of light,

dT, dt are the offsets of the receiver and satellite clocks from GPS time respectively,

$d_{ion,L1}$ is the ionospheric delay on L1,

$\gamma = \left(\frac{f_1}{f_2}\right)^2 = \left(\frac{77}{60}\right)^2$ is the L1, L2 frequency ratio squared,

d_{trop} is tropospheric delay,

b^{s_i,L_1} , b^{s_i,L_2} are the satellite instrumental delays on P1 and P2 respectively for satellite s_i ,
 b_{r_j,L_1} , b_{r_j,L_2} are the receiver instrumental delays on P1 and P2 respectively for receiver r_j ,
 mp_{P_1} , mp_{P_2} are the multipath on P1 and P2 measurements respectively,
 ε_{P_1} , ε_{P_2} are the receiver noise on P1 and P2 respectively.

After subtracting eqn. (4.2) pseudorange observation equation from eqn. (4.1), and re-arranging the equation, we get:

$$P_1 - P_2 = (1 - \gamma) \cdot d_{ion,L_1} + \left[b^{s_i,L_1} - b^{s_i,L_2} + b_{r_j,L_1} - b_{r_j,L_2} \right] + v_P, \quad (4.3)$$

where

$$v_P = mp_{P_1} - mp_{P_2} + \varepsilon_{P_1} - \varepsilon_{P_2}. \quad (4.4)$$

Note in eqn. (4.3) that the ionospheric term cannot be measured directly from the pseudorange measurement due to the term in square brackets on the right hand side of the equation which is a slowly varying term in time. Since the ionospheric term cannot be measured directly it needs to be estimated along with the term in square brackets in eqn. (4.3).

The first order approximation of the Appleton-Hartree formula also gives an expression for the ionospheric delay in terms of TEC (see eqn. (2.11)):

$$d_{ion,L_1} = 40.3 \cdot \frac{TEC}{f_1^2}. \quad (4.5)$$

Note that I used 3 digits for the factor “40.3”. Using 3 digits gives us cm level accuracy for the ionospheric delay. The eqn. (4.5) neglects the higher than 2nd terms in the Appleton-Hartree formula (see Section 2.2). By doing so, we introduce cm level errors into the computed ionospheric delay which is in accordance with the 3 digits used for the factor 40.3 in eqn. (4.5).

After combining eqns. (4.3) and (4.5), the expression for the total electron content using pseudorange observations in TECU is:

$$\text{TEC}_p = 9.52 \cdot (P_2 - P_1), \quad (4.6)$$

which is an unambiguous but noisy and therefore imprecise observable.

The observation equations for the carrier phase measurements are:

$$\Phi_1 = \rho + c \cdot (dT - dt) + \lambda_1 N_1 - d_{\text{ion},L1} + d_{\text{trop}} + b^{\varphi,s_i,L1} + b_{\varphi,r_j,L1} + mp_{\varphi_1} + \varepsilon_{\varphi_1}, \quad (4.7)$$

$$\Phi_2 = \rho + c \cdot (dT - dt) + \lambda_2 N_2 - \gamma \cdot d_{\text{ion},L1} + d_{\text{trop}} + b^{\varphi,s_i,L2} + b_{\varphi,r_j,L2} + mp_{\varphi_2} + \varepsilon_{\varphi_2}, \quad (4.8)$$

where

Φ_1, Φ_2 are the carrier phase observations on L1 and L2 respectively in distance units,

λ_1, λ_2 are the wavelengths of the L1 and L2 carriers respectively,

N_1, N_2 are the unknown L1 and L2 integer carrier phase ambiguities respectively,

$b^{\varphi,s_i,L1}, b^{\varphi,s_i,L2}$ are the satellite instrumental delays on L1 and L2 carrier phase respectively for satellite s_i ,

$b_{\varphi,r_j,L1}, b_{\varphi,r_j,L2}$ are the receiver instrumental delays on L1 and L2 carrier phase respectively for receiver r_j ,

$mp_{\varphi_1}, mp_{\varphi_2}$ are the multipath on L1 and L2 carrier phase measurements respectively,

$\varepsilon_{\varphi_1}, \varepsilon_{\varphi_2}$ are the noise on L1 and L2 respectively, and the other terms as defined for eqns.

(4.1) and (4.2).

After subtracting eqn. (4.8) carrier phase observation equation from eqn. (4.7), and then re-arranging the equation, we get:

$$\Phi_1 - \Phi_2 = (\gamma - 1) \cdot d_{ion,L1} + [b^{s_i} + b_{r_j}] + N_1 \lambda_1 - N_2 \lambda_2 + v_\varphi, \quad (4.9)$$

where

$$v_\varphi = mp_{\varphi_1} - mp_{\varphi_2} + \varepsilon_{\varphi_1} - \varepsilon_{\varphi_2}, \quad (4.10)$$

and

b^{s_i} is the satellite differential delay corresponding to $b^{\varphi,s_i,L1}$ minus $b^{\varphi,s_i,L2}$ for satellite s_i ,

b_{r_j} is the receiver differential delay corresponding to $b_{\varphi,r_j,L1}$ minus $b_{\varphi,r_j,L2}$ for receiver r_j ,

and the sum of the satellite and receiver differential delays is often referred to in this dissertation as satellite-receiver differential delays.

Comparing eqn. (4.9) with eqn. (4.3) will show that I assumed different satellite and receiver instrumental delays for the pseudorange and carrier phase observations to take into account the different tracking loops for the code and carrier phase. However, the instrumental delays on carrier phase measurements can be lumped together with the

constant carrier phase ambiguity ($N_1\lambda_1 - N_2\lambda_2$ terms in eqn. (4.9)) and so they do not need to be treated differently from the instrumental delays for the pseudorange measurements.

Similarly to eqn. (4.6), after combining eqns. (4.9) and (4.5), the expression for the total electron content using carrier phase observations in TECU is:

$$\text{TEC}_\varphi = 9.52 \cdot (\Phi_1 - \Phi_2), \quad (4.11)$$

which is a very precise but ambiguous observable. Assuming that the multipath on carrier phase observations can amount up to a quarter of a wavelength [Langley, 1996], and using eqn. (4.11), we can determine that the L1 minus L2 carrier phase ionospheric observables have a precision of about 0.7 TECU. However, this is not accuracy due to the fact these observables are biased (see eqn. (4.9)) by a term caused by the satellite and receiver differential delays and carrier phase ambiguities. Furthermore, the ratio of multipath effects on the carrier phase as compared to the multipath observed on the P code is proportional to their respective wavelengths [Klobuchar, 1996]. This works out to be about 100 TECU for the precision of the P code ionospheric observables (eqn. (4.6)). This is about 2 orders of magnitude larger than the precision of the carrier phase ionospheric observables (eqn. (4.11)).

To take advantage of the very precise but ambiguous Φ_1 minus Φ_2 carrier phase and the unambiguous but less precise P_1 minus P_2 observables, we can combine these two by

“levelling” the Φ_1 minus Φ_2 phase ionospheric observables using the P_1 minus P_2 pseudorange ionospheric observables:

$$\text{TEC}_{\text{comb}_i} = \text{TEC}_{\varphi_i} - \frac{\sum_{j=-\frac{n}{2}}^{\frac{n}{2}} p_j [\text{TEC}_{\varphi_j} - \text{TEC}_{P_j}]}{\sum_{j=-\frac{n}{2}}^{\frac{n}{2}} p_j}, \quad (4.12)$$

where i and j are indices for ionospheric observables to be levelled starting at the beginning of an arc, $i = 1, 2, \dots, n$ with the total number of observations n in an arc; and $j = -\frac{n}{2}, \dots, \frac{n}{2}$, in the case of n is an even number (see eqn. (4.12)), and $j = -\frac{n-1}{2}, \dots, \frac{n+1}{2}$, in the case of n is an odd number. For each phase-connected data arc, I set the level of L1 minus L2 carrier phase observables TEC_{φ_i} using all P_1 minus P_2 pseudorange observables TEC_{P_j} in the same phase-connected arc. In implementing this approach, I did not use any arc lengths shorter than 20 minutes resulting in a minimum of 40 observations needed (30 minute sampling rate) to set the level of the TEC_{φ_i} . The 20 minute arc length minimum is a tradeoff between not eliminating too many observations but at the same time using long enough arcs to be able to precisely set the level of the ambiguous ionospheric phase observables. An 18 minute arc length cutoff was also suggested by Runge et al. [1995]. I also used a simple weighting scheme with individual weights, $p_j = \frac{1}{j^2}$ when setting the level of the TEC_{φ_i} for each arc. I put the highest weight on the data in the middle of the arc and the lowest to the observations at both ends

of the arc corresponding to the lowest satellite elevation angles thereby minimizing the effect of multipath and noise. This weighting scheme based on satellite elevation dependence was originally suggested by Runge et al. [1995]. I used a 15 degree elevation cutoff angle throughout the processing using as many observations as possible while using the weighting scheme described above.

A modified version of PhasEdit version 2.0, an automatic data editing program [Freymueller, personal communication, 1995], was used to detect bad points and cycle slips, repair cycle slips and adjust phase ambiguities. The original PhasEdit 2.0 program takes advantage of the high precision dual frequency pseudorange measurements to adjust L1 and L2 phases by an integer number of cycles to agree (when expressed in distance units) with the pseudorange measurements. I have modified the program to form the observables according to eqn. (4.6) and eqn. (4.11) to level, using the formula in eqn. (4.12), the L1 minus L2 carrier phase ionospheric observables with the P1 minus P2 pseudorange ionospheric observables. Subsequently, a modified version of the University of New Brunswick's Differential POsitioning Program (DIPOP) [Langley et al., 1984] package was used to estimate ionospheric parameters and satellite-receiver differential delays using a Kalman filter algorithm as described in the next section.

4.2.2 Estimation Strategy

In this section, I will describe the principles behind the UNB estimation strategy published in Komjathy and Langley [1996a]. I model the ionospheric measurements from a dual frequency GPS receiver with the commonly used single layer ionospheric model using the observation equation:

$$I_{r_j}^{s_i}(t_k) = M(e_{r_j}^{s_i}) \cdot \left[a_{0,r_j}(t_k) + a_{1,r_j}(t_k) \cdot d\lambda_{r_j}^{s_i} + a_{2,r_j}(t_k) \cdot d\phi_{r_j}^{s_i} \right] + b_{r_j} + b^{s_i}, \quad (4.13)$$

where

$I_{r_j}^{s_i}(t_k)$ is the L1 minus L2 phase-levelled ionospheric observations in units of TECU, generated by using eqn. (4.12) at epoch t_k made by receiver r_j observing satellite s_i ,

$M(e_{r_j}^{s_i})$ is the thin-shell elevation angle mapping function projecting the line-of-sight measurement to the vertical with $e_{r_j}^{s_i}$ being the unrefracted elevation angle of satellite s_i viewed by receiver r_j at the subionospheric point – the intersection of the ray path of a signal propagating from the satellite to the receiver with a thin spherical shell (see e.g., Schaer et al. [1995]),

$a_{0,r_j}, a_{1,r_j}, a_{2,r_j}$ are the parameters for spatial linear approximation of TEC to be estimated per station, r_j , assuming a first-order Gauss-Markov stochastic process [Gail et al., 1993],

$d\lambda_{r_j}^{s_i} = \lambda_{r_j}^{s_i} - \lambda_0$ is the difference between the longitude of a subionospheric point and the longitude of the mean sun,

$d\varphi_{r_j}^{s_i} = \varphi_{r_j}^{s_i} - \varphi_{r_j}$ is the difference between the geomagnetic latitude of the subionospheric point and the geomagnetic latitude of the station, and b_{r_j}, b^{s_i} refer to the receiver and satellite differential delays respectively (for more details see eqn. (4.9)).

The three parameters $a_{0,r_j}, a_{1,r_j}, a_{2,r_j}$ in eqn. (4.13) are estimated for each station using a Kalman filter approach. The prediction and update equations for the state estimation are described by e.g., Schwarz [1987], Coster et al. [1992] and van der Wal [1995]. For detailed explanation, the reader is referred to the Kalman filter equations in Appendix 1. Due to the highly varying ionospheric conditions during one of the test observation windows processed, I allowed the model to follow a relatively high 1 TECU per 2 minute change in the total electron content which resulted in the process noise variance rate of change being $0.008 \text{ TECU}^2/\text{second}$ characterizing the uncertainties of the dynamic ionospheric model. For the variance of the measurement noise, I used 1 TECU^2 – the assumed uniform uncertainty in the observations. The 1 TECU^2 measurement noise variance was determined by computing the approximate precision of the L1 minus L2 carrier phase observations to take into account the multipath and noise characteristics of the carrier phase observations as described for eqn. (4.11). For the correlation time of states, I used 1 hour corresponding to the fact that I output the TEC maps (see Section 4.2.5) every hour. Observations used for generating the hourly maps range from 30

minutes before to 30 minutes after the hour. As an example, for generating a TEC map for UT 14:00, I used GPS data between UT 13:30 and 14:30.

The Kalman filter states estimate the combined satellite-receiver differential delays for station Madrid, one of the European IGS stations. Madrid is usually selected by other processing and analysis centers so that it is feasible to compare satellite-receiver differential delay estimates between different research centers. In a network solution, additional differential delay parameters for the rest of the stations have to be estimated based on the fact that the other receivers have different differential delays. Therefore, for each station other than station Madrid, an additional differential delay parameter was estimated which is the difference between the receiver differential delay of a station in the network and station Madrid. This technique is described by e.g., Sardon et al. [1994].

I chose a solar-geomagnetic reference frame based on sun-fixed longitude and geomagnetic latitude since the main reason for the ionosphere's existence is the interaction of ionizing radiation (principally from solar ultraviolet and x-ray emissions) with the earth's atmosphere and magnetic field [Langley, 1996]. Furthermore, the ionosphere varies much more slowly in sun-fixed reference frame than in an earth-fixed one. The use of such a reference frame results in more accurate ionospheric delay estimates when using Kalman filter updating [Mannucci et al., 1995].

4.2.3 Ionospheric Shell Height Determination

Apart from the estimation strategy, there are two parameters which deserve special attention. A parameter that affects the TEC estimation is the assumed height of the ionospheric shell which plays a role in computing the coordinates of the subionospheric points. It is also an input parameter of the $M(e_{f_j}^{s_i})$ mapping function which itself I consider the second important parameter that deserves to be investigated (see eqn. (4.13)). I assessed several different mapping functions with the aim of reducing mapping function errors for low elevation angle satellites. The mapping functions investigated will be discussed in the next section. The single layer ionospheric model assumes that the vertical TEC can be approximated by a thin spherical shell which is located at a specified height above the earth's surface. This altitude is often assumed to correspond to the maximum electron density of the ionosphere. Furthermore, it is usually assumed that the ionospheric shell height has no temporal or geographical variation and therefore it is set to a constant value regardless of the time or location of interest. A sensitivity analysis has been conducted using different ionospheric shell heights. I looked at the effect of different fixed ionospheric shell heights of 300, 350, and 400 km and also included variable heights computed by the IRI-90 model using F2 layer peak heights. The results will be discussed in Section 5.1.2.

After I used the IRI-90 model for ionospheric shell height determination, described above, I carried on with the investigation. This time, I integrated the predicted electron densities through the six subregions of IRI-90 to compute even more accurate ionospheric

shell heights using a rigorous approach. I determined the predicted median height of the total electron content using a numerical integration procedure with a step size of 1 km presented in Komjathy and Langley [1996c]. The median height is the height at which 50% of the TEC lies below and 50% lies above. I integrated the electron densities up to an altitude of 1000 km, consequently electron content above 1000 km (plasmaspheric electron content) has not been considered at this stage. However, for the night-time total electron content near sunspot minimum, the effect of the plasmasphere should be less than about 50 percent [Davies, 1990]. So, by not taking the plasmaspheric electron content into account which has an effect primarily on the night-time TEC predictions, one can be in error by about 2 to 3 TECU depending on the geomagnetic latitude of the station. This method seems to be a more rigorous approach compared to the fixed ionospheric shell height approach. I used this method to describe the temporal and spatial variation of ionospheric shell height for each IGS station used both during the regional and the global ionospheric model tests.

4.2.4 Ionospheric Mapping Functions

One of the major error sources in the ionospheric modelling is the ionospheric mapping function that projects the line-of-sight TEC into the vertical. The easiest way is to compute the elevation angle of the satellite at the ionospheric pierce (penetration) point assuming a single layer ionospheric shell with a fixed height. This could be a fair assumption for mid-latitude conditions and low solar activity times. However, the

geometric assumption could break down at low and high latitude regions where the TEC gradients are high and highly variable. I designed an experiment to investigate the behaviour of different mapping functions under mid-latitude conditions.

In the first phase of the experiment, the idea is that by forming the geometry free (ionospheric) combination of the phase-levelled (L1 minus L2) or pseudorange observations (P1 minus P2), we could compute the difference between the receiver differential delays (let us call this between-receiver differential delays). This can be achieved by forming the single differences of the undifferenced geometry free (P1 minus P2) or (L1 minus L2) observations between two receivers with respect to a particular satellite while performing a zero-baseline test (that is, running two GPS receivers off the same antenna). By doing so, we can eliminate the ionospheric delays (since we are looking at the same ionosphere by running the two receivers off the same antenna), and also the multipath which has the same effect on the GPS signals since the two receivers share the same antenna. What we are left with is the combined noise of the two receivers and the differences in the receiver differential delays (satellite differential delays cancel out as well when forming the single differences with respect to one satellite). If the noise is low we should be able to compute the differences of the receiver differential delays by averaging the single differences of the geometry free combination over a few hours of observations.

We can also describe the experiment above by using observation equations:

$$I_{r_i}^{s_i}(t_k) = \text{TEC}_{L.O.S.,r_i}^{s_i} + b_{r_i} + b^{s_i}, \quad (4.14)$$

$$I_{r_2}^{s_i}(t_k) = \text{TEC}_{\text{L.O.S.},r_2}^{s_i} + b_{r_2} + b^{s_i}, \quad (4.15)$$

where

$I_{r_1}^{s_i}(t_k)$, $I_{r_2}^{s_i}(t_k)$ are the phase-levelled ionospheric observations for receiver one, r_1 , and receiver two, r_2 , corresponding to satellite s_i at epoch t_k ;

$\text{TEC}_{\text{L.O.S.},r_1}^{s_i}$ and $\text{TEC}_{\text{L.O.S.},r_2}^{s_i}$ are the line-of-sight TECs corresponding to satellite s_i for receiver one and receiver two, respectively; and

b_{r_1} , b_{r_2} , b^{s_i} are the receiver and satellite differential delays as defined in eqn. (4.13). After forming the single differences of the observations between two receivers looking at the same satellite we get:

$$\Delta I_{r_1 r_2}^{s_i}(t_k) = I_{r_1}^{s_i}(t_k) - I_{r_2}^{s_i}(t_k) = b_{r_1} - b_{r_2}. \quad (4.16)$$

Note that the line-of-sight TEC terms cancel out due to the fact that both receivers operate using the same antenna, therefore both receivers look at exactly the same cross-section of the ionosphere. So, we are left with the $b_{r_1} - b_{r_2}$ which can be inferred using eqn. (4.16) as well as estimated using the UNB estimation strategy described in Section 4.2.2.

In the second phase of the experiment, I used the UNB strategy (Section 4.2.2) to estimate the between-receiver differential delays by setting one receiver differential delay to zero (as most research centers do with the Madrid station) and estimating the delay of the other (between-receiver differential delay). We would only need to estimate one set of stochastic parameters for the ionosphere since both receivers are looking at the same

ionosphere which will make the differential delay estimates stronger. The experiment involves the use of different elevation cutoff angles and mapping functions for the estimation. By knowing the “true” between-receiver differential delay from the first part of the experiment we can do a study on using different mapping functions. Which one works better at low elevation angles? The best mapping function should give us the best agreement with the between-receiver differential delays computed by the method described in the first part. The best mapping function would allow us to separate the elevation-dependent TEC from the satellite-receiver differential delays even at low elevation cutoff angles. Using low elevation cutoff angles e.g., 10 or 15 degrees we will be able to get better coverage of the region of the ionosphere the receiver is collecting data from. If we wish to perform long observation sessions, it is also possible to study the drift in the receiver differential delays. Since UNB is located in a mid-latitude region, currently during low solar activity period, it is fairly straight forward to estimate ionosphere parameters above Fredericton, N.B., Canada which would allow us to concentrate on the receiver differential delays using this mapping function study.

Three different mapping functions were investigated in this study. The first mapping function was the one proposed by Clynch et al. [1989]:

$$Q(E) = a_0 + a_1 x^2 + a_2 x^4 + a_3 x^6, \quad (4.17)$$

where

$$x = 1 - \frac{2}{\pi} \cdot E \quad \text{and} \quad a_0 = 1.0206, \quad a_1 = 0.4663 \quad a_2 = 3.5055 \quad a_3 = -1.8415 \quad \text{and} \quad E \text{ is the}$$

unrefracted elevation angle of the satellite. Clynch et al. [1989] state that a least squares fit

was used to estimate the mapping function coefficients fitted to a homogeneous “thick” spherical shell between altitudes of 200 and 600 km. To test the mapping function, raytracing was performed using the Bent-model-derived realistic ionospheric electron density profiles at 36 stations uniformly distributed around the world with four azimuth and 6 elevation angles at each station used to estimate the coefficients. The study showed that at 10 degrees cutoff angle, the mapping function was in error by 10% r.m.s. of the ionospheric delay, whereas at 30 degree elevation angle the r.m.s. error was less than 3%.

The second mapping function investigated is that used by the Broadcast model which is an approximation to the standard geometric mapping function computing the secant of the zenith angle at the ionospheric shell pierce point. The Broadcast model mapping function assumes a 350 km ionospheric shell height. The approximation is within 2 percent of the exact value of the mapping function for the elevation angles from 5 degrees to 90 degrees [Klobuchar, 1975]. The Broadcast model ionospheric mapping function is [Klobuchar, 1986]:

$$F(E) = 1 + 2 \cdot \left(\frac{96 - E}{90} \right)^3, \quad (4.18)$$

where E is the unrefracted elevation angle of the satellite in degrees at the user’s location.

The third mapping function I investigated is the standard geometric mapping function which computes the secant of the zenith angle of the satellite at the ionospheric pierce point. In a trigonometric form it can be written as follows [Mannucci et al., 1993]:

$$M(E) = \left(1 - \left(\frac{\cos E}{1 + \frac{h}{R_E}} \right)^2 \right)^{\frac{1}{2}}, \quad (4.19)$$

which is equivalent to

$$M(E) = \frac{1}{\cos \left(\arcsin \left[\cos(E) \frac{R_E}{R_E + h} \right] \right)}, \quad (4.20)$$

where

R_E is the earth's radius,

h is the ionospheric shell height.

The standard geometric mapping function can be used with a fixed ionospheric shell height (e.g., 350, 400 and 450 km are the most commonly used height values). In the UNB approach as described earlier, for the value “ h ”, I use the varying ionospheric shell height as function of geographic latitude, longitude and, Universal Time. The results of the data analysis and assessment of the performance of the different mapping functions will be described in detail in Section 5.5.

4.2.5 Interpolation Scheme Used to Create, Display and Use the UNB TEC Maps

After estimating three stochastic parameters for each IGS station for a time interval of 60 minutes, the next step is to create TEC hourly maps using a 1 degree by 1 degree grid

spacing (see Chapter 5) for regional TEC maps and a 5 degree by 5 degree grid spacing (see Chapter 6) for global TEC maps. As a reminder, to estimate the Kalman filter states, 30 minutes' worth of data before the hour and 30 minutes' worth of data after the hour was used. This seems to be a fair tradeoff between the necessity for the data to provide sufficient spatial coverage and the temporal variability of the ionosphere over a time span of 60 minutes. More frequent update intervals can easily be accommodated in the UNB algorithm. According to eqn. (4.13), I evaluated the ionospheric model (see the brackets in eqn. (4.13)) for the four stations closest to the grid node at which a TEC value is computed and then I computed the inverse distance squared weighted average of the individual TEC data values corresponding to the four IGS stations as described by

$$TEC_i = \frac{\sum_{j=1}^4 \frac{1}{d_j^2} \cdot TEC_{IGS_j}}{\sum_{j=1}^4 \frac{1}{d_j^2}}, \quad (4.21)$$

where

TEC_i is the computed TEC value for grid node i ,

TEC_{IGS_j} is the computed TEC value based on the estimated ionospheric model parameters

for IGS station j ,

d_j is the distance between IGS station j and the grid node i .

This particular weighting function scheme was used to take into account the spatial decorrelation of the ionosphere. The closer a particular grid node is to an IGS station, the more weight I put on the TEC values computed by evaluating the ionospheric model

describing the temporal and spatial variation of the ionosphere above the particular IGS station. Other research centers use, e.g., bicubic spline interpolation [Press et al., 1986] to obtain smooth TEC gradients on a global scale for distant geographic locations where the temporal and spatial coverage of the data is poor [Yuan et al., 1996].

The MATLAB software package was used to create contour maps of the global TEC values. Examples of such contour maps are displayed in Appendix 2 and will be further explained in Chapter 6. In order for the maps not to look too crowded, I used only 10 contour levels. In the case of the 1993 global TEC maps, I experienced maximum TEC values of about 80 TECU in the equatorial region, therefore the contours correspond to the levels of 8, 16, 24, ... ,80 TECU. The MATLAB contour algorithm works as follows: given the vertex values of each quad (4 grid nodes form a quad) computed using eqn. (4.21), MATLAB linearly interpolates along the quad's edges to find the point where the contour crosses. This is done for all edges, and the contours are formed by drawing straight lines between these interpolated points.

I used a standard interpolation scheme to find TEC values inside the 5 degree by 5 degree grid nodes, produced by the inverse distance weighting function scheme described above, in order to use them, e.g., to provide ionospheric corrections for single frequency GPS users or for single frequency altimetry measurements. The algorithm is often used for geoid and surface topographic data interpolation and is also referred to as the standard mean sea level algorithm. It involves only simple algebra providing a continuous surface

[Junkins et al., 1973]. It is a weighting function approach for modelling irregular surfaces and provides a simple procedure for approximating an irregular surface from regularly spaced data. The mathematical formulation for the interpolated TEC values, $TEC_p(\varphi, \lambda)$, is:

$$TEC_p = \sum_{i=1}^4 W_i(x, y) TEC_i, \quad (4.22)$$

where the general equation for the weighting function has been derived to ensure the first degree continuity (agreement between neighboring surfaces, defined by adjacent grid values, and partial derivatives), hence no sharp gradients are present [Junkins et al., 1973]:

$$W(x, y) = x^2 y^2 (9 - 6x - 6y + 4xy), \quad (4.23)$$

and TEC_i are the TEC values at the four corners of a square, or rectangle, as shown in Figure 4.1:

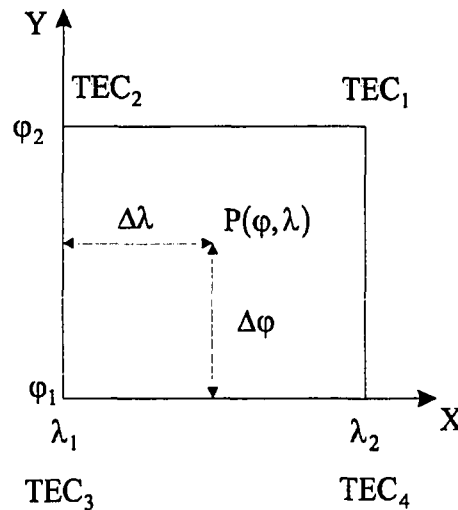


Figure 4.1: Interpolation method used to compute TEC between grid TEC values.

where

$$x = \frac{\lambda - \lambda_1}{\lambda_2 - \lambda_1}, \quad (4.24)$$

$$y = \frac{\phi - \phi_1}{\phi_2 - \phi_1}. \quad (4.25)$$

TEC_p is the interpolated TEC value at desired point P, whose geographic coordinates are (ϕ, λ) , and

$$W_1(x, y) = W(x, y), \quad (4.26)$$

$$W_2(x, y) = W(1 - x, y), \quad (4.27)$$

$$W_3(x, y) = W(1 - x, 1 - y), \quad (4.28)$$

$$W_4(x, y) = W(x, 1 - y). \quad (4.29)$$

I used this interpolation scheme to find a TEC value at any given geographic location defined by a regularly spaced grid of TEC data, e.g., for comparison with TOPEX/Poseidon-derived TEC data. The same interpolation scheme could be used to find TEC correction values for single frequency GPS users at a given location. Also, other ionospheric data processing centers provide their TEC products in a grid format therefore this interpolation scheme could be used to interpolate TEC values using TEC maps derived by others.

4.2.6 Plasmaspheric Electron Content Model

In the plasmasphere which may be thought of starting above an altitude of say 1000 km, the positive ions are mostly H⁺; hence, the term plasmasphere is synonymous with the term protonosphere [Davies, 1990].

In order to compare TEC measurements from independent sources such as GPS and TOPEX/Poseidon, I decided to use an empirical plasmaspheric electron content model to account for the electron densities from 1000 km up to the orbital altitude of the GPS satellites which is about 20,200 km. The model was developed by Gallagher et al. [1988]. It is based on a data base derived from measurements taken by the Retarding Ion Mass Spectrometer on the Dynamics Explorer 1 satellite. The data was collected during 1981 and 1982, shortly after a solar minimum. The empirical model is based on empirical expressions that can be used to reproduce electron density at arbitrary locations in the plasmasphere for given conditions. The spatial dependence of the plasmaspheric electron density is governed by the L-shell. The L-shell is the surface traced out by a particle moving around the earth's geomagnetic field lines.

For the electron densities, the Gallagher model uses the following empirical formula:

$$\text{LOG}_{10}(N) = a_1 \cdot F(L) \cdot G(L) \cdot H(L), \quad (4.30)$$

where

$$F(L) = a_2 - e^{a_3 \left(1 - a_4 \cdot e^{-h(L,\varphi)/a_5} \right)}, \quad (4.31)$$

$$G(L) = a_6 \cdot L + a_7, \quad (4.32)$$

$$H(L) = \left(1 + \left(\frac{L}{a_8} \right)^{2(a_9-1)} \right)^{-\left(\frac{a_9}{a_9-1} \right)}, \quad (4.33)$$

with

$$a_1 = 1.4, a_2 = 1.53, a_3 = -0.036, a_4 = 30.76, a_5 = 159.9, a_6 = -0.87 + 0.12 \cdot e^{-\frac{x^2}{9}},$$

$$a_7 = 6.27, a_8 = 0.7 \cdot \cos\left(2\pi \frac{MLT - 21}{24}\right) + 4.4, a_9 = 15.3 \cdot \cos\left(2\pi \frac{MLT}{24}\right) + 19.7,$$

with electron densities, N ; magnetic local time, MLT , defined by the geomagnetic longitude of the mean sun; and $-12 \leq x \leq 12$ MLT in hours; geomagnetic latitude, φ ; and height above the surface of the earth, $h(L, \varphi)$

where

$$h(L, \varphi) = R \cdot L \cdot \cos^2 \varphi - 6371, \quad (4.34)$$

with a starting altitude of 1000 km above the surface of the earth; earth radius, R ; and L is the L -shell parameter value measured in earth radii. $a_1 - a_9$ are the parameters used to fit eqn. (4.30) to the logarithm of the electron density, N . The parameter a_6 controls the electron density gradient in the inner plasmasphere, a_8 and a_9 determine the location and slope of the plasmasphere, respectively. The $F(L)$ term is a modified Chapman layer [Davies, 1990], and $G(L)$ is a linear L -shell model which has been found to be the best representation of the inner plasmaspheric electron density profiles. The $H(L)$ term represents the shape and the location of the plasmopause.

Since the source code of this model was not available I coded up the model to compute electron densities up to the altitudes of the GPS satellites using a step size of 100 km. In the next step, I integrated the electron densities to obtain the plasmaspheric electron content. To summarize: the model provides variations in the plasmaspheric electron density as a function of geomagnetic latitude, L-shell values, and geomagnetic local time. The algorithm does not model diurnal, seasonal or solar cycle variations of the plasmaspheric electron content. A more computationally extensive model is under development which will take into account these variations [Gallagher, personal communication, 1996].

4.2.7 International Reference Ionosphere 1995 Modifications

In this section, I will give an overview of the latest IRI model enhancement which is designated by the ionospheric community as IRI-95, followed by the description of the modifications I made to the model. The backbone of the model are the numerical maps describing the F2-peak plasma frequency f_oF2 and the propagation factor $M(3000)F2$. The latter is closely related to the maximum usable frequency $MUF(3000)$ which is the highest frequency that can be received at the distance of 3000 km after refraction in the ionosphere [McNamara, 1991]. The temporal and spatial variation of f_oF2 and $M(3000)F2$ are described by the Comité Consultatif International des Radiocommunications (CCIR) coefficients. More recently, the International Union of

Radio Science (URSI) numerical map coefficients have been developed for use in describing the foF2 distribution. Both CCIR and URSI coefficients use a sixth order Fourier representation for the diurnal and seasonal variation of the foF2 whereas CCIR uses a fourth order Fourier series for the description of the M(3000)F2 propagation factor. From the numerical description point of view, both foF2 and M(3000)F2 quantities are represented by a function $\Omega(\varphi, \lambda, t)$ with geographic latitude, φ ; longitude, λ ; and Universal Time (UT), t as variables:

$$\Omega(\varphi, \lambda, t) = a_0(\varphi, \lambda) + \sum_{j=1}^h [a_j(\varphi, \lambda) \cos jt + b_j(\varphi, \lambda) \sin jt], \quad (4.35)$$

where

$$a_j(\varphi, \lambda) = \sum_{k=0}^n U_{2j,k} G_k(\varphi, \lambda), \quad (4.36)$$

$$b_j(\varphi, \lambda) = \sum_{k=0}^n U_{2j-1,k} G_k(\varphi, \lambda), \quad (4.37)$$

are the Fourier coefficients. In $\Omega(\varphi, \lambda, t)$, the parameter h is the order of the Fourier series ($h = 6$ for foF2 and $h = 4$ for M(3000)F2) representing the diurnal variation of foF2 and M(3000)F2 parameters [Davies, 1990]. $G_k(\varphi, \lambda)$ in eqns. (4.36) and (4.37) contains the geographical coordinate functions in the form of spherical Legendre functions up to a harmonic order of nine (foF2) and seven (M(3000)F2) in longitude. They are represented by the expressions $\sin^q \mu \cdot \cos^m \varphi \cdot \cos m\lambda$ and $\sin^q \mu \cdot \cos^m \varphi \cdot \sin m\lambda$ respectively, where q is the highest degree in latitude for each longitude harmonic m and μ is the modified dip latitude

$$\tan \mu = \frac{\Psi}{\sqrt{\cos \phi}}, \quad (4.38)$$

where ψ is the geomagnetic dip latitude. The presence of the F2 layer is controlled not only by the geographic latitude and longitude but also by the geomagnetic dip latitude, and hence the parameter ψ must be included in the model [Bilitza, 1990]. The variable n is related to the sum of the highest degrees of latitude for each longitude harmonic ($n = 76$ for foF2 and $n = 49$ for M(3000)F2). The global description of Legendre functions $G_k(\phi, \lambda)$ is applied to each Fourier coefficient. The numerical maps that have been derived using some 180 ionosonde stations worldwide, are defined by two sets of coefficients representing low and high solar activity times for each month ($n \cdot (2h+1) = 988$ coefficients for foF2 and 441 for M(3000)F2) [NSSDC, 1996a]. To obtain values for intermediate levels of solar activity and for a particular day of a month, linear interpolation is used [McNamara and Wilkinson, 1983].

For computing foF2 using the CCIR/URSI numerical maps, the IRI-95 model uses the 12-month-smoothed global effective sunspot number (IG_{12} index) as an indication of solar activity [Davies, 1990]. The IG_{12} index is recommended, due to the way it is derived (see Section 2.1.5.4), as an alternative to 12-month-smoothed sunspot numbers R_{12} when predictions are made with the aid of the numerical map coefficients of ionospheric characteristics [NSSDC, 1996b]. In my approach, I included an additional scaling factor $K(\phi, \lambda, t)$ that I use to determine an inferred effective sunspot number (inferred IG_{12} index) which is defined as the product of the IG_{12} index and the scaling factor. I

implemented an efficient search technique to find the scaling factor that results in the best match between the IRI-95 model predicted TEC and the GPS-derived TEC. The search technique includes a change of the initial value for the scaling factor ($K = 1$) by a small amount and continuous monitoring of the difference between the IRI-95 prediction and the “ground truth” value (GPS-derived TEC). The search for the correct scaling factor is carried out until the difference between the IRI-95 predictions and the GPS-derived TEC values are less than a predefined value (0.5 TECU). The search is efficient because the change in K depends on the difference between the IRI-95 predictions and the ground-truth, and optimizes the number of runs required to arrive at the 0.5 TECU level difference.

Numerically, the coefficient sets for eqns. (4.36) and (4.37) can be described by

$$U_{2j,k} = \left[U_{2i,k}^{\text{low}} \frac{IG_{12}}{100} + U_{2i,k}^{\text{high}} \left(1 - \frac{IG_{12}}{100} \right) \right] \cdot K(\varphi, \lambda, t), \quad (4.39)$$

$$U_{2j-1,k} = \left[U_{2i-1,k}^{\text{low}} \frac{IG_{12}}{100} + U_{2i-1,k}^{\text{high}} \left(1 - \frac{IG_{12}}{100} \right) \right] \cdot K(\varphi, \lambda, t), \quad (4.40)$$

where the coefficient sets for the high and low solar activity can be distinguished. (The original versions for eqns. (4.39) and (4.40) do not contain the scaling factor K but are otherwise identical to eqns. (4.39) and (4.40) shown here.) For the coefficient sets used to compute $M(3000)F2$, the 12-month-smoothed sunspot number R_{12} is used by the IRI-95 model. For every IRI-95 run during the search, a new value for parameter $\Omega(\varphi, \lambda, t)$ (i.e., $foF2$ and $M(3000)F2$) is used to compute the F2 layer peak electron densities and peak electron density heights to help in constructing a new IRI-95 profile. The computation of

peak electron densities and peak density heights of different layers (D, E, F1, and F2) is described by Bilitza [1990]. The next step is the integration of the electron densities along the IRI-95 profile up to an altitude of 1,000 km. Above this altitude, I also consider the plasmaspheric electron content. The model I use in considering the plasmaspheric electron content was described in Section 4.2.6. To summarize the procedure, the IRI-95 model profile is adjusted by using an inferred IG number which after scaling the CCIR/URSI coefficient sets and adding the plasmaspheric electron content produces the GPS-inferred TEC:

$$TEC_{GPS} = TEC_{IRI-95} + TEC_{plasmaspheric_EC} \quad (4.41)$$

For the integration to obtain TEC predictions, a step size of 1 km was used. Upon finding the correct scaling factor K, modified foF2 and M(3000)F2 coefficient sets are produced allowing us to construct the updated IRI-95 profile, and consequently obtain the updated TEC value.

In this chapter, I have laid down the theoretical foundation of my work. In the next chapter, I will describe the application of the developed algorithm in an IGS campaign in which UNB participated. By taking part in this experiment I had the privilege to collaborate with other IGS processing and analysis centers while gaining tremendous experience in “fine-tuning” my software and learning about regional ionospheric modelling. In the next chapter, I will describe a sensitivity analysis I performed in using different elevation cutoff angles, ionospheric shell heights and the effect of a geomagnetic

disturbance on the TEC estimates. I will also demonstrate the practical implications of the modifications I did to the IRI-95 model.

CHAPTER 5

REGIONAL IONOSPHERIC MODELLING: A SENSITIVITY ANALYSIS

In Section 4.2, I described the algorithm I developed to model the diurnal and spatial variation of the ionosphere. To demonstrate the capabilities of the model, UNB participated in two GPS campaigns. During the first campaign, the UNB regional ionospheric modelling technique was demonstrated. Simultaneously, I performed a sensitivity analysis on the ionospheric shell height determination and a study on ionospheric mapping functions. After fine-tuning my algorithms and software, I turned my attention to modelling the temporal and spatial variation of the *global* ionosphere. This subsequent work will be discussed in Chapter 6.

5.1 The UNB Regional Ionospheric Modelling Based on an IGS Campaign: A Sensitivity Analysis

Along with several other research groups, UNB participated in an experiment to assess the capabilities of GPS data to provide TEC values. Organized under the auspices of the International GPS Service for Geodynamics (IGS) and the Orbit Attitude Division of the European Space Agency's European Space Operations Centre (ESA/ESOC), the experiment involved the processing and analysis of a 5 week long data set (GPS weeks 823 through 827; 15 October to 18 November 1995) of dual frequency GPS data from the

stations of the IGS network. I have analysed the GPS data sets collected by receivers at 6 of the European IGS stations. The results of data processing and analysis were previously reported by Langley and Komjathy [1996]. The stations are Madrid, Grasse, Matera, Brussels, Wettzell, and Onsala and are identified on the map in Figure 5.1 and listed in Table 5.1. The differences in geomagnetic latitudes of stations Madrid, Grasse, and Matera are less than 5 degrees, and 3.3 degrees in the case of stations Brussels and

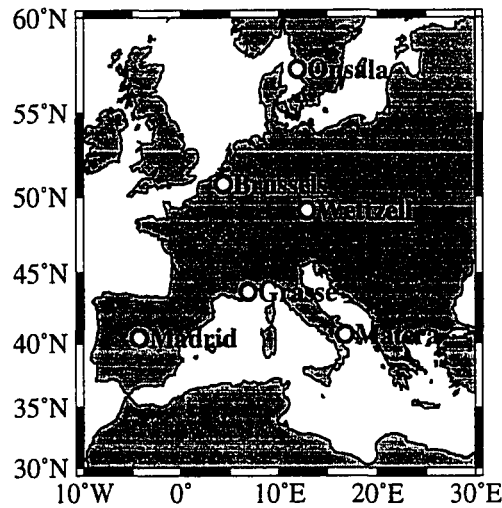


Figure 5.1: Locations of IGS stations used for regional ionospheric modelling.

Table 5.1: List of IGS stations used for regional ionospheric modelling.

Station	Geographic lat. in deg.	Geographic long. in deg.	Geomagnetic lat. in deg.
Madrid, Spain	40.4	-4.2	42.8
Grasse, France	43.7	6.9	45.4
Matera, Italy	40.6	16.7	40.5
Brussels, Belgium	50.8	4.4	52.7
Wettzell, Germany	49.1	12.9	49.4
Onsala, Sweden	57.4	11.9	57.4

Wetzell. Therefore, we can identify three distinct latitude regions in the test network (1. Madrid, Grasse, Matera; 2. Brussels, Wetzell; 3. Onsala). All 6 stations use Allen Osborne Associates TurboRogue receivers.

During the first week of the designated GPS data set, a geomagnetic disturbance occurred [NGDC, 1997a]. The planetary equivalent amplitude of magnetic activity, A_p , suggests that the magnetic disturbance started on 18 October 1995 (day of year 291) and lasted for about 6 days until 23 October 1995 (day 296). The peak ($A_p = 111$) occurred on 19 October 1995. The magnetic disturbance on day 292 affected the diurnal variation of the total electron content. The effect of this disturbance on the UNB TEC estimates was investigated and is described in Section 5.1.3.

5.1.1 The Effect of Different Elevation Cutoff Angles

I investigated the effect of using different elevation cutoff angles on the TEC estimates and satellite-receiver differential delays. Since the idea behind ionospheric modelling using uncalibrated dual frequency GPS receivers is to separate TEC from satellite-receiver differential delays, it is crucial to know the minimum elevation cutoff angle we can use without mismodelling the TEC due to the higher noise on observations with lower elevation angles. Or alternatively, what is the maximum elevation cutoff angle that is still acceptable without mismodelling the satellite-receiver differential delays. I considered three different elevation angle cutoff angles: 15, 20, and 25 degrees. Figure 5.2 shows the

differences in TEC estimates of 15 and 20 degrees with respect to those computed using a 25 degree cutoff angle for Madrid, Brussels, and Onsala. These differences are displayed in separate graphs to illustrate the small differences. I used a 25 degree elevation cutoff

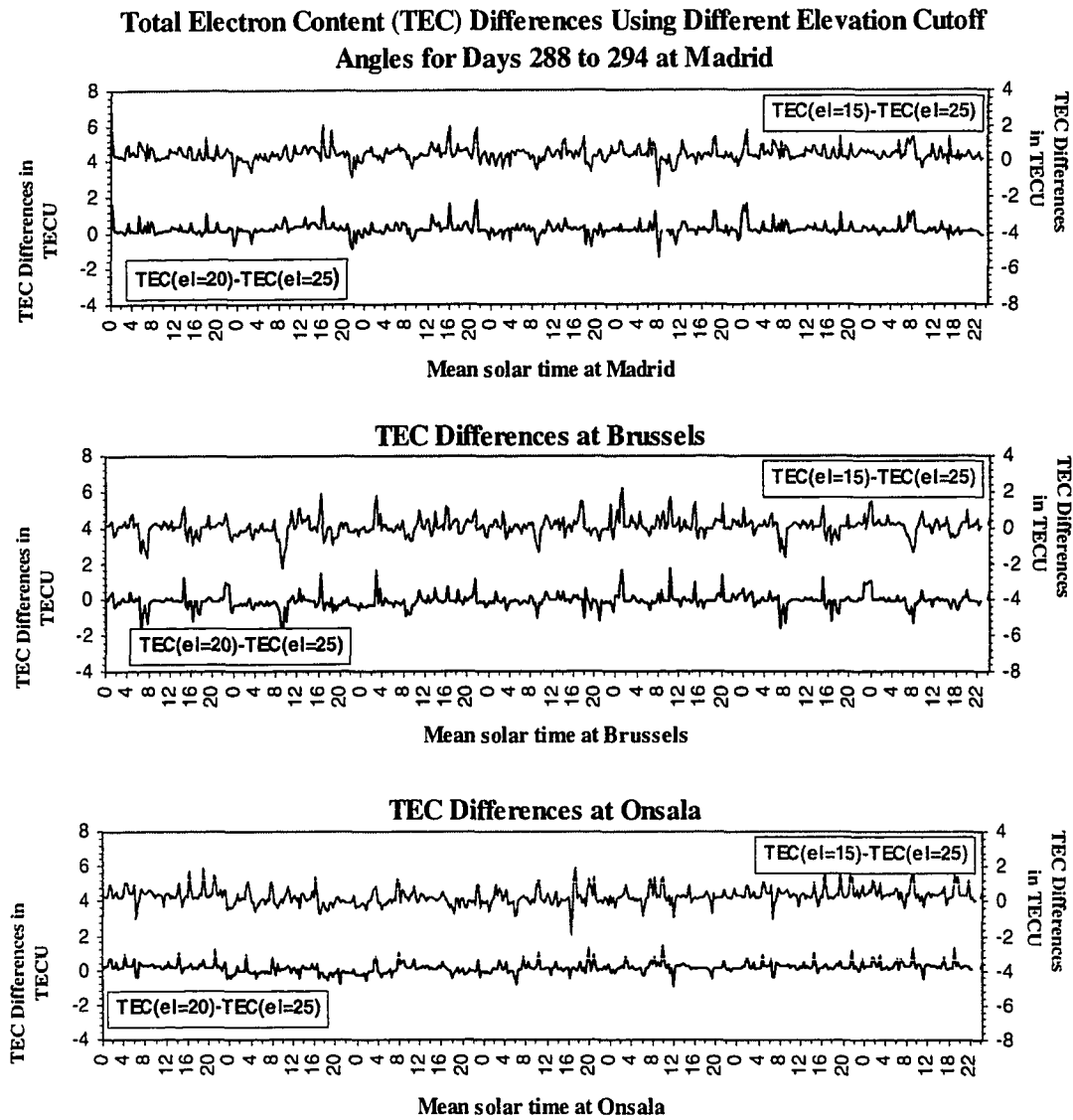


Figure 5.2: Comparison of TEC estimates using different elevation cutoff angles.

angle as a reference for the other two since this solution was expected to be the least noisy as we can see by looking at the r.m.s. of L1 minus L2 ionospheric residuals in Table 5.2 (for further explanation see Section 5.1.2). These stations represent the three different geomagnetic latitude regions from the network of stations I investigated (see Table 5.1).

Table 5.2: Summary of comparison of differential delay differences between UNB and DLR and r.m.s. of UNB ionospheric residuals.

	Elevation cutoff angle cutoff in degrees								
	15			20			25		
Shell height in km	mean of diff. in ns	s.d. of diff. in ns	r.m.s. of UNB res. in TECU	mean of diff. in ns	s.d. of diff. in ns	r.m.s. of UNB res. in TECU	mean of diff. in ns	s.d. of diff. in ns	r.m.s. of UNB res. in TECU
IRI	0.66	0.38	1.09	0.67	0.40	1.00	0.66	0.40	0.91
300	0.54	0.34	1.07	0.58	0.37	0.98	0.59	0.38	0.90
350	0.44	0.31	1.06	0.50	0.34	0.97	0.53	0.36	0.90
400	0.35	0.28	1.04	0.43	0.32	0.96	0.47	0.34	0.89

It appears that the peak-to-peak variation of the differences formed by the 15 and 25 degree elevation cutoff angle solutions is larger than the one formed by the 20 and 25 degree solutions which is what we would expect knowing that there are noisier observations included when computing the solution with a 15 degree cutoff angle. Using different elevation cutoff angles produces maximum differences in TEC estimates at the 2 TECU level. These differences can also be characterized by a mean of 0.3 TECU and standard deviation of 0.5 TECU with respect to the TEC values obtained using a 25 degree elevation cutoff angle as “truth”. This maximum peak to peak variation in TEC using different elevation cutoff angles occurred at station Onsala. Based on my investigation, it seems to be worthwhile using a lower e.g., 15 degree elevation cutoff angle, since the maximum error we introduce into the TEC estimates is always less than 2

TECU and it is typically at the 1 TECU level. There appears to be a tradeoff between the 1 TECU level uncertainty, that one introduces into the TEC estimates using lower elevation cutoff angle; and the advantage of more data which will make the estimation process stronger. This advantage of using a lower elevation cutoff angle can be of twofold. First, we will better able to separate the TEC from the satellite-receiver differential delay as we shall see in Section 5.5 provided that we use a “good” ionospheric mapping function allowing us to use observations at lower e.g., 15 degrees satellite elevation angle. An interesting analogy to that is the tropospheric parameter estimation, using a lower elevation cutoff angle with a good tropospheric mapping function. This will enable us to come up with a stronger estimate for the height component of a GPS baseline. The second advantage using a lower elevation cutoff angle in the case of the ionospheric studies is better spatial data coverage, hence the ionospheric model will better able to approximate the behaviour of the real ionosphere. This will be particularly important for modelling the temporal and spatial variations of the global ionosphere which will be demonstrated in Chapter 6.

5.1.2 The Effect of Ionospheric Shell Height

Another parameter that affects the TEC estimation is the height of ionospheric shell which plays an important role in computing the coordinates of the subionospheric points. It is also an input parameter of the $M(e_{rj}^{si})$ mapping function (see eqn. (4.13)). As a reminder,

the single layer ionospheric model assumes that the ionosphere can be approximated by a thin spherical shell. It is usually assumed that the ionospheric shell height has no temporal

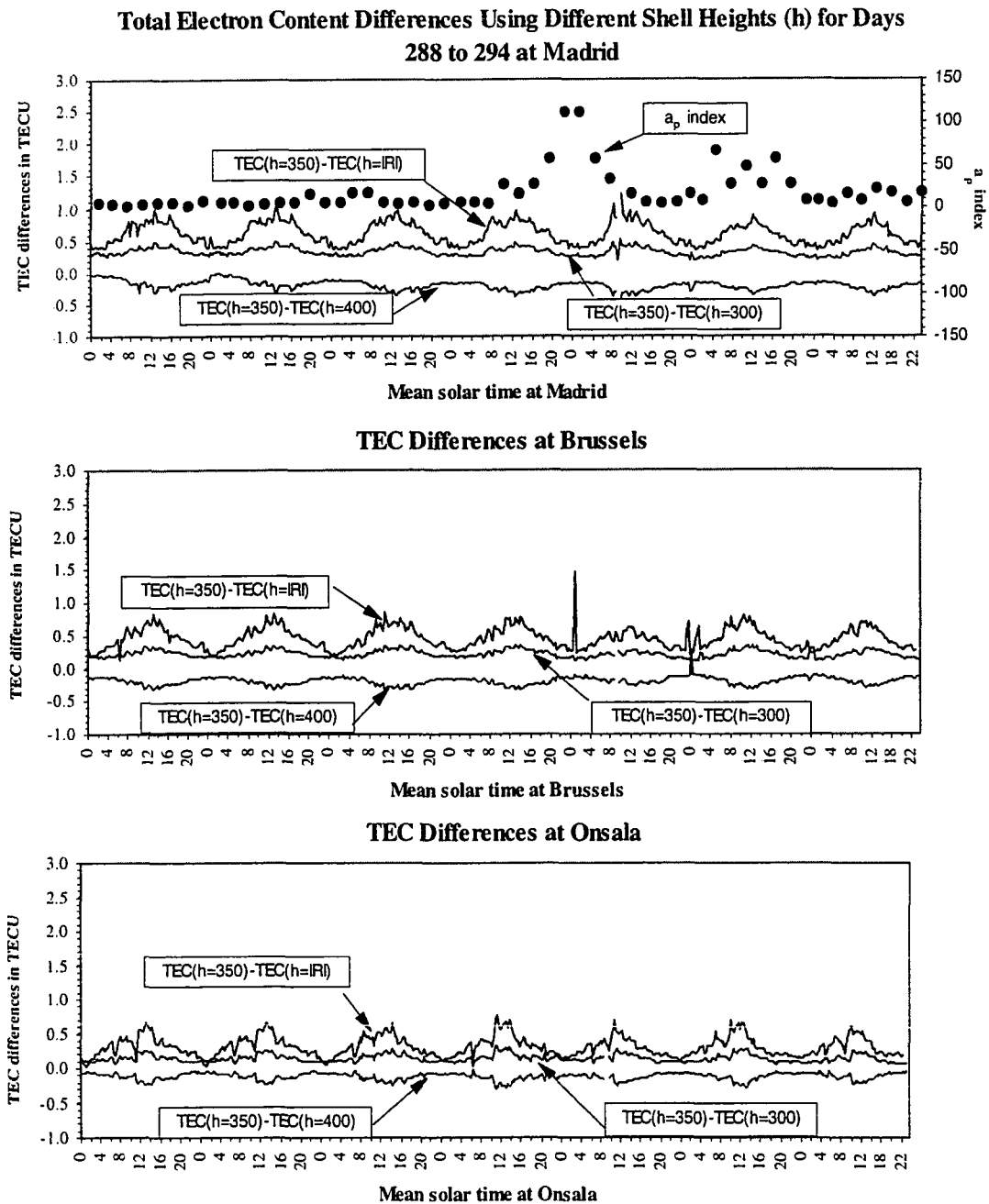


Figure 5.3: Comparison of TEC estimates using different ionospheric shell heights.

or geographical variation and therefore it is set to a constant value regardless of the time or location of interest. This height is often assumed to correspond to the maximum electron density of the ionosphere. In my investigation I looked at fixed heights of 300, 350, and 400 km and also included variable heights computed by the IRI-90 model using F2 layer peak heights.

The TEC differences shown in Figure 5.2 were obtained using a 350 km shell height. In Figure 5.3, I plotted the differences between corresponding TEC estimates for the three representative stations using different ionospheric shell heights and a “standard height” of 350 km. I used a 15 degree elevation cutoff angle to generate the TEC estimates used in the Figure 5.3. The differences tend to decrease the further north the station is. Since the IRI-90’s F2 layer critical heights take the geographical and temporal variation into account, there is a larger periodic variation of the differences involving IRI-90 heights. In looking at Figure 5.3, the largest differences between two different solutions appear to be at the 1 TECU level at the Madrid station.

I computed the mean of the daily satellite-receiver differential delays for 7 days. I also obtained a set of bias estimates computed by Deutsche Forschungsanstalt für Luft und Raumfahrt (DLR) Fernerkundungsstation, Neustrelitz, Germany [DLR, 1995]. After computing the mean of the corresponding values obtained from DLR for all 7 days I computed the differences of the corresponding biases. After that, I calculated the mean and standard deviation of the differences computed by UNB’s (using different elevation

cutoff angles and different ionospheric shell heights) and DLR's results (using 16 stations with a 20 degree elevation cutoff angle and a 400 km ionospheric shell height [Sardon, 1996]). The means and standard deviations are listed in Table 5.2. The differences between UNB's and DLR's individual differential delay range between 0.01 and 1.10 ns. It is clear that the mean of the differences in biases decreases as higher ionospheric shell heights are chosen. It appears that choosing different elevation cutoff angles has no significant impact on the bias differences. The largest bias differences occur using the F2 layer critical heights computed by the IRI-90 model. This is mainly because IRI-90 predicts the critical heights to be between 220 and 340 km depending on location and time of the day. The largest bias, standard deviation and r.m.s. of the UNB residuals indicate that the IRI-90-derived F2 layer critical heights are not appropriate to use as an approximation for ionospheric shell heights. The smallest r.m.s. of residuals resulted in using 400 km shell height with 15, 20, or 25 degree elevation cutoff angles. This is a clear indication that using 400 km shell height is closest to the "truth". Overall, a 400 km shell height with 25 degrees elevation cutoff angle gave us the smallest r.m.s. of residuals which can be explained by the fact that at 25 degrees elevation cutoff angle we would expect the smallest noise level in the ionospheric observations. Despite of this, lower elevation cutoff angles might still be useful as explained in Section 5.1.1. The differences between the two institutions' results may also be due to the fact that the UNB network consisted of only 6 stations. A larger number of stations would provide more accurate differential delay values as well as TEC estimates.

5.1.3 The Effect of a Geomagnetic Disturbance

The geomagnetic disturbance on day 292 affected the diurnal variation of the total electron content. As an example, I display the diurnal variation of the UNB estimates of TEC for two days at station Madrid (see Figure 5.4) and Onsala (see Figure 5.5) the two stations furthest apart in my network. For day 288, the geomagnetic field was quiet and for day 292 the geomagnetic disturbance reached its peak.

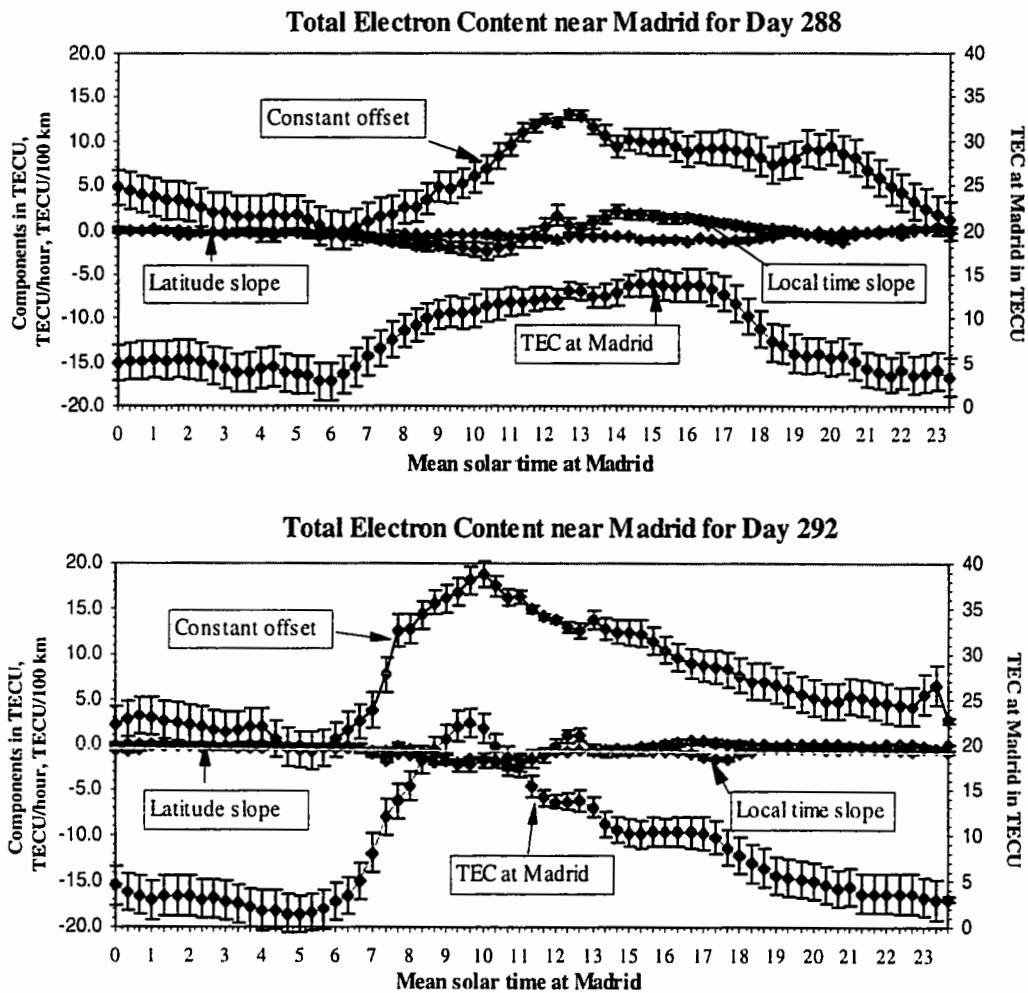


Figure 5.4: An example of the diurnal variation of TEC for magnetically quiet and disturbed days for station Madrid.

I was interested in investigating whether the UNB algorithm was able to follow the rapidly changing ionospheric conditions on day 292. The two upper panels of Figure 5.4 and Figure 5.5 display three curves representing coefficients a_{0,r_j} , a_{1,r_j} , a_{2,r_j} (see eqn. (4.13)) with their corresponding (one-sigma) error bars. These coefficients represent a constant offset, local time slope and latitude slope of the modelled vertical TEC, respectively, in the vicinity of a station.

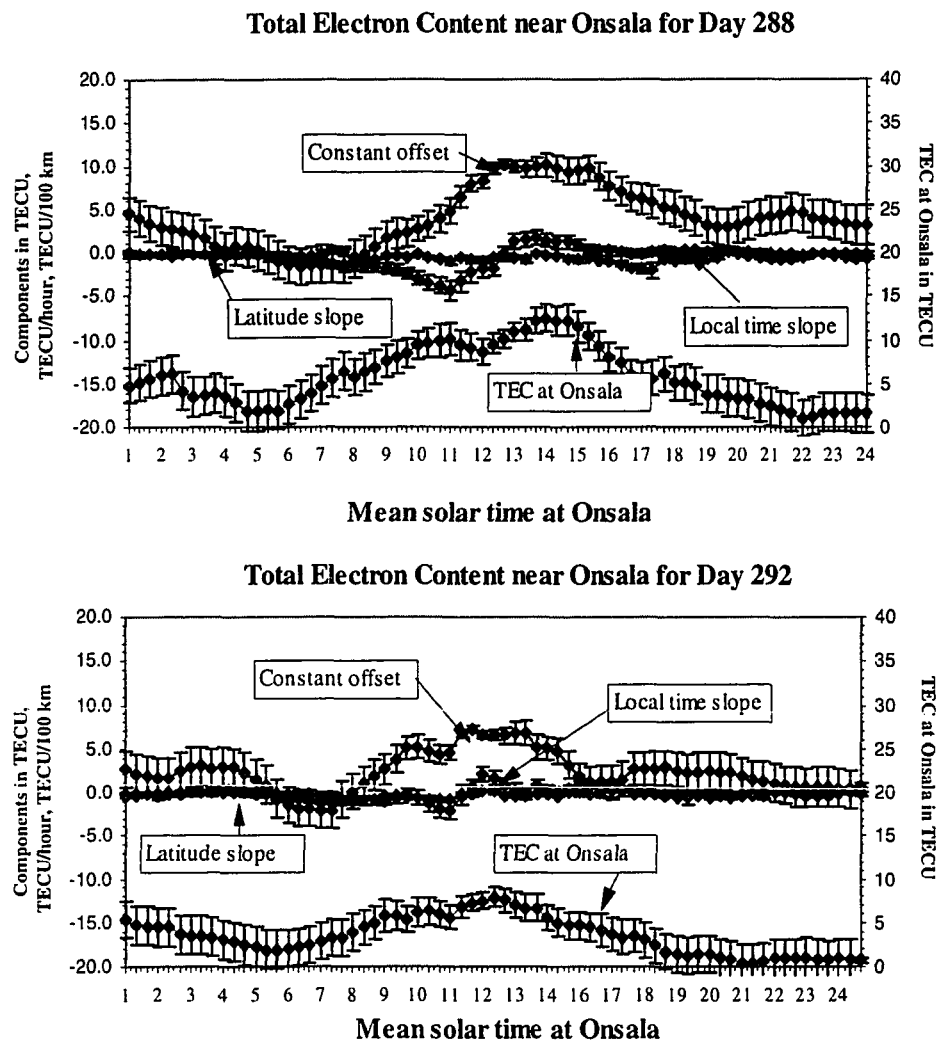


Figure 5.5: An example of the diurnal variation of TEC for magnetically quiet and disturbed days for station Onsala.

The panels also show the vertical TEC computed by evaluating the vertical TEC model in eqn. (4.13) (see expression in brackets). I also plotted error bars representing the formal (one-sigma) errors of the estimation. The error bars of the UNB TEC estimates appear to be at the 2 TECU level for night time and about 1 to 2 TECU for day time observations. The difference of the size of error bars for the day time and night time periods is indicative of the fact that during the day the algorithm is better able to separate the satellite elevation angle dependent TEC from the satellite elevation angle independent satellite-receiver differential delays. The reason that the vertical TEC is not equal to a constant offset is that I used a solar-geomagnetic coordinate system which assumes that the main part of the ionization in the ionosphere is caused by the sun and the effect of the geomagnetic field. Had I used an earth-fixed coordinate system, the constant offset would have been equal to the vertical TEC. It has been shown that using a solar-geomagnetic coordinate system produces more accurate TEC estimates than that of earth-fixed coordinate system [Mannucci et al., 1995]. This is mainly because stations can be tied together in a solar-geomagnetic coordinate system having an effect on each other's approximation of the vertical TEC described by the three stochastic parameters in the case of the UNB approach. The shape of the diurnal curves on day 288 and 292 are significantly different. On day 288, the largest TEC value at Madrid is around 15 TECU whereas on day 292, the largest TEC at Madrid is around 25 TECU. In the case of station Onsala, on day 288 the largest TEC at Onsala was about 13 TECU, whereas on day 292 the largest value turned out to be around 10 TECU. Figure 5.6 shows the UNB ionospheric residuals for all 6 stations for the geomagnetically active day 292. It is clear that the UNB algorithm was

capable of following the highly dynamic ionospheric conditions induced the geomagnetic disturbance. The residuals indicate a smooth performance of the model when using the UNB technique for modelling the vertical TEC. As we can see in the figure, the residuals seem to be somewhat larger at night time when it might be more difficult to separate TEC from the satellite-receiver differential delays.

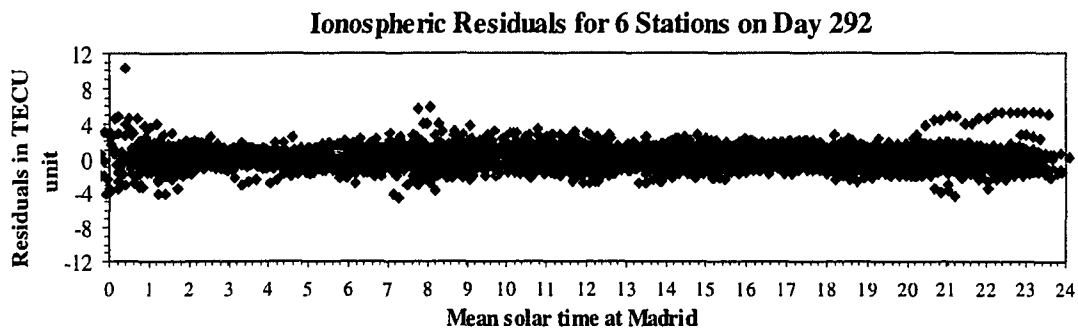


Figure 5.6: Ionospheric residuals for geomagnetically active day 292.

In Figure 5.7, I display TEC diurnal curves for all stations for GPS week 823 when the geomagnetic disturbance occurred. I also plotted the TEC values predicted by the IRI-90 model. It is very interesting to see that on day 292, at stations Madrid, Grasse and Matera, the peak TEC values increased considerably compared to peaks for the previous days. On the other hand, for stations Brussels, Wettzell and Onsala, the GPS-derived TEC estimates show peaks with smaller size than the ones on the previous days. On the bottom panel of Figure 5.7 is also shown the planetary equivalent amplitude of the geomagnetic field variation [NGDC, 1997a]. We can see that large TEC variations on day 292 were preceded by the magnetic field disturbance starting on day 291. Day 292 seemed to be the most variable among the 7 days under investigation. The bottom panel of Figure 5.4 and Figure 5.5 suggest that there are no major difficulties for the UNB algorithm to follow

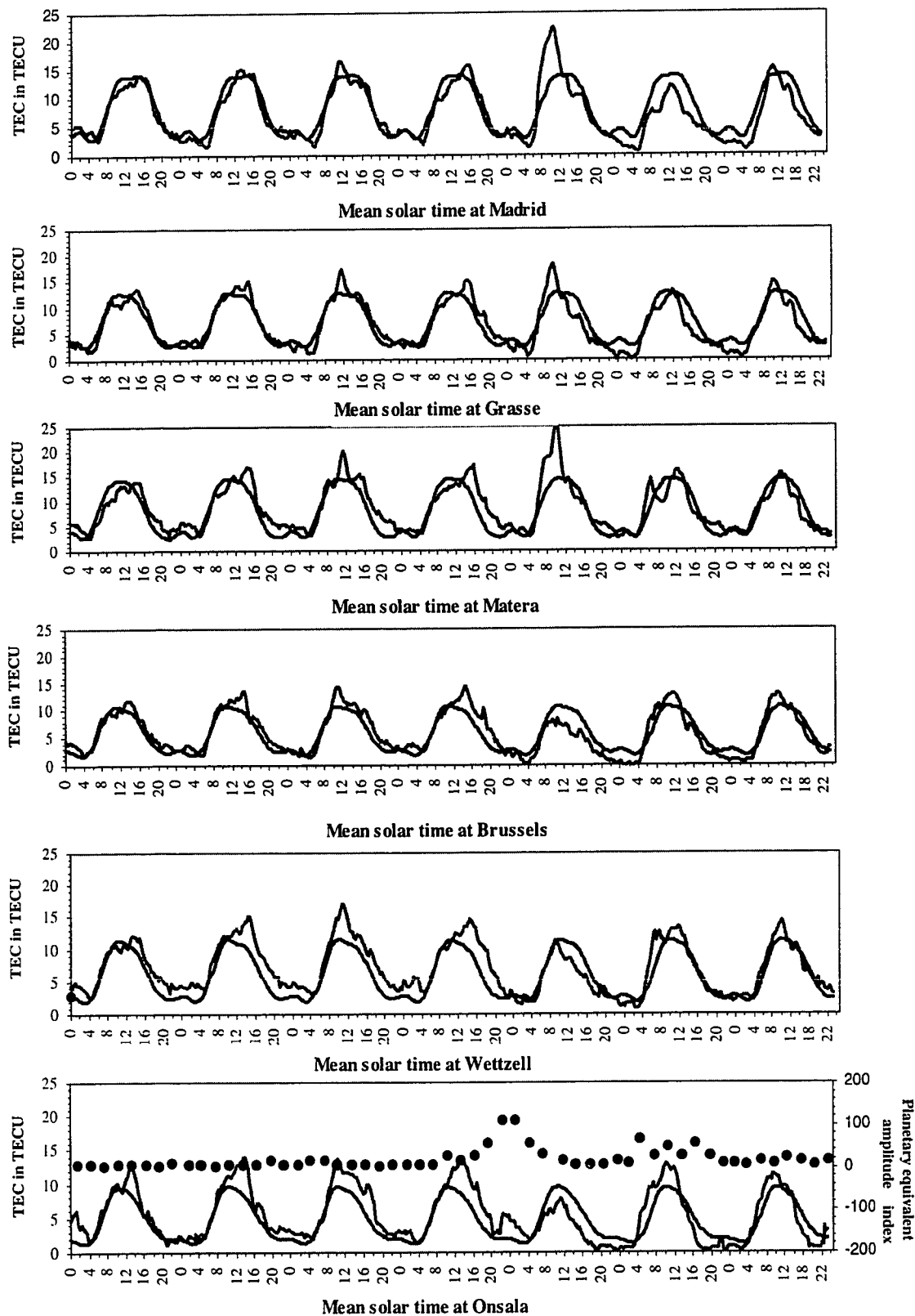


Figure 5.7: Diurnal variation of TEC for 7 consecutive days using a network of 6 IGS stations (darker, smoother curve represents the IRI-90 predictions).

ionospheric variations induced by the geomagnetic field disturbance. This statement may only hold for the current low solar activity period. The effect of a major geomagnetic field disturbance on GPS-derived global TEC estimates will be investigated in Chapter 6.

In this study I also found that even though the geomagnetic disturbance started during European night-time, it only caused a TEC increase (stations Madrid, Grasse, Matera) and decrease (Brussels, Wettzell) on the following day around noon (day 292). The fact that I detected at some stations a TEC increase and at others a TEC decrease may suggest that the magnetic disturbance was moving equatorward which is a well known feature of such disturbances [Davies, 1990]. In Figure 5.7, I also displayed the total electron content computed by the IRI-90 model (darker, smoother curve).

Table 5.3: Comparison of GPS-derived TEC estimates with IRI-90 predictions.

	Mean of differences in TECU	S.d. of differences in TECU
Madrid	-0.7	1.5
Grasse	-0.4	1.8
Matera	0.5	2.3
Brussels	0.2	1.5
Wettzell	1.1	1.7
Onsala	0.3	1.5

I computed the differences of IRI-90 predicted and GPS-estimated TEC values. The means of the differences and the standard deviations for the 6 stations are summarized in Table 5.3. When computing the mean of differences, I used 7 days of data. The IRI-90 predictions seem to be too good compared to the results described in Chapter 3 and published earlier by Komjathy et al. [1996b]. This may be due to the fact that this

investigation used data from a period of lower solar activity compared to those of the data in Chapter 3 which represented solar activity conditions from April 1994 to January 1995. This conclusion is also supported by the research conducted by Newby [1992]. In his thesis, Newby looked at high, medium and low solar activity conditions. It was also shown that the IRI-86 model performance based on low solar activity conditions showed good agreement with Faraday rotation data at the 1.8 TECU level.

5.1.4 Conclusion of the Sensitivity Analysis

I investigated the effect of using different elevation cutoff angles and ionospheric shell heights on TEC estimates and satellite-receiver differential delays. I found that using different elevation cutoff angles had an impact on TEC estimates always less than 2 TECU, typically at the 1 TECU level. Also, several ionospheric shell heights were looked at. The research has shown that at the 2 TECU level, the ionospheric estimates using different heights agree depending on geographic location and time of the day. I also compared the UNB satellite-receiver differential delay estimates with results from DLR. I found an agreement at the 0.5 ns level. The differences of the biases computed by UNB and DLR indicate that using different elevation cutoff angles appears not to have a significant influence on the biases. However, it was found that using higher ionospheric shell heights decreased the bias differences significantly. The comparison of the UNB TEC estimates with TEC predictions obtained using the IRI-90 model showed that for the

particular data set mean of the differences was always less than 1.1 TECU and the standard deviation was always less than 2.3 TECU.

The algorithm was successful in following highly varying ionospheric conditions due to a magnetic disturbance. Due to the limited data set investigated, it is also important to point out that the conclusions presented here are likely specific for mid-latitude stations during low solar activity conditions.

5.2 The Varying Ionospheric Shell Height: A New Concept

After the initial results of using the IRI-90 model for ionospheric shell height determination during the sensitivity analysis discussed in Section 5.1.2, I decided to look more closely at the effect of the ionospheric shell height. In a subsequent investigation, as discussed in Section 4.2.3, I used the IRI-90 model to compute even more accurate ionospheric shell heights by integrating the predicted electron densities through the six subregions of the IRI-90 profile. As a reminder, ionospheric shell height predictions were obtained upon reaching 50 percent of the predicted total electron content during the numerical integration procedure using a step size of 1 km (determination of median height). I computed the predicted total electron content up to an altitude of 1000 km (for illustration see Figure 5.8), consequently, plasmaspheric electron content has not been considered here (this effect was discussed earlier in Section 4.2.3). I believe computing the median height provides a more rigorous approach compared to what has been described in

Section 5.1.2. Note, as illustrated in Figure 5.8, that the predicted ionospheric shell height is always slightly above the height of the F2 layer peak electron density since the topside region of the ionosphere usually contains more electrons than the bottomside. The predicted ionospheric shell heights are used as input to the UNB software for estimating TEC maps as well as satellite-receiver differential delays. The theoretical and practical consideration for this technique was elaborated by Komjathy and Langley [1996c; 1996d].

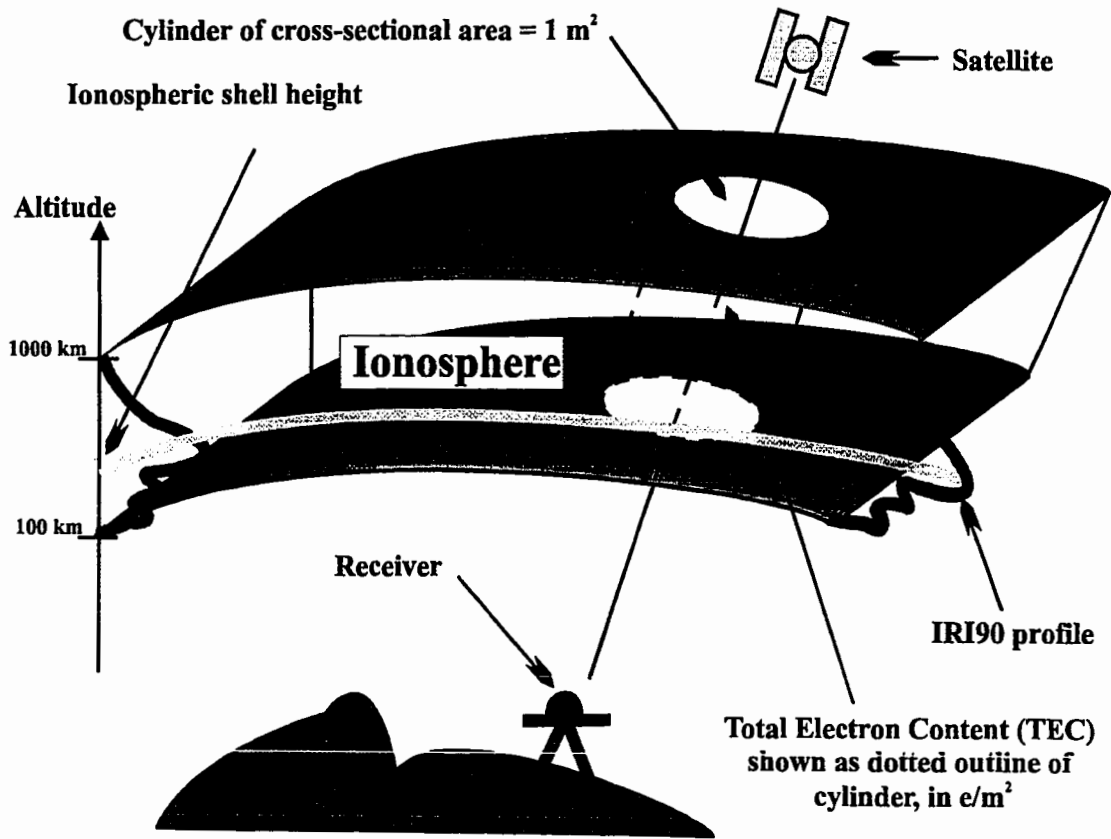


Figure 5.8: Illustration of ionospheric shell height determination.

For the investigation, I used the IRI-90-model-derived ionospheric shell height predictions as input to the UNB DIPOP-based processor. As a first step, I computed the

IRI-90 predicted total electron content by integrating the predicted electron densities along the IRI-90 profile. A simplified version of the profile can be seen in Figure 5.9 (for an explanation of the symbols, see Hakegard [1995] or Bilitza [1990]). Secondly, I used these TEC predictions to integrate the electron densities along the profile again. This time, the goal was to determine the height at which 50 percent of the total electron content was reached. I did this for all six stations used for data processing for the 21 days under investigation. As an example, I plotted the predicted ionospheric shell heights for day 288 in Figure 5.10. We can clearly see a diurnal variation of the IRI-90-model-derived ionospheric shell height. The shell height seems to peak at night-time values of about 400 km and goes down to day-time values typically at the 300 km level. Diurnal curves were plotted for all 6 stations for day 288. There are noticeable differences from station to

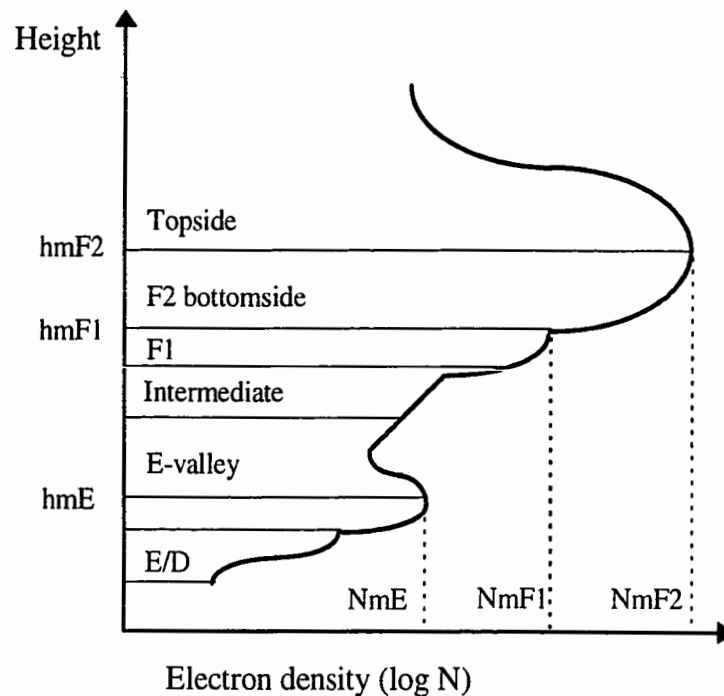


Figure 5.9: IRI-90 profile (after Hakegard, [1995]).

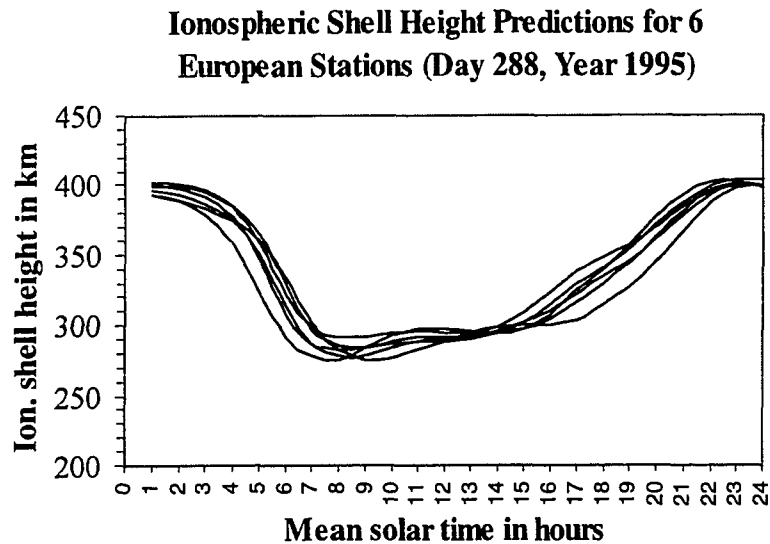


Figure 5.10: The diurnal variation of the ionospheric shell height.

station even under the current low solar activity conditions. The differences in values of the ionospheric shell height computed using the method described above for this regional network and for GPS weeks 823 to 825 was between 10 and 30 km depending on the time of the day.

For a better understanding of the magnitude range of the varying ionospheric shell height, I computed the predicted ionospheric shell heights for high (year 1990), medium (year 1992) and low (year 1995) solar activity conditions. In Figure 5.11, I have plotted the diurnal curves for the two stations that are furthest apart in the network: stations Madrid and Onsala. Each diurnal curve represents the conditions for one month of the year and the sequence of curves displays not only the diurnal variation but also the seasonal variation of the ionospheric shell height. Note that the x axis is a category time

axis on which the 12 diurnal curves have been plotted one after the other each representing a “typical day” of a month. The typical day was arbitrarily chosen to be the

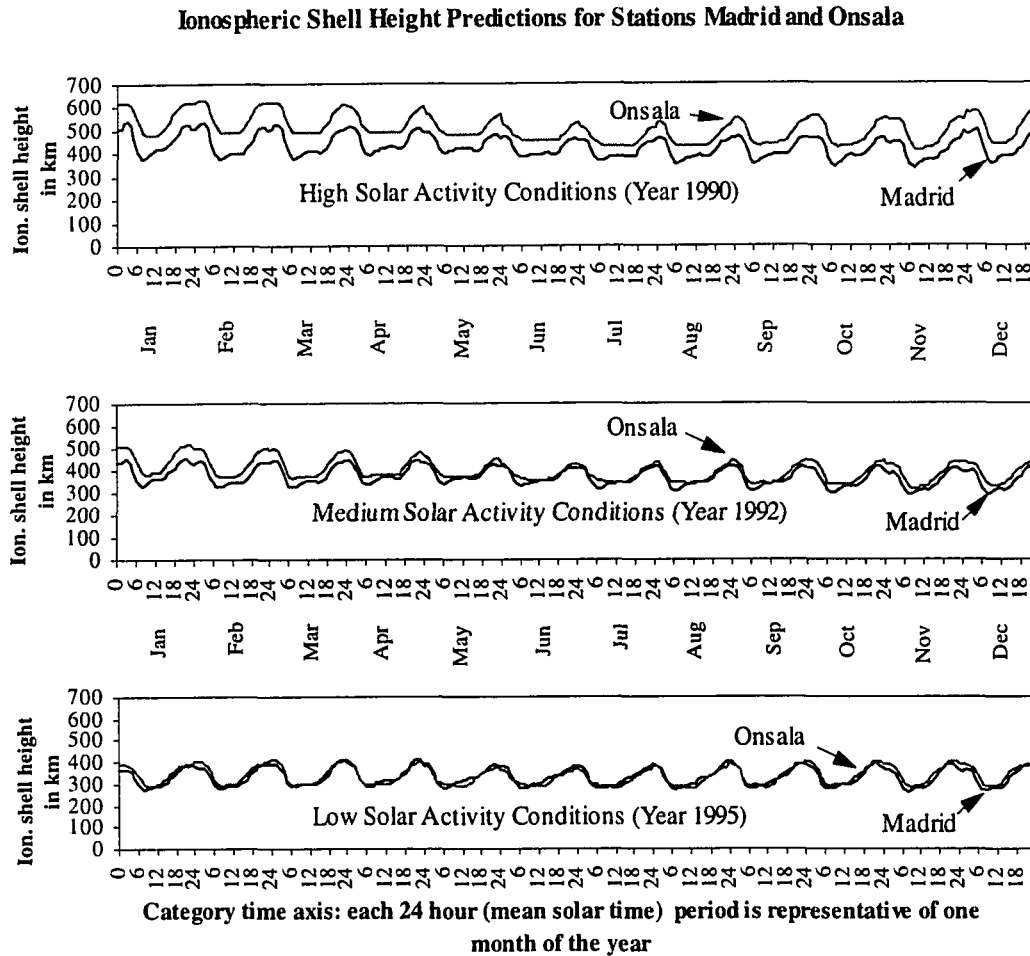


Figure 5.11: Ionospheric shell height predictions using the IRI-90 model.

15th day of the month for illustration purposes. A small discontinuity is visible between some of the curves at 24 hours reflecting month-to-month variations. During high solar activity conditions, the peak to peak variation of the diurnal curve is between about 400 and 600 km, depending on season and geographic location of the station. During medium solar activity conditions, the variation is between about 300 and 500 km. For low solar

activity conditions this variation is between about 300 and 400 km. As solar activity decreases, the dependency on geographic location, at least for the two European stations, becomes less significant. For high solar activity conditions, station Onsala (furthest north in the network) had the highest ionospheric shell heights. Also, during winter months the separation between shell heights predicted for stations Onsala and Madrid seems to be larger than for the rest of the year.

For high solar activity conditions, based on the 6 stations investigated, the average ionospheric shell height is around 466 km; for medium solar activity conditions, 385 km; for low solar activity conditions, 335 km. It seems that the diurnal, seasonal, solar-cycle and spatial variations of the ionospheric shell heights are primarily associated with the temporal and spatial variation of the F2 layer peak electron density. The effect of using a commonly adopted fixed ionospheric shell height on the TEC and satellite-receiver differential delays was investigated in Section 5.1.2. It was found that using different fixed values for the ionospheric shell height has an effect on the TEC estimates typically at the 1 TECU level. I also discovered that the effect seems to be significant in the case of the satellite-receiver differential delays. The new UNB-developed IRI-model-based varying ionospheric shell heights as input to the UNB model produces TEC and satellite-receiver differential delay estimates that are yet again somewhat different from those obtained using a fixed ionospheric shell height. To determine the magnitude of the differences, I produced a set of TEC and differential delay estimates using both a commonly adopted fixed ionospheric shell height (400 km) and varying ionospheric shell heights predicted by

the IRI-90 model as described earlier. 21 days' worth of data was used for this investigation. I differenced the means (over 21 days) of the differential delay estimates for each satellite and station using the varying IRI-90-model-predicted and 400 km ionospheric shell heights. The differences in differential delays can be seen in Figure 5.12. The differences are less than 0.3 ns with a mean of 0.14 ns and mean standard deviation of 0.13 ns. In Figure 5.12, the error bars represent the mean standard deviation of the UNB differential delay estimates. I also produced hourly TEC maps at a 1 degree by 1 degree grid spacing for the region. I produced the TEC maps by evaluating at each grid node the expression for the spatial linear approximation of TEC described by the three parameters estimated for each IGS station. For evaluating the model at each grid node, I used the three estimated parameters from the nearest IGS station. I used both the varying and 400 km ionospheric shell heights to compute different sets of ionospheric maps. I differenced the corresponding TEC values at each grid node that were computed for each hour of the 21 days under investigation. The differences are plotted in the form of a histogram in Figure 5.13. The histogram is based on 640,584 ((31 by 41 grid) times (24 hours) times (21 days)) TEC estimates. 53 percent of the differences fall into a bin that can be characterized with a lower boundary of -0.5 TECU and upper boundary of 0 TECU. The mean of the differences is -0.34 TECU and its associated standard deviation is 0.58 TECU. Note that the TEC differences were formed by subtracting TEC values using a 400 km shell height from those using the IRI-90-derived shell height TEC values.

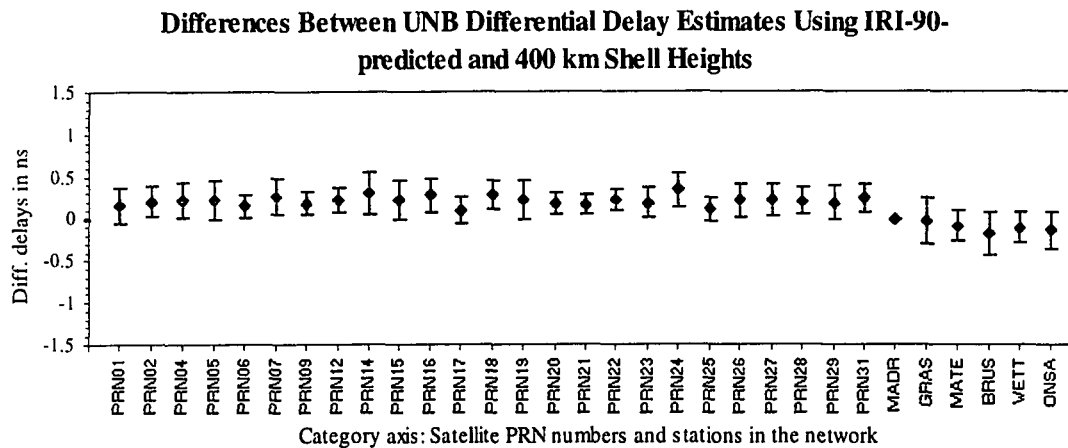


Figure 5.12: Comparison of satellite-receiver differential delay estimates using IRI-90-derived and 400 km ionospheric shell heights.

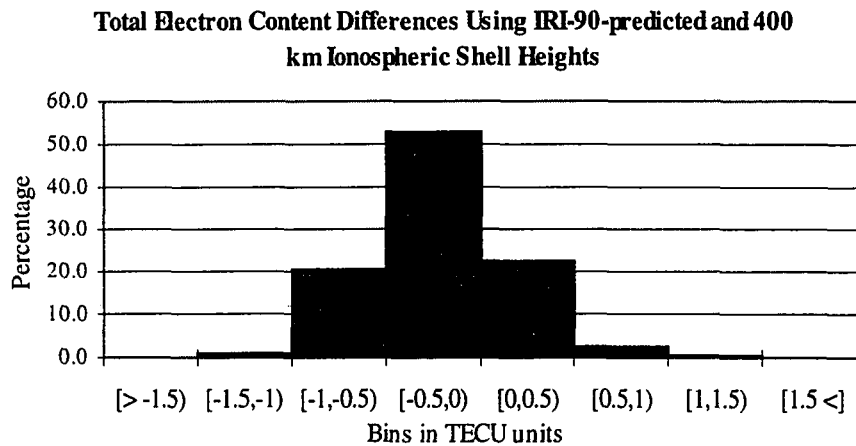


Figure 5.13: Comparison of TEC estimates using IRI-90-derived and 400 km ionospheric shell heights.

I concluded from this investigation that taking the temporal and spatial variation of the ionospheric shell height into account has an effect on the TEC estimates of up to 1 TECU, and 0.3 ns in the case of the differential delay estimates. These values will likely only hold for mid-latitude conditions at low solar activity levels. As we have seen earlier in Figure 5.11, during higher solar activity times, we can expect these differences to increase. The 1

TECU level differences are fairly small and may be within the error bars of the TEC estimates. Therefore, I decided not to compare the UNB TEC estimates (maps) with those obtained by other research groups participating in the campaign to try to determine the effects of using different values for the ionospheric shell height. Furthermore, the differences between ionospheric modelling methods used by different groups would make it difficult to draw conclusions on the specific effect of their selected ionospheric shell heights.

Instead, I computed the means and the standard deviations of the UNB daily differential delays for 21 days. I also obtained a set of differential delay estimates computed by two of the other participating members of the ionospheric experiment, namely, the Deutsche Forschungsanstalt für Luft und Raumfahrt (DLR) Fernerkundungsstation, Neustrelitz, Germany and the European Space Agency's European Space Operation Centre (ESA/ESOC), Darmstadt, Germany [ESA/ESOC, 1996]. After computing the means and standard deviations of the differential delays obtained from DLR and ESOC for 21 days, I computed the differences of the corresponding means. The differences among the 3 analysis centers' results are displayed in Figure 5.14.

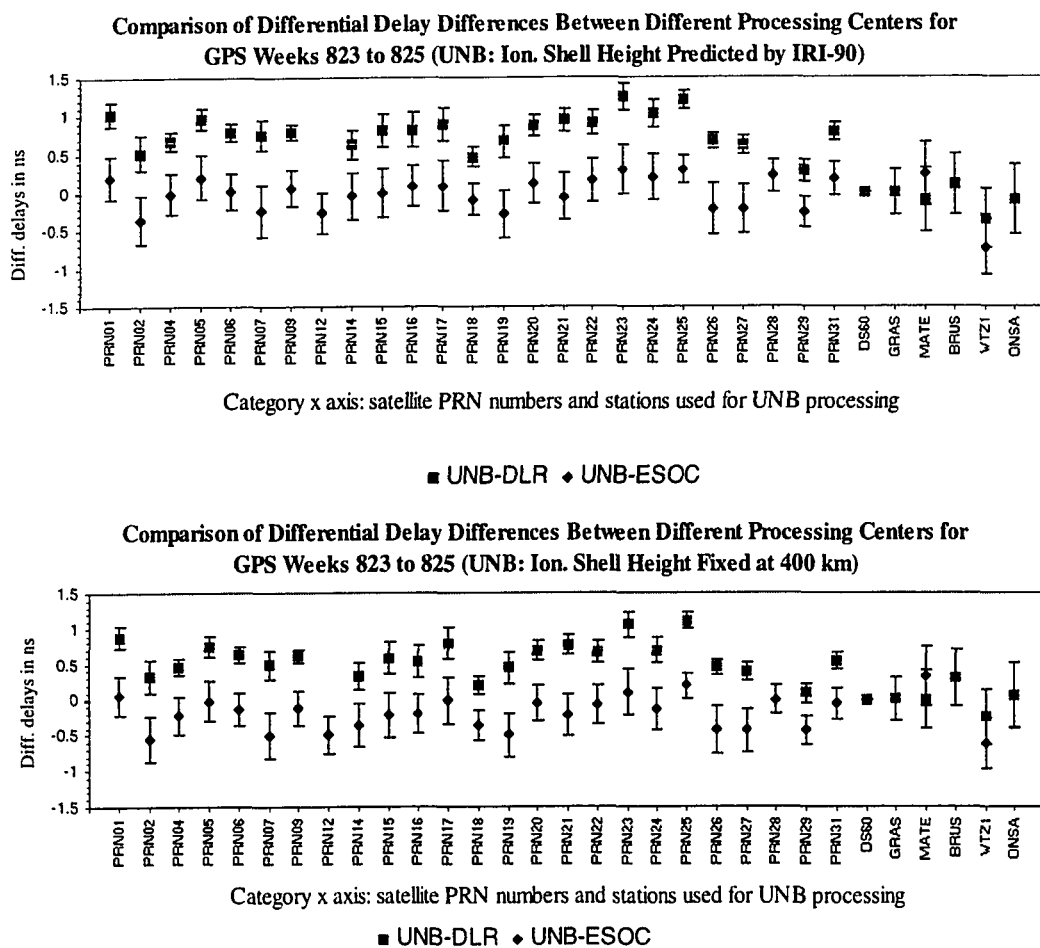


Figure 5.14: Comparison of differential delay differences between IGS processing centers.

The differences were formed as UNB minus DLR and UNB minus ESOC using both the IRI-90-derived shell height results (upper panel) and the UNB results using the 400 km shell height (lower panel). Note in Figure 5.14 that satellites PRN12 and PRN28 were not used by DLR and stations Grasse and Brussels were not processed by ESOC. The associated standard deviations of the differential delays about the means of the two other processing centers were also plotted. The standard deviations of the means of the UNB differential delays were plotted earlier in Figure 5.12 and have not been considered in computing the error bars in Figure 5.14. The differences of the differential delay estimates

are at the 1 ns level for both shell height models (upper and lower panels). It is interesting to see that there is a clear bias between the DLR and ESOC satellite differential delays. A small part of the bias can be explained by the fact that the ESOC algorithm uses 350 km for the ionospheric shell height whereas the DLR algorithm uses 400 km. As my investigation indicated in Figure 5.12, a 0.14 ns level bias can be expected between the differential delay differences using the IRI-90-derived differential delays and the ones obtained using 400 km. However, a 1 ns level difference indicates that there are effects coming from other differences in the algorithms used by the processing centers. The fact that the UNB-ESOC differences do not seem to show a consistent bias might be explained by the fact that the mean of the IRI-90-predicted diurnal variation of the ionospheric shell height is around 335 km under low solar activity conditions which is close to the 350 km height used by ESOC.

One of the potential error sources that may contribute significantly to the UNB error budget is the mapping function error. Since I used a simple secant mapping function at this stage, this could introduce errors at low elevation angles (between 20 and 30 degrees). As a reminder, throughout the processing, I used a 15 degree elevation cutoff angle. The very ability to do ionospheric modelling is based on the possibility of separating estimates of TEC from differential delays by using the elevation angle dependence of the TEC variation. Should this separation suffer from mapping function errors, a bias could be introduced into both the TEC and differential delay estimates. This issue will be addressed in Section 5.5.

It seems that using pre-defined values for ionospheric shell height has a scaling effect on the differential delay estimates. The results presented in Section 5.1.2 were also indicative of this. The lower the ionospheric shell height is set (arbitrarily or otherwise) from the “true” value, the higher the estimated differential delays will be. Furthermore, this effect seems to have an opposite sign in the case of the TEC estimates: The lower the ionospheric shell height is set from the true value, the lower TEC estimates can be expected. This scaling effect might be explained by the fact the ionospheric shell height (fixed or varying) is acting like a constraint around which the “real” ionospheric shell height is located. The error coming from the inappropriately set ionospheric shell height will propagate into the differential delay estimates resulting in higher values for the differential delay estimates. Using pre-defined fixed values for the ionospheric shell height may lead to errors both in the satellite-receiver differential delays and the TEC estimates. This conclusion seems to be supported by the maximum 0.3 ns error in differential delay differences I found which corresponds to about 1 TECU. This also corresponds to the maximum TEC differences using different shell heights that were found to be at the 1 TECU level (Figure 5.13). Using 400 km as a fixed ionospheric shell height during low solar activity conditions overestimates the day-time TEC by up to 1 TECU assuming that the IRI-90-derived ionospheric shell height predictions are free of error. In the case of the satellite-receiver differential delays, using a fixed 400 km ionospheric shell height underestimates the differential delays by up to 0.3 ns under the same assumption. I believe these numbers would be even higher for higher solar activity conditions. An approximate

value for the error we can expect by inappropriately setting the ionospheric shell height is about 0.5 TECU for every 50 km error in the height. This number corresponds to about 0.14 ns in the case of the differential delays. Also, these numbers could be different when modelling the ionosphere by fitting polynomials to the diurnal variation of TEC over a certain period of time. This procedure inherently averages over different ionospheric shell heights. This can also be a feasible explanation for my not detecting differences between the UNB and ESOC differential delay estimates.

5.2.1 Conclusions of the Investigation on the Varying Ionospheric Shell Height

The concept of accounting for the temporal and spatial variation of the ionospheric shell height using the IRI-90 model has been described. It was shown that over a small regional network of IGS stations, the predicted ionospheric shell height can vary with geographic location, time of day, season, and solar activity. After comparing the UNB results with those obtained earlier using a fixed ionospheric shell height, I found differences in the differential delays of up to 0.3 ns. A similar study was conducted for the TEC estimates and I discovered that the estimates can be different by as much as 1 TECU when the temporal and spatial variation of the ionospheric shell height is not considered. In my opinion these differences can be even larger during high solar activity conditions.

Furthermore, taking into account the temporal and spatial variation of the ionospheric shell height provides a more rigorous approach when estimating ionospheric model

parameters along with satellite-receiver differential delays. By inappropriately setting the ionospheric shell height, we can expect a possible 0.5 TECU level error for every 50 km error in the shell height. For the differential delays, the equivalent error level is about 0.14 ns for each 50 km.

5.3 Improvement of the International Reference Ionosphere 1995 Model

I used the UNB hourly TEC maps each consisting of 1,271 (31 by 41) gridded TEC values for the European region encompassing the 5 weeks' worth of GPS data for the data analysis. I computed hourly scaling factors at 1 degree by 1 degree spacing according to the modifications described in Section 4.2.7. This resulted in the computation of 1,054,930 scaling factors using the UNB search technique. The scaling factors for every other UT hour were then used subsequently to compute a scaling factor for the UT hour in between using a linear interpolation. Following that, the modified IRI-95 model was used to predict the TEC for this hour and for a particular geographic location. For verifying my results, I also evaluated the original version of IRI-95 for computing TEC at each grid point for the whole data set. The results of these investigations were published by Komjathy and Langley [1996e].

For illustrative purposes, I chose three stations from the 6 European stations used to create ionospheric maps to display the different ionospheric modelling techniques currently used and implemented at UNB. The three stations are Madrid, Brussels and Onsala,

encompassing three different geomagnetic latitude regions used for the European data processing. In Figure 5.15, I have plotted TEC predictions and estimates for the period of 15 to 22 October 1995 (GPS week 823) using 4 different ionospheric modelling techniques. These are the original IRI-95 predicted TEC, the updated IRI-95 using the GPS-derived TEC maps, the Parameterized Ionospheric Model (PIM) predictions [Daniell et al., 1995], and the GPS-derived TEC values. Also plotted are the 12-month-smoothed IG_{12} indices as well as the inferred IG_{12} indices using my computed scaling factor. In Figure 5.15, we can see that the global empirical ionospheric model IRI-95 and the physics-based numerical model PIM predict somewhat different shapes for the diurnal TEC variation.

None of the models could predict the effect of the geomagnetic disturbance of day 292 on the TEC variation. This is despite the fact that the PIM model uses daily values for both solar flux and geomagnetic data as input parameters as opposed to the IRI-95 models where only the 12-month-smoothed IG_{12} index and sunspot number R_{12} are used as input.

The GPS-derived TEC values and the updated IRI-95 predictions seem to agree well for the most part, indicating that under quiet geomagnetic conditions the updating technique seems to be successful. On day 292, when the geomagnetic disturbance started, the differences are much larger suggesting that the updating process was less successful. The larger variations in the inferred IG_{12} index during the geomagnetically disturbed days (on days 292 and 293) suggest that under disturbed ionospheric conditions, finding the

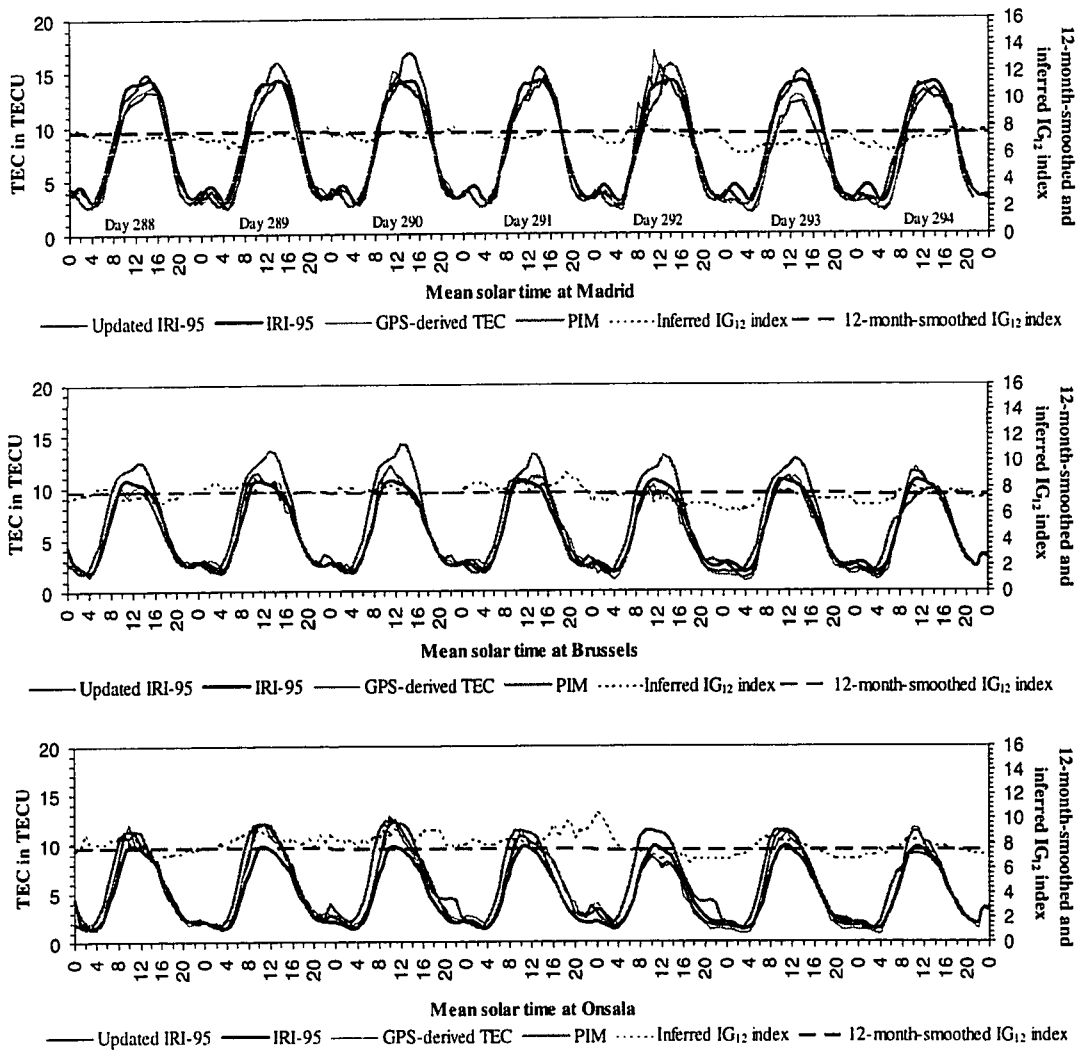


Figure 5.15: Illustration for different ionospheric modelling techniques currently used at UNB.

correct scaling factor may be more difficult. The inferred IG₁₂ index shows fluctuations during the week which seem to start in the north with station Onsala (on day 291) and subsequently move south to station Madrid (on day 292). This could be explained by the fact that the magnetic disturbance has its commencement phase for different geomagnetic latitudes at different times.

For high latitude stations such as Onsala, the PIM model seems to provide closer agreement with the GPS-derived TEC values compared to the IRI-95 model performance. The reason for this is that the PIM model includes a high latitude model for predicting electron densities above 51 degrees geomagnetic latitude [Daniell et al., 1995].

Since the TEC maps produced by the IGS analysis and processing centers may become official IGS products in the foreseeable future [Feltens, 1996; Schaer et al., 1996], the UNB technique could become an efficient method of providing ionospheric range error corrections for single frequency GPS receivers. The UNB technique could be applied to update IRI-95 on an hourly basis (depending on the availability of the TEC maps) and could use the updated CCIR/URSI coefficient sets for computing predictions between two updates. I used two-hourly updates to be able to compare the updated IRI-95 with the GPS-derived TEC in between. In Section 1.2.2, I provided a short description of other research centers' ionospheric estimation techniques whose products could also be potentially available for updating the IRI-95 model.

A more frequent update interval (e.g., one hour) would provide more precise scaling factors, therefore more reliable updated IRI-95 predictions. The reason I used two-hourly updates was to verify my results using GPS-derived TEC values already available for each hour. I modified the source code of the IRI-95 model so that it can be used for different post-processing software packages such as UNB's Differential Positioning Program (DIPOP) package to provide ionospheric range error corrections when only single frequency GPS observations are available. In a post-processing scenario, updating of IRI-

95 could be performed by using hour-long TEC observations before and after the epoch for which we require TEC predictions. This would be followed by e.g., a linear interpolation between the two hourly scaling factors.

Assuming that the GPS-derived TEC maps are free of error, I computed the r.m.s. differences between the updated IRI-95 predictions and the GPS-derived TEC maps as well as the original IRI-95 predictions and the GPS-derived TEC maps. For computing statistics, I used all 5 weeks worth of GPS data and the computed scaling factors. I computed hourly r.m.s. differences as well as daily and overall r.m.s. differences between the updated and non-updated IRI-95 with respect to the GPS-derived TEC values.

In Figure 5.16, we can see the hourly r.m.s. differences for the first week under investigation. The hourly r.m.s. differences have been derived using all 1,271 observations pertaining to each hourly map. From Figure 5.16, we can see that the updated IRI-95 model provides smaller r.m.s. differences than the original one in all cases. It is also interesting to note that on day 292, the geomagnetic disturbance resulted in the update to the IRI-95 model using the UNB technique being less successful. The rate of change of the TEC may have been so rapid that the algorithm was unable to compute a valid scaling factor that could be used for updating IRI-95. A more sophisticated approach than the linear interpolation procedure is needed when the ionosphere is disturbed. This argument seems to be supported also by the fact that during day-time hours, the updated IRI-95

seems to show larger r.m.s. differences than the night-time ones. This is due to the rapid changes in the TEC during day-time hours.

I also computed the daily r.m.s. differences for all 35 days' worth of GPS data. In Figure 5.17, I display these differences. The peak on day 292 represents the large r.m.s. difference caused by the geomagnetic disturbance that we can also see in Figure 5.16. There are 3 more peaks which are apparent in the time series. These could be due to day-to-day variations in the TEC which are not modelled well by global empirical models such as the IRI-95. Its coefficient set is based on the monthly median diurnal variation of the foF2 and M(3000)F2 parameters. After updating IRI-95, these peaks have been reduced indicating that the updating procedure was successfully completed. Figure 5.17 gives a clear indication that for all 35 days investigated, I achieved improvement in TEC predictions over the original IRI-95 model predictions.

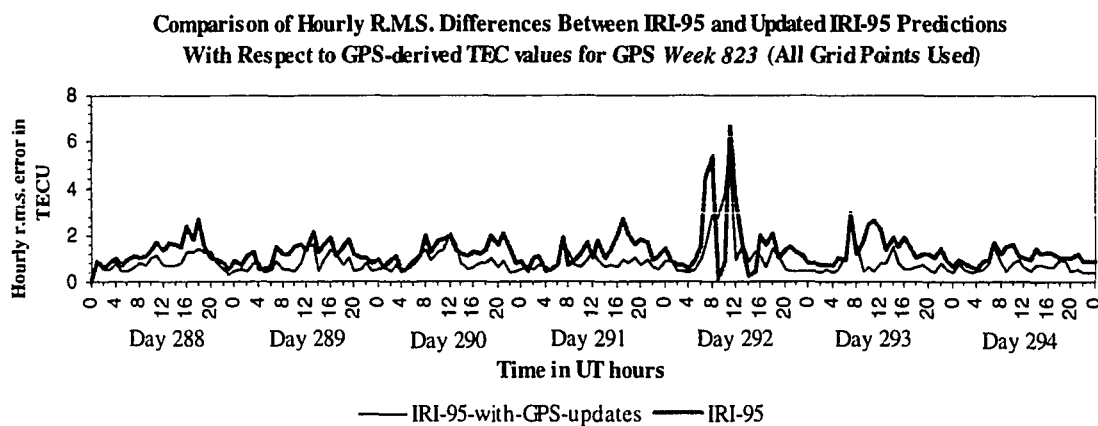


Figure 5.16: Hourly r.m.s. statistics to support the IRI-95 update procedure.

Comparison of Daily R.M.S. Differences Between IRI-95 and Updated IRI-95 Predictions With Respect to GPS-derived TEC values for GPS Weeks 823 to 827 (All Grid Points Used)

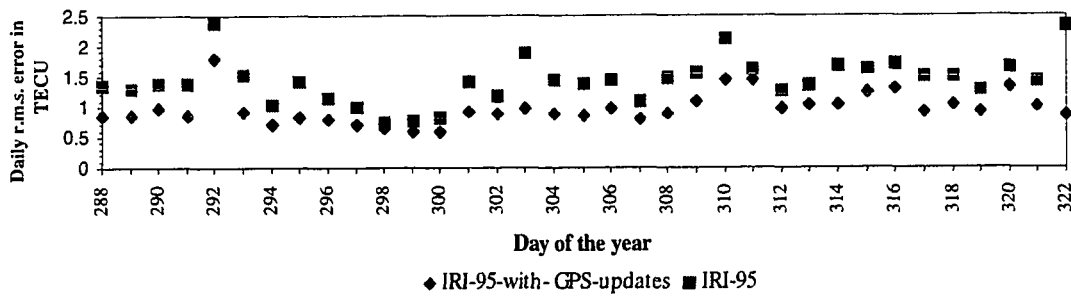


Figure 5.17: Daily r.m.s. statistics to support the IRI-95 update procedure.

Table 5.4: Summary of the weekly statistics to support the IRI-95 update procedure.

GPS week	R.m.s. of differences between original IRI-95 predictions and GPS-derived TEC values in units of TECU	R.m.s. of differences between updated IRI-95 predictions and GPS-derived TEC values in units of TECU	Improvement in %
823	1.5	1.0	31.4
824	1.1	0.7	32.0
825	1.4	0.9	37.4
826	1.6	1.2	26.1
827	1.6	1.1	35.5
Average	1.5	1.0	32.5

I also computed overall statistics. It was found that after updating IRI-95 using the GPS-derived TEC values, r.m.s. differences were reduced significantly as opposed to not updating it (i.e., using the original IRI-95). The weekly and overall statistics have been summarized in Table 5.4. The summary of the weekly statistics shows that the r.m.s. differences between the original IRI-95 and the GPS-derived TEC are at the 1.5 TECU level compared to the differences between the updated IRI-95 and GPS-derived TEC which are at the 1 TECU level. The weekly improvements range from 26 to 37 percent with an overall average of 32.5 percent.

After extensive testing, and making IRI-95 more efficient to run, it was found that it takes about 0.03 seconds of CPU time to compute TEC or ionospheric range error corrections for one epoch at any geographic location using the modified version of the IRI-95 model with or without the GPS updates. I used a Sun Microsystems 85 MHz MicroSPARC II processor for all data processing.

Table 5.5: Summary of CPU times concerning the IRI-95 update procedure.

GPS week	CPU time	CPU time in seconds	Number of scaling factors multiplied by two	Seconds/run
823	3h 28m 12.4s	12,492.4	421,972	0.0296
824	3h 30m 49.7s	12,649.7	421,972	0.0300
825	3h 30m 43.1s	12,643.1	421,972	0.0300
826	3h 30m 24.2s	12,624.3	421,972	0.0299
827	3h 30m 35.0s	12,635.0	421,972	0.0299
Sum	17h 30m 44.5s	63,044.5	2,109,860	0.0299

In Table 5.5, the CPU time and the number of runs are indicated for each GPS week processed. The values in the table include running the model with the pre-computed scaling factors as well as without the scaling factors for each grid node under investigation encompassing all 5 weeks' worth of GPS data. In Table 5.5, note that the number of scaling factors is the same for each GPS week indicating that this number corresponds to twice the number of TEC grid points used for the data analysis. Over two million runs were completed to compute the hourly, daily and overall statistics.

I also measured the time it takes to compute the scaling factors for the hourly TEC maps. I counted the number of runs needed to arrive at the 0.5 TECU level difference

between the UNB GPS-derived TEC values and the IRI-95 predictions. In Figure 5.18, the average number of IRI-95 runs for a grid point are plotted against UT hours for GPS week 823. On the right-hand y axis, the required time to compute the scaling factors for an hourly map is displayed. It is clear that it takes more IRI-95 runs to compute the scaling factors for a daytime observation since the ionosphere is more variable during the daytime. For computing scaling factors, I did not start the iteration process using scaling factors from previous hours which would have made it less time consuming (since they are correlated) to compute the correct scaling factor for the subsequent hour.

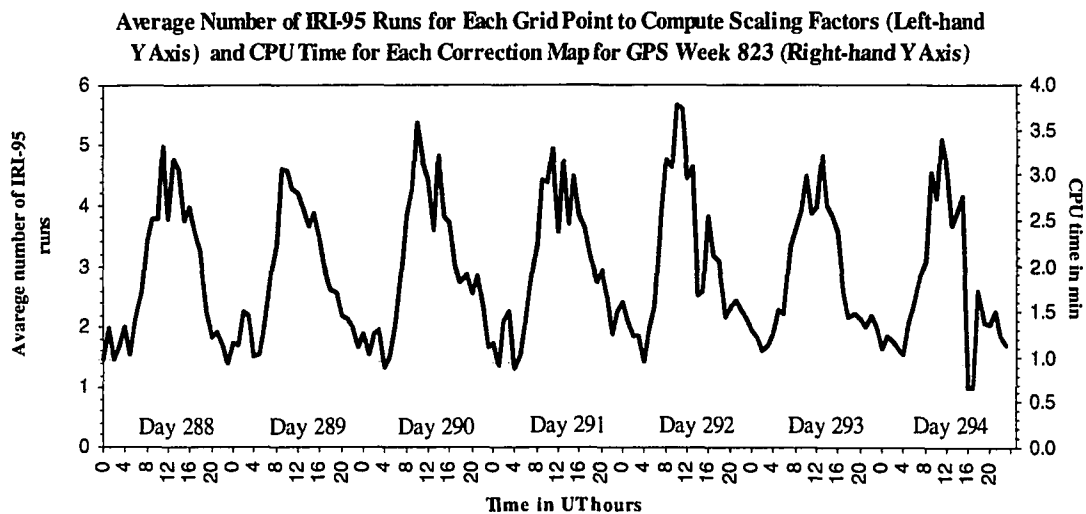


Figure 5.18: Number of IRI-95 runs required to arrive at the proper scaling factor.

The reason for this approach is that the purpose of using this technique is to make use of the availability of the hourly TEC maps only before and after an epoch (without having to process other maps). This can be an advantage for a single frequency user who wants to update the IRI-95 model in order to improve IRI-95-derived TEC predictions which can subsequently be applied to correct the single frequency GPS observations. Also, a user is

not required to compute scaling factors for each grid point but only those gridpoints that are of interest in the vicinity of the single frequency user's geographic location. In this study, I used all grid nodes for the sake of completeness and for the development of the statistics.

Another potential application of the UNB technique could be to provide real-time ionospheric range error corrections for single frequency GPS users. The UNB technique generates TEC maps using a Kalman filter type estimation. Therefore, the technique could be used to process dual frequency GPS data as they become available in near real-time. The frequency of producing TEC maps can easily be increased from 1 map per hour. Highly varying ionospheric and geomagnetic conditions may require more frequent TEC maps. Subsequently, the UNB TEC maps (as the output of the Kalman filter type estimation) could be used to update the IRI-95 model coefficient set as described. In a real-time scenario, the updating could be performed by using the latest available scaling factor from the previous hour. Since my modified version of IRI-95 runs quite efficiently, it may be feasible to compute ionospheric range error corrections for each satellite at every observation epoch and geographic location. These ionospheric range error corrections could then be forwarded to the user in real-time.

5.3.1 Conclusions of the IRI-95 Modifications

In the research reported in this section, I investigated the use of TEC estimates from dual frequency GPS observations provided by 6 of the IGS stations to update the latest IRI model, IRI-95. I used a 5 week long GPS data set from the European region to compute scaling factors for IRI-95's CCIR/URSI coefficient sets and to provide evidence that the update procedure has been successful.

The overall statistics revealed that after updating the IRI-95 model, the r.m.s. of the differences between the updated IRI-95 model and the GPS-derived TEC, as well as the original IRI-95 predictions and the GPS-derived TEC values, decreased by an overall 32.5 percent. These results are likely only valid for a mid-latitude region under low solar activity conditions. After extensive testing and modifications of the IRI-95 model, I found that, using a modern workstation, the UNB version takes about 0.03 seconds on average to compute TEC or ionospheric range error corrections for each epoch at any location.

The UNB technique could be used as an alternative to the Broadcast model to provide ionospheric range error corrections for single frequency users. The relatively short execution time of the modified version of IRI-95 makes it possible to use this technique both for real-time and post-processing purposes. The backbone of this technique is the TEC maps that could become available either from use of the UNB Kalman filter type estimation or from some other source such as ionospheric maps which may be produced by the IGS in the near future.

5.4 Comparison of UNB's Regional TEC Maps with Those of Other Research Centers

The UNB regional TEC maps were delivered to IGS for comparison purposes. An independent comparison of the quality of the maps has been performed by Feltens et al. [1996] as well as Jakowski and Sardon [1996]. In this section, I will summarize their findings.

A comparison of the regional TEC maps from the Center for Orbit Determination in Europe (CODE) and UNB performed by Feltens et al. [1996] revealed that a -1.5 TECU level bias can be seen between the UNB and CODE results. The TEC values in the CODE maps seem to be consistently smaller than those in the UNB maps. The standard deviation of the daily mean differences between the CODE and UNB results seem to be at the 1 to 3 TECU level. The results were based on the comparison of the regional TEC maps for three consecutive weeks.

The comparison between the DLR and UNB results shows no significant bias between the TEC maps produced by the two processing centers. The daily TEC differences between DLR and UNB seem to vary between 1 and 3 TECU. The standard deviation of the daily differences were also found to be between 1 and 3 TECU.

The comparison between the ESOC and UNB results can be subdivided into three parts: the comparison with the ESOC spherical harmonics approach, the local polynomial

approach, and the Gauss-exponential (GE) functions approach [Feltens et al., 1996]. In the case of the spherical harmonics, the agreement between ESOC and UNB over the European region is good. A mean bias of -1 TECU can be detected, that is the values in the ESOC maps seem to be below those in the UNB maps. The ESOC local polynomial comparison with UNB shows a very close agreement with a 0 to 1 TECU level daily bias and a 0 to 1 TECU level standard deviation. The comparison between the GE-functions and the UNB TEC maps shows about 1 to 3 TECU as a mean bias and 1 TECU standard deviation about the mean.

The comparisons of the satellite and receiver differential delays between different processing centers indicate an offset of the DLR series of about 1 nanosecond with respect to the ESOC results. On the other hand, the UNB satellite and receiver differential delays seem to be very close to the ESOC results. The possible reason for that is the fact the different processing centers use different values for the ionospheric shell height.

The comparison performed by Jakowski and Sardon [1996] revealed that for the first 12 days of the 3 consecutive GPS weeks under investigation (for the description of the IGS campaign see Section 5.1), the DLR and UNB day-time TEC results agree very well but for the rest of the data set the maximum daily differences were between 2 to 4 TECU.

The differences in the results between the different processing centers are due to the fact that the different processing centers use different estimation techniques, different

values for the ionospheric shell height and different mapping functions. The UNB sensitivity analysis has focused on the issues of the ionospheric shell height and the mapping functions. The issue of the mapping function will be addressed in Section 5.5. I found that a 0.5 TECU level error is introduced for every 50 km error in the shell height. This seems to be consistent with the TEC differences described above. However, it is difficult to pinpoint which of the reasons (estimation technique, shell height, or mapping functions) causes the differences in results between the processing centers. It is most likely a combination of all three. Also, in order to determine the accuracy of the UNB TEC products, one has to use an independent data source other than GPS provided TEC data. One of these data sources is derived from TOPEX/Poseidon data and this technique was used to estimate the accuracy of the UNB global TEC maps. It is discussed in Chapter 6.

5.5 Investigation of Different Ionospheric Mapping Functions

During the development of my algorithm, I discovered that the ionospheric mapping functions can have a significant impact on the TEC and satellite differential delays estimates. Therefore, I designed an experiment to investigate the ionospheric mapping functions that are currently available to the ionospheric community. The theoretical considerations and the algorithm have already been elaborated in Section 4.2.4. In this section, I will describe the actual experiment and its results.

I collected 24 hours of GPS data starting at 12:00 local time on June 24th, 1996 in Fredericton, New Brunswick, Canada, using two Ashtech Z-12 dual frequency GPS receivers in a configuration where both receivers were fed from the same Ashtech antenna (zero baseline experiment).

As a first step, I formed the single difference (between receiver) ionospheric observations according to eqn. (4.16). In the scope of my research, the particular advantage of performing the zero baseline experiment is that after forming the between-receiver single difference pseudorange ionospheric observables, all error sources cancel except for the combination of the two receivers' noises and the differences between the two receivers' differential delays (for more information see Section 4.2.4). In other words, error sources such as receiver and satellite clock errors, tropospheric errors, satellite-receiver differential delays can be eliminated. Multipath error is also eliminated using the zero-baseline configuration since both receivers are receiving the same signal affected by multipath. The resulting time series for the test is displayed in Figure 5.19. The mean of the measured differential delay differences was found to be 0.73 ns with a standard deviation of 0.42 ns. The 0.73 ns level bias corresponds to the "true" between-receiver differential delay (BRDD-true). The combined receiver noise can be considered zero mean noise, therefore, the standard deviation about the mean of the BRDD-true corresponds to the combination of the two receivers' noise on the P1 and P2 observations. The combined noise (0.42 ns) is equivalent to about 19 cm on L1 (1 ns differential code delay corresponds to 0.464 m range error on L1). Unfortunately, we cannot use the more

precise raw carrier phase ionospheric observables to plot similar time series and compute the BRDD-true. The reason is that we cannot distinguish between receiver differential delays and the carrier phase ambiguity (see eqn. (4.9)) as they are usually lumped together and estimated using the pseudorange ionospheric observables using the technique of phase-levelling (see Section 4.2.1).

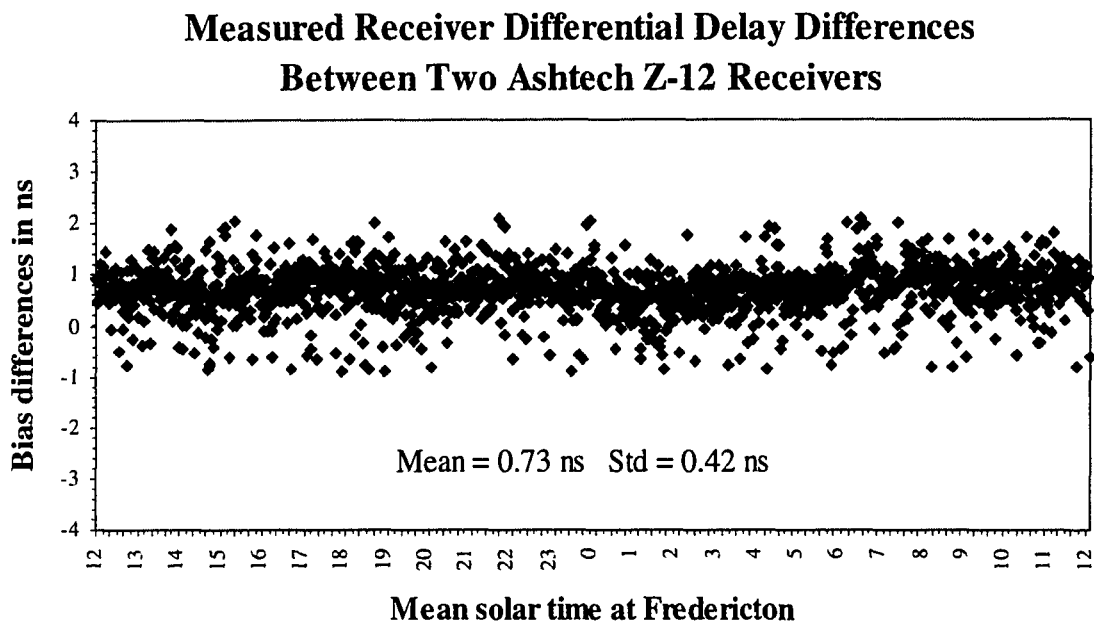


Figure 5.19: Measured between-receiver differential delays during the zero baseline experiment.

As a second step, I used the UNB software to process the data from both receivers to estimate ionospheric parameters. The algorithm was described in Section 4.2.2. The diurnal variation of the TEC is displayed in Figure 5.20. We can clearly see the difference between the day-time TEC with a maximum of about 12 TECU and the night-time TEC with a minimum of about 3 TECU. The estimated ionospheric parameters include three

stochastic parameters and satellite differential delays as well as receiver differential delay difference between the two Ashtech Z-12 receivers. In Figure 5.20, I also plotted the estimated standard deviation of the individual parameter values as well as the standard deviation for the TEC. The between-receiver differential delay (BRDD-true) had been determined previously by forming the single differences of the phase-levelled ionospheric observables between the two receivers with respect to a particular satellite.

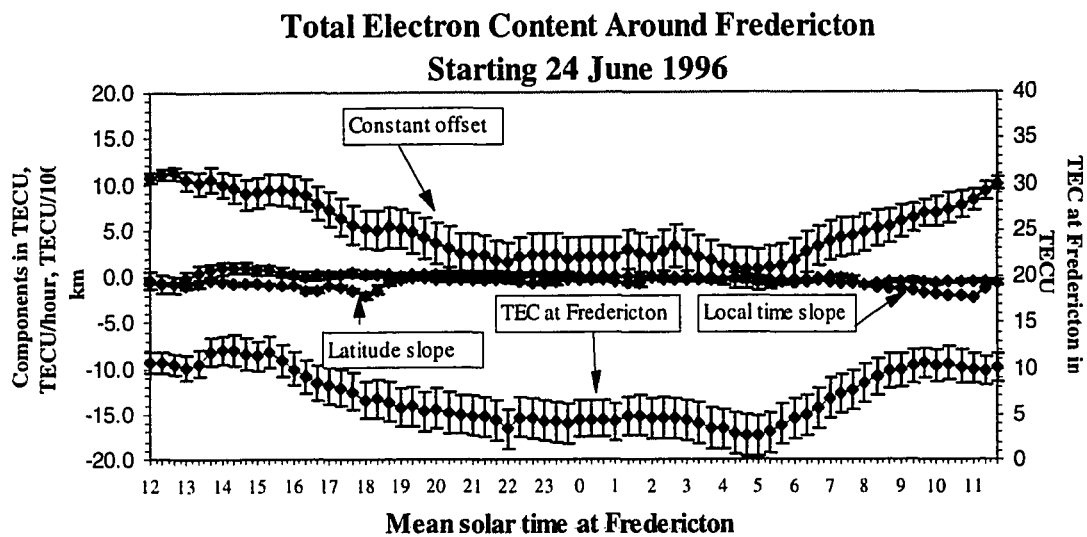


Figure 5.20: Zero-baseline experiment at the University of New Brunswick, Fredericton, Canada.

To compare the measured true between-receiver ionospheric differential delays (BRDD-true) with the estimated ones (BRDD-est.), I used different elevation cutoff angles and ionospheric mapping functions to find out which mapping function works best under the conditions of the experiment. For processing the data, I used three different elevation cutoff angles: 15, 20, and 25 degrees. The ionospheric mapping functions were

as follows: Clynych, Broadcast, and the geometric mapping function with 400 km shell height, and the geometric mapping function with varying ionospheric shell height.

In Table 5.6, we can clearly see that the value for the BRDD-true lies somewhere between the values estimated by the UNB technique using different ionospheric mapping functions along with various elevation cutoff angles. My aim was to determine which ionospheric mapping function I should use for ionospheric modelling keeping in mind that the lower the elevation cutoff angle I use, the better chance we have to more precisely separate the total electron content from the hardware related bias. However, with a lower elevation cutoff angle we may potentially run to into problems generating the ionospheric observable since the data is noisier with satellites at lower elevation cutoff angles.

Table 5.6: Investigation of different ionospheric mapping functions using various elevation cutoff angles.

Mapping functions	Elevation Cutoff Angles in degrees								
	15			20			25		
	BRDD-est. in ns	BRDD-est. minus BRDD-true in ns	Est. sigma in ns	BRDD-est. in ns	BRDD-est. minus BRDD-true in ns	Est. sigma in ns	BRDD-est. in ns	BRDD-est. minus BRDD-true in ns	Est. sigma in ns
Clynych	0.83	0.10	0.25	0.89	0.16	0.40	0.90	0.17	0.45
Broadcast	0.85	0.12	0.28	0.92	0.19	0.45	0.81	0.08	0.42
Geometric with 400 km shell height	0.63	-0.10	0.26	0.58	-0.15	0.48	0.55	-0.18	0.53
Geometric with varying ionospheric shell height	0.64	-0.09	0.20	0.64	-0.09	0.52	0.61	-0.12	0.58

BRDD = Between-Receiver Differential Delay Estimate

Assuming that the mean measured value for BRDD is correct (= 0.73 ns), we can see that the results using the Clynych and the Broadcast mapping functions overestimate BRDD regardless of what elevation cutoff angle we use. This might be due to the fact that during the derivation of the Broadcast mapping function, the author used 350 km for the

ionospheric shell height [Klobuchar, 1975]. In the case of the Clynch mapping function, a homogeneous shell between 200 and 600 km was applied using electron density profiles from the Bent model [Newby, 1992]. In Table 5.6, I have displayed the differences between the UNB estimated BRDD and the true BRDD. Also displayed are the standard deviations of the estimated BRDD (formal error). We can see that the differences in all cases are smaller than the worst case estimated standard deviations for BRDD which are 0.8, 1.5 and 1.6 TECU for elevation cutoff angles 15, 20, and 25 degrees respectively (1 ns differential delay corresponds to 2.85 TECU). These numbers for the estimated standard deviation for BRDD-est. seem to be realistic. However, since the differences between the true and estimated values are smaller than the estimated standard deviation for BRDD, it makes the comparison statistically not significant.

The geometric mapping function with 400 km shell height resulted in underestimation of BRDD. It seems that the real mean ionospheric shell height on days June 24th and 25th, 1996, in the vicinity of Fredericton was between 350 and 400 km. This seems to be supported by the fact that the geometric mapping function with varying ionospheric shell height resulted in the marginally good agreement with the true value for 15 and 20 degrees elevation cutoff angles. For 25 degrees elevation cutoff angle, the Broadcast model seems to be in marginally better agreement with the true value. This is somewhat surprising since the Broadcast model only assumes a 350 km mean ionospheric shell height. The results for the 15 and 20 degree elevation cutoff angles appear to be supported by my findings in Section 5.2 where I found that the lower the ionospheric shell height is set from the “true”

value, the higher the estimated differential delays will be. These results were also previously published [Komjathy and Langley, 1996a; 1996b].

By looking at the BRDD estimates, it seems that the lower elevation cutoff angles provided better agreement with the true value for a particular mapping function. This might be due to the fact that at lower elevation angles the separation between the TEC and hardware biases can be performed more successfully. This is also supported by the fact that the estimated standard deviation of BRDD becomes larger at higher elevation cutoff angles.

5.5.1 Conclusions of the Ionospheric Mapping Function Investigation

Based on a limited data set, I can conclude that the standard geometric mapping function performed marginally better than the other available mapping functions investigated except for an elevation cutoff angle of 25 degrees. The comparison of the standard geometric mapping function (400 km shell height) with varying shell height reveals that the UNB varying shell height concept with the standard geometric mapping function for elevation cutoff angles 15 and 20 degrees appears to perform marginally better than the conventional geometric mapping function with fixed shell height. However, the agreement between the estimated and true BRDD appears to be only marginal since the estimated standard deviation of BRDD is larger than the differences between the true and estimated BRDD. More sophisticated estimation techniques for producing the levelled ionospheric

observable and improvements of the estimation strategy might give the potential to lower the formal error for BRDD and produce statistically significant results.

One has to bear in mind that the data set I used for this experiment was collected in a mid-latitude region during low solar activity times where we typically do not expect large gradients of the TEC. At higher solar activity times, and for middle, low or high latitude regions, I would expect even better performance from the standard geometric mapping function with varying ionospheric shell height due to the fact that the inappropriately set ionospheric shell height would correspond to larger errors. This would be particularly true for higher solar activity conditions.

In this chapter, I described my results concerning the UNB regional ionospheric modelling technique, the IRI-95 modifications and a study on ionospheric mapping functions. Based on these results I decided to make a further step and extend the technique to global ionospheric TEC mapping. The results of this investigation will be explained in the next chapter.

CHAPTER 6
GLOBAL IONOSPHERIC MODELLING: DATA PROCESSING AND
ANALYSIS OF RESULTS

After developing the tools and learning about regional ionospheric modelling based on the IGS campaign described in Chapter 5, I decided to utilize my expertise and investigate the temporal and spatial variation of the global ionosphere. I have made enhancements to the UNB software to be able to independently produce global TEC maps (5 degree by 5 degree spacing) on an hourly basis. Then I ingested the UNB global TEC maps into a modified version of the International Reference Ionosphere (IRI-95) model to update its CCIR/URSI coefficient sets on an hourly basis as described in Section 4.2.7. I used the updated IRI-95 coefficients for improved IRI-95 predictions by the modified IRI-95 model as a sophisticated interpolator between two GPS-derived hourly TEC updates. The updating procedure, i.e., the computation of scaling parameter, can be performed either for every grid node at each hour separately as it is the case with the UNB regional TEC maps or it can be performed using the 4 TEC grid values closest to the geographic location for which we require precise TEC predictions. The latter method was used for the UNB global TEC maps used in the TOPEX/Poseidon comparisons since we only needed precise TEC predictions for discrete geographic locations specified by the location of the satellite altimeter.

In this chapter, I will first describe single frequency satellite radar altimetry as a potential application that requires a global ionospheric modelling technique such as UNB's to minimize the ionospheric effect on the single frequency measurements. After that, I will introduce a GPS campaign in which UNB participated to demonstrate the capabilities to provide ionospheric delay corrections for single frequency radar altimetry. This will be followed by a discussion of the data processing and analysis of results.

6.1 A Potential Application: Single Frequency Radar Altimetry

Current and planned satellite missions such as the European Remote Sensing Satellites (ERS-1, ERS-2), the upcoming Geosat Follow-on (GFO), and ENVISAT missions are or will be equipped with single frequency radar altimeters to obtain ocean height measurements for study of ocean circulation and its variability. Unlike with dual frequency altimeters such as the primary one onboard the TOPEX/Poseidon (T/P) satellite, the path delay due to the ionosphere cannot directly be removed from the altimeter range measurements. For a radar altimeter operating at a frequency of 13.6 GHz such as the one on board GFO, this path delay can be as much as 20 cm at solar maximum or during solar storms. Therefore, to be able to utilize the ocean height measurements obtained with single frequency radar altimeters, we will have to use alternative means to remove the propagation delay imposed by the ionosphere [Born and Katzberg, 1996].

The Geodetic Research Laboratory of the University of New Brunswick participated in a workshop convened by the University of Colorado - Colorado Center for Astrodynamics Research (CCAR) and NASA to characterize the impact of ionospheric delay on the ocean science conducted with single frequency radar altimeter data. The purpose of the workshop was to find out what state-of-the-art techniques are currently available for mitigating such effects [Born and Katzberg, 1996].

TEC data derived from the T/P dual frequency altimeter measurements were used to provide ground-truth against which I compared GPS-derived ionospheric delay corrections based on the UNB technique. Two three-day time series of T/P-derived TEC data obtained in 1993 and 1995 was made available by the workshop organizers for comparison purposes. Global Ionosphere Maps (GIMs) generated by the NASA Jet Propulsion Laboratory (JPL) from GPS ground receivers data using a similar technique to UNB's were also provided for scientific investigation for the same time period.

The JPL GIMs were obtained from station-to-satellite line-of-sight (LOS) carrier phase data mapped to the vertical at the point of intersection of the LOS with an ionosphere shell model at 350 km altitude. The TEC obtained at 642 globally distributed points were then interpolated to a global grid with 1 degree by 1 degree spacing. The 642-point files from which the 1 degree by 1 degree grid files were obtained were also made available [Yuan et al., 1996]. The algorithm for generation of the GIMs has been described by Wilson and Mannucci [1993, 1994].

There were several different techniques demonstrated by the participants at the workshop that could directly or potentially be used to provide ionospheric delay corrections. These techniques can use, e.g., the state-of-the-art global empirical and physics-based ionospheric models. One such technique was demonstrated by Bilitza [1996b] using the International Reference Ionosphere 1995. The IRI-90 and IRI-95 model performances were compared against T/P data by Urban et al. [1996]. Daniell and Anderson [1996] showed that the Parameterized Ionospheric Model (PIM) itself or PIM's real-time version updated by GPS-inferred TEC called PRISM could also be a potential candidate for providing the ionospheric corrections [Gold et al., 1996]. The ionospheric occultation technique (GPS/Met) could potentially be used, however, this technique is limited to the spatial and temporal distribution of the occultation points and its use might not be practical for this application at this stage [Schreiner and Exner, 1996]. Picot and Escudier [1996] suggest DORIS-derived TEC data to provide ionospheric corrections. Computerized Ionospheric Tomography (CIT) combined with Transit-derived TEC data was demonstrated by Coker et al. [1996] to provide 1 TECU level agreement with T/P-derived TEC data.

The set of requirements determined by NASA limits the error boundaries for the ionospheric delay modelling for single frequency altimetry. Since we are expecting a 2 mm/year mean sea level rise over the coming years, the rate of change of the ionospheric errors should not be more than 1 mm/year (0.5 TECU/year). Errors in measurements of

interannual variations in the equatorial sea level should not be larger than 1 cm (5 TECU on 13.6 GHz) to enable us to study important climate change such as El Nino cycles. There are further stringent requirements concerning general circulation as well as long waves and mesoscale variations of the oceans [Born and Katzberg, 1996].

6.2 The UNB Ionospheric Modelling Technique for Correcting Single Frequency Altimeter Data

It was demonstrated at the workshop that UNB can independently provide global ionospheric maps. The UNB global ionospheric mapping technique is very similar to the UNB regional ionospheric mapping technique that has been described in Chapter 5. However, I had to make enhancements to the regional mapping technique to accommodate the large total number of stochastic parameters and satellite-receiver differential delays. The estimated stochastic parameters describe the temporal and spatial variation of the TEC using a spatial linear approximation of the TEC computed for each globally distributed IGS station. The UNB global ionospheric modelling algorithm also uses a varying ionospheric shell height concept separately computed for each IGS station worldwide taking into account the geographic and temporal variation of the shell height based on the method discussed in Section 4.2.3. The varying ionospheric shell height for each globally distributed IGS station was used as an input parameter when mapping the line-of-sight TEC into the vertical using a commonly adopted geometric mapping function as described in Section 4.2.4. The UNB-derived hourly global 5 degree by 5 degree TEC

maps are constructed at any grid node by using the three stochastic parameters defining a local ionospheric model for each IGS station. The TEC estimates for any grid node is defined by using the models of the four nearby IGS stations weighting them by the inverse distance squared as discussed in Section 4.2.5.

Updating the IRI-95 coefficient sets was performed in a manner similar to that described in Section 4.2.7 taking into account that the inferred IG index is the function of geographic latitude, longitude and Universal Time. This was achieved somewhat differently from what was earlier described in the case of the regional ionospheric mapping technique. Instead of computing an inferred IG index for every grid node of the regional TEC map, I only computed an inferred IG index for the four grid nodes surrounding the geographic location of the T/P TEC measurement for which I need GPS-derived TEC data. The reason for this simplification was that I had T/P data only for a distinct set of points described by the T/P trajectory so we do not need to compute inferred IG index for every grid node of the global GPS-derived TEC map. To find the correct IG index, I used the empirical plasmaspheric electron content model described in Section 4.2.6 which takes into account the electron content between an altitude of 1000 km and the GPS satellites' altitude.

I produced hourly snapshots of the global ionosphere using GPS data only. As part of the data analysis, I have also compared the updated IRI-95 predictions using the UNB global TEC maps, the original IRI-95 predictions, and GIMs against 6 days' worth of T/P-

derived TEC data. The analysis of these results will be explained in Section 6.3. The T/P-derived TEC data was provided as 60-second smoothed TEC measurements. To find the TEC values from the 5 degree by 5 degree spaced global TEC maps at the geographic locations of the T/P measurements, I used the weighting function approach for modelling irregular surfaces (see Section 4.2.5). The comparison between the T/P-derived TEC data and the updated IRI-95 data requires taking into account the fact that the orbital altitude of the T/P spacecraft is about 1340 km and hence I had to use the adopted plasmaspheric electron content model (see Section 4.2.6) to account for the ionospheric region between 1000 km and 1340 km:

$$\text{TEC}_{\text{TOPEX}} = \text{TEC}_{\text{IRI-95--updated}} + \text{TEC}_{\text{plasmaspheric}_{1000-1340\text{km}}} \quad (6.1)$$

6.3 Data Processing and Analysis of Results

For the ionospheric workshop, I processed GPS data from a global network of 33 IGS stations (Figure 6.1) spanning 3 consecutive days in 1993 (March 13th to 15th, medium solar activity period) and data from 74 IGS stations (Figure 6.2) spanning 3 consecutive days in 1995 (April 6th to 8th, low solar activity period). An additional day's worth of global GPS data (March 26, 1993) was also processed to help validate the UNB global TEC maps using Faraday rotation data. A total of 354 station-days of GPS data were processed for the data analysis described in this chapter. The raw GPS data was provided by the Scripps Orbit and Permanent Array Center [SOPAC, 1996]. The list of stations, their SOPAC site code names, used in Figures 6.1 and 6.2, and station geographic

locations can be found in Table 6.1. Preliminary results of the data processing were presented by Komjathy et al. [1996a].

IGS Stations Used for Data Processing Between 13 and 15 March 1993

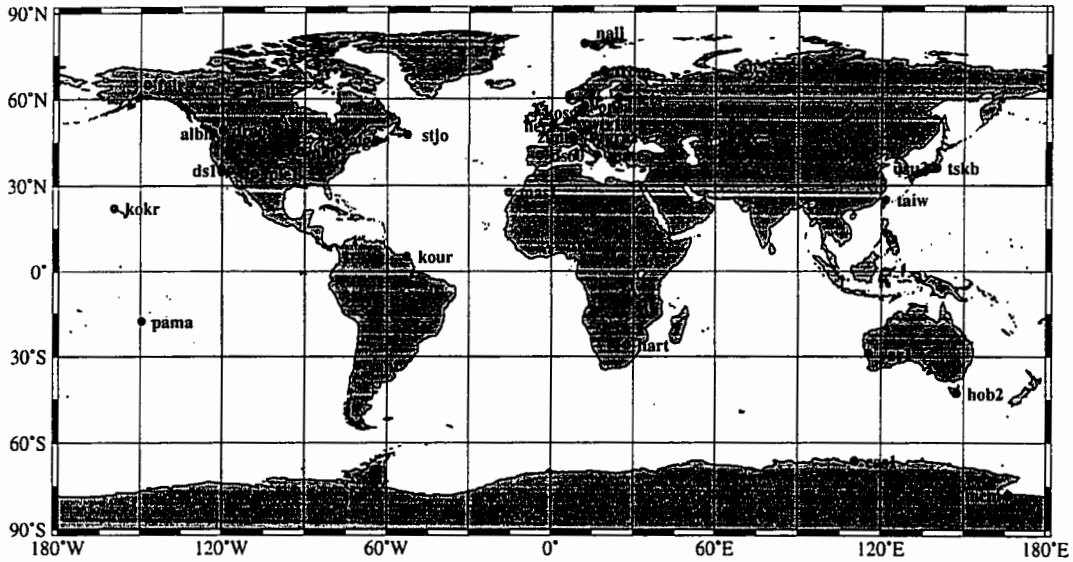


Figure 6.1: IGS stations used for the 1993 global ionospheric data processing.

IGS Stations Used For Data Processing Between 6 and 8 April 1995

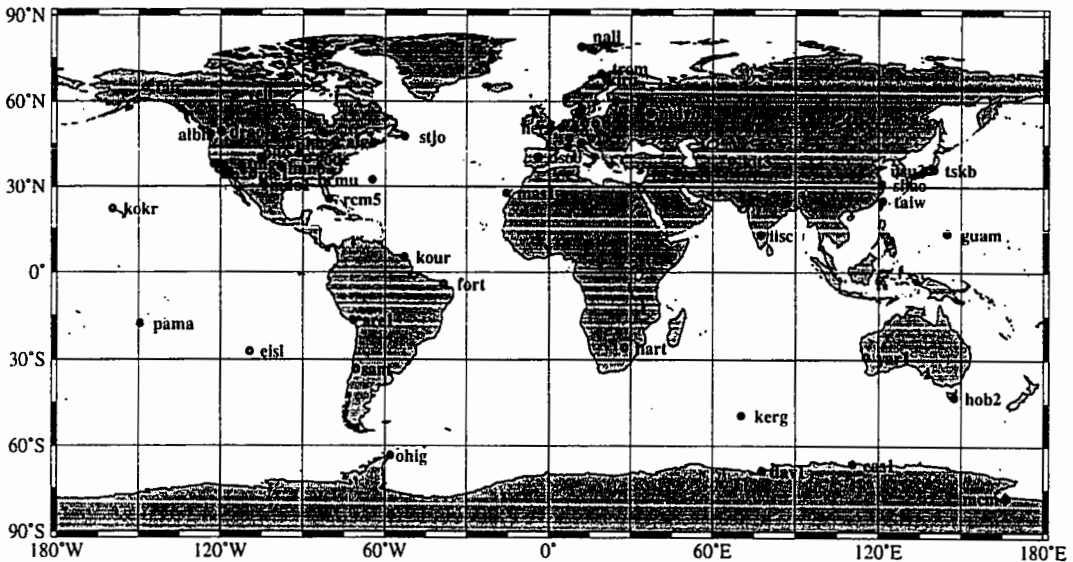


Figure 6.2: IGS stations used for the 1995 global ionospheric data processing.

Table 6.1: List of GPS stations used for the global ionospheric data processing.

Abbreviation	Station Name	Country	Long. (E) in degrees	Lat. (N) in degrees	1993	1995
albh	Victoria, BC	Canada	-123.5	48.4	*	*
algo	Algonquin Park, ON	Canada	-78.1	46.0	*	*
aoal	Westlake, CA	USA	-118.8	34.2		*
are1	Arequipa	Peru	-71.5	-16.5		*
blyt	Blythe, CA	USA	-114.7	33.6		*
bor1	Borowiec	Poland	17.1	52.3		*
bran	Burbank, CA	USA	-61.7	34.2		*
brib	Briones, CA	USA	-122.2	37.9		*
brmu	Bermuda	Bermuda Islands	-64.7	32.4		*
brus	Brussels	Belgium	4.4	50.8		*
carr	Parkfield, CA	USA	-120.4	35.9		*
cas1	Casey	Antarctica	110.5	-66.3	*	*
casa	Mammoth Lakes, CA	USA	-118.9	37.6		*
chil	Chilao, CA	USA	-118.0	34.3		*
chtp	Chatsworth, CA	USA	-118.4	34.2		*
clar	Claremont, CA	USA	-117.7	34.1		*
cmbb	Columbia, CA	USA	-120.4	38.0		*
crfp	Yucaipa, CA	USA	-117.1	34.0		*
dav1	Davis	Antarctica	78.0	-68.6		*
denc	Denver, CO	USA	-104.9	39.8		*
drao	Penticton, BC	Canada	-119.6	49.3	*	*
ds10	Goldstone, CA	USA	-116.9	35.4	*	*
ds60	Robledo	Spain	-4.2	40.4	*	*
eisl	Easter Island	Chile	-109.4	-27.1		*
fair	Fairbanks, AK	USA	-147.5	65.0	*	*
fort	Fortaleza	Brazil	-38.4	-3.9		*
gode	Greenbelt, MD	USA	-88.4	39.8		*
gras	Caussols	France	6.9	43.8		*
graz	Graz	Austria	15.5	47.1	*	*
guam	Dededo	Guam	144.9	13.6		*
hart	Pretoria	South Africa	27.7	-25.9	*	*
hers	Hailsham	United Kingdom	0.3	50.9	*	*
hob2	Hobart, Tasmania	Australia	147.4	-42.8	*	*
iisc	Bangalore	India	77.6	13.0		*
joze	Jozefoslaw	Poland	21.0	52.1		*
kerf	Port aux Francais	Kerguelen Islands	70.3	-49.4		*
kiru	Kiruna	Sweden	21.0	67.9		*
kit3	Kitab	Uzbekistan	66.9	39.1		*
kokr	Kokee Park, HI	USA	-159.7	22.1	*	*
kosg	Kootwijk	The Netherlands	5.8	52.2	*	*
kour	Kourou	French Guiana	-52.8	5.3	*	*
lama	Olsztyn	Poland	20.7	53.9		*
lmno	Lamont, OK	USA	-97.5	36.7		*
mas1	Maspalomas	Spain	-15.6	27.8	*	*
mate	Matera	Italy	16.7	40.6	*	*
mcm4	Ross Island	Antarctica	166.7	-77.8	*	*
mdo1	Fort Davis, TX	USA	-104.0	30.7		*
mdvo	Mendeleevo	Russia	37.2	56.0		*
mets	Kirkkonummi	Finland	24.4	60.2	*	*

nall	Ny Alesund	Norway	11.9	78.9	*	*
nlib	North Liberty, IA	USA	-91.6	41.8	*	*
ohig	O'Higgins	Antarctica	-57.9	-63.3		*
onsa	Onsala	Sweden	11.9	57.4	*	*
pama	Pamatai	Tahiti	-149.6	-17.6	*	*
piel	Pie Town, NM	USA	-108.1	34.3	*	*
pltc	Platteville, CO	USA	-104.7	40.2		*
pots	Potsdam	Germany	13.1	52.4		*
rcm5	Perrine, FL	USA	-80.4	25.6		*
sant	Santiago	Chile	-70.7	-33.2	*	*
shao	Sheshan	China	121.2	31.1		*
stjo	St. John's, NF	Canada	-52.7	47.6	*	*
taiw	Taipei	Taiwan	121.5	25.0	*	*
tibb	Tiburon, CA	USA	-122.4	37.9		*
tmgo	Table Mt., CO	USA	-105.2	40.1		*
trom	Tromsøe	Norway	18.9	69.7	*	*
tskb	Tsukuba	Japan	140.1	36.1	*	*
upad	Padova	Italy	11.9	45.4		*
usu3	Usuda	Japan	138.4	36.1	*	*
vill	Villafranca	Spain	-4.0	40.4		*
wtz1	Wetzell	Germany	12.9	49.1	*	*
yar1	Yaragadee	Australia	115.3	-29.0	*	*
yell	Yellowknife, NT	Canada	-114.5	62.5	*	*
zimm	Zimmerwald	Switzerland	7.5	46.9	*	*
zwen	Zwengorod	Russia	36.8	55.7		*
TOTAL					33	74

When comparing the distribution of the IGS stations between 1993 and 1995 (Figure 6.1 and Figure 6.2 respectively), we can clearly see that the spatial distribution of the GPS stations for the 1995 data set is superior to that for 1993. This is especially true for the equatorial region where the GPS coverage is much poorer in 1993. From the ionospheric research point of view, it is unfortunate that there had been fewer IGS stations available in 1993 during the period of medium solar activity. It is very important to realize that the number of IGS stations in coastal regions has also increased making it possible to provide better ionospheric corrections for the single frequency altimeter measurements over the oceans. However, the very fact that there are more than twice as many IGS stations available in 1995 than in 1993 does not imply that the spatial coverage usable for altimetry

had increased by the factor of two, since most of the new stations were established deep inside the continental regions improving the coverage over land and having very little or no contribution to the spatial coverage over the oceanic regions.

In Figure 6.3, I show an example of an hourly snapshot of the global ionosphere using the UNB technique. The figure refers to 15:00 hours UT (from this point on denoted as “15h”) of 8 April 1995. The highest TEC values occur in the equatorial region and they are as high as 55 TECU. The UNB algorithm was able to recover the equatorial anomaly and the equatorial trough. The mid-latitude region seems to provide a smooth transition between the low and high latitude regions of the global ionosphere. An additional 14 examples of hourly TEC maps are included in Appendix 2. I also produced movies in Motion Picture Experts Group (MPEG) format for all 6 days under investigation. Each movie features 24 hourly global UNB TEC maps (examples can be seen in Appendix 2) showing how the ionosphere changes from one hour to the next [Komjathy and Langley, 1997a; 1997b]. Each hourly global TEC map uses GPS observations only processing one hour’s worth of GPS data extending from 30 minutes before to 30 minutes after the hour. For the 1993 data, please note the “colorbar” indicates that the largest TEC value which occurs in the equatorial region amounts to about 80 TECU. This level of ionospheric activity in the equatorial region is consistent with the findings of Wild [1994] and Wanninger [1993].

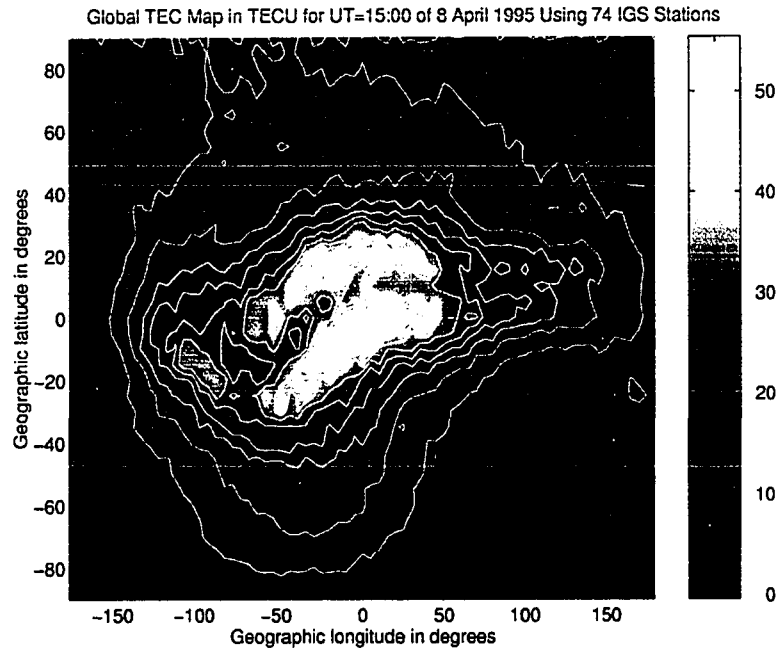


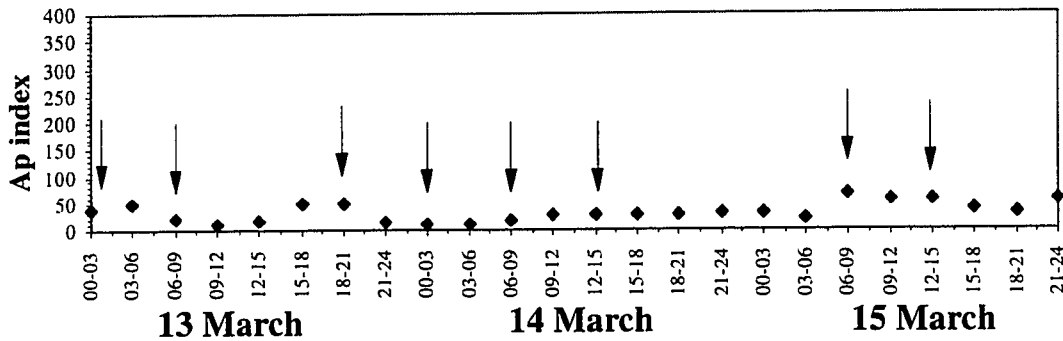
Figure 6.3: An example of hourly snapshot of the global ionosphere.

In Appendix 2, further examples of hourly TEC maps are displayed for UT 2h, 8h, 21h of 13 March 1993; 3h, 8h, 15h of 14 March 1993; 8h, 13h of 15 March 1993; 0h, 17h of 6 April 1995; 0h, 17h of 7 April 1995; and 1h, 10h of 8 April 1995. In the case of the 1993 data, we can clearly see that the lack of coverage of IGS stations in the low latitude region causes apparent discontinuities and large gradients in the equatorial region. This applies for all of the examples from the 1993 maps except for UT 2h of 13 March 1993 where the low, middle, and high latitude TEC contour lines seem to show smooth transitions between the geographic regions. Despite the problems due to the spatial coverage of the IGS stations in the equatorial region, the data and algorithms were still able to recover the general form of the equatorial anomaly using only 33 IGS stations. The UT 8h of 13 March 1993 map shows difficulties in resolving the equatorial anomaly and the equatorial trough. Maps for UT 21h of 13 March and UT 3h of 14 March 1993 seem to indicate that

the characteristics for the low latitude ionosphere can be recovered more successfully than it was the case for UT 8h of 13 March 1993. In the subsequent cases for UT 8h, 15th of 14 March and UT 8h, 13h of 15 March 1993 further examples are shown to illustrate the difficulties in recovering the low latitude signatures of the ionosphere depending on the location of the equatorial anomaly. In conclusion, the apparent discontinuities in the 1993 maps are due to the limited data coverage of the IGS stations.

In case of the 1995 low solar activity data, we can clearly see that the spatial and temporal coverage has improved over the 1993 data because twice as many stations were used to generate the maps. In Figure 6.4, I display the A_p planetary equivalent amplitude for the 6 days under investigation [NGDC, 1997a]. The arrows indicate the epochs of the examples for the hourly TEC maps that have been included in Figure 6.3 and Appendix 2. Examples of TEC maps for undisturbed ionospheric conditions are UT 0h, 17h of 6 April 1995, and 0h of 7 April 1995. It is interesting to see that at UT 17h of 7 April 1995, the global ionosphere appears to become disturbed which might be indicative of a severe geomagnetic storm ($A_p = 207$) which occurred at about that time. Also, a couple of hours after that (see map UT 1h of 8 April 1995), the ionosphere seems to have become quiet again corresponding to an A_p index of 27. At UT 10h of 8 April 1995 the global TEC map shows a somewhat disturbed signature suggesting a minor geomagnetic storm period

Ap Index for March 13-15, 1993



Ap Index for April 6-8, 1995

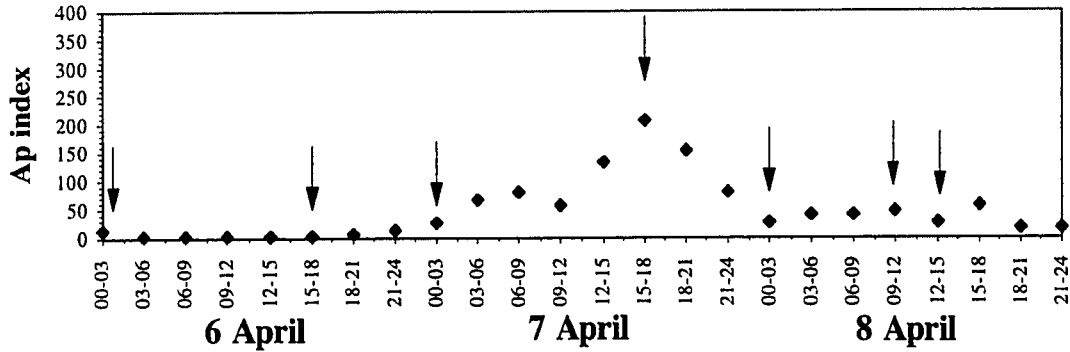


Figure 6.4: Indication of geomagnetic field disturbance (the arrows indicate the epochs of hourly TEC maps included in this dissertation).

($A_p = 48$) in Figure 6.4. In the case of the 1993 data, the effect of geomagnetic disturbances cannot be recognized in the figures. This could be due to the fact that for the three day period in 1993, most of the time the A_p index indicates geomagnetically active but not storm conditions (A_p average is about 30). The exception is the time period between UT 6h and 15h of 15 March 1993 during which the A_p index was as high as 67. Two maps have been included in Appendix 2 from that time period, however, the effect of a possible disturbance cannot be detected in the maps. The reason for this could be that even though the A_p index indicates a major storm condition, the spatial and temporal

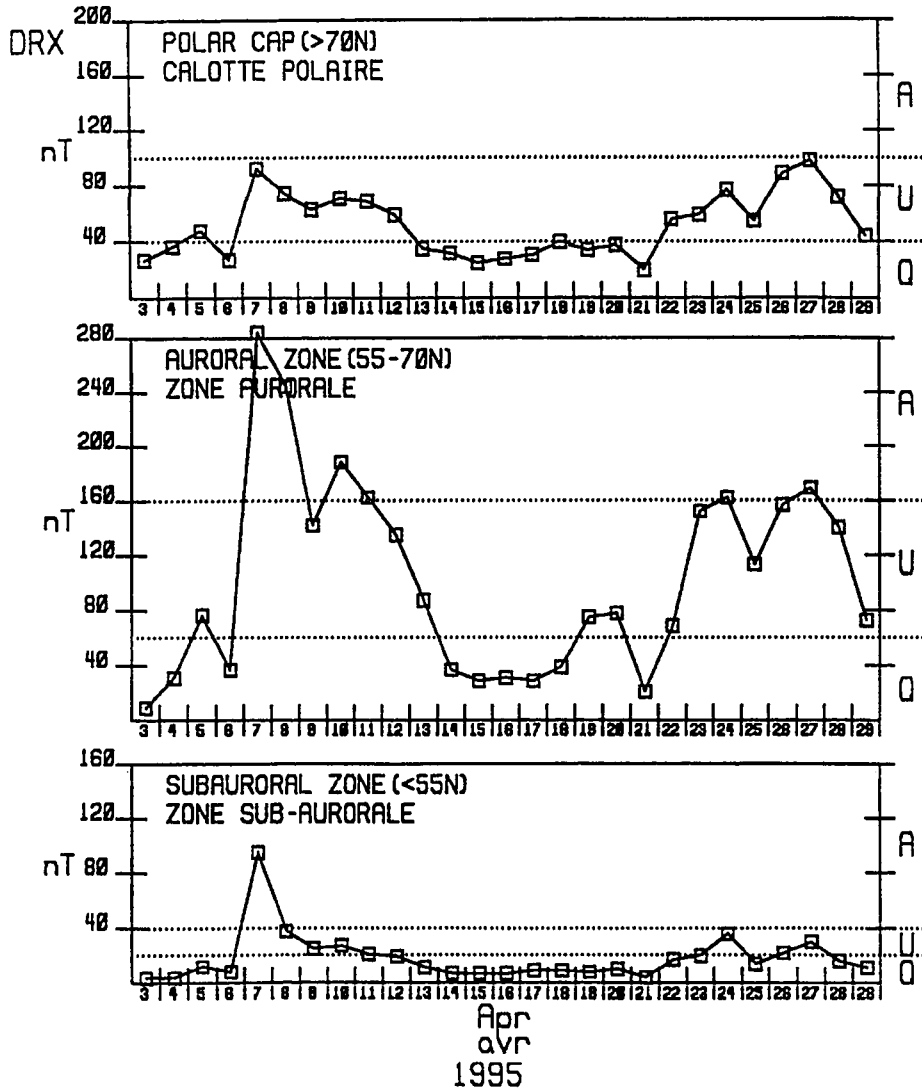
resolution of the GPS data did not make it possible to detect such a phenomenon. This seems to be supported by the fact that in the case of the 1995 data, for UT 10h of 8 April the A_p index showed geomagnetic storm conditions with a relatively small $A_p = 56$. Despite this, a disturbed signature could be detected in the corresponding TEC map. In Figure 6.5, I display the Geological Survey of Canada's determination of geomagnetic field variations for the polar, auroral and sub-auroral regions for April 1995 indicating that indeed the geomagnetic field reached a disturbed level on April 7th, 1995 and stayed active and unsettled through 8 April 1995. It is this disturbance that the UNB algorithm was able to detect using GPS-derived TEC data. Comparing the maps of 6 April 1995 with the ones from 7 and 8 April 1995, GPS-derived TEC maps for day 6 April 1995 clearly show no indication of disturbed contour lines while the maps for 7 and 8 April 1995 display disturbed conditions.

Once I had the hourly global TEC maps produced, I used them to update the IRI-95 model and compute TEC predictions for the T/P epochs and geographic locations. The updated IRI-95 model enhanced with the plasmaspheric electron content model was then used to compute TEC predictions at the T/P epochs and locations. This technique is intended to demonstrate that the updated IRI-95 model would be an alternative for providing ionospheric delay corrections for future single frequency altimeter missions. In the case of the GFO mission, the updated IRI-95 model could be used to integrate the electron density up to the orbital altitude of the satellite which is to be about 700 km.

Rotation : 2208

GSC/CGC OTTAWA

REVIEW OF GEOMAGNETIC ACTIVITY : DRX INDEX
 COMPTE RENDU DE L'ACTIVITÉ MAGNÉTIQUE : INDICE DRX



Q, U and A represent quiet, unsettled and active levels of geomagnetic activity.
 Q, U et A représentent des niveaux calmes, agités, et actifs de l'activité géomagnétique.

Figure 6.5: Geomagnetic activity for the 1995 data (courtesy of the Geological Survey of Canada).

Figures 6.6 to 6.8 and those in Appendix 3 show comparisons of TEC determinations from the original IRI-95, the updated IRI-95, the UNB TEC maps, JPL GIMs and the

plasmaspheric electron content model. The backbone of the comparison is the T/P-derived TEC data that had been provided for the workshop participants. As a reminder, the T/P TEC data is derived using dual frequency radar altimeter observations over the oceans. The T/P data set was provided as 60 second smoothed data reducing the noise of the raw T/P measurement. Anomalous data points such as those over land masses and ice cover were removed by the University of Colorado [Gold, 1996]. The accuracy of such T/P data is considered to be better than 3 TECU [Yuan et al., 1996]. There are 26 T/P passes for each of the 6 days investigated. For each T/P pass, I computed the original IRI-95 predictions and the updated IRI-95 TEC using the UNB TEC maps. I also plotted the GIM TEC values for each of the individual T/P epochs. The notations UNB TEC (before) and UNB TEC (after) stand for the UNB TEC values before and after the hour nearest the T/P epoch since the UNB algorithm provides TEC data on an hourly basis. Note that I only plotted TEC values for each technique where I had T/P data values available. This is the explanation for the unevenly spaced data values plotted. For each T/P pass, I produced three plots: the first one shows the TEC vs. latitude (Figure 6.6 and top panel of figures in Appendix 3) (the mean and the standard deviation of the differences are also displayed in Table 6.2), the second one shows the differences with respect to the T/P-derived TEC (Figure 6.7 and center part of figures in Appendix 3) assuming that the T/P derived TEC is free of errors, and the third plot shows the T/P pass ground trajectory plotted on a world map (Figure 6.8 and bottom panel of figures in Appendix 3) (the circles represent the T/P epochs; the triangles represent the IGS stations used for data processing for that particular day). The data points are only connected to guide the eyes. I produced 26 passes times 3

plots/pass times 6 days = 468 plots. I have chosen 11 representative sets to include in the dissertation; one pass is shown as an example in Figures 6.6 to 6.8 and 10 more passes are included in Appendix 3). Results of the comparison were previously presented by Komjathy and Langley [1997a] and Komjathy et al. [1997]. Here, I will point out some of the characteristics of each these sample passes.

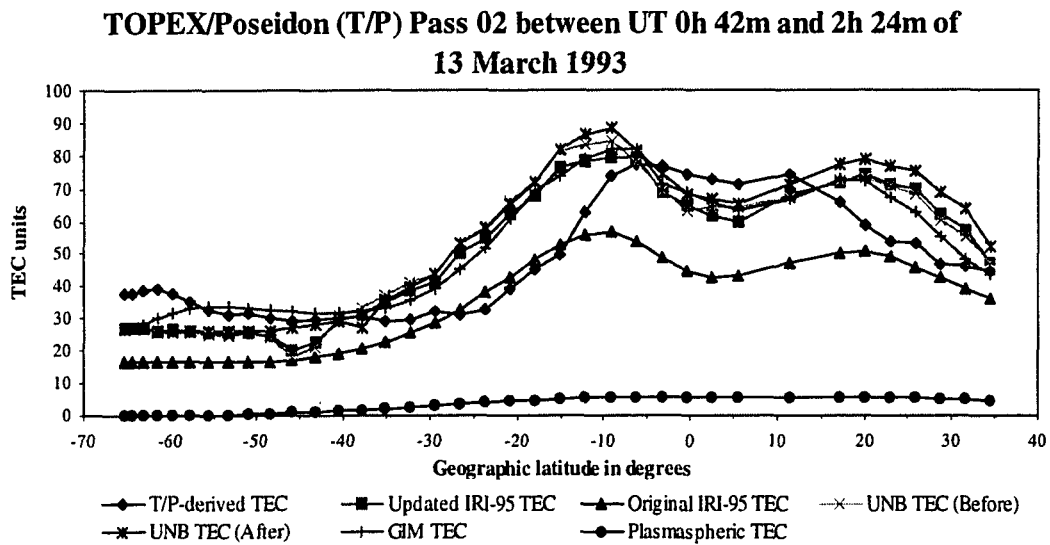


Figure 6.6: An example of the comparison of different techniques with T/P data.

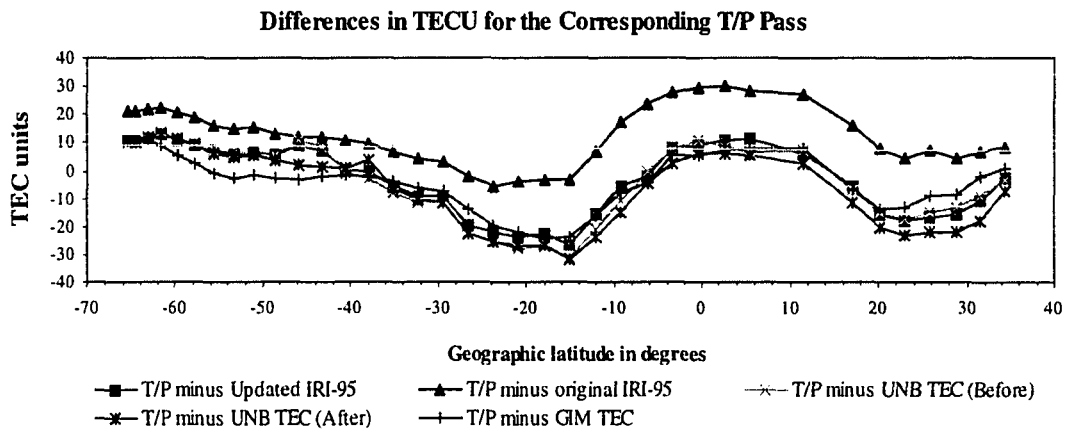


Figure 6.7: An example of the differences of TEC between different techniques with respect to a T/P pass.

Corresponding T/P Ground Trajectory

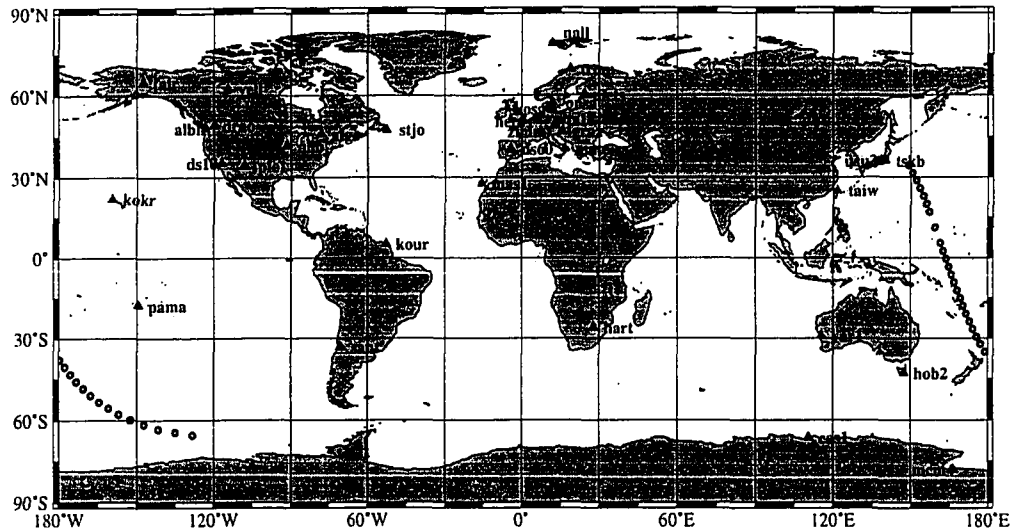


Figure 6.8: An example displaying the T/P pass 02 of 13 March 1993.

Pass 02, 13 March 1993: In Figure 6.6, the plot displays a day-time pass with a maximum TEC of about 90 TECU around the equatorial region at 20 degrees either side of the equatorial anomaly. The original IRI-95 underestimates the TEC over the entire region whereas the UNB and GIM estimates follow a similar signature. The southern hemisphere mid-latitude region shows a 20-30 TECU level discrepancy from the T/P-derived TEC data. This might be due to the fact there are no IGS stations available in that region and that the UNB and GIM estimates are correspondingly affected. On the other hand, the northern hemisphere mid-latitude region shows an increasing agreement with the T/P data as the T/P pass gets closer to the station Tsukuba (tskb) (see Figure 6.8) indicating a 3 TECU level agreement between the T/P-derived TEC data and the updated IRI-95 model using the UNB TEC maps. The 3 TECU level agreement corresponds to the

accuracy of T/P measurements [Yuan et al., 1996]. I also plotted in Figure 6.7 the differences between the different techniques and the T/P TEC values.

The mean, the standard deviation of the differences for all examples and the r.m.s. of the mean differences are summarized in Table 6.2. As seen in the table, the updated IRI-95 model results show a smaller bias in all 11 representative examples and a smaller standard deviation in 10 of 11 cases with respect to the original IRI-95 predictions. In 6 of 11 examples, the UNB results show smaller biases with respect to the T/P data compared to the GIMs. The smaller bias could be explained by the fact that the UNB technique also takes into account the plasmaspheric electron content when comparing GPS-derived TEC data with T/P TEC data. Some of the larger differences between the UNB maps and GIMs could be explained by the fact that different sets of GPS stations were used to derive the GIMs. Table 6.2 also indicates that in the case of the 11 representative cases, the r.m.s. of the mean differences turned out to be 3.1 TECU for the UNB and 3.8 TECU for the JPL GIM results.

Table 6.2: Summary of statistics comparing the different TEC techniques with the 11 representative T/P passes

	T/P minus Updated IRI-95 TEC		T/P minus Original IRI-95 TEC		T/P minus UNB TEC (Before)		T/P minus UNB TEC (After)		T/P minus GIM TEC	
	Mean of the Diff. in TECU	S. D. of the Diff. in TECU	Mean of the Diff. in TECU	S. D. of the Diff. in TECU	Mean of the Diff. in TECU	S. D. of the Diff. in TECU	Mean of the Diff. in TECU	S. D. of the Diff. in TECU	Mean of the Diff. in TECU	S. D. of the Diff. in TECU
02 of 13 March 1993	-2.5	12.4	12.8	10.0	-3.4	13.6	-5.6	13.8	-3.6	9.8
07 of 13 March 1993	6.9	11.2	12.6	11.5	2.8	9.3	5.1	10.4	1.8	8.6
24 of 13 March 1993	0.5	6.6	14.4	8.0	-0.8	6.1	-3.2	7.2	-6.9	4.6
23 of 14 March 1993	-5.3	11.5	9.5	14.9	-6.1	11.0	-10.5	11.9	-7.9	9.0
06 of 15 March 1993	2.7	7.7	8.5	8.6	-1.4	6.7	0.3	6.6	-2.7	7.9
04 of 6 April 1995	0.5	5.6	-4.4	7.3	0.7	5.9	0.4	5.7	-1.9	4.0
11 of 7 April 1995	1.6	6.0	4.3	7.1	2.2	5.7	1.9	5.8	0.8	5.7
23 of 7 April 1995	2.3	8.2	6.4	9.5	2.8	8.5	2.5	8.3	0.3	7.9
03 of 8 April 1995	-0.8	3.9	-2.6	5.0	-0.7	4.0	-1.0	4.0	2.4	3.2
21 of 8 April 1995	2.6	3.4	4.4	4.9	3.1	3.6	2.9	3.5	2.6	2.4
23 of 8 April 1995	2.2	4.5	2.6	5.1	3.1	5.1	2.1	4.5	3.6	4.5
R.m.s of the Mean Diff.	3.1		8.6		2.9		4.3		3.8	

The subsequent 10 examples can be found in Appendix 3 displaying the results the same way as for the cases of Figures 6.6 to 6.8. The set of figures in Appendix 3 is ordered according to the passes explained below.

Pass 07, 13 March 1993: The plot shows a night-time pass with a maximum TEC of about 80 TECU with the T/P data clearly showing the equatorial anomaly. Both UNB and GIM estimates smooth out the equatorial anomaly which might have resulted from the lack of stations nearby. The IRI-95 model underestimates the TEC by about 40-50 TECU at the equatorial anomaly. Updating the original IRI-95 model using the UNB-derived TEC data reduces the mean differences between the T/P minus IRI-95 and T/P minus updated IRI-95 by about 50 percent.

Pass 24, 13 March 1993: The plot shows a day-time pass with a maximum TEC of about 85 TECU in the equatorial region. There seems to be overall good agreement between the updated IRI-95 and the T/P data. However, a 20 TECU level difference can be seen in the equatorial region, which again, might be due to the lack of IGS stations in that region. Stations Kokee Park (kokr) and Pamatai (pama) are nearby the T/P pass ground track so as a result there appears to be a good agreement between the updated IRI-95 and T/P at about 20 degrees either side of the equator. The original IRI-95 underestimates TEC over all latitude regions.

Pass 23, 14 March 1993: The plot shows a day-time pass. Both the UNB maps and GIMs seem to be overestimating TEC over the mid-latitude regions. On the other hand, in the equatorial region, both the UNB maps and GIMs underestimate the TEC. The original IRI-95 predictions are in a good agreement with the T/P-derived TEC data. Large differences between the TEC maps and T/P data are indicative of the lack of IGS stations in the Pacific region.

Pass 06, 15 March 1993: The plot shows a night-time pass for medium solar activity period. It indicates a good agreement between the different techniques in the mid-latitude regions. Larger differences can be seen in the equatorial region. However, both GIMs and UNB maps seem to be able to recover the equatorial anomaly on either side of the geomagnetic equator.

Pass 04, 06 April 1995: The plot shows a day-time T/P pass during a period of low solar activity with a maximum TEC at the 40 TECU level in the equatorial region. There seems to be a good agreement between the different techniques in the mid-latitude regions. This agreement extends to the equatorial region, as the equatorial anomaly seems to have been recovered. UNB TEC values seem to be close to the T/P data. The original IRI-95 predictions overestimate TEC in the equatorial region.

Pass 11, 07 April 1995: The plot displays a day-time T/P pass. Good agreement with the T/P data seems to have been achieved by both UNB maps and GIMs. It is interesting

to see a signature in the T/P data in the southern hemisphere mid-latitude region between latitudes 15 and 40 degrees which may be indicative of the geomagnetic disturbance affecting the TEC. Neither the GIMs nor the UNB maps are able to detect that particular signature.

Pass 23, 07 April 1995: The plot displays a day-time T/P pass. Good agreement can be seen between the different techniques in the mid-latitude region. However, the equatorial region shows larger differences between the different techniques. The equatorial anomaly seems to be well detected by T/P data. UNB maps and GIMs also follow the spatial variation in the equatorial region. There seems to be a large 40 TECU level incorrect T/P data point from the Great Lakes area. The fact that the T/P data is incorrect seems to be supported by the fact that there are numerous GPS stations nearby indicating a smaller 10 TECU level TEC.

Pass 03, 08 April 1995: The plot shows a day-time T/P pass over the Pacific region. There is a good agreement among the different techniques. The equatorial anomaly could also be detected. The UNB TEC estimates seem to show a small bias with respect to T/P data. There seems to be a large T/P value (28 TECU) at -24.1 degrees latitude which might be due to a localized ionospheric disturbance in the equatorial region. Due to the lack of nearby IGS tracking stations, none of the other techniques seem to be able to detect the possible phenomenon.

Pass 21, 08 April 1995: The plot displays a day-time T/P pass. A very good agreement among the different techniques in the southern hemisphere mid-latitude region is noted. In the northern hemisphere mid-latitude region, T/P TEC values are larger by about 5 TECU which might be due to the combination of uncertainties in T/P measurements and the UNB estimates.

Pass 23, 08 April 1995: The plot shows a day-time T/P pass over the Pacific region. It shows a good agreement in the southern hemisphere mid-latitude region. In the equatorial region, larger differences are seen as expected due to the lack of GPS station coverage. UNB maps and GIMs show a very close agreement.

Figures 6.9 to 6.11 show the comparisons between the original and the updated IRI-95 model performance with respect to all T/P passes for the three days in 1993, and in Figures 6.12 to 6.14 for the three days in 1995 assuming that the T/P TEC values provide us with an errorless ground-truth. The data points in the figures refer to the mean, and the error bars correspond to the standard deviation of the differences between the updated and original IRI-95 predictions with respect to the T/P data. We can clearly see that the mean differences for the three days were reduced to 1.7, 0.5, and -1.2 TECU from 10.8, 9.1 and 6.5 TECU by updating IRI-95. The ranges of the mean standard deviations have also been reduced following the update procedure. In the case of the 1995 data, I also achieved an improvement in 2 of the 3 days in reducing the mean differences with respect to the T/P data. The ranges of the mean standard deviations were reduced for all three days.

Updated IRI-95, mean = 1.7, $3.7 \leq \sigma \leq 12.1$ TECU
 Original IRI-95, mean = 10.8, $3.5 \leq \sigma \leq 14.7$ TECU

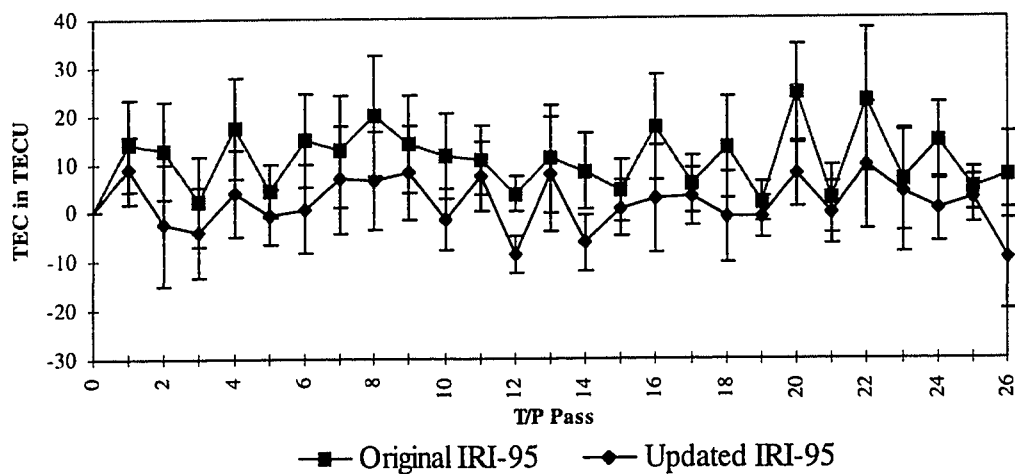


Figure 6.9: Comparison of updated IRI-95 and original IRI-95 with T/P for 13 March 1993.

Updated IRI-95, mean = 0.5, $3.3 \leq \sigma \leq 16.1$ TECU
 Original IRI-95, mean = 9.1, $2.5 \leq \sigma \leq 16.9$ TECU

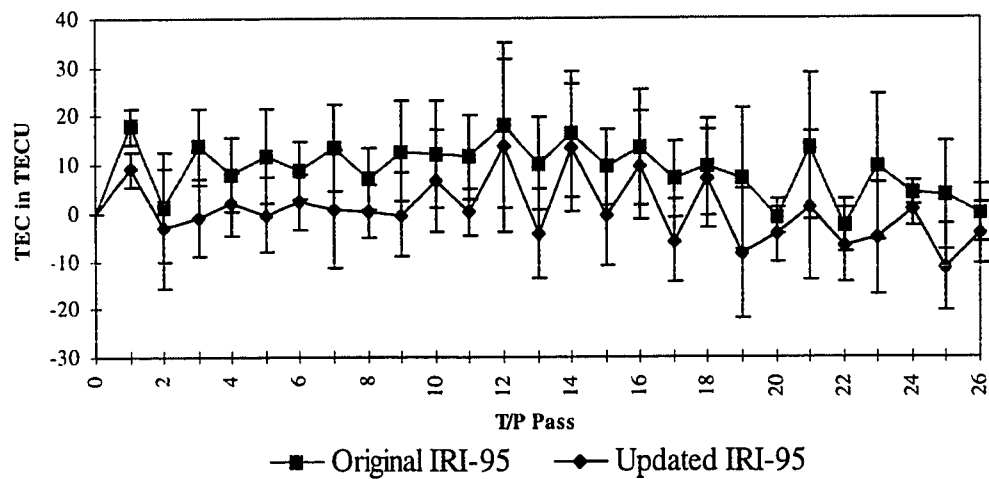


Figure 6.10: Comparison of updated IRI-95 and original IRI-95 with T/P for 14 March 1993.

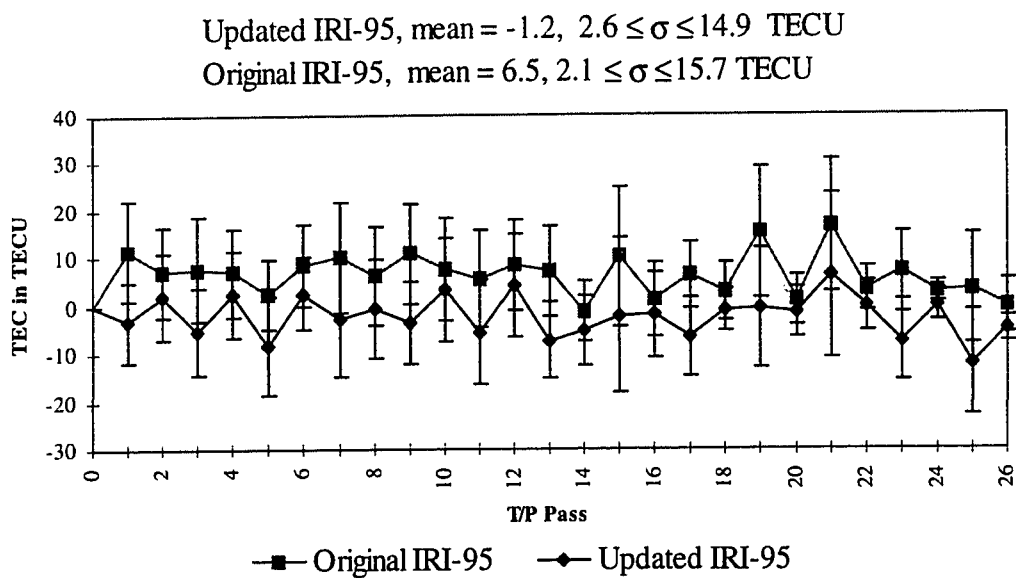


Figure 6.11: Comparison of the UNB global TEC maps with T/P-derived TEC data for 15 March 1993.

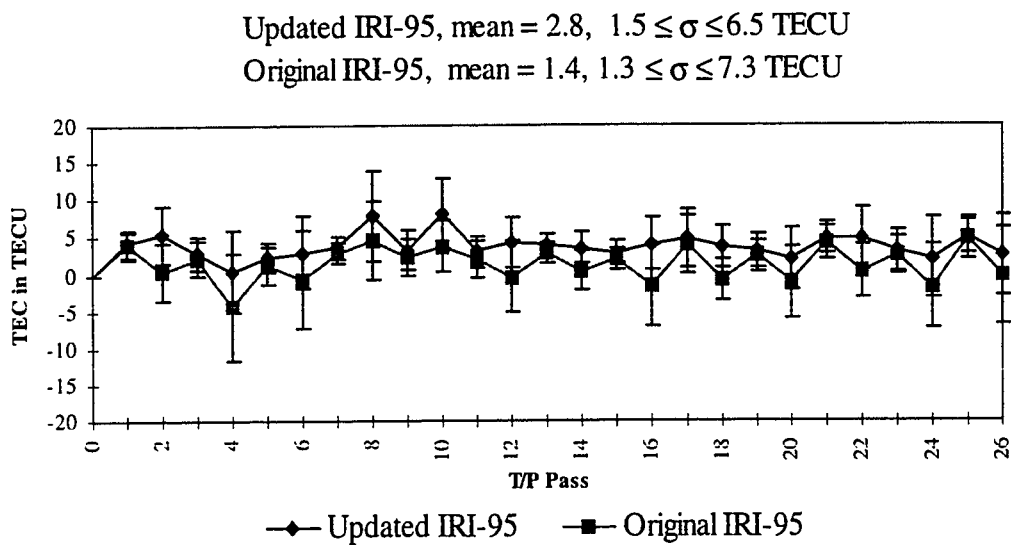


Figure 6.12: Comparison of the UNB global TEC maps with T/P-derived TEC data for 6 April 1995.

Updated IRI-95, mean = 1.8, $1.7 \leq \sigma \leq 7.2$ TECU
 Original IRI-95, mean = 3.3, $1.9 \leq \sigma \leq 9.3$ TECU

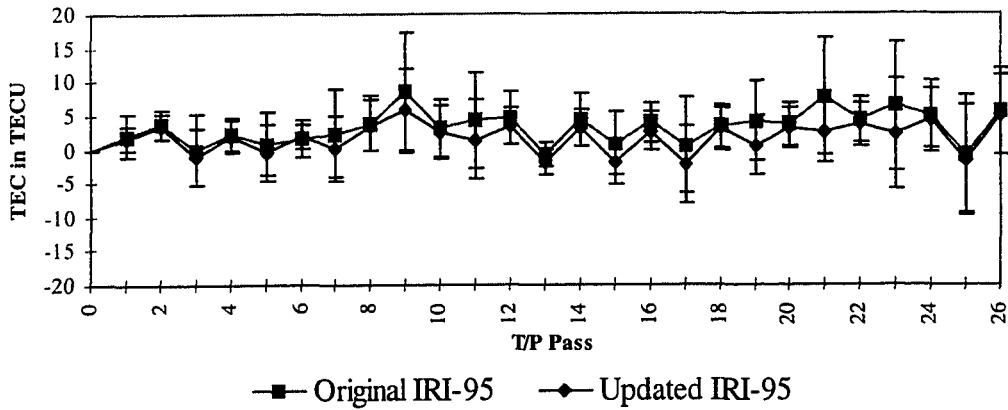


Figure 6.13: Comparison of the UNB global TEC maps with T/P-derived TEC data for 7 April 1995.

Updated IRI-95, mean = 0.8, $1.1 \leq \sigma \leq 6.4$ TECU
 Original IRI-95, mean = 1.2, $0.9 \leq \sigma \leq 8.6$ TECU

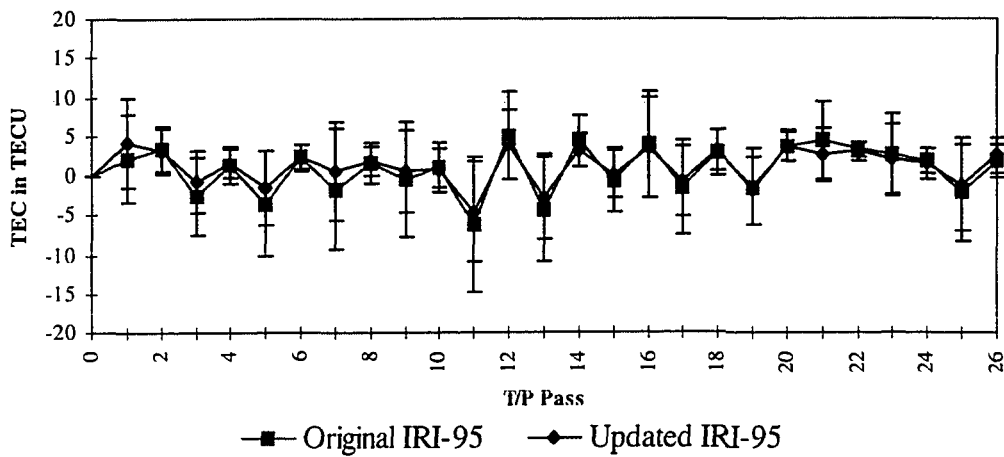


Figure 6.14: Comparison of the UNB global TEC maps with T/P-derived TEC data for 8 April 1995.

We can conclude that the success of globally updating IRI-95 using GPS data strongly depends on the level of solar and geomagnetic activity and the number of IGS stations

used for deriving the UNB TEC maps. In the equatorial region, due to the lack of GPS stations, limited success was achieved using the updating procedure (it could be better in the future if more stations were to be added). The effectiveness of the updating procedure also depends on the distance between the IGS stations and the position of the T/P measurement. An easy way to check the validity of the updated IRI-95 values is the direct comparison of the T/P data and the UNB TEC values at times when the T/P ground tracks are near any of the IGS stations (look for nearby or overlapping “triangles” and “circles” in Figure 6.8 or Appendix 3, and then identify the corresponding latitude in the top and center panels of the corresponding figures).

Based on 6 days’ worth of T/P and GPS data, I obtained the following results in predicting TEC along the T/P ground tracks:

	Updated IRI-95 (all units in TECU)			Original IRI-95 (all units in TECU)		
	average mean	average s.d.	s.d. range (min, max)	average mean	average s.d.	s.d. range (min, max)
13-Mar-93	1.7	7.7	$3.7 \leq \sigma \leq 12.1$	10.8	8.7	$3.5 \leq \sigma \leq 14.7$
14-Mar-93	0.5	8.8	$3.3 \leq \sigma \leq 16.1$	9.1	9.5	$2.5 \leq \sigma \leq 16.9$
15-Mar-93	-1.2	8.5	$2.6 \leq \sigma \leq 14.9$	6.5	9.2	$2.1 \leq \sigma \leq 15.7$
06-Apr-95	2.8	3.2	$1.5 \leq \sigma \leq 6.5$	1.4	3.6	$1.3 \leq \sigma \leq 7.3$
07-Apr-95	1.8	4.0	$1.7 \leq \sigma \leq 7.2$	3.3	4.9	$1.9 \leq \sigma \leq 9.3$
08-Apr-95	0.8	3.7	$1.1 \leq \sigma \leq 6.4$	1.2	4.4	$0.9 \leq \sigma \leq 8.6$

Table 6.3: Summary of results from the comparison between UNB global TEC maps and T/P-derived TEC data.

These results were obtained from two sets of 3 days’ worth of global GPS data during a) a period of medium solar activity, for which there was a better than 9 TECU level (1 sigma) agreement in the TEC on a global scale between the T/P-derived TEC data and

UNB's technique, and b) during a period of low solar activity for which UNB's results agreed with the T/P data at a better than 5 TECU level (1 sigma). The results show significant improvements in the mean differences after updating IRI-95 for the days in 1993. The results assume that the T/P-derived TEC is representative of the true TEC. The typical formal errors for the UNB TEC maps for 1995 is about 2 to 3 TECU. The measurement error of the T/P data is about 3 TECU [Yuan et al., 1996]. This seems to be in agreement with the better than 5 TECU level agreement I found in the case of the 1995 data. For the medium solar activity 1993 data, the typical error bars for the UNB TEC maps are about 3 to 4 TECU. If we assume that the T/P data error bar is about 3 TECU for the 1993 then the better than 9 TECU level agreement between the updated IRI-95 and T/P data suggests that the poorer accuracy for the UNB TEC maps is due to the sparse spatial coverage of the IGS stations in 1993. This seems to be supported by the fact that the better agreement of results for the 1995 data is coincident with a doubling of IGS stations. However, the 1995 data was taken during a period of low solar activity which may have made the TEC modelling easier. In the case of the 1993 data, not only were fewer stations available for processing but the ionosphere itself was characteristic of medium solar activity conditions. It appears that the lack of spatial coverage of IGS stations may have been the main problem and not the fact that the ionosphere was more active in 1993 than in 1995. The 1995 data was indicative of a major geomagnetic disturbance, and still the UNB technique was able to detect the variations in the global TEC.

Some of differences between the UNB and night time T/P data can perhaps be explained by a possible 5 TECU level bias in the T/P night time data. There is some evidence to suspect that the biases set for night time T/P passes is too low in order to assure that all data is positive [Coker et al., 1996].

I would also like to point out that providing TEC data over the oceans in the form of global TEC maps is one of the most difficult tasks of the ionospheric modelling techniques using GPS due to the lack of nearby GPS stations providing limited temporal and spatial coverage. Having considered this, the reader can probably appreciate the fact that the statistics developed will provide the worst case scenario for the UNB global ionospheric modelling technique.

I also decided to acquire Faraday rotation data to perform an independent “spot-check” on the UNB GPS-inferred TEC maps in order to verify the algorithm. I was unable to obtain Faraday rotation data for any of the three day periods designated for processing for the workshop. Therefore, I acquired Faraday rotation data for the nearest day to the period covered by the 1993 data. I found data for 26 March 1993. The data was provided by the Solar Terrestrial Dispatch at the University of Lethbridge, Canada. The six different stations for which I acquired hourly TEC data are: Palehua, HI; Taoyuan, Taiwan; Cape Canaveral, FL; Osan, Korea; Boulder, CO and Anchorage, AK. The comparison of the UNB TEC values and the Faraday rotation data displayed in Figures 6.15 to 6.20 shows that the r.m.s. of the differences between the Faraday rotation TEC and the UNB TEC

values are 12.7 for Palehua, 8.9 for Taoyuan, 8.7 for Cape Canaveral, 6.0 for Osan, 3.3 for Boulder and 5.2 for Anchorage (all in TECU). However, a rigorous comparison requires that I take into account the electron content above 2000 km (the Faraday rotation data provides total electron content up to 2000 km, see Section 2.5.5). I also computed the differences between the Faraday rotation data and the UNB TEC values when taking into account the electron content between 2000 km and the orbital altitude of the GPS satellites (20,200 km). The r.m.s. of the differences turned out to be 12.1 for Palehua, 7.7 for Taoyuan, 5.3 for Cape Canaveral, 4.3 for Osan, 3.4 for Boulder, and 5.2 for Anchorage. I used the plasmaspheric electron content model introduced in Section 4.2.6. After applying the plasmaspheric electron content model, I achieved better agreement between the Faraday rotation data and the UNB TEC data in the case of Palehua, Taoyuan, Cape Canaveral, and Osan. No improvement can be seen in the case of Boulder and Anchorage. The reason for this can be seen in Figure 6.19. For the Boulder station the plasmaspheric electron content prediction is very small (about 0.5 TECU), and for Anchorage, there is no plasmaspheric electron content prediction due to the high geomagnetic latitude. The Faraday rotation data I obtained was raw data; it had not been checked by the providers for errors such as cycle slips. This could be a possible explanation for the bias that we can see in the Osan plot between the updated IRI-95 and the Faraday data. The typical formal error on the UNB TEC estimates is about 3 to 4 TECU for the 1993 data and 2 to 3 TECU for 1995 data. The typical error for the Faraday rotation data is about 5 percent of the total electron content [Titheridge, 1972]. That is the error would be less than 5 TECU for Palehua, 4 for Taoyuan, 2.3 for Cape Canaveral, 3.8

for Osan, 1.8 for Boulder, and 2.5 for Anchorage. The Faraday rotation measurement error seems to be in agreement with the 3 to 4 UNB TEC error bars. An exception appears to be station Palehua for which case a 12.1 TECU r.m.s. error was found. A more than 5 TECU level Faraday rotation data error can be suspected in this case since there is a nearby IGS station Kokee Park, HI which provided sufficient data coverage to derive part of the UNB TEC maps in this region (see station “kokr” in Figure 6.8). Note that for station Anchorage (Figure 6.20) we have a data gap between UT 5 and 16 hours.

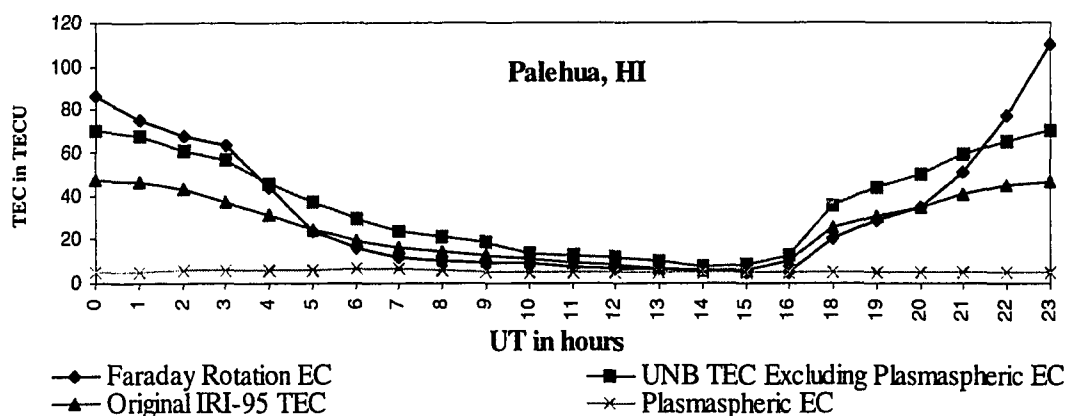


Figure 6.15: Comparison of different techniques with Faraday rotation data for 26 March 1993 at Palehua, HI.

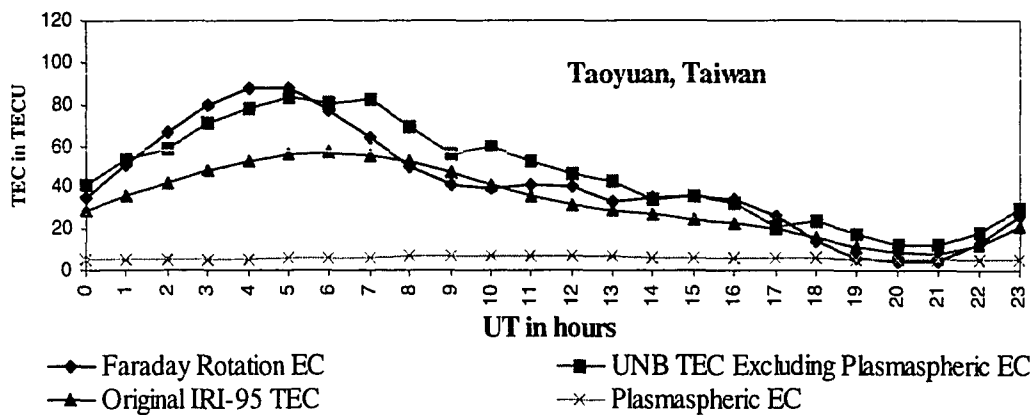


Figure 6.16: Comparison of different techniques with Faraday rotation data for 26 March 1993 at Taoyuan, Taiwan.

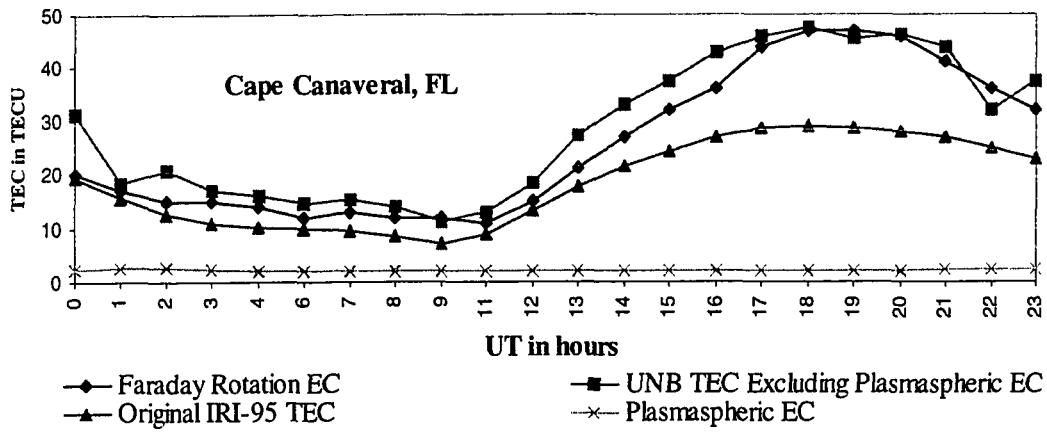


Figure 6.17: Comparison of different techniques with Faraday rotation data for 26 March 1993 at Cape Canaveral, FL.

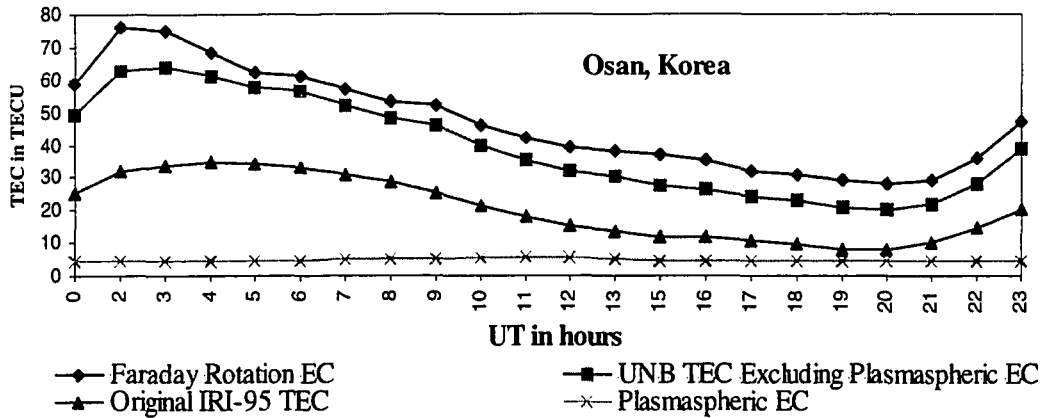


Figure 6.18: Comparison of different techniques with Faraday rotation data for 26 March 1993 at Osan, Korea.

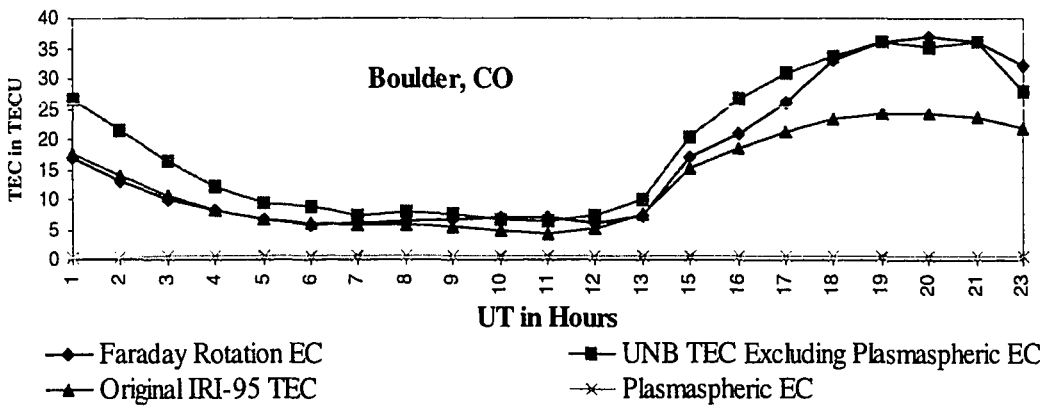


Figure 6.19: Comparison of different techniques with Faraday rotation data for 26 March 1993 at Boulder, CO.

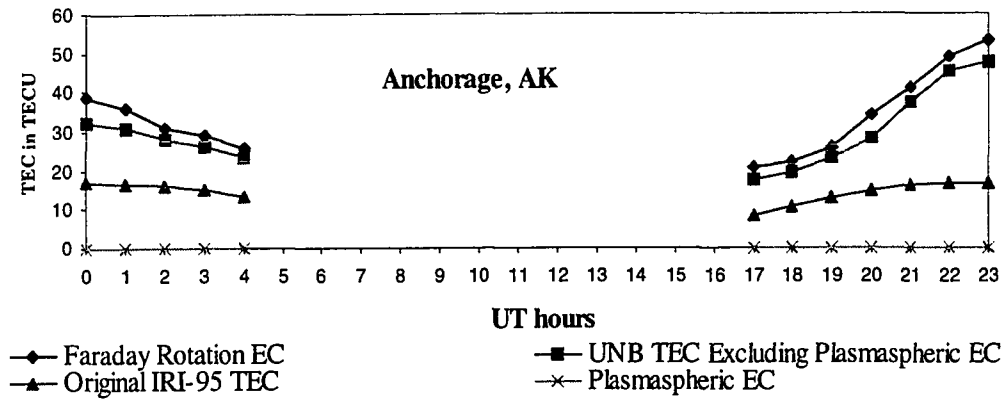


Figure 6.20: Comparison of different techniques with Faraday rotation data for 26 March 1993 at Anchorage, AK.

In this chapter I have described and illustrated the UNB global ionospheric mapping technique. I also compared results with those of other independent techniques. In the next chapter, I will summarize all my results and give recommendations for future research.

CHAPTER 7

CONCLUSIONS AND RECOMMENDATIONS FOR FUTURE RESEARCH

In the first part of this chapter I will summarize the conclusions of my research. There are several areas of this study that can be further explored or in which further developments can be made based on my results. These thoughts will be summarized in the second part of the chapter.

7.1 Conclusions of the Research

During the first part of the research, I evaluated the capability of global empirical ionospheric models including the IRI-90, and GPS single frequency Broadcast models in providing ionospheric range error corrections. Based on a limited data set for investigating the long-term stability of the Broadcast model for a period of low solar activity, I found that the IRI-90 model performance was better than that of the Broadcast model both for day-time and night-time observations.

I have developed the capabilities to perform regional ionospheric modelling using a modified version of the UNB DIPOP software package. I performed a sensitivity analysis on the TEC and satellite-receiver differential delays as a function of elevation cutoff angle, ionospheric shell height, and ionospheric mapping function. I participated in an IGS

campaign to process and analyse a 5 week long GPS data set in order to compare the ionospheric products between IGS processing centers. This experiment was the first of its kind among the IGS activities. I also made modifications to the International Reference Ionosphere 1995 to update its coefficient sets using GPS data. An inferred IG index is computed for any geographic location to provide a scaling parameter for the CCIR/URSI coefficient set which results in more accurate TEC predictions by the IRI-95 model. The updated IRI-95 model could efficiently be used, for example, to provide ionospheric corrections for single frequency GPS receivers either in post-processing or even in real-time mode. After updating the IRI-95 model using the UNB-derived regional TEC maps, I achieved an overall 32.5% accuracy improvement over the original IRI-95 predictions. Another application of the updated IRI-95 model with the UNB-derived TEC could be its use as a sophisticated interpolator between two GPS-derived hourly TEC maps to help improve the accuracy of the GPS-derived TEC estimates for any epoch in between.

The experience I gained in regional ionospheric modelling encouraged me to further enhance the UNB software to produce global TEC maps. The sensitivity analysis of the ionospheric parameters has proven to be useful in the case of the global ionospheric modelling. For the ionospheric workshop at the University of Colorado, I demonstrated the UNB-derived global TEC maps on 3 days' worth of global GPS data (33 IGS stations for each day) at a medium solar activity time (year 1993) and 3 days' worth of global GPS data (74 IGS stations for each day) at a low solar activity time (year 1995). An additional day's worth of global GPS data was also processed to help validate the UNB global TEC

maps using Faraday rotation data. Snapshots of the global ionosphere using GPS data were also produced [Komjathy and Langley, 1997b]. The UNB global TEC modelling includes the new concept of the varying ionospheric shell height determination as well as the use of an empirical plasmaspheric electron content model when updating the IRI-95 model. I also performed a comparison between the updated IRI-95 predictions using the UNB global TEC maps, the original IRI-95 predictions, and JPL-derived GIMs against 6 days' worth of T/P-derived TEC data. The results showed that based on 3 days' worth of global GPS data during a medium solar activity time in 1993, there was better than a 9 TECU level (1 sigma) agreement in the TEC on a global scale with the T/P-derived TEC data using the UNB technique. For the low solar activity 1995 data, the UNB results agreed with the T/P data at better than the 5 TECU level (1 sigma). In the case of the 1995 data, the typical error of the UNB maps is 2 to 3 TECU whereas the T/P measurement error is claimed to be less than 3 TECU. In the case of the 1993 data, typical UNB errors are at the 3 to 4 TECU. The 9 TECU level agreement between T/P and UNB results seems to be indicative of the lack of adequate spatial coverage of IGS stations in 1993 to model global TEC.

The UNB GPS-data-updated IRI-95 coefficient sets have been demonstrated to be capable of providing a means for ionospheric delay corrections for single frequency radar altimeter missions such as the upcoming GFO mission. Since the spacecraft will be orbiting "inside" the ionosphere, the GPS-updated IRI-95 electron density profile would allow the integration of electron densities up to the spacecraft altitude to remove the bias

imposed by the ionosphere. This would not be possible using GPS-derived TEC only since it provides integrated electron content up to the altitude of the GPS satellites (20,200 km).

7.2 Recommendations for Future Work

There are several potential areas that would be worthwhile further exploring both from the scientific and practical points of view. From the scientific point of view, the results presented in this dissertation have shown that GPS could potentially be used to detect ionospheric disturbances. The real-time processing of a continuously operating network of GPS receivers could possibly allow monitoring of ionospheric disturbances caused by solar and/or geomagnetic disturbances. This would be an interesting study for the Canadian region, where the ionospheric and geomagnetic disturbances are of utmost importance due to the fact that in Canada we are facing not only the typically calm mid-latitude ionospheric conditions but also the challenges of the high-latitude ionosphere with a wide variety of complex ionospheric features.

The IGS workshop in which UNB participated proved to be very useful. The comparison of ionospheric products between different processing and analysis centers showed that there are differences among the deduced TEC and satellite-receiver differential delays due to the differences between the processing and analysis centers' algorithms. The IGS workshop was meant to be a first step towards a series of discussions that would result in ionospheric products such as TEC maps and satellite-receiver

differential delays eventually becoming official IGS products. Further GPS campaigns are recommended to compare ionospheric products among research centers. The campaign in which UNB was involved was concerned with data from a low solar activity period only. Further comparisons are recommended for medium and high solar activity periods, and especially for periods with active solar and geomagnetic conditions. Further analysis is needed to compare global TEC maps between different processing centers to determine the reason for some of the larger TEC differences seen between the research centers' results in the low latitude region. This would be very useful as more IGS stations become available, and therefore, the TEC maps are expected to become more accurate. Efforts should also be continued to compare GPS-derived TEC values with those of other state-of-the-art independent TEC data sources such as T/P-derived TEC, Transit-inferred TEC and DORIS-derived TEC data.

The ionospheric global TEC mapping and its application to provide ionospheric corrections for single frequency altimeters combined with the IRI-95 model showed that GPS-derived TEC data can successfully be used to update the IRI-95 model. Further studies are recommended to investigate data from periods of high solar activity. The highly variable ionosphere would make the update procedure less successful which is one of the limitations of this technique. Further studies are recommended in combining 2 or 3 hourly TEC maps to update the IRI-95 using e.g., a quadratic interpolation of the inferred solar effective sunspot number between 2 hourly updates. This could be especially useful

for high solar activity periods in low and high latitude regions under disturbed ionospheric and geomagnetic conditions.

Further improvements are recommended to enhance the UNB global TEC algorithm. This would include the use of a higher order surface to model the vertical TEC in low and high latitude regions. A more recent plasmaspheric electron content model is also recommended for inclusion in the UNB algorithm; one that takes the solar and seasonal variation of the plasmaspheric electron content into account. Further improvement can be made on the global TEC algorithm in the low and high latitude regions where the spatial coverage is poorer. Global ionospheric models such as IRI-95 and PIM could be used to enhance the spatial coverage in those regions. As more IGS stations become available, GPS could also provide a unique opportunity to investigate the plasmaspheric electron content in conjunction with e.g., ionosonde-updated IRI-95 or PIM models under the assumption that these models would provide the ground-truth up to the altitude of 1000 km. The spatial and temporal resolution of the TEC maps could significantly be improved by eventually including data from dual frequency GLONASS receivers.

Investigations are recommended to be continued in the area of further improving the IRI-95 model. GPS will continue to provide a state-of-the-art TEC data source with which IRI-95 TEC predictions can be compared. There is an on-going investigation in the ionospheric research community to improve the IRI-95 topside profile for which GPS could provide an excellent TEC data source in conjunction with ionosonde data sets

providing critical frequencies for the bottomside of the ionosphere. The IRI working group has also been putting great efforts into improving IRI-95 at the low latitude regions. Again, as more IGS stations become available, GPS could be a valuable research tool to help the ionospheric community. Current IRI-95 efforts regarding enhancement for geomagnetic storm time conditions could also be assisted by using GPS TEC data sets as ground-truth.

As a next generation of ionospheric products, the UNB 2-dimensional TEC maps could perhaps be combined with electron density profiles derived from GPS/Met occultation data. This would eventually allow us to provide 3-dimensional electron density profiles. Electron density profiles provided by other independent techniques such as Incoherent Backscatter Radar or NNSS satellites could also be combined with the 2-dimensional TEC maps to investigate 3-dimensional electron density profiles. The derived electron density profiles could perhaps be used to improve the IRI-95 profile shape in low and high latitude regions.

As a possible future scientific contribution to ionospheric science and to the aviation community, the UNB regional ionospheric modelling technique is easily adaptable to the Wide Area Augmentation System (WAAS) ionospheric grid modelling procedure. The modifications to the UNB's most recent version of the ionospheric modelling software package would be straight forward. Such modification would include, according to the WAAS specifications, the ionospheric grid correction updating every 5 minutes which can

be easily accommodated using the UNB Kalman filter estimation technique. Using a modified version of the UNB regional ionospheric modelling technique, one could include GPS data sets from several independent sources such as the IGS stations, WAAS Reference Stations, and Canadian Active Control System stations all of which could be processed together to determine the accuracy of the WAAS ionospheric corrections.

The results outlined in this dissertation could be of great interest to the on-going WAAS developments. The proposed WAAS ionospheric grid correction algorithm uses an assumed 400 km for the ionospheric shell height. It was shown in the dissertation that taking into account the temporal and spatial variation of the ionospheric shell height provides a more rigorous approach when estimating ionospheric model parameters along with satellite-receiver differential delays. In the context of the WAAS coverage area, it would be worthwhile investigating the effect of the varying ionospheric shell height concept for the medium and high latitude Canadian region. This investigation may also require that one has to take a closer look at the currently used ionospheric mapping function when projecting the line-of-sight TEC into the vertical for high-latitude regions. The currently used ionospheric mapping function in the WAAS model, for example, assumes a fixed ionospheric shell height. This may be acceptable for the mid-latitude (CONUS) region but may not be adequate for the Canadian high-latitude (trough and auroral) regions.

The reader may have developed an appreciation for the fact that there is a tremendous potential for GPS to help the ionospheric community, and the ionospheric community can also be of assistance to the GPS user community in the interpretation of the ionospheric features that can be detected using GPS. Regional and global ionospheric modelling using GPS will continue to provide us with a unique new opportunity to study and understand the regional and global ionosphere for many years to come.

REFERENCES

- Anderson, D.N., J.M. Forbes, and M. Codrescu (1989). "A Fully Analytical Low- and Middle-Latitude Ionospheric Model." *Journal of Geophysical Research*, Vol. 94, No. A2, pp. 1520-1524.
- Anderson, D.N., M. Mendillo, and B. Herniter (1987). "A Semi-Empirical Low-Latitude Ionospheric Model." *Radio Science*, Vol. 22, No. 2, pp. 292-306.
- Anderson, H. and L. Johnson (1996). "Ionospheric Climatology from TOPEX/Poseidon Measurements." In the *Report of the Workshop for Ionospheric Delay Correction For Single-Frequency Radar Altimetry*, Colorado Center for Astrodynamics Research of the University of Colorado, 24-25 September.
- ARINC Research Corporation (1992). GPS Interface Control Document ICD-GPS-200: Navstar GPS Space Segment and Aviation User Interfaces. Fountain Valley, California.
- Ashtech (1997) "Ashtech Z-12 Field Surveyor GPS Receiver Technical Specifications." <http://www.ashtech.com/pages/products/surveying/z-12-field.html>. Accessed 4 July 1997.
- Austen, J.R., S.J. Franke, and C.H. Liu (1988). "Ionospheric Imaging Using Computerized Tomography." *Radio Science*, Vol. 23, No. 3, pp. 299-307.
- Bassiri, S. and G. A. Hajj (1993). "Higher-Order Ionospheric Effects on the Global Positioning System Observables and Means of Modelling Them." *Manuscripta Geodaetica*, Vol. 18, pp. 280-289.
- Bent, R.B. and S.K. Liewellyn (1973). Documentation and Description of the Bent Ionospheric Model. Space and Missiles Organization, Los Angeles, CA. AFCRL-TR-73-0657.
- Beutler, G. (1995). "Extracting Information Concerning the Ionosphere Using the IGS Network." *EOS Transactions of the American Geophysical Union*, Vol. 76, No. 17, Supplement, p. 86 (abstract).
- Bilitza, D. (ed.) (1990). International Reference Ionosphere 1990. Report Number NSSDC/WDC-A-R&S 90-22, National Space Science Data Center/World Data Center A for Rockets and Satellites, Lanham, MD.

- Bilitza, D. (1996a). "International Reference Ionosphere 1995." National Space Science Data Center, <http://nssdc.gsfc.nasa.gov/space/model/ionos/iri.html>. Accessed 9 December 1996.
- Bilitza, D. (1996b). "Improved IRI Model for Single-Frequency Altimeters." In the *Report of the Workshop for Ionospheric Delay Correction for Single-Frequency Radar Altimetry*, Colorado Center for Astrodynamics Research of the University of Colorado, 24-25 September.
- Bishop, G.J., D.S. Coco, and C. Coker (1991). "Variations in Ionospheric Range Error with GPS Look Direction." *Proceedings of ION GPS-91, the 4th International Technical Meeting of the Satellite Division of The Institute of Navigation*, Albuquerque, NM, 11-13 September, The Institute of Navigation, Alexandria, VA, pp. 1045-1054.
- Bishop, G.J., S. Basu, K. Groves, M. Smitham, K. Lehneis, D. Jacobs, P. Gehred, D. Howell, G. Bainum, and D. Goldizen (1996). "Upcoming Ionospheric Impacts on GPS at Solar Max: What Do We Know/What Do We Need?" *Proceedings of ION GPS-96, the 9th International Technical Meeting of the Satellite Division of The Institute of Navigation*. Kansas City, MO, 17-20 September, The Institute of Navigation, Alexandria, VA, pp. 595-604.
- Bishop, G.J., A.J. Mazzella, and E.A. Holland (1995). "Application of Score Techniques to Improve Ionospheric Observations" *Proceedings of ION GPS-95, the 8th International Technical Meeting of the Satellite Division of The Institute of Navigation*, Palm Springs, CA, 12-15 September, The Institute of Navigation, Alexandria, VA, pp. 1209-1218.
- Born, G. and S. Katzberg (1996). "Introductory Remarks, Science Requirements." In the *Report of the Workshop for Ionospheric Delay Correction for Single-Frequency Radar Altimetry*, Colorado Center for Astrodynamics Research of the University of Colorado, 24-25 September.
- Brunini, C. and A. Kleusberg (1996). "Mapas Globales de Retardo Ionosferico Vertical a Partir de Observaciones GPS." *Proceedings of the Fourth International Congress on Earth Sciences*, Santiago, Chile, August 5 -9 (in press).
- Brunner, F.K. and M. Gu (1991). "An Improved Model for the Dual Frequency Ionospheric Correction of GPS Observations." *Manuscripta Geodaetica*, Vol. 16, No. 3, pp. 205-214.
- Chao, Y., Y. Tsai, T. Walter, C. Kee, P. Enge, and B. Parkinson (1996). "An Algorithm for Inter-Frequency Bias Calibration and Application to WAAS Ionospheric Modelling." *ION GPS-95, Proceedings of the 8th International Technical Meeting of*

the Satellite Division of The Institute of Navigation, Palm Springs, CA, 12-15 September, The Institute of Navigation, Alexandria, VA, pp. 639-646.

Chiu, Y.T. (1975). "An Improved Phenomenological Model for Ionospheric Density" *Journal of Atmospheric and Terrestrial Physics*, Vol. 37, pp. 1563-1570.

Clynch, J.R., D.S. Coco, C. Coker, and G.J. Bishop (1989). "A Versatile GPS Ionospheric Monitor: High Latitude Measurements of TEC and Scintillation." *Proceedings of ION GPS-89, the 2nd International Technical Meeting of the Satellite Division of The Institute of Navigation*, Colorado Springs, CO, 22-27 September, The Institute of Navigation, Washington, pp. 445-450.

Coco, D.S., C. Coker, and J.R. Clynch (1990). "Mitigation of Ionospheric Effects for Single-Frequency GPS Users." *ION-GPS-90, Proceedings of the 3rd International Technical Meeting of the Satellite Division of the Institute of Navigation*, Colorado Springs, CO, 19-21 September, The Institute of Navigation, Washington, pp. 169-174.

Coco, D.S., C.E. Coker, S.R. Dahlke, and J.R. Clynch (1991). "Variability of GPS Satellite Differential Group Delay Biases." *IEEE Transactions on Aerospace Systems*, Vol. 27, No. 6, pp. 931-938.

Cohen, C.E., B. Pervan, and B.W. Parkinson (1992). "Estimation of Absolute Ionospheric Delay Exclusively Through Single-Frequency GPS Measurements." *Proceedings of ION GPS-92, the 5th International Technical Meeting of the Satellite Division of The Institute of Navigation*, Albuquerque, NM, 16-18 September, The Institute of Navigation, Alexandria, VA, pp. 325-330.

Coker, C., G. Bust, and G. Kronschnabl (1996). "Ionospheric Specification Using Ionospheric Tomography and GPS: Improving Single-Frequency Altimeter Data By Specifying the Ionosphere in 4D Using Computerized Ionospheric Tomography and GPS Total Electron Content." In the *Report of the Workshop for Ionospheric Delay Correction for Single-Frequency Radar Altimetry*, Colorado Center for Astrodynamics Research of the University of Colorado, Boulder, CO, 24-25 September.

Coster, A.J., E.M. Gaposchkin, and L.E. Thornton (1992). "Real-Time Ionospheric Monitoring System Using GPS." *Navigation: Journal of the Institute of Navigation*, Vol. 39, No. 2, pp. 191-204.

Danaher, J., A. Balendra, M. Danaher, E. Erpelding, R. Gerlach, and J. Baser (1993). "GLONASS Dual Frequency Ionosphere Sounder." *Proceedings of the 6th International Technical Meeting of the Satellite Division of The Institute of Navigation*, Salt Lake City, UH, 22-24 September, The Institute of Navigation, Alexandria, VA, pp. 1363-1372.

- Daniell, R.E. and D.N. Anderson (1996). "Future Plans for PRISM Development." In the *Report of the Workshop for Ionospheric Delay Correction for Single-Frequency Radar Altimetry*, Colorado Center for Astrodynamics Research of the University of Colorado, Boulder, CO, 24-25 September.
- Daniell, R.E., L.D. Brown, D.N. Anderson, M.W. Fox, P.H. Doherty, D.T. Decker, J.J. Sojka, and R.W. Schunk (1995). "Parameterized Ionospheric Model: A Global Ionospheric Parameterization Based on First Principles Models." *Radio Science*, Vol. 30, No. 5, pp. 1499-1510.
- Daniell, R.E., L.D. Brown, and R.W. Simon (1996). "A New Improved Ionospheric Correction Algorithm for Single Frequency GPS Receivers." *Proceedings of ION GPS-96, the 9th International Technical Meeting of the Satellite Division of The Institute of Navigation*. Kansas City, MO, 17-20 September, The Institute of Navigation, Alexandria, VA, pp. 635-640.
- Davies, K. (1966). *Ionospheric Radio Propagation*. Dover Publications, Inc., New York.
- Davies, K. (1990). *Ionospheric Radio*. Peter Peregrinus Ltd., London, United Kingdom.
- DLR Fernerkundungsstation Neustrelitz (1995). Ionospheric Database, <ftp://ftp.nz.dlr.de/pub/navigation/bias>. Accessed 15 December 1995.
- El-Arini, M.B., R.S. Conker, T.W. Albertson, J.K. Reagan, J.A. Klobuchar, and P.H. Doherty (1994). "Comparison of Real-Time Ionospheric Algorithms For a GPS Wide-Area Augmentation System (WAAS)." *Navigation: Journal of Institute of Navigation*, Vol. 41, No. 4, pp. 393-413.
- European Space Agency's European Space Operations Centre (ESA/ESOC) (1996). Ionospheric Database, ftp://nng.esoc.esa.de/pub/gps_data/GPS_IONO, Accessed 14 February 1996.
- Feltens, J. (1996). "Ionosphere Models - A New Product of IGS?" In *Proceedings of the 1996 IGS Workshop*, Silver Spring, MD, 19-21 March, pp. 177-179.
- Feltens, J., J.M. Dow, T.J. Martin-Mur, C. Garcia Martinez, and M.A. Bayona-Perez (1996). "Verification of ESOC Ionospheric Modeling and Status of IGS Intercomparison Activity." In *Proceedings of the 1996 IGS Workshop*, Silver Spring, MD, 19-21 March, pp. 205-219.
- Flechtner, F. (1997). "Modelling of the Ionosphere with PRARE." Presented at the Joint COST/IRI Workshop "New Developments in Ionospheric Modelling and Prediction." Institute of Atmospheric Physics, Kühlungsborn, Germany, 27-30 May.

- Frey Mueller, J. (1995). Department of Geophysics, Stanford University, Stanford, CA, Personal communication, 15 January.
- Frey Mueller, J. (1997). "GPS Technology." GPSTech Mailing List, gpstech@cotopaxi.stanford.edu.
- Gail, W.B., B. Prag, D.S. Coco, and C. Coker (1993). "A Statistical Characterization of Local Mid-latitude Total Electron Content." *Journal of Geophysical Research*, Vol. 98, No. A9, pp. 15,717-15,727.
- Gallagher, D.L. (1996). Marshall Space Flight Center, Huntsville, AL, Personal communication, September 1996.
- Gallagher, D.L., P.D. Craven, and R.H. Comfort (1988). "An Empirical Model of the Earth's Plasmasphere." *Advances in Space Research*, Vol. 8, No. 8, pp. (8)15-(8)24.
- Gao, Y., P. Heroux, and J. Kouba (1994). "Estimation of GPS Receiver and Satellite L1/L2 Signal Delay Biases Using Data from CACS." *Proceedings of KIS94, the International Symposium on Kinematic Systems in Geodesy, Geomatics, and Navigation*, Banff, Alberta, Canada, 30 August - 2 September, Department of Geomatics Engineering, The University of Calgary, Calgary, Alberta, Canada, pp. 109-117.
- Geoforschungszentrum (1997). "Two-Way PRARE." Geoforschungszentrum Potsdam Home Page, <http://www.gfz-potsdam.de/pb1/PRARE/PRARE-2way.html>, Accessed 27 January 1997.
- Georgiadou, Y. and A. Kleusberg (1988). "On the Effect of Ionospheric Delay on Geodetic Relative GPS Positioning." *Manuscripta Geodaetica*, Vol. 13, No. 1, pp. 1-8.
- Gold, K. (1996). Colorado Center for Astrodynamics Research of the University of Colorado, Personal communication, 5 September.
- Gold, K., G. Born, J. Armstrong, and G. Davis (1996). "Results of Assimilating GPS Data into PRISM 1.6." In the *Report of the Workshop for Ionospheric Delay Correction for Single-Frequency Radar Altimetry*, Colorado Center for Astrodynamics Research of the University of Colorado, Boulder, CO, 24-25 September.
- Hajj, G. and L. Romans (1996). "Ionospheric Profiling Using GPS/Met Data." *Proceedings of the 1996 IGS Workshop*, Silver Spring, MD, 19-21 March, pp. 379-396.
- Hakegard, O.P. (1995). *A Regional Ionospheric Model for Real-time Predictions of the Total Electron Content in Wide Area Differential Satellite Navigation Systems*. Dr.

Eng. thesis, Norwegian Institute of Technology, Trondheim, Norway, Rapport 429506.

Hall, M.P.M. and L.W. Barclay (1989). *Radiowave Propagation*, Peter Peregrinus Ltd., London, United Kingdom.

Haystack Observatory (1996a). "Sample Ionogram without Frequency Restrictions." Millstone Hill Observatory Home Page, <http://digisonde.haystack.edu/sample.gif>. Accessed 5 February 1996.

Haystack Observatory (1996b). "Incoherent Scatter Radar Tutorial." Millstone Hill Observatory Home Page, <http://www.haystack.edu/midas/inscal.html>. Accessed 27 November 1996.

Ho, C.M., A.J. Mannucci, U.J. Lindqwister, X. Pi, and B.T. Tsurutani (1996). "Global Ionosphere Perturbations Monitored by the Worldwide GPS Network." *Geophysical Research Letters*, Vol. 23, No. 22. pp. 3219-3222.

Hoffmann-Wellenhof, B., H. Lichtenegger, and J. Collins (1994). *GPS Theory and Practice*, 3rd rev. ed., Springer-Verlag Wien, Vienna, Austria.

Howe, B. (1996). "Simulations of Ionospheric Tomography." In the *Report of the Workshop for Ionospheric Delay Correction for Single-Frequency Radar Altimetry*, Colorado Center for Astrodynamics Research of the University of Colorado, Boulder, CO, 24-25 September.

Hunsucker, R.D. (1991) *Radio Techniques for Probing the Ionosphere*, Springer-Verlag, New-York.

Jakowski, N. and E. Sardon (1996). "Comparison of GPS/IGS-Derived TEC Data with Parameters Measured by Independent Ionospheric Probing Techniques." *Proceedings of the 1996 IGS Workshop*, Silver Spring, MD, 19-21 March, pp. 221-230.

Jakowski, N., E. Sardon, E. Engler, A. Jungstand, and D. Klän (1996). "Relationships Between GPS-Signal Propagation Errors and EISCAT Observations." *Annales Geophysicae*, Vol. 14, pp. 1429-1436.

Junkins J.L., G.W. Miller, and J.R. Jancaitis (1973). "A Weighting Function Approach to Modelling of Irregular Surfaces." *Journal of Geophysical Research*, Vol. 78, No. 11, pp. 1794-1803.

Kaplan, E.D. (ed.) (1996). *Understanding GPS Principles and Applications*, Artech House, Boston.

- Kleusberg, A. (1986). "Ionospheric Propagation Effects in Geodetic Relative GPS Positioning." *Manuscripta Geodaetica*, Vol. 11, No. 4, pp. 256-261.
- Kleusberg, A. (1990). "Comparing GPS and GLONASS." *GPS World*, Vol. 1, No. 6, pp. 52-54.
- Kleusberg, A. and P. Teunissen (eds.) (1996). *GPS for Geodesy*, International School, Delft, The Netherlands, 26 March - 1 April, 1995. Springer-Verlag, New York.
- Klobuchar, J.A. (1975). "A First-order Worldwide Ionospheric Delay Algorithm." Air Force Cambridge Research Laboratories, Hanscom AFB, MA, AFCRL-TR-75-0502.
- Klobuchar, J.A. (1986). "Design and Characteristics of the GPS Ionospheric Time Delay Algorithm for Single-Frequency Users." *Proceedings of the PLANS-86 conference*, Las Vegas, NV, 4-7 November, pp. 280-286.
- Klobuchar, J.A. (1991). "Ionospheric Effects on GPS." *GPS World*, Vol. 2, No. 4, pp. 48-51.
- Klobuchar, J.A. and P. H. Doherty (1990). "The Statistics of Ionospheric Time Delay for GPS Ranging on L1." *Proceedings of the ION GPS-90, the 3rd International Technical Meeting of the Satellite Division of The Institute of Navigation*, Colorado Springs, CO, 19-21 September, The Institute of Navigation, Washington, DC, pp. 161-168.
- Klobuchar, J.A. (1996). "Ionospheric Effects on GPS." in *Global Positioning System: Theory and Applications*, Volume 163, Progress in Astronautics and Aeronautics, American Institute of Aeronautics and Astronautics, Washington, DC.
- Komjathy, A. and R.B. Langley (1995). *The Halifax GPS Precision Approach Trial: A Report on In-Depth Data Analysis*. Final Report for Transport Canada Aviation, February, 249 pp.
- Komjathy, A. and R.B. Langley (1996a). "An Assessment of Predicted and Measured Ionospheric Total Electron Content Using a Regional GPS Network." *The Proceedings of the National Technical Meeting of the Institute of Navigation*, Santa Monica, CA, 22-24 January, The Institute of Navigation, Alexandria, VA, pp. 615-624.
- Komjathy A. and R.B. Langley (1996b). "Towards an Improved Ionospheric Modelling Technique for Single-frequency GPS Users: A Sensitivity Analysis." Presented at the Faculty of Electrical Engineering of the Czech Technical University, Prague, Czech Republic, 1 March, Overheads available on the World Wide Web server of the Geodetic Research Laboratory of the University of New Brunswick, Canada in

PostScript format at <<http://gauss.gge.unb.ca/grads/attila/papers/papers.htm>>. Accessed 17 June 1997.

- Komjathy, A. and R.B. Langley (1996c). "High Precision Ionospheric Modelling: Results, Facts and Limitations." Presented at the Satellite Geodetic Observatory, Penc, Hungary, 5 March.
- Komjathy, A. and R.B. Langley (1996d). "The Effect of Shell Height on High Precision Ionospheric Modelling Using GPS." In *Proceedings of the 1996 IGS Workshop*, Silver Spring, MD, 19-21 March, pp. 193-203.
- Komjathy, A. and R.B. Langley (1996e). "Improvement of a Global Ionospheric Model to Provide Ionospheric Range Error Corrections for Single-frequency GPS Users." *The Proceedings of the 52nd Annual Meeting of the Institute of Navigation*, Cambridge, MA, 19-21 June, The Institute of Navigation, Alexandria, VA, pp. 557-566.
- Komjathy, A. and R.B. Langley (1997a). "Ionospheric Delay Correction for Single-Frequency Radar Altimetry." Presented at the Jet Propulsion Laboratory, Pasadena, CA, 12 March.
- Komjathy, A. and R.B. Langley (1997b). "Temporal and Spatial Variation of the Global Ionosphere." MPEG movies for 13-15 March 1993, and 6-8 April 1995, <http://gauss.gge.unb.ca/grads/attila/movie/>. Accessed 8 June 1997.
- Komjathy, A., R.B. Langley, and D. Bilitza (1996a). "Updating the International Reference Ionosphere Using a Global Network of GPS Stations: Preliminary Results." In the *Report of the Workshop for Ionospheric Delay Correction for Single-Frequency Radar Altimetry*, Colorado Center for Astrodynamics Research of the University of Colorado, Boulder, CO, 24-25 September.
- Komjathy, A., R.B. Langley, and D. Bilitza (1997). "Ingesting GPS-Derived TEC Data into the International Reference Ionosphere for Single-Frequency Radar Altimeter Ionospheric Delay Corrections." Presented at the Workshop for "New Developments in Ionospheric Modelling and Prediction" at the Institute of Atmospheric Physics (Institut für Atmosphärenphysik, IAP), Kühlungsborn, Germany, 27-31 May.
- Komjathy, A., R.B. Langley, and F. Vejraska (1995). "A Comparison of Predicted and Measured Ionospheric Range Error Corrections." *EOS Transactions of the American Geophysical Union*, Vol. 76, No. 17, Supplement, p. 87 (abstract).
- Komjathy, A., R.B. Langley, and F. Vejraska (1996b). "Assessment of Two Methods to Provide Ionospheric Range Error Corrections for Single-frequency GPS Users." In *GPS Trends in Precise Terrestrial, Airborne, and Spaceborne Applications, the Proceedings of International Association of Geodesy Symposium*, No. 115, Boulder, CO, 3-4 July 1995, Springer-Verlag, New York, pp. 253-257.

- Langley, R.B. (1992). "The Effect of the Ionosphere and Troposphere on Satellite Positioning Systems." *Proceedings of Symposium on Refraction of Transatmospheric Signals in Geodesy*, J.C. de Munck, and T.A. Spoelstra (Eds.) Netherlands Geodetic Commission, Publications on Geodesy, New Series No. 36, The Hague, The Netherlands, 19-22 May, p. 97 (abstract). The paper is available on the University of New Brunswick's Web server at <http://gauss.gge.unb.ca/canspace/UNB.DENHAAG.ATMOS.PAPER.PS.Z>
- Langley, R.B. (1996). "Propagation of the GPS Signals" in *GPS for Geodesy*, International School, Delft, The Netherlands, 26 March - 1 April, 1995. Springer-Verlag, New York.
- Langley, R.B. (1997a). "Navstar GPS Internet Connections." <http://gauss.gge.unb.ca/GPS.INTERNET.SERVICES.HTML>. Accessed 26 January 1997.
- Langley, R.B. (1997b). "Canadian Space Geodesy Forum." CANSPACE Mailing List, canspace@unb.ca.
- Langley, R.B. (1997c). "The GPS Error Budget." *GPS World*, Vol. 8, No. 3, pp. 51-56.
- Langley, R.B. (1997d). "GLONASS: Review and Update." *GPS World*, Vol. 8, No. 7, 46-51.
- Langley, R.B. and A. Komjathy (1996). "High Precision Ionospheric Total Electron Count Mapping Using the Navstar Global Positioning System" Presented at the American Geophysical Union Western Pacific Geophysics Meeting, Brisbane, Australia, 23-27 July 1996.
- Langley, R.B., K. Doucet, and A. Kleusberg (1991). "The Testing of Global Positioning System Receivers under Ionospheric Influences." *Energy, Mines and Resources Canada*, Ottawa, EMR Contract Report No. 91-006, Geodetic Research Laboratory, Department of Surveying Engineering, University of New Brunswick, Fredericton, N.B., Canada.
- Langley, R.B., G. Beutler, D. Delikaraoglou, B. Nickerson, R. Santerre, P. Vanicek, and D.E. Wells (1984). "Studies in the Application of the Global Positioning System to Differential Positioning." Department of Surveying Engineering Technical Report No. 108, University of New Brunswick, Fredericton, N.B., Canada.
- Lanyi, G.E. and T. Roth (1988). "A Comparison of Mapped and Measured Total Ionospheric Electron Content Using Global Positioning System and Beacon Satellite Observations." *Radio Science*, Vol. 23, No. 4, pp. 483-492.

- Lechner, W, C. Reigber, and H. Wilmes (1989). "The Precise Range and Range Rate Equipment PRARE: System Description and Future Perspectives." *Proceedings of the 2nd International Technical Meeting of the Satellite Division of The Institute of Navigation*, Colorado Springs, CO, September 27-29, pp. 67-70.
- Leick, A. (1995). *GPS Satellite Surveying*. 2nd ed., John Wiley & Sons, Inc., New York.
- Leitinger, R., G.K. Hartmann, F.-J. Lohmar, and E. Putz (1984). "Electron Content Measurement with Geodetic Doppler Receivers." *Radio Science*, Vol. 19, No. 3, pp. 789-797.
- Levy, M.F. and R.A. Bamford (1997). "Validation of N(H) Profile Models by Oblique Incidence Sounding Data." Presented at the Joint COST/IRI Workshop "New Developments in Ionospheric Modelling and Prediction." Institute of Atmospheric Physics, Kühlungsborn, Germany, 27-30 May.
- Loh, R., V. Wullschlegel, B. Elrod, M. Lage, and F. Haas (1995). "The U.S. Wide-Area Augmentation System (WAAS)." *Navigation: Journal of The Institute of Navigation*, Vol. 42, No 3, pp. 435-465.
- Loh, R. (1995). "GPS Wide Area Augmentation System" *The Journal of Navigation*, The Royal Institute of Navigation, Cambridge University Press, Vol. 48, No 2, pp. 180-191.
- Mannucci, A. J., B.D. Wilson, and C.D. Edwards (1993). "A New Method for Monitoring the Earth's Ionospheric Total Electron Content Using the GPS Global Network." *Proceedings of ION GPS-93, the 6th International Technical Meeting of the Satellite Division of The Institute of Navigation*, Salt Lake City, UT, 22-24 September, The Institute of Navigation, Alexandria, VA, pp. 1323-1332.
- Mannucci, A.J., B. Wilson, and D. Yuan (1995). "An Improved Ionospheric Correction Method for Wide-Area Augmentation Systems." *Proceedings of ION GPS-95, the 8th International Technical Meeting of the Satellite Division of The Institute of Navigation*, Palm Springs, CA, 12-15 September, The Institute of Navigation, Alexandria, VA, pp. 1199-1208.
- McNamara, L.F. (1991). *The Ionosphere: Communications, Surveillance, and Direction Finding*. Krieger Publishing Company, Malabar, FL.
- McNamara, L.F. (1994). *Radio Amateurs Guide to the Ionosphere*. Krieger Publishing Company, Malabar, FL.
- McNamara, L.F. and O.J. Wilkinson (1983). "Prediction of Total Electron Content Using the International Reference Ionosphere." *Journal of Atmospheric and Terrestrial Physics*, Vol. 45, No. 2/3, pp. 169-174.

- Melbourne, W.G., E.S. Davis, C.B. Duncan, G.A. Hajj, K.R. Hardy, E.R. Hardt, E.R. Kursinski, T.K. Meehan, L.E. Young, and T.P. Yunck (1994). "The Application of Spaceborne GPS to Atmospheric Limb Sounding and Global Change Monitoring." JPL Publication 94-18, Jet Propulsion Laboratory, Pasadena, CA.
- National Geophysical Data Center, NGDC (1997a). Geomagnetic Database, ftp://ftp.ngdc.noaa.gov/STP/GEOMAGNETIC_DATA/INDICES/KP_AP/1994. Accessed 13 June 1997.
- National Geophysical Data Center, NGDC (1997b). Solar Sunspot Number Database, ftp://ftp.ngdc.noaa.gov/STP/SOLAR_DATA/SUNSPOT_NUMBERS/SMOOTHED. Accessed 13 June 1997.
- National Research Council (NRC) of Canada (1997). Dominion Radio Astrophysical Observatory, DRAO 10cm SOLAR RADIO NOISE PATROL Database, http://www.drao.nrc.ca/icarus/www/sol_home.shtml. Accessed 13 June 1997.
- National Space Science Data Center, NSSDC (1996a). Ionosphere, <http://nssdc.gsfc.nasa.gov/space/model/ionos/ccir.html>. Accessed 26 May 1996.
- National Space Science Data Center, NSSDC (1996b). Ionospheric Indices, <http://www.ngdc.noaa.gov:80/stp/iono/if2ig.html>. Accessed 18 May 1996.
- Newby, S.P. (1992). *An Assessment of Empirical Models for the Prediction of the Transionospheric Propagation Delay of Radio Signals*. M.Sc.E. thesis, Department of Surveying Engineering Technical Report No. 160, University of New Brunswick, Fredericton, N.B., Canada.
- Newby, S.P. and R.B. Langley (1992). "Three Alternative Empirical Ionospheric Models — Are They Better Than the GPS Broadcast Model?" *Proceedings of 6th International Geodetic Symposium on Satellite Positioning*, Columbus, OH, 17-20 March, pp. 240-244.
- Newby, S.P., R.B. Langley, and H.W. Janes (1990). "Ionospheric Modelling for Single Frequency Users of the Global Positioning System: A Status Report." In *Proceedings of 2nd International Symposium on Precise Positioning with the Global Positioning System*, Ottawa, Ontario, Canadian Institute of Surveying and Mapping, pp. 429-443.
- Pakula, W.A., P.F. Fougere, J.A. Klobuchar, H.J. Kuenzler, M.J. Buonsanto, J.M. Roth, and J.C. Foster. (1995). "Tomographic Reconstruction of the Ionosphere Over North America With Comparisons To Ground-based Radar." *Radio Science*, Vol. 30, No. 1, pp. 89-103.

- Parkinson B.W., J.J. Spilker, P. Axelrad, and P. Enge (eds.) (1996). *Global Positioning System: Theory and Applications*, Volume 163, Progress in Astronautics and Aeronautics, American Institute of Aeronautics and Astronautics, Washington, DC.
- Picot, N. (1997). French Space Agency (CNES), Personal communication, 15 April 1997.
- Picot, N. and P. Escudier (1996). "DORIS Ionospheric Results." In the *Report of the Workshop for Ionospheric Delay Correction for Single-Frequency Radar Altimetry*, Colorado Center for Astrodynamics Research of the University of Colorado, Boulder, CO, 24-25 September.
- Press, W.H., B.P. Flannery, S.A. Teukolsky, and W.T. Vetterling (1986). *Numerical Recipes The Art of Scientific Computing*, Cambridge University Press, Cambridge.
- Ratcliffe, J.A. (1970). *Sun, Earth and Radio*. McGraw-Hill Book Company, New York.
- Raymund, T. (1993). *Development and Applications of Ionospheric Tomography*. Ph.D. thesis, University of Illinois at Urbana-Champaign, Urbana-Champaign, IL.
- Raymund, T. (1997) Center for Ionospheric Research at the Applied Research Laboratories of the University of Texas at Austin, Personal communication, traymund@arlut.utexas.edu. 6 July 1997.
- Rishbeth, H. and O.K. Garriott (1969). *Introduction to Ionospheric Physics*, Academic Press, New York.
- Runge, T., U. Lindqwister, A. Mannucci, M. Reyes, B. Wilson, and D. Yuan (1995). "Generation of GPS Observables for Global Ionospheric Mapping." *EOS Transactions of the American Geophysical Union*, Vol. 76, No. 17, Supplement, p. 87 (abstract).
- Salzmann, M.A. (1988). *Some Aspects of Kalman Filtering*. Department of Surveying Engineering Technical Report No. 140, University of New Brunswick, Fredericton, N.B., Canada.
- Santerre, R. (1989). *GPS Satellite Sky Distribution: Impact on the Propagation of Some Important Errors in Precise Relative Positioning*. Ph.D. Dissertation, Department of Surveying Engineering Technical Report No. 145, University of New Brunswick, Fredericton, N.B., Canada.
- Sardon, E. (1996). "Description of the Modelling Technique at DLR." Message Sent to "GPS for IONospheric Research" (IONO) Mailing List maintained by UNB, esardon@gmv.es, 15 February 1996.

- Sardon, E., N. Jakowski, and N. Zarraoa (1995). "Permanent Monitoring of TEC Using GPS Data: Scientific and Practical Aspects." *EOS Transactions of the American Geophysical Union*, Vol. 76, No. 17, Supplement, p. 87 (abstract).
- Sardon, E., A. Rius, and N. Zarraoa (1994). "Estimation of the Transmitter and Receiver Differential Biases and the Ionospheric Total Electron Content from Global Positioning System Observations." *Radio Science*, Vol. 29, No. 3, pp. 577-586.
- Satellite Encyclopedia Online, The (1997). "Alouette Missions." <http://www.tele-satellit.com/tse/online/index.shtml>. Accessed 26 January 1997.
- Schaer, S., G. Beutler, L. Mervart, and M. Rothacher (1995). "Global and Regional Ionosphere Models Using the GPS Double Difference Phase Observable." *Proceedings of the 1995 IGS Workshop*, Potsdam, Germany, 15-17 May, pp. 77-92.
- Schaer, S., G. Beutler, M. Rothacher, and T.A. Springer (1996). "Daily Global Ionospheric Maps on GPS Carrier Phase Data Routinely Produced by CODE Analysis Center." *Proceedings of the 1996 IGS Workshop*, Silver Spring, MD, 19-21 March, pp. 181-192.
- Schreiner, W. and M. Exner (1996). "GPS/Met Ionospheric Results at UCAR". In the *Report of the Workshop for Ionospheric Delay Correction for Single-Frequency Radar Altimetry*, Colorado Center for Astrodynamics Research of the University of Colorado, Boulder, CO, September 24-25.
- Schwarz, K.P. (1987). "Kalman Filtering and Optimal Smoothing." *Papers for the CISM Adjustment and Analysis Seminars*, 2nd ed., The Canadian Institute of Surveying and Mapping, Ottawa, Ontario, Canada, pp. 230-264.
- Scripps Orbit and Permanent Array Center (SOPAC) (1996). "SOPAC Data Browser." <http://lox.ucsd.edu/docs/static/other.html>. Accessed 8 August 1996.
- Seeber, G. (1993). *Satellite Geodesy*, Walter de Gruyter, Berlin.
- Serway, A.R. (1986). *Physics for Scientists and Engineers*, 2nd ed., Saunders College Publishing, New York.
- SPACEWARN Bulletin SPX-520 (1997). "SPACEWARN Activities: A Publication of NASA NSSDC/WDC-A-R&S and the WWAS for ISES/COSPAR." <http://nssdc.gsfc.nasa.gov/spacewarn/spx520-catiradiobeacon.html>. 4 July 1997.
- Stewart, P. (1997). "The Reduction of Differential Ionospheric Delay for GPS Carrier Phase Ambiguity Resolution." M.Sc.Eng. Thesis, Department of Geodesy and Geomatics Engineering, University of New Brunswick, Fredericton, N.B., Canada.

- Tascione, T.F. (1988). *Introduction to Space Environment*, Orbit Book Company, Malibar, Florida.
- Titheridge, J.E. (1972). "Determination of Ionospheric Electron Content from the Faraday Rotation of Geostationary Satellite Signals." *Planetary Space Science*, Vol. 20, pp. 353-369.
- Titheridge, J.E. (1988). "The Real Height Analysis of Ionograms: A Generalized Formulation." *Radio Science*, Vol. 23, pp. 831-849.
- TOPEX/Poseidon (1997). "TOPEX/Poseidon: The Ocean Topography Experiment." <http://topex-www.jpl.nasa.gov/>. Accessed 10 January 1997.
- Urban, T., P.A.M. Abusali, and C.K. Shum (1996). "Comparison of Ionospheric Models for Single Frequency Altimeters." In the *Report of the Workshop for Ionospheric Delay Correction for Single-Frequency Radar Altimetry*, Colorado Center for Astrodynamics Research of the University of Colorado, Boulder CO, 24-25 September.
- Xia R. (1992). "Determination of Absolute Ionospheric Error Using a Single Frequency GPS Receiver." *Proceedings of ION GPS-92, the 5th International Technical Meeting of the Satellite Division of The Institute of Navigation*, Albuquerque, NM, 16-18 September, The Institute of Navigation, Alexandria, VA, pp. 483-490.
- Yeh, K.C. and T.D. Raymund (1991). "Limitations of Ionospheric Imaging by Tomography." *Radio Science*, Vol. 26, No. 6, pp. 1361-1380.
- Yuan, D., B. Wilson, A. Mannucci, and U. Lindqwister (1996). "Using GPS for Single-Frequency Altimeter Calibration." In the *Report of the Workshop for Ionospheric Delay Correction for Single-Frequency Radar Altimetry*, Colorado Center for Astrodynamics Research of the University of Colorado, Boulder, CO, 24-25 September.
- van der Wal, A.D. (1995). *Evaluation of Strategies for Estimating Residual Neutral-atmosphere Propagation Delay in High Precision Global Positioning System Data Analysis*. M.Sc.Eng. thesis, Department of Geodesy and Geomatics Engineering Technical Report No. 177, University of New Brunswick, Fredericton, N.B., Canada.
- Vanicek, P. and E.J. Krakiwsky (1986). *Geodesy, the Concepts.*, 2nd rev. ed., North-Holland, Amsterdam, The Netherlands.
- Walford, J. (1995). *GPS Subsidence Study of the Costa Bolivar Oil Field, Venezuela*. M.Sc.E. thesis, Department of Geodesy and Geomatics Engineering Technical Report No. 174, University of New Brunswick, Fredericton, N.B., Canada.

- Wanninger, L. (1993). "Effects of the Equatorial Ionosphere on GPS." *GPS World*, Vol. 4, No. 7, pp. 48-53.
- Webster, I.R. (1993). *A Regional Model for the Prediction of Ionospheric Delay for Single Frequency Users of the Global Positioning System*. M.Sc.Eng. thesis, Department of Surveying Engineering Technical Report No. 166, University of New Brunswick, Fredericton, N.B., Canada.
- Wells, D.E., N. Beck, D. Delikaraoglou, A. Kleusberg., E.J. Krakiwsky, G. Lachapelle, R.B. Langley, M. Nakiboglu, K.P. Schwarz, J.M. Tranquilla, and P. Vanícek (1987). *Guide to GPS Positioning*, Canadian GPS Associates, Fredericton, N.B., Canada
- Wells, D., R.B. Langley, A. Komjathy, and D. Dodd (1995) "Acceptance Tests on Ashtech Z-12 Receivers." Final Report for Public Works and Government Services Canada, February.
- Wild, U. (1994). *Ionosphere and Geodetic Satellite Systems: Permanent GPS Tracking Data For Modelling and Monitoring*, Ph.D. dissertation, Geodätische-geophysikalische Arbeiten in der Schweiz, Zürich, Switzerland, Vol. 48.
- Wilson, B.D. and A.J. Mannucci (1993). "Instrumental Biases in Ionospheric Measurements Derived from GPS Data." *Proceedings of ION GPS-93, the 6th International Technical Meeting of the Satellite Division of The Institute of Navigation*, Salt Lake City, UT, 22-24 September, The Institute of Navigation, Alexandria, VA. pp. 1343-1351.
- Wilson, B.D. and A.J. Mannucci (1994). "Extracting Ionospheric Measurements from GPS in the Presence of Anti-spoofing." *Proceedings of ION GPS-94, the 7th International Technical Meeting of the Satellite Division of The Institute of Navigation*, Salt Lake City, UT, 20-23 September, The Institute of Navigation, Alexandria, VA., Vol. 2, pp. 1599-1608.
- Zarraoa, N, E. Sardon, D. Klähn, and A. Jungstand (1995). "Evaluation of GLONASS Performance in Practical Application: Comparison with GPS-based Ionospheric TEC Values." *Proceedings of ION GPS-95, the 8th International Technical Meeting of the Satellite Division of The Institute of Navigation*, Palm Springs, CA, 12-15 September, The Institute of Navigation, Alexandria, VA, pp. 1031-1039.

APPENDIX 1

KALMAN FILTER ESTIMATION

The literature dealing with Kalman filtering is extensive. I followed Salzmann [1988], Schwarz [1987], Coster et al. [1992] and van der Wal [1995] during the design stage of the filter. In this appendix, I used the standard notation by van der Wal [1995] which is based on the standards for the UNB Differential Positioning Program package [Langley et al., 1984].

Kalman filtering includes a sequential estimation of states where they are based on past and present observations. The main components of Kalman filtering are the dynamics model, the transition matrix, prediction and update equations, and the Kalman gain matrix. The dynamics model describes the time-dependency of the state parameters; that is how the state parameters to be estimated change (e.g., linearly) from one state to another. The transition matrix $\underline{\Phi}_{k,k-1}$ is used to describe the change of the parameters from state $\hat{\underline{x}}_{k-1}$ (the state at time index $k-1$) to $\hat{\underline{x}}_k(-)$ (the state at time index k before updating) according to eqn. (Ap1.1):

$$\hat{\underline{x}}_k(-) = \underline{\Phi}_{k,k-1} \hat{\underline{x}}_{k-1}, \quad (\text{Ap1.1})$$

The sign(-) stands for the process of prediction before any observations at epoch k are used. The covariance matrix of the optimal estimate is $\underline{C}_k^x(-)$ at epoch k :

$$\underline{C}_k^x(-) = \underline{\Phi}_{k,k-1} \underline{C}_{k-1}^x \underline{\Phi}_{k,k-1}^T + \underline{C}_{k,k-1}^u, \quad (\text{Ap1.2})$$

where

$\underline{C}_{k,k-1}^u$ is the system noise covariance matrix describing the uncertainty in the dynamics model. Equations (Ap1.1) and (Ap1.2) are considered to be the prediction equations. As soon as observations at epoch k are available, we can form the Kalman filtering update equations:

$$\hat{\underline{x}}_k(+)=\hat{\underline{x}}_k(-)+\underline{K}_k[\underline{l}_k-\underline{A}_k\hat{\underline{x}}_k(-)], \quad (\text{Ap1.3})$$

where

$\hat{\underline{x}}(+)$ refers to the updated state,

\underline{K} is the Kalman gain matrix (weight matrix) describing how much weight we want to put on observations before the last update, and the observation since the last update,

\underline{l} is the current observation vector,

\underline{A} is the design matrix.

The covariance matrix of the updated optimal state estimates is:

$$\underline{C}_k^x(+)=[\underline{I}-\underline{K}_k\underline{A}_k]\underline{C}_k^x(-), \quad (\text{Ap1.4})$$

where

\underline{I} is the identity matrix,

Finally, the Kalman gain matrix can be obtained as:

$$\underline{K}_k=\underline{C}_k^x(-)\underline{A}_k^T[\underline{A}_k\underline{C}_k^x(-)\underline{A}_k^T+\underline{C}_k^e]^{-1}, \quad (\text{Ap1.5})$$

where

\underline{C}^e is the measurement noise describing the uncertainty in the observation model. A first-order Gauss-Markov stochastic process is used to describe the ionospheric variability:

$$x_{k+1} = m \cdot x_k + \omega_{GM} \quad (\text{Ap1.6})$$

where

ω_{GM} is a Gaussian random variable with zero mean, variance σ_{GM}^2 , and “m” is measure of correlation between adjacent states:

$$m = \exp\left[\frac{-\Delta t}{\tau_{GM}}\right], \quad (\text{Ap1.7})$$

and

$$E[\omega_{GM}^2] = \sigma_{GM}^2 (1 - m^2), \quad (\text{Ap1.8})$$

where

$E[.]$ is the statistical expectation operator,

τ_{GM} is the correlation time,

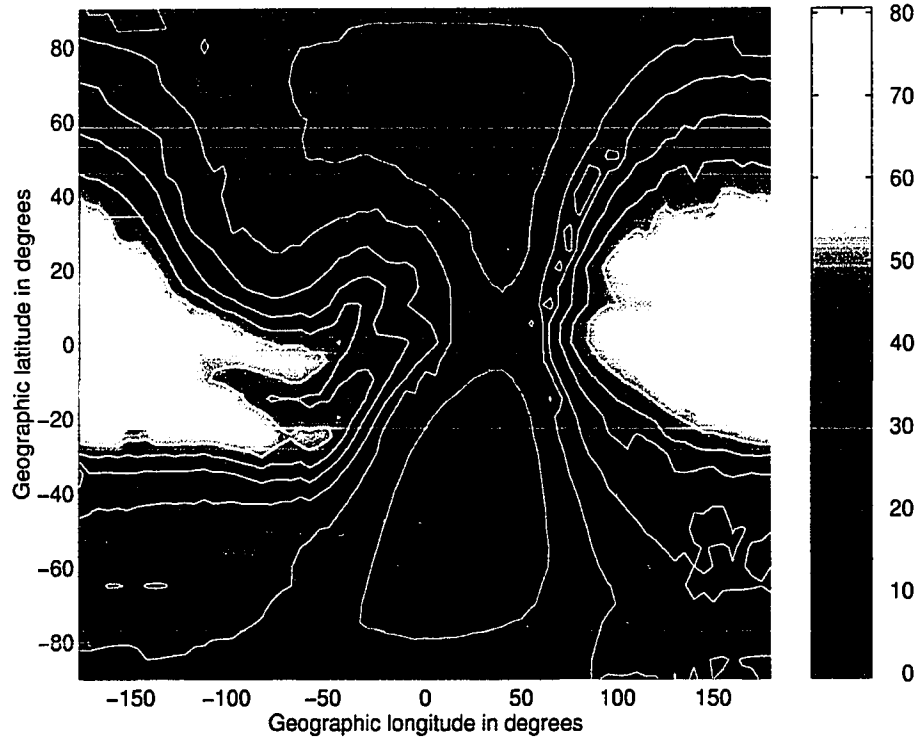
Δt is the interval between two state updates,

σ_{GM}^2 is the Gauss-Markov process noise variance.

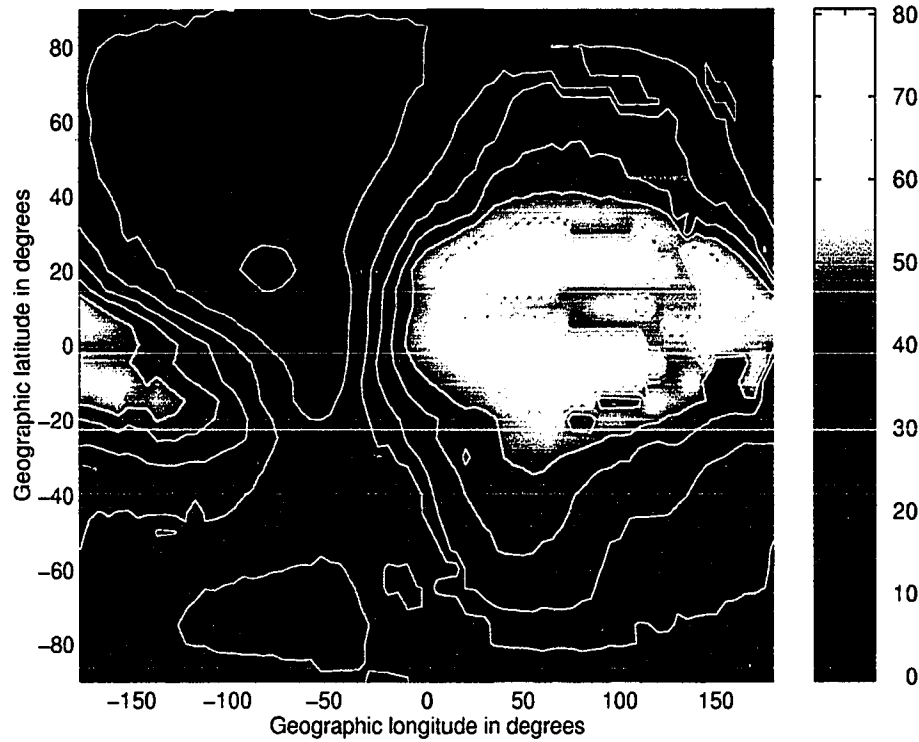
For my data processing, values chosen for these parameters are discussed in Section 4.2.2.

APPENDIX 2
THE UNB HOURLY GLOBAL IONOSPHERIC TOTAL ELECTRON CONTENT
MAPS

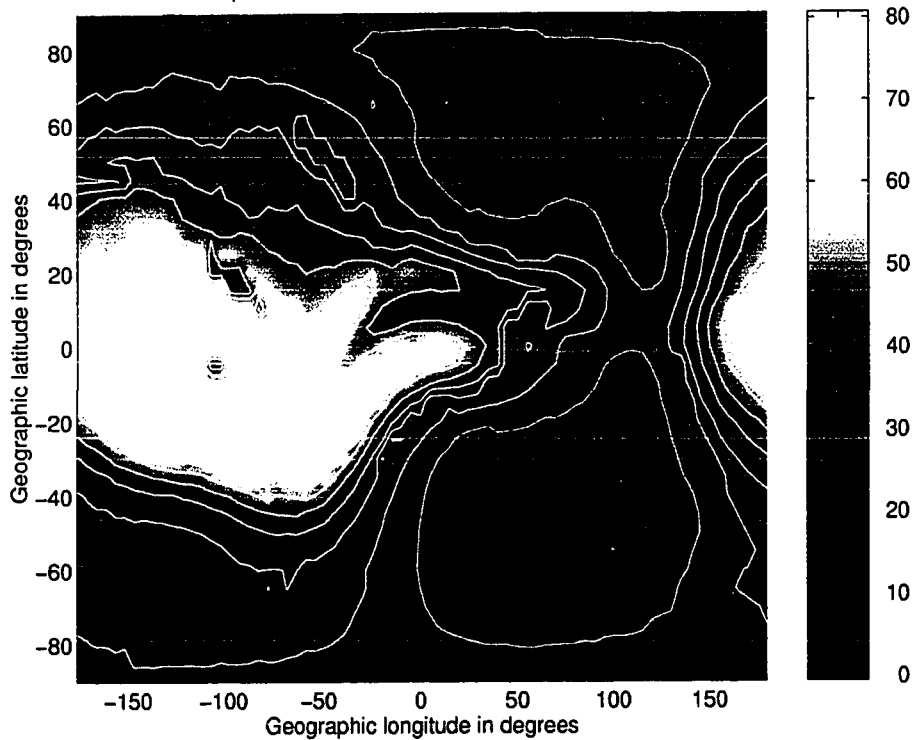
Global TEC Map in TECU for UT=02:00 of 13 March 1993 Using 33 IGS Stations



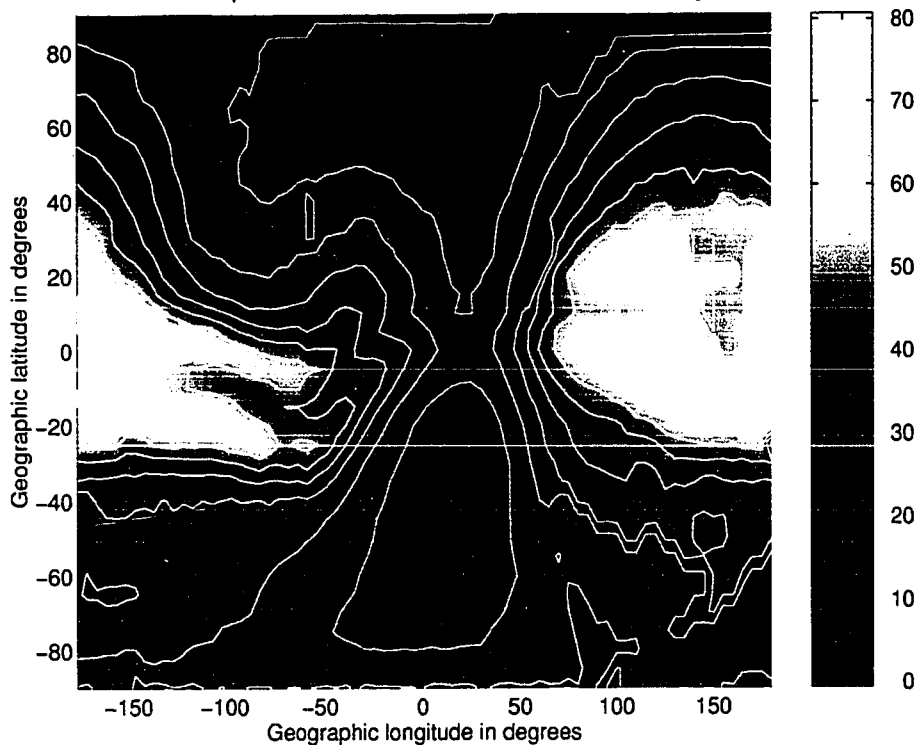
Global TEC Map in TECU for UT=08:00 of 13 March 1993 Using 33 IGS Stations



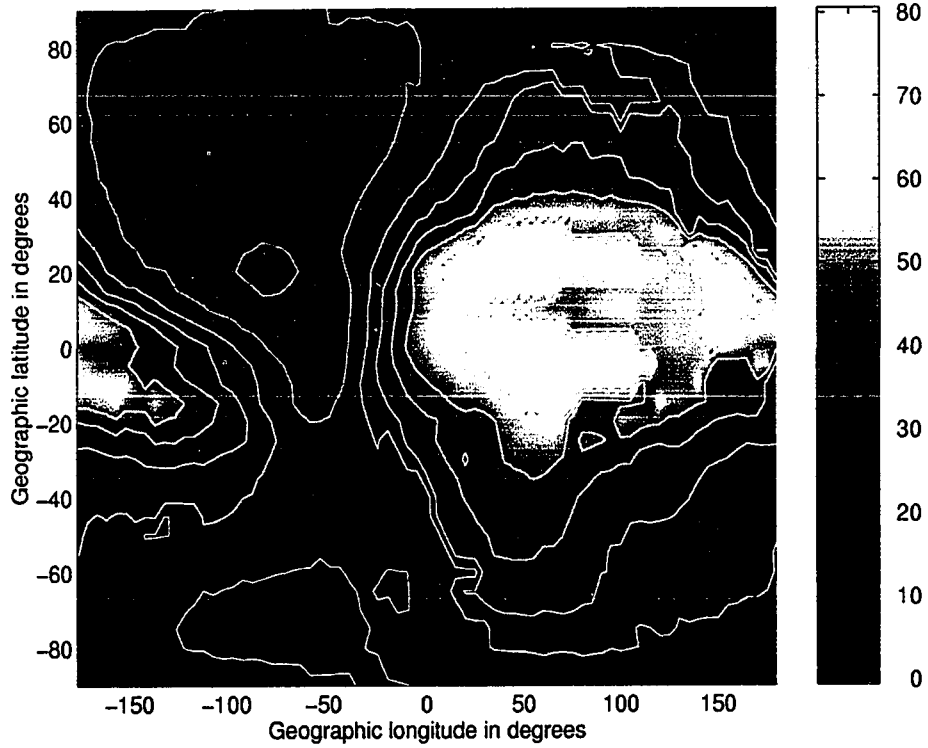
Global TEC Map in TECU for UT=21:00 of 13 March 1993 Using 33 IGS Stations



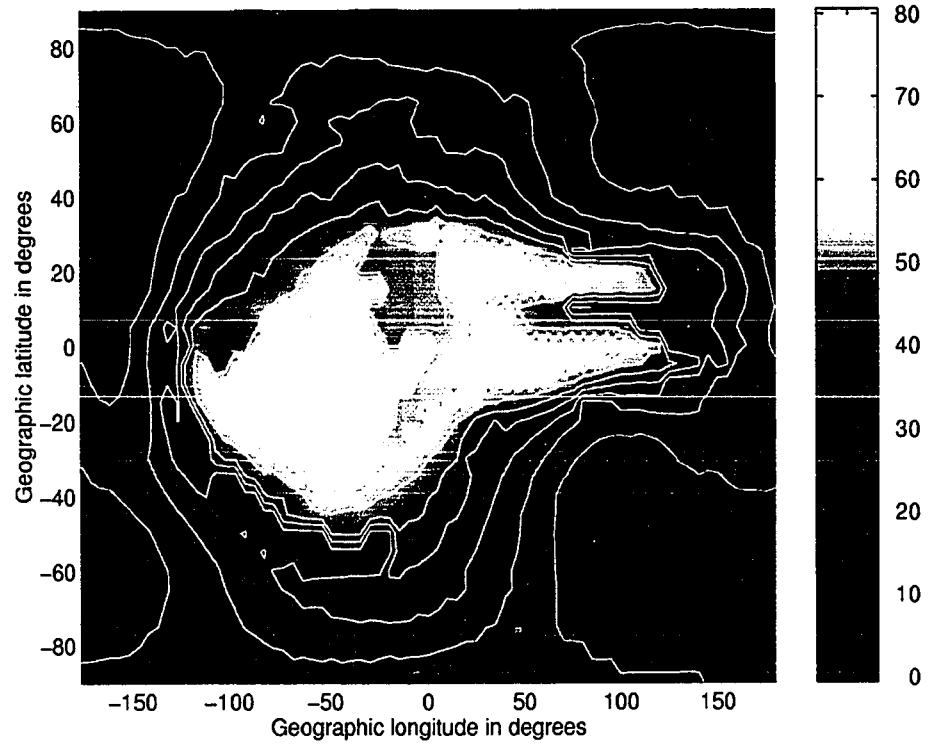
Global TEC Map in TECU for UT=03:00 of 14 March 1993 Using 33 IGS Stations



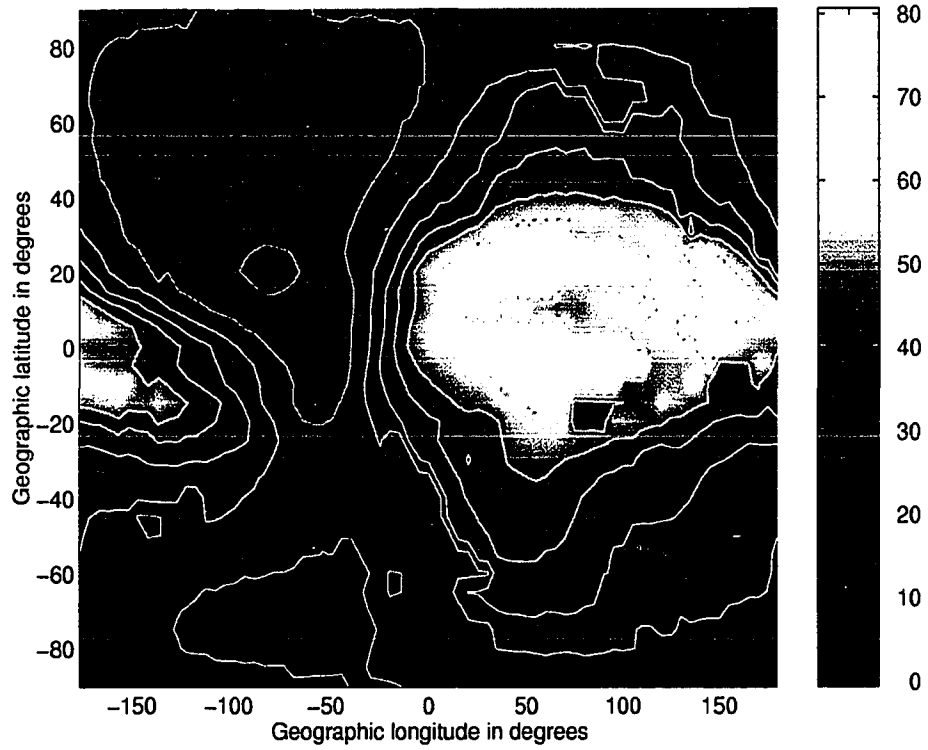
Global TEC Map in TECU for UT=08:00 of 14 March 1993 Using 33 IGS Stations



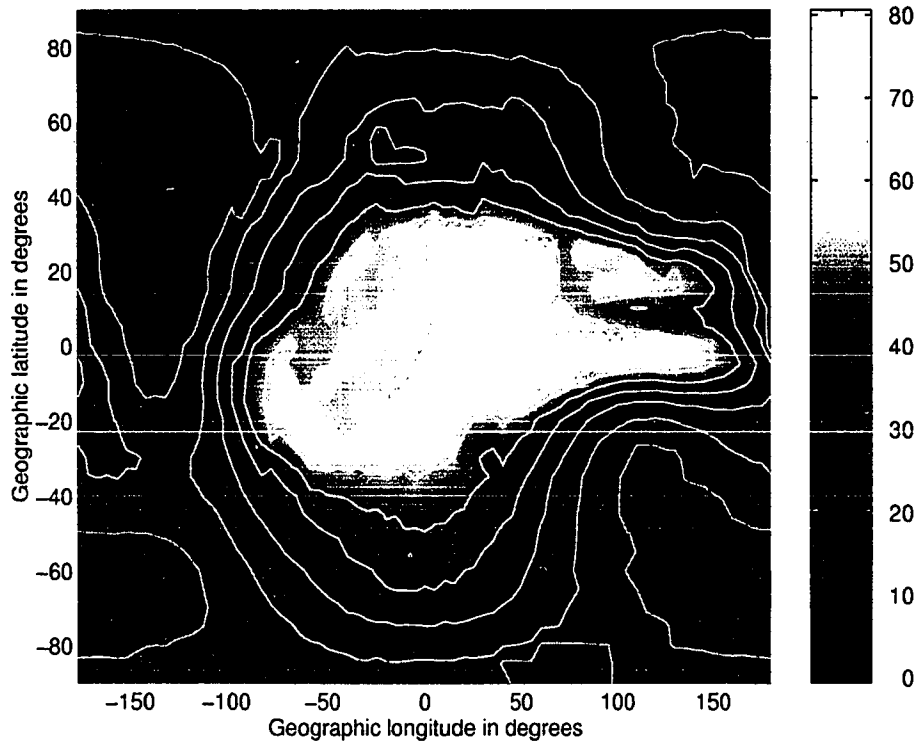
Global TEC Map in TECU for UT=15:00 of 14 March 1993 Using 33 IGS Stations



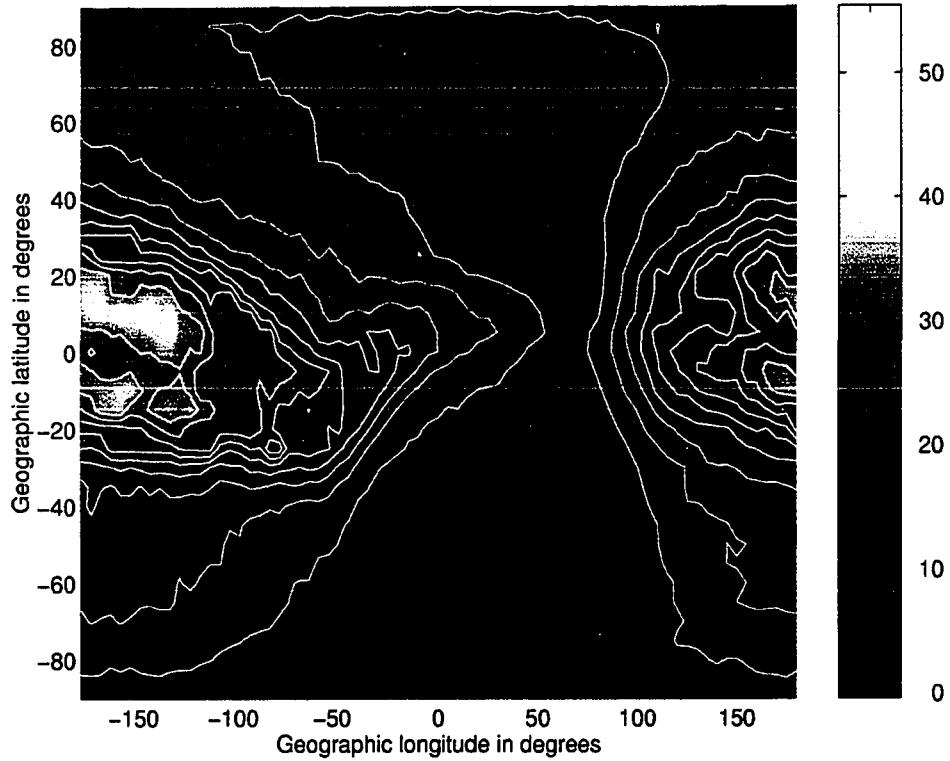
Global TEC Map in TECU for UT=08:00 of 15 March 1993 Using 33 IGS Stations



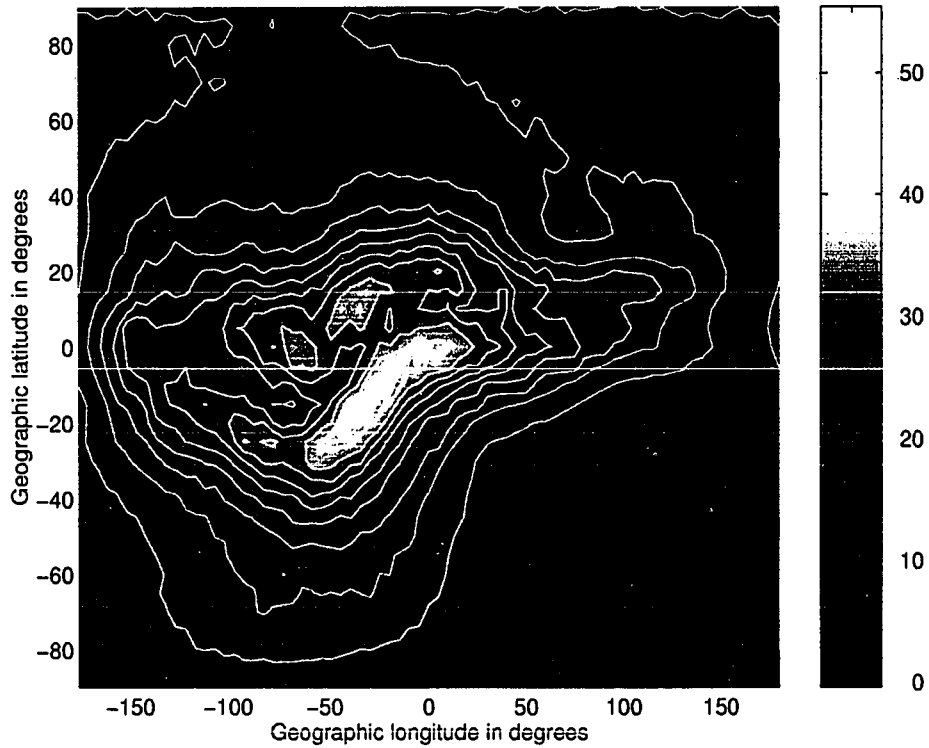
Global TEC Map in TECU for UT=13:00 of 15 March 1993 Using 33 IGS Stations



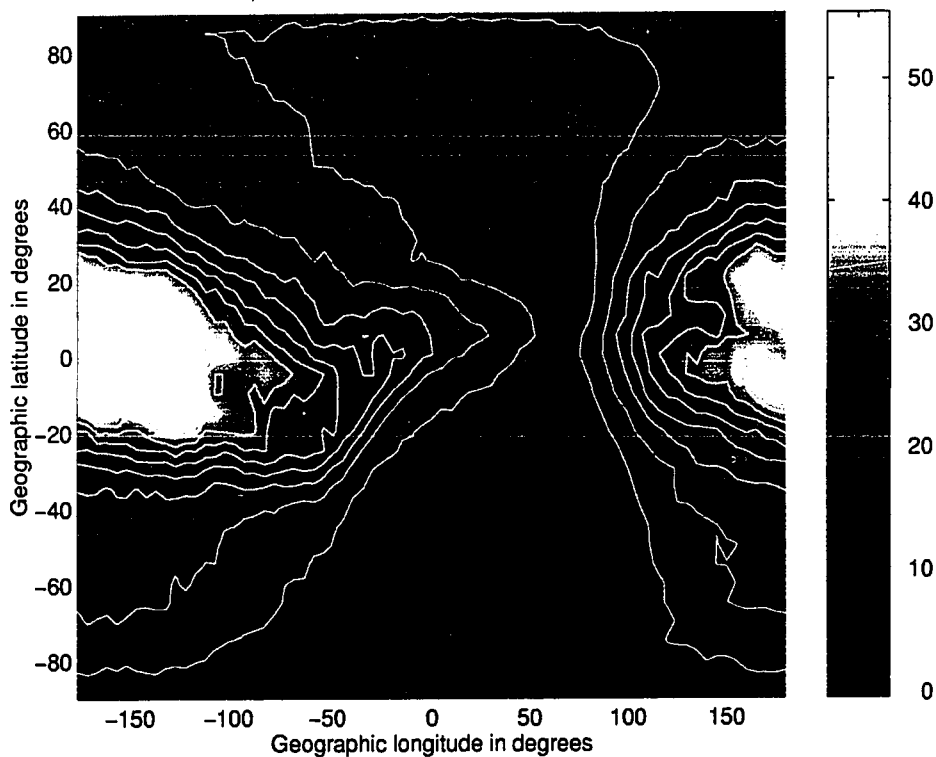
Global TEC Map in TECU for UT=00:00 of 6 April 1995 Using 74 IGS Stations



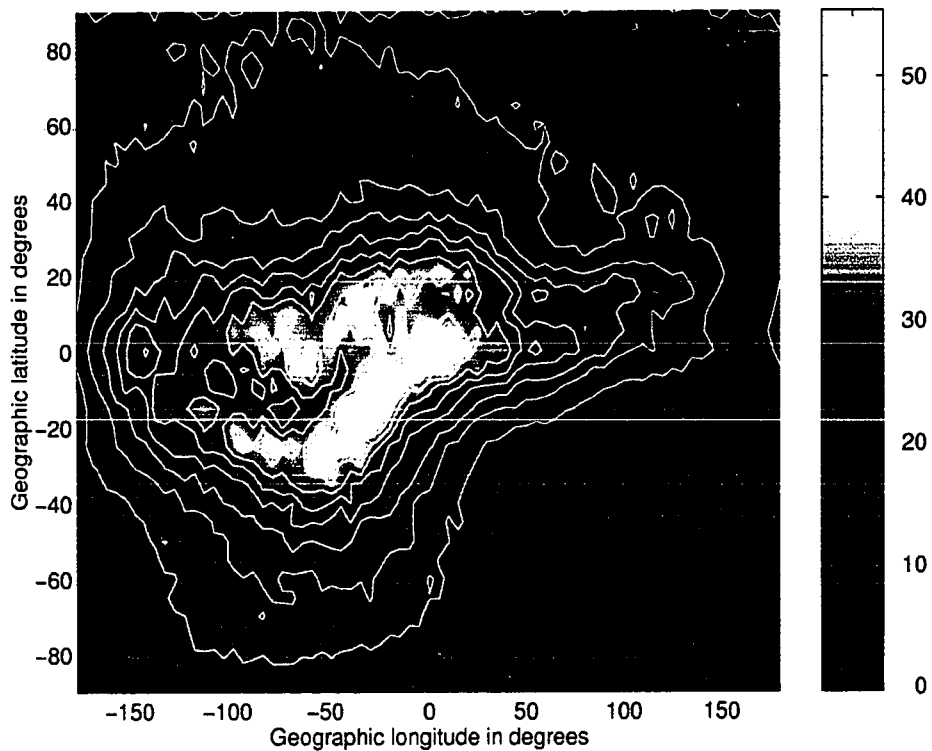
Global TEC Map in TECU for UT=17:00 of 6 April 1995 Using 74 IGS Stations



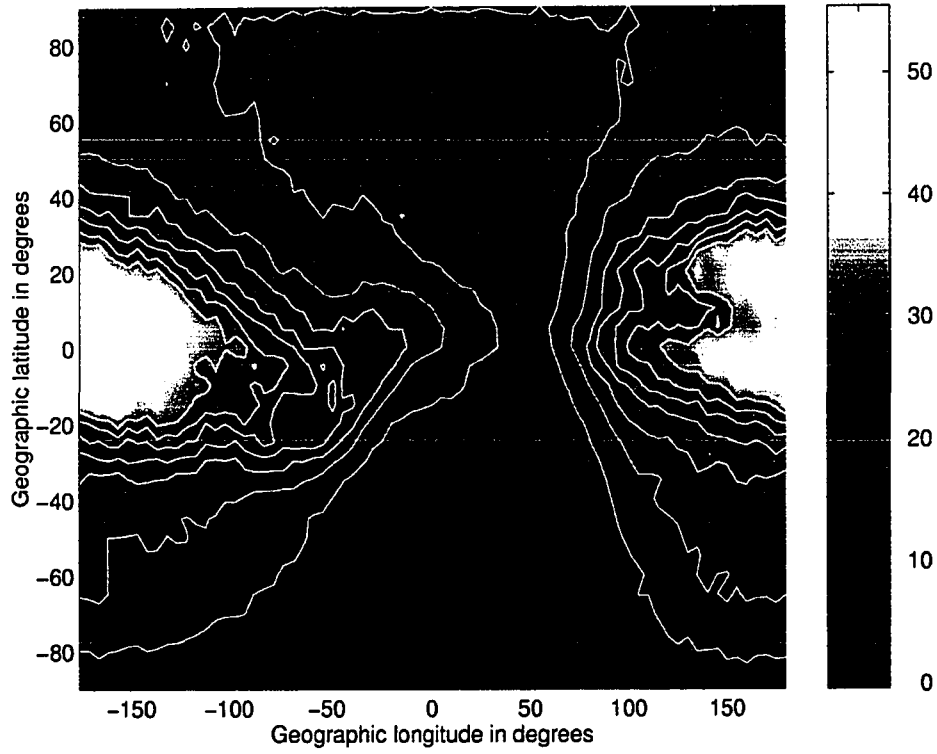
Global TEC Map in TECU for UT=00:00 of 7 April 1995 Using 74 IGS Stations



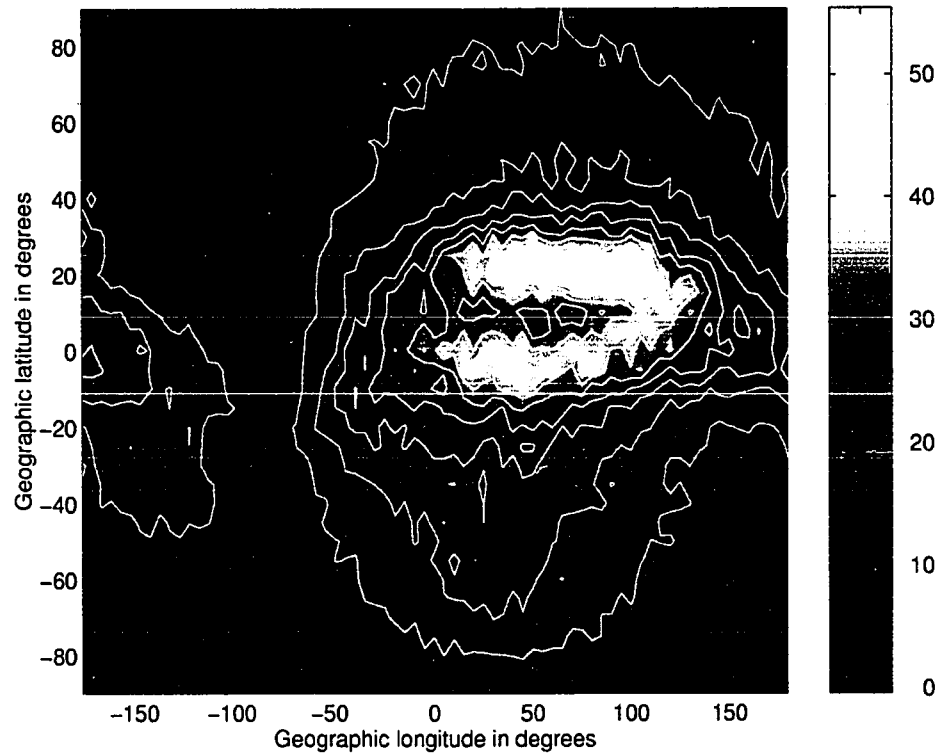
Global TEC Map in TECU for UT=17:00 of 7 April 1995 Using 74 IGS Stations



Global TEC Map in TECU for UT=01:00 of 8 April 1995 Using 74 IGS Stations

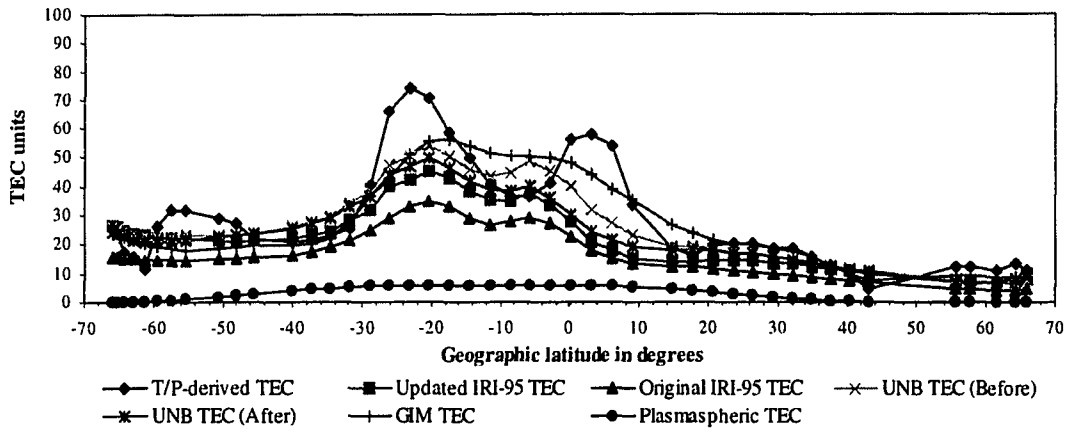


Global TEC Map in TECU for UT=10:00 of 8 April 1995 Using 74 IGS Stations

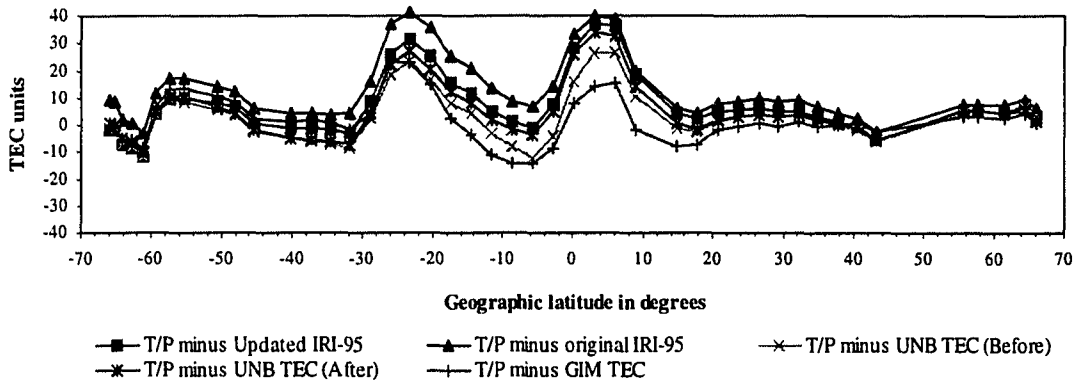


APPENDIX 3
COMPARISON OF UPDATED IRI-95 MODEL WITH OTHER INDEPENDENT
TECHNIQUES

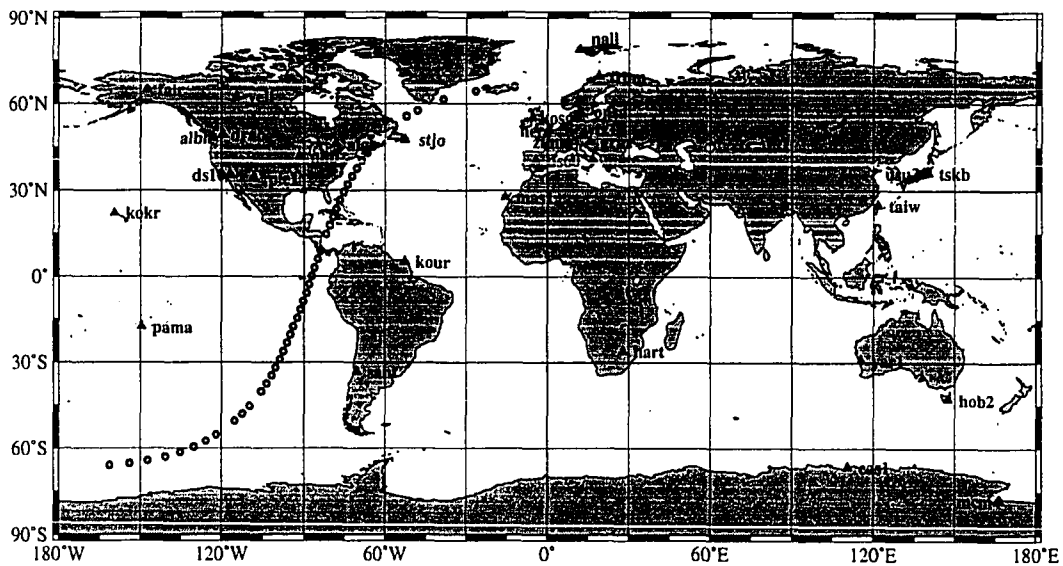
**TOPEX/Poseidon (T/P) Pass 07 between UT 5h 12m and 6h 06m of
13 March 1993**



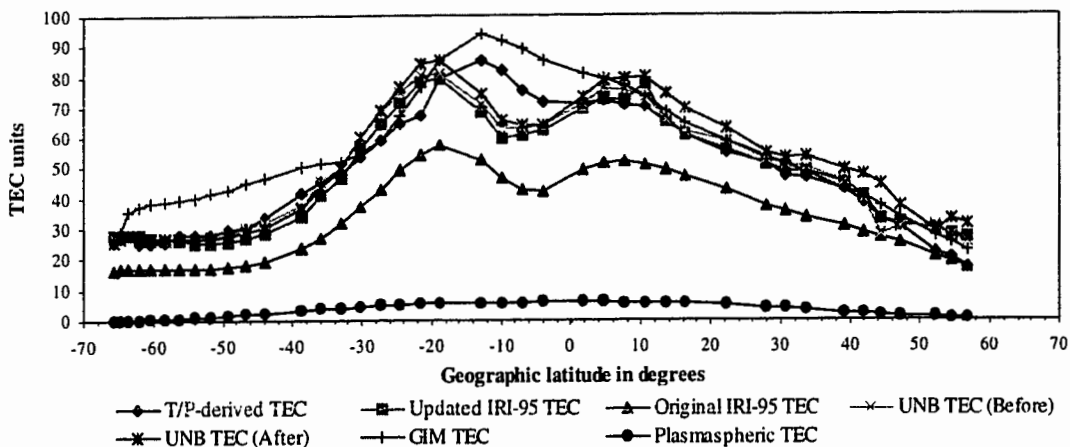
Differences in TECU for the Corresponding T/P Pass



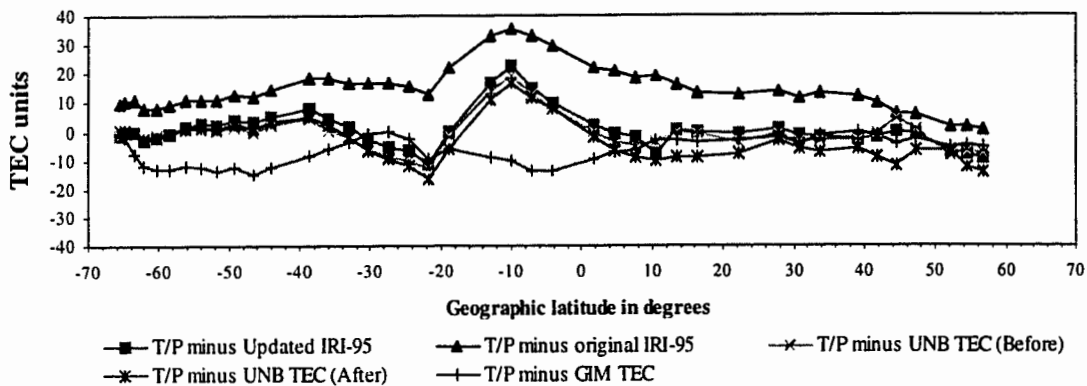
Corresponding T/P Ground Trajectory



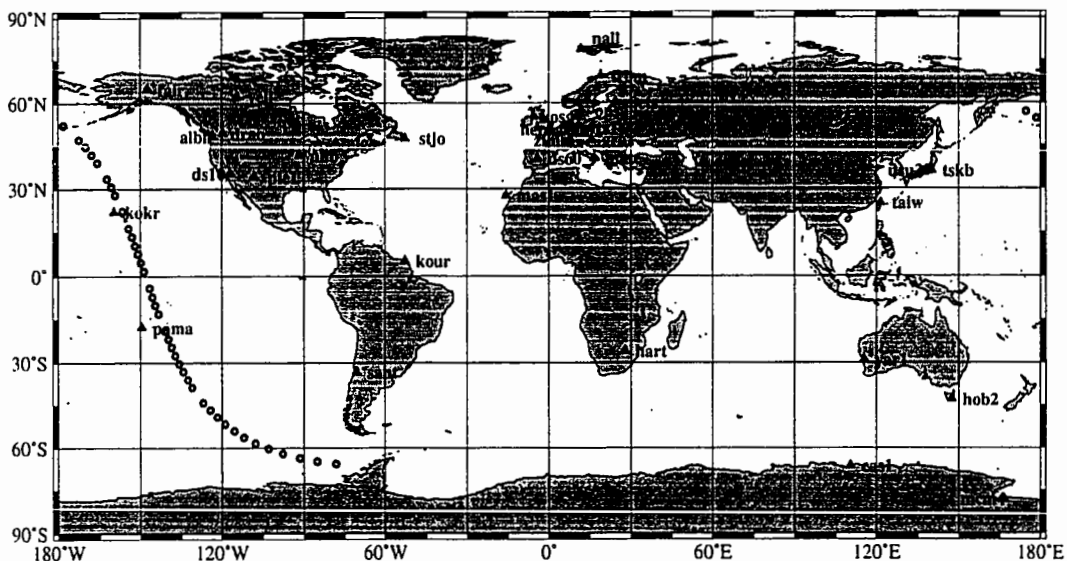
**TOPEX/Poseidon (T/P) Pass 24 between UT 21h 14m and 22h 01m
of 13 March 1993**



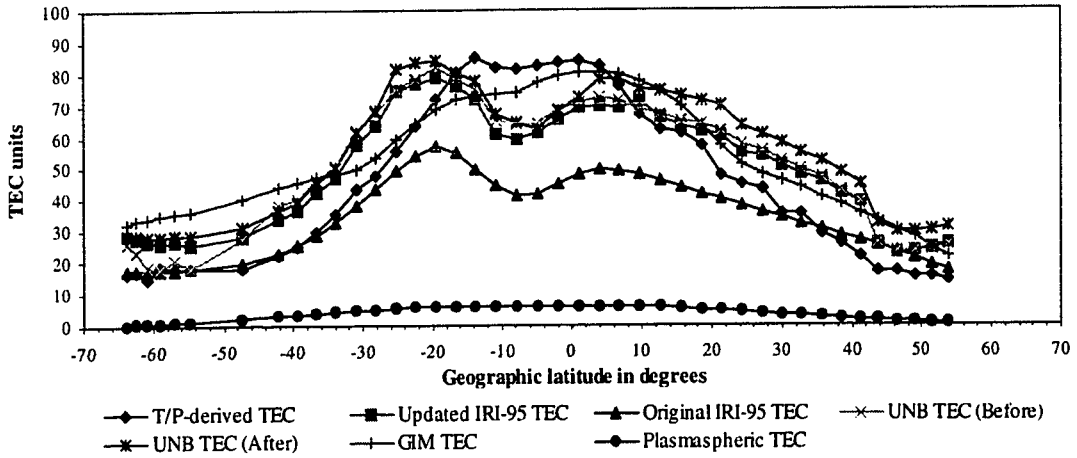
Differences in TECU for the Corresponding T/P Pass



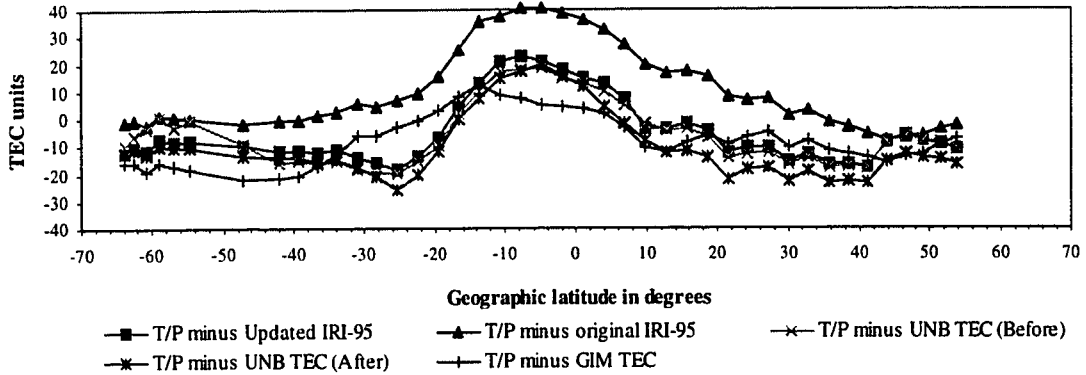
Corresponding T/P Ground Trajectory



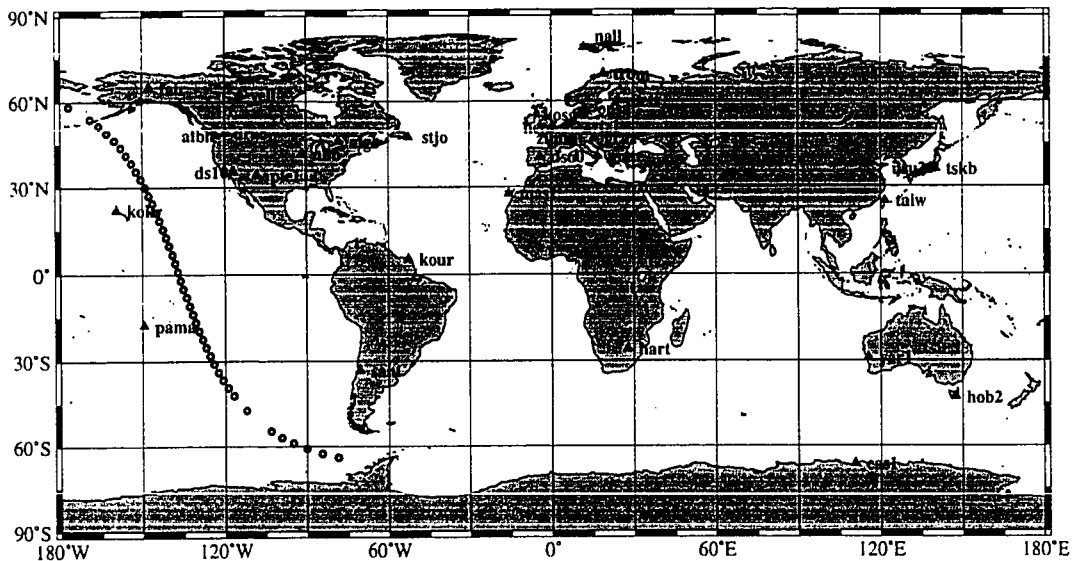
TOPEX/Poseidon (T/P) Pass 23 between UT 20h 4m and 20h 50m of 14 March 1993



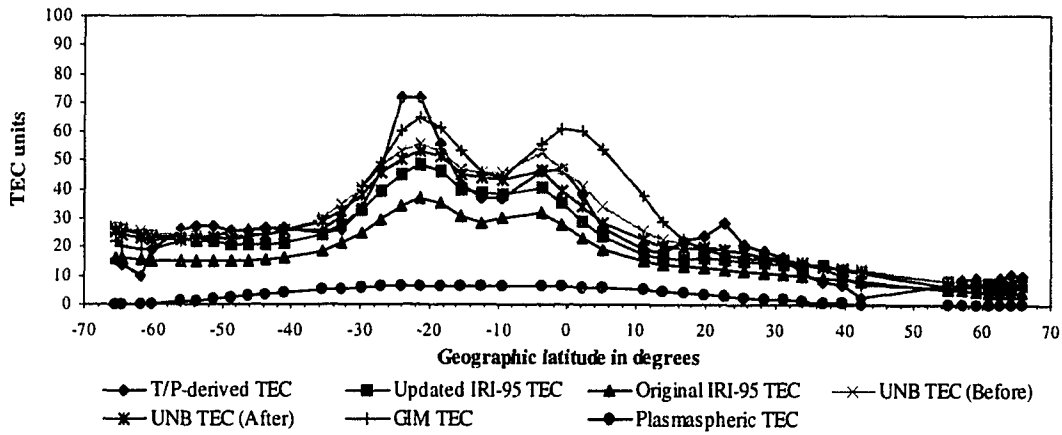
Differences in TECU for the Corresponding T/P Pass



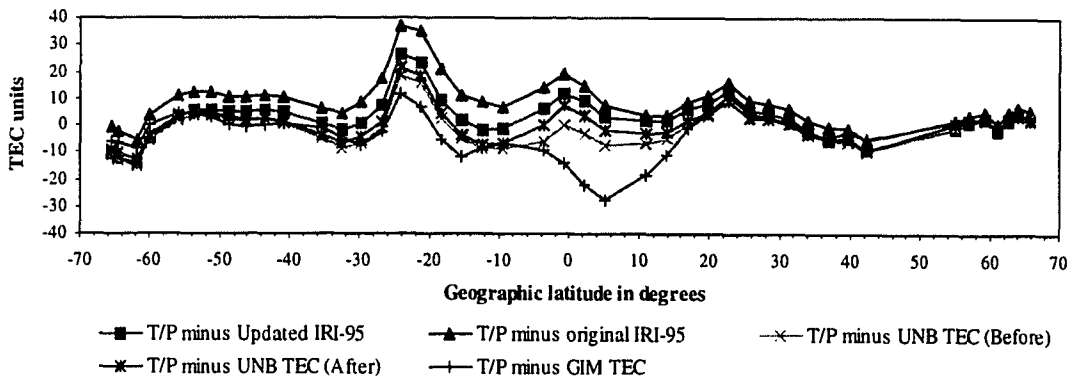
Corresponding T/P Ground Trajectory



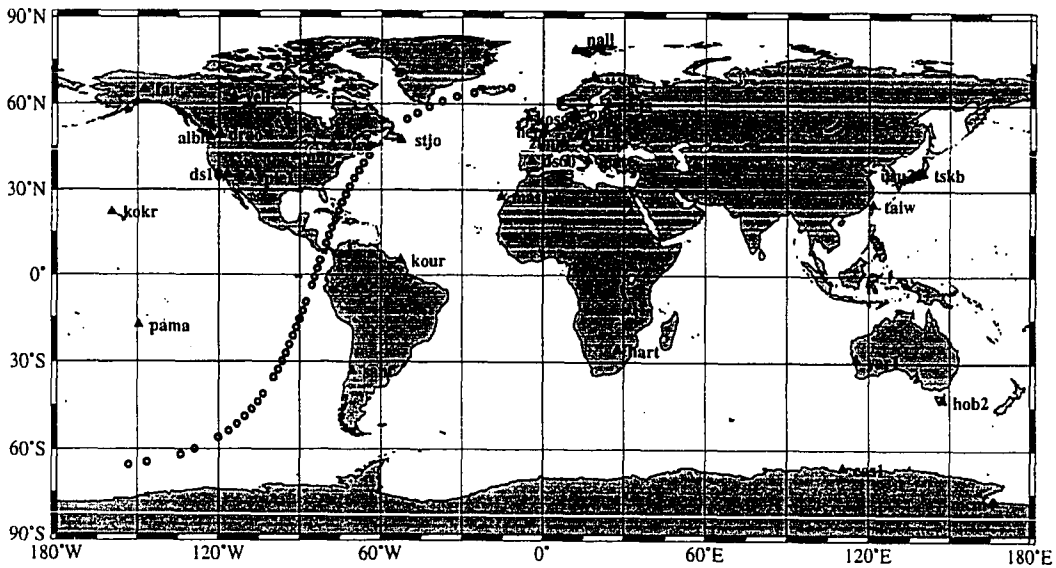
**TOPEX/Poseidon (T/P) Pass 06 between UT 4h 25m and 5h 18m of
15 March 1993**



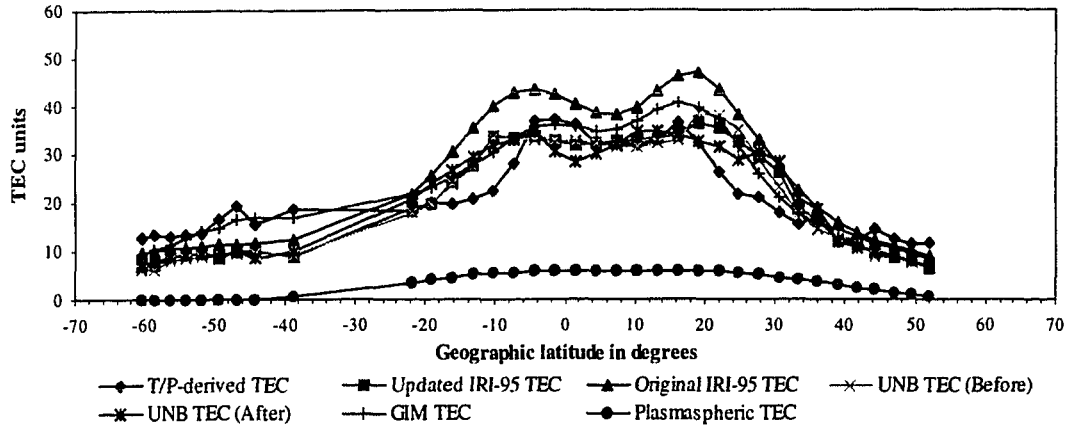
Differences in TECU for the Corresponding T/P Pass



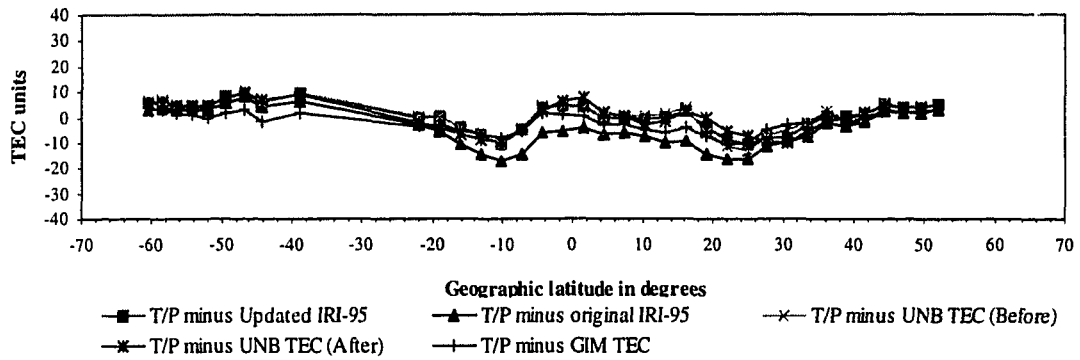
Corresponding T/P Ground Trajectory



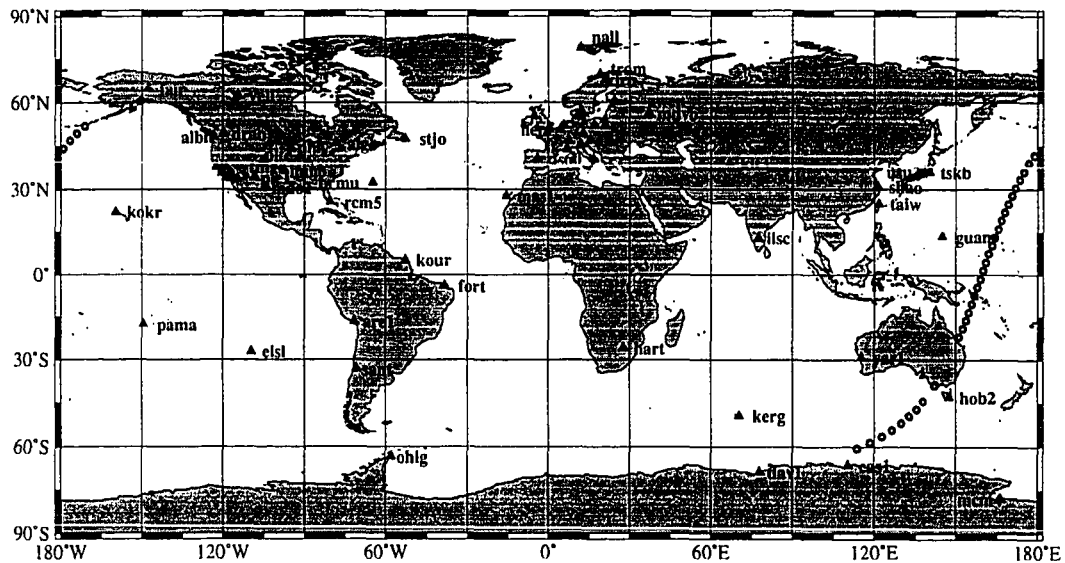
**TOPEX/Poseidon (T/P) Pass 04 between UT 2h 54m and 3h 35m of
6 April 1995**



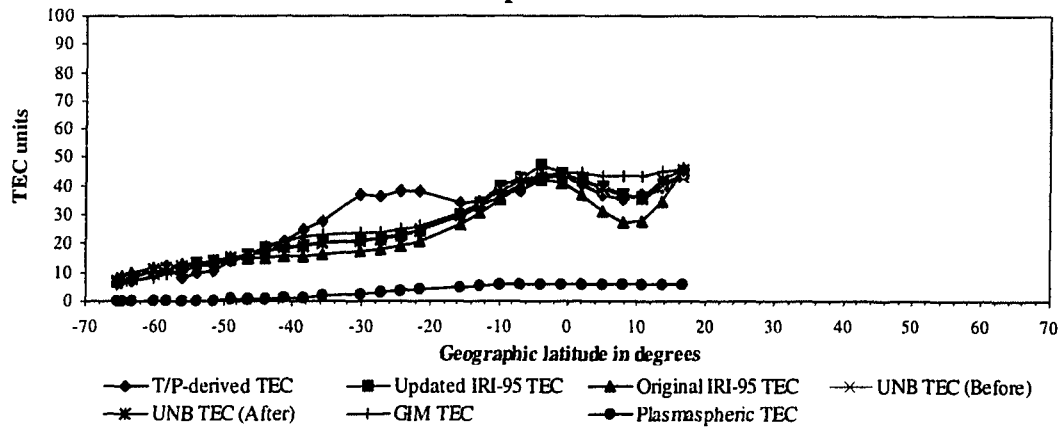
Differences in TECU for the Corresponding T/P Pass



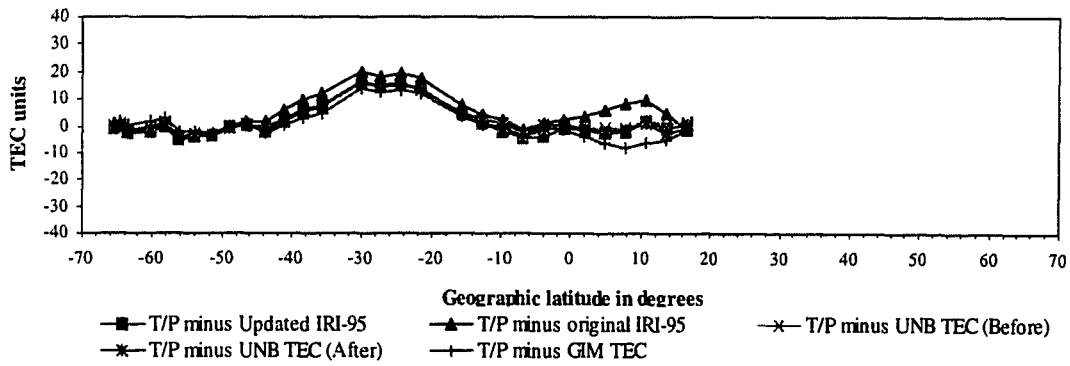
Corresponding T/P Ground Trajectory



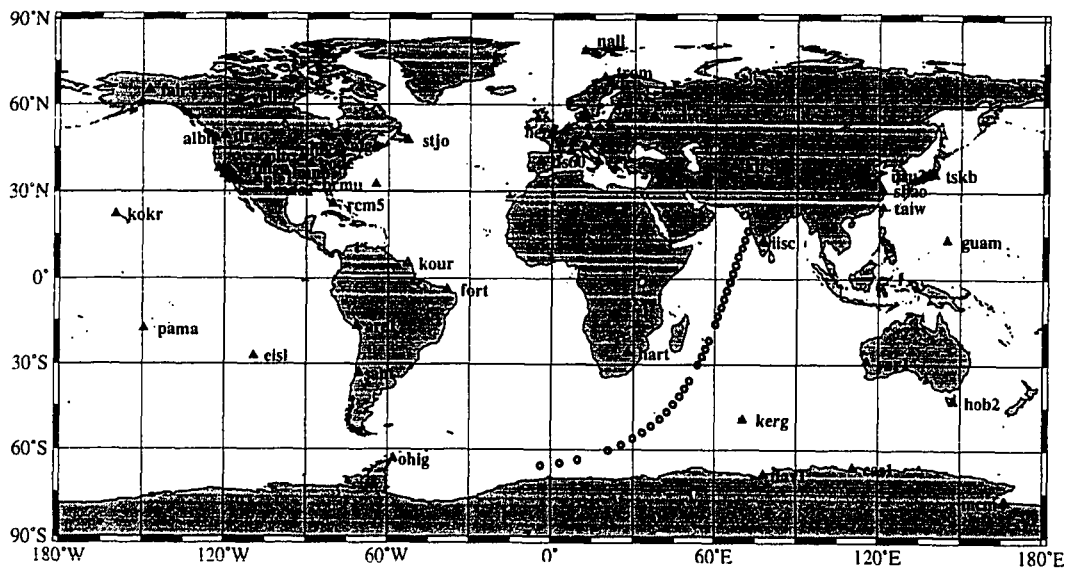
**TOPEX/Poseidon (T/P) Pass 11 between UT 8h 49m and 9h 21m of
7 April 1995**



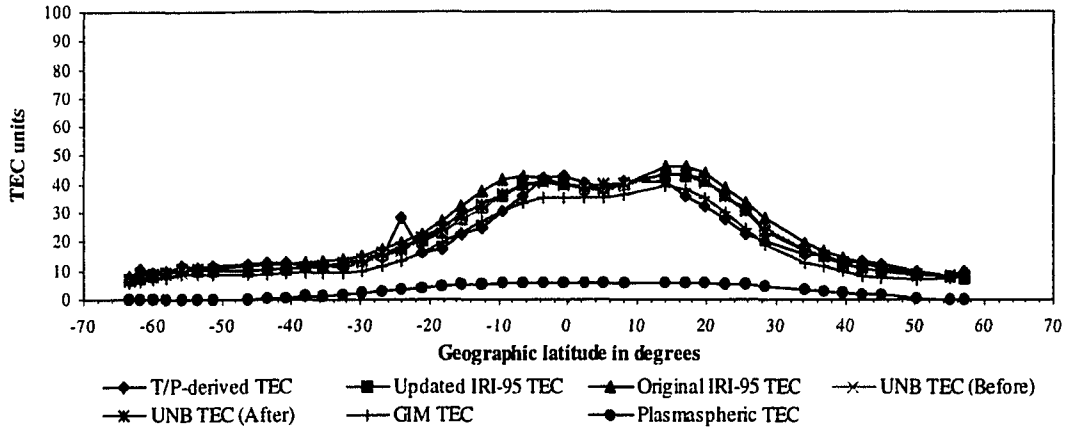
Differences in TECU for the Corresponding T/P Pass



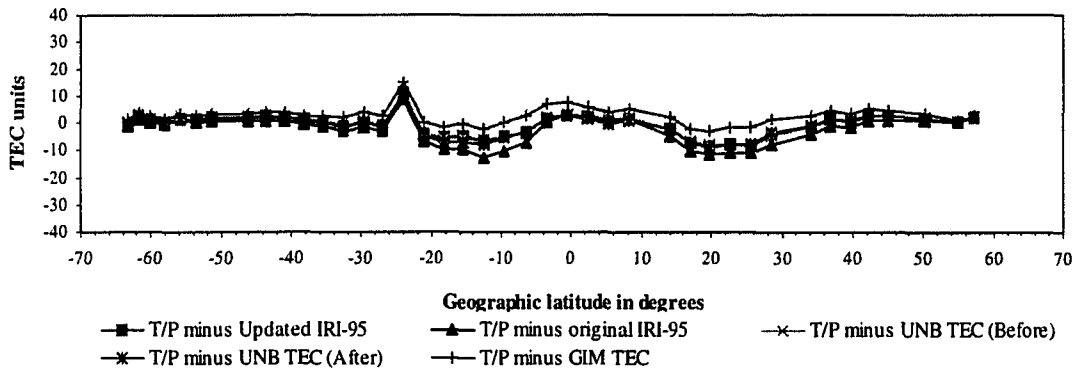
Corresponding T/P Ground Trajectory



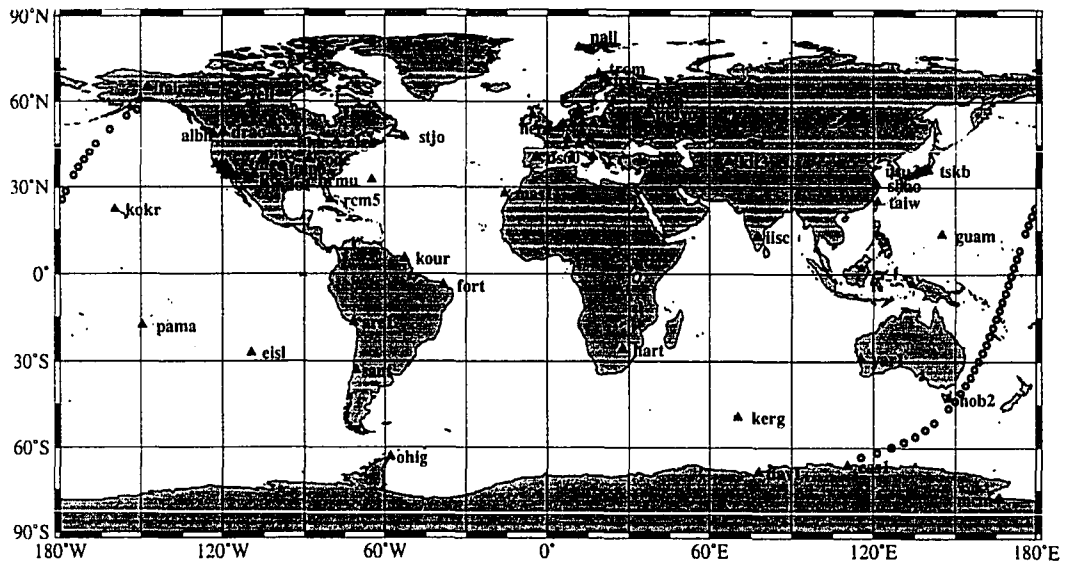
**TOPEX/Poseidon (T/P) Pass 03 between UT 1h 43m and 2h 28m of
8 April 1995**



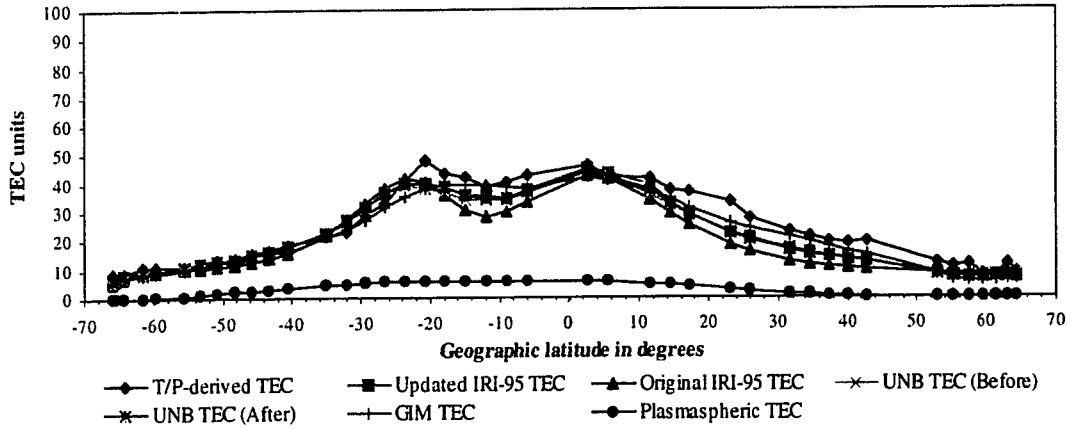
Differences in TECU for the Corresponding T/P Pass



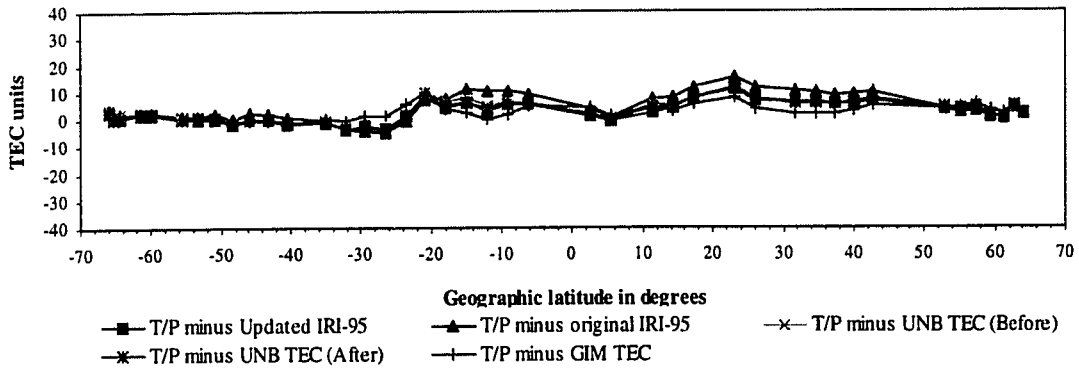
Corresponding T/P Ground Trajectory



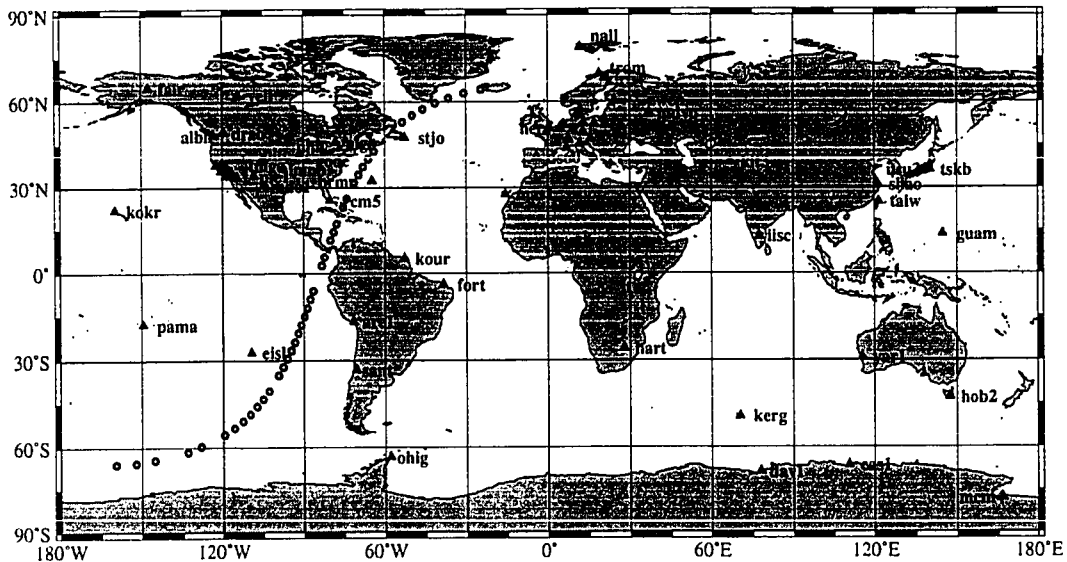
**TOPEX/Poseidon (T/P) Pass 21 between UT 18h 32m and 19h 24m
of 8 April 1995**



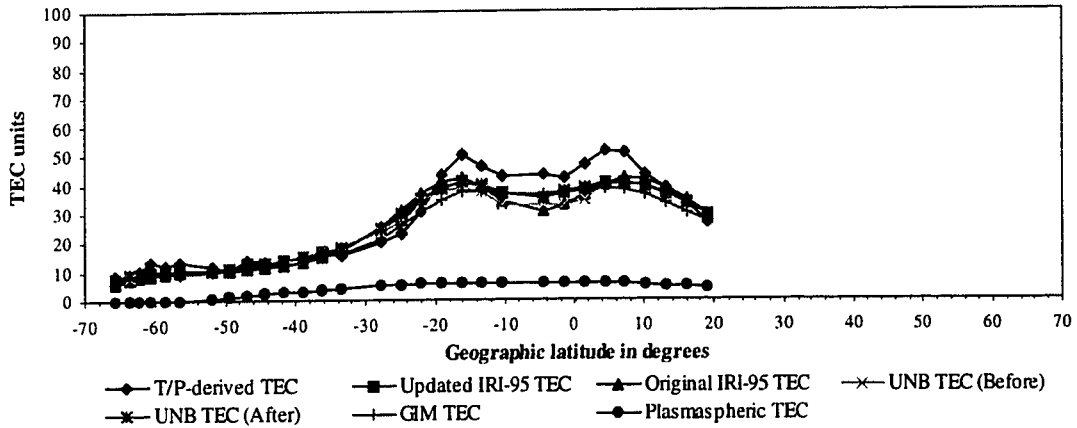
Differences in TECU for the Corresponding T/P Pass



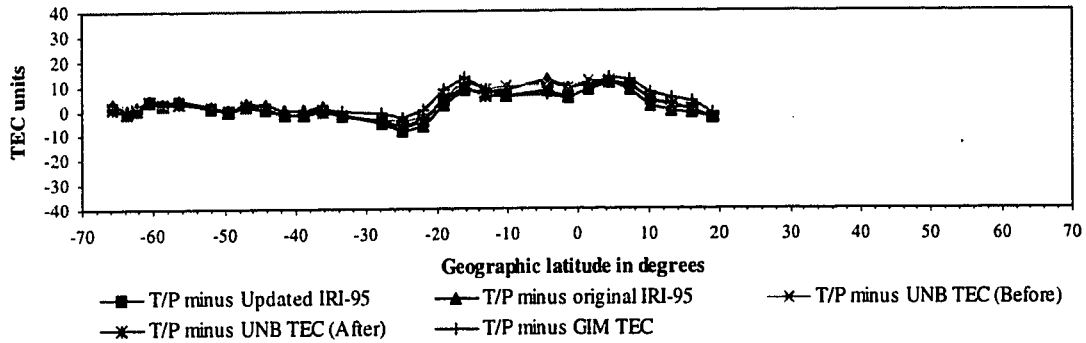
Corresponding T/P Ground Trajectory



**TOPEX/Poseidon (T/P) Pass 23 between UT 20h 25m and 20h 58m
of 8 April 1995**



Differences in TECU for the Corresponding T/P Pass



Corresponding T/P Ground Trajectory

